AKADEMIA GÓRNICZO-HUTNICZA IM. STANISŁAWA STASZICA W KRAKOWIE

FIELD OF SCIENCE: Engineering and technology

SCIENTIFIC DISCIPLINE: Environmental engineering, mining and energy

DOCTORAL DISSERTATION

Functional oxygen electrodes for Solid Oxide Cells based on Cu-containing perovskite-type oxides

Author: Keyun Li

Supervisor: prof. dr hab. inż. Konrad Świerczek

Completed at: AGH University of Krakow
Faculty of Energy and Fuels
Department of Hydrogen Energy

Kraków, 2024

Acknowledgments

This work was realized within the Opus project funded by the National Science Centre, Poland, (NCN) on the basis of the decision number UMO-2020/37/B/ST8/02097.

Raman spectroscopy measurements were conducted on the apparatus purchased with financial support from the AGH Excellence Initiative - Research University program (IDUB AGH, Action 8).

The author acknowledges the Polish National Agency for Academic Exchange NAWA, which sponsored a 3-month scientific internship abroad.

The international internship was realized at the Catalonia Institute for Energy Research IREC, Barcelona, Spain, specifically within the cooperation with the Laboratory of Nanoionics and Fuel Cells led by Prof. Albert Tarancón.

A part of the experiments was conducted using the research infrastructure of the AGH Centre of Energy, AGH University of Krakow.

Faithfully and sincerely, it is quite an enjoyment to recall the whole PhD study.

I regard it as undeniably challenging, but quite valuable and memorable at the same time. Throughout the whole doctoral study, there are endless things and people I should express my gratitude and appreciation.

First of all, I would like to thank Prof. Konrad Świerczek, who has guided me along the research career of PhD, his expertise and devotion to the research have led me into the bigger world in the energy materials.

Secondly, I am very grateful to every lab member, especially, Prof. Wojciech Zając, Dr. Piotr Winiarz, Dr. Agnieszka Brzoza-Kos, Dr. Juliusz Dąbrowa, Dr. Marta Gajewska and Dr. Anna Stępień, who have helped and inspired me along the whole PhD career. Moreover, many of my coworkers in the lab, and friends in AGH University of Krakow, they are always nice and warm-hearted.

Last but not least, I would like thank my family members, they give me the strongest support whenever I need help.

Table of Contents

Abstract xi

Streszczenie xv

Lists of abbreviations and symbols xix

Introduction ..... **- 1 -**

1. Energy resources and transitions - historical perspective ..... **- 3 -**

2. Electricity and its production ..... **- 9 -**

2.1. Coal ..... - 14 -

2.2. Natural gas ..... - 15 -

2.3. Oil ..... - 17 -

2.4. Hydropower ..... - 17 -

2.5. Nuclear power ..... - 18 -

2.6. Wind energy ..... - 20 -

2.7. Solar power ..... - 21 -

2.8. Combined heat and power (CHP) generation ..... - 22 -

3. Hydrogen and its role in the energy transition ..... **- 25 -**

3.1. Physicochemical properties of hydrogen ..... - 26 -

3.2. Production of hydrogen ..... - 27 -

3.3. Hydrogen storage ..... - 33 -

3.4. Contemporary and future hydrogen applications ..... - 36 -

4. Introduction of fuel cells, with an emphasis on Solid Oxide cells and oxygen electrode materials ..... - 39 -

4.1. Solid Oxide (Fuel) Cells ..... - 43 -

4.2. Perovskite oxides for SOCs oxygen electrodes ..... - 50 -

5. Copper as the B-site element in perovskite-type oxides ..... - 57 -

6. Aim of the work and initial hypotheses ..... - 63 -

6.1. Objectives of this thesis ..... - 63 -

6.2. Related literature-based hypotheses ..... - 65 -

Experimental methods **..... - 67 -**

7. Methodology ..... - 69 -

7.1. Synthesis methods ..... - 69 -

7.2. Calculations of the entropy metric for the multicomponent samples ..... - 75 -

7.3. Samples characterization ..... - 76 -

7.3.1. X-ray diffraction ..... - 76 -

7.3.2. Oxygen stoichiometry determination ..... - 79 -

7.3.3. Raman spectroscopy ..... - 80 -

7.3.4. Density Functional Theory (DFT) calculations ..... - 81 -

7.3.5. Electrical conductivity measurements ..... - 81 -

7.3.6. Chemical compatibility tests ..... - 82 -

7.3.7. Scanning electron microscopy (SEM) studies ..... - 83 -

7.3.8. Transmission electron microscopy (TEM) studies ..... - 83 -

7.4. Preparation and characterization of electrochemical properties of cells ..... - 84 -

7.4.1. Manufacturing of symmetrical cell ..... - 84 -

7.4.2. Manufacturing of electrolyte- and anode-supported full cells ..... - 85 -

7.4.3. Measurements of electrochemical properties of cells ..... - 86 -

7.4.4. Distribution of Relaxation Times (DRT) analysis ..... - 87 -

Results and discussion **..... - 89 -**

8. Physicochemical properties of $La_{1.5}Ba_{1.5}Cu_3O_{7\pm\delta}$..... - 91 -

9. Physicochemical properties of $GdBa_{0.5}Sr_{0.5}Co_{2-x}Cu_xO_{5+\delta}$ ..... - 103 -

10. Physicochemical properties of $La_{0.6}Sr_{0.4}Ni_{0.15}Mn_{0.15}Fe_{0.15}Cu_xCo_{0.55-x}O_{3-\delta}$. - 117 -

11. Electrochemical properties of the developed oxygen electrodes in IT-SOCs..... ..... - 131 -

11.1. $La_{1.5}Ba_{1.5}Cu_3O_{7\pm\delta}$ as the oxygen electrode material ..... - 131 -

11.2. $GdBa_{0.5}Sr_{0.5}Co_{2-x}Cu_xO_{5+\delta}$ as the oxygen electrode materials ..... - 137 -

11.3. $La_{0.6}Sr_{0.4}Ni_{0.15}Mn_{0.15}Fe_{0.15}Cu_xCo_{0.55-x}O_{3-\delta}$ as the oxygen electrode materials .... - 152 -

12. Improvement of selected oxygen electrodes by electrospinning..... - 161 -

12.1. Electrospun GBSCC0911 applied as the oxygen electrode material..... - 161 -

12.2. Electrospun LSNMFCC0550 and LSNMFCC2035 applied as the oxygen electrode materials ..... - 166 -

13. Conclusions..... - 173 -

13.1. Perspectives ..... - 176 -

References..... - 177 -

Abstract

This dissertation is dedicated to studies and development of the functional oxygen electrodes for Solid Oxide Cells (SOCs) based on perovskite-type materials, in which expensive and toxic cobalt was either partially or fully replaced by the copper element. The feasibility of such doping is analyzed especially concerning the intermediate temperature range of application, 600-800 °C, in the so called IT-SOCs.

The thesis comprises three main parts, with the initial three chapters discussing the energy resources and the previous energy transitions, role of the electricity in the current society, and emergence of hydrogen as a new energy carrier, respectively. This is followed by the chapter 4, in which fuel cells are presented, with a special emphasis on the SOCs and oxygen electrodes used in their construction. Finally, copper is introduced as a candidate dopant element in perovskite-type oxides. The presented overview in these *Introduction* chapters 1-4 clearly shows that there is an enormous demand for the green energy, which will further grow in the future. The IT-SOCs technology, which can provide reversible and effective energy conversion between (surplus) electricity and hydrogen, can be regarded as one of the most promising, clean energy options. It is expected to play a key role in the ongoing energy transition toward the renewable energy resources, and should help to achieve the Net Zero Emissions goal. However, addressing the current drawbacks of the IT-SOCs is of a great importance, and it appears that different problems associated with the oxygen electrode materials constitute the main hinderances for such cells, preventing them from being highly-efficient, stable, and manufactured at cheaper costs. It can be stated that one of the fundamental issues, which must be resolved, is to tackle the high reliance on cobalt element in the current oxygen electrode materials. Copper, as a common and cheaper chemical element, can be possibly used as the alternative to replace cobalt to a different extent, since it features suitable characteristics, and may yield doped materials with comparable electrocatalytic performance (chapter 5).

Based on the presented considerations, the main idea and initial motivation related to the implemented studies are stated in the chapter 6, with the specific aim to develop new types of the complex perovskite-type oxides, having either limited Co content, or Co-free alternatives, which possess suitable set of the physicochemical properties, and exhibit satisfactory electrocatalytic features, so that they can be applied to prepare oxygen electrodes for IT-SOCs. Three different groups of candidate oxygen electrode materials were selected, including Co-free $La_{1.5}Ba_{1.5}Cu_3O_{7\pm\delta}$, Cu-doped $GdBa_{0.5}Sr_{0.5}Co_{2-x}Cu_xO_{5+\delta}$, as well as $La_{0.6}Sr_{0.4}Ni_{0.15}Mn_{0.15}Fe_{0.15}Cu_xCo_{0.55-x}O_{3-\delta}$ with the multicomponent occupancy at the B-site.

The related information about synthesis methods (including sol-gel, solid-state, and electrospinning routes) and characterization techniques are presented in the *Experimental methods* section (chapter 7). Details are included about the conducted X-ray diffraction experiments at room temperature and high temperatures, microstructural studies, oxygen nonstoichiometry evaluation, thermogravimetric analysis, Raman spectroscopy measurements, as well as Density Functional Theory calculations, electrical conductivity measurements, and chemical compatibility tests. Also, comprehensive data are provided

concerning manufacturing of symmetrical and full cells with oxygen electrodes based on the selected Cu-containing materials. The chapter is further supplemented with methodologies concerning evaluation of the electrocatalytic performance, including electrode polarization resistance determination, as well as advanced analysis by the Distribution of Relaxation Times method.

The obtained experimental data are discussed in the *Results and discussion* section comprising chapters 8-10, with physicochemical properties of the three studied systems, and chapters 11 and 12, presenting the electrochemical data for the manufactured cells, respectively. Firstly, $La_{1.5}Ba_{1.5}Cu_3O_{7\pm\delta}$ oxide is characterized in details (chapter 8). The material can be prepared by the common sol-gel and solid-state synthesis methods at temperatures below 1000 °C in air. It demonstrates an interesting, triple perovskite-type structure, with particular La/Ba and oxygen sublattice occupancies. It also exhibits good thermal stability up to 900 °C, which is sufficient for the operation of IT-SOCs. $La_{1.5}Ba_{1.5}Cu_3O_{7\pm\delta}$ shows suitable chemical compatibility with the commonly used $La_{0.8}Sr_{0.2}Ga_{0.8}Mg_{0.2}O_{3-\delta}$ (LSGM) electrolyte material, indicating the feasibility of manufacturing the electrode layers. This is further confirmed by the sufficient total electrical conductivity, and moderate thermal expansion coefficient, as compared to the Co-based perovskite materials. The electrode layer sintering temperature is low, and can be further optimized (800 °C). The performed characterization of the electrochemical properties of the $La_{1.5}Ba_{1.5}Cu_3O_{7\pm\delta}$ oxygen electrode on the LSGM electrolyte indicate polarization resistance value as low as 0.019 Ω cm^2 at 750 °C. The results of a full cell show that a peak power density over 530 mW cm^{-2} can be obtained at 800 °C, but notably, at lower temperatures, over 160 mW cm^{-2} and 250 mW cm^{-2} can be achieved, respectively at 600 °C and 650 °C. The electrode shows also good performance in the electrolysis mode. Overall, the results confirm that it is feasible to develop the totally Co-free oxygen electrode material that can maintain excellent electrocatalytic performance at the intermediate temperatures.

In the second studied system (chapter 9), $GdBa_{0.5}Sr_{0.5}Co_{2-x}Cu_xO_{5+\delta}$ series of oxides is subsequently proposed. The materials exhibit the double perovskite-type structure, and can be prepared by the sol-gel route. However, higher Cu content makes the synthesis problematic, and as confirmed by the X-ray diffraction results, the phase-pure samples can be synthesized when the x is equal to or lower than 1.15. At the same time, since decreasing of the cobalt content is of importance, the final selected compositions are in the range of $1 \leq x \leq 1.15$. As documented by the characterization of physicochemical properties, $GdBa_{0.5}Sr_{0.5}Co_{2-x}Cu_xO_{5+\delta}$ oxides maintain the tetragonal symmetry from room temperature up to 1000 °C in air. Importantly, their thermal expansion coefficients are still under $20 \cdot 10^{-6}$ K^{-1} at elevated temperatures, which is remarkable for such Co-containing oxides. They also demonstrate adequate values of the total electrical conductivity and good chemical compactivity with LSGM and $Ce_{0.9}Gd_{0.1}O_{2-\delta}$ (GDC) electrolyte materials. In the electrochemical properties characterizations, the composition with a relatively high copper content, $GdBa_{0.5}Sr_{0.5}Co_{0.9}Cu_{1.1}O_{5+\delta}$, turns out to yield the lowest polarization resistance value of 0.017 Ω cm^2 at 850 °C, which proves effectiveness of the undertaken strategy of cobalt substitution with copper. Moreover, with the adopted Distribution of Relaxation Times analysis, the rate-limiting step of operation of the

$GdBa_{0.5}Sr_{0.5}Co_{0.9}Cu_{1.1}O_{5+\delta}$ electrode is identified as the reduction of the previously adsorbed and dissociated oxygen. This enabled also to study the influences of the current collector and electrolyte on the performance. Finally, the right direction to improve such type of electrode materials in the future could be unveiled. Interestingly, the electrocatalytic properties of the $GdBa_{0.5}Sr_{0.5}Co_{0.9}Cu_{1.1}O_{5+\delta}$ oxygen electrode can be enhanced by application of the electrospinning method for preparation of the nanofiber materials. After the proper sintering, the special morphology can facilitate the oxygen reduction reaction. Also, $GdBa_{0.5}Sr_{0.5}Co_{0.9}Cu_{1.1}O_{5+\delta}$ and its higher Co content counterpart, $GdBa_{0.5}Sr_{0.5}CoCuO_{5+\delta}$ electrodes demonstrate exceptional output performance in the full cells, with the peak power density output exceeding 1200 mW cm^{-2} at 850 °C, as well as good performance in the reversible mode. This proves that the functional oxygen electrodes may be obtained based on the double perovskite materials with the decreased Co content.

Finally, considering the interesting features of the emerging high-entropy oxides, not only modification of Cu/Co ratio, but introduction of multiple 3*d* metal elements, such as Ni, Mn, and Fe, can be also taken into account. Single perovskite-type oxides with the multicomponent occupancy at the B-site, $La_{0.6}Sr_{0.4}Ni_{0.15}Mn_{0.15}Fe_{0.15}Cu_xCo_{0.55-x}O_{3-\delta}$, are proposed, with the structural results suggesting that the pure-phase samples can be obtained in the range of $0.05 \leq x \leq 0.2$. This also ensures limiting the Co content. The oxide samples demonstrate *R*-3*c* rhombohedral symmetry, which is maintained up to 900 °C in air. The whole series demonstrates very high total electrical conductivity values over 200 S cm^{-1}. Along with the good chemical stability with LSGM and GDC, $La_{0.6}Sr_{0.4}Ni_{0.15}Mn_{0.15}Fe_{0.15}Cu_xCo_{0.55-x}O_{3-\delta}$ layers can be manufactured on both commonly used electrolyte materials. Although, in the electrochemical tests the $La_{0.6}Sr_{0.4}Ni_{0.15}Mn_{0.15}Fe_{0.15}Cu_{0.20}Co_{0.35}O_{3-\delta}$ electrode performed worse than the material with the highest Co content, with the application of the electrospinning method, the polarization resistance values of such electrode can be largely improved, decreasing to e.g. 0.014 Ω cm^2 at 850 °C. Last but not least, the $La_{0.6}Sr_{0.4}Ni_{0.15}Mn_{0.15}Fe_{0.15}Cu_{0.20}Co_{0.35}O_{3-\delta}$-based full cell allows reaching a peak power density of over 1100 mW cm^{-2} at 850 °C, and also shows promising performance in the electrolysis mode. Overall, this indicates feasibility of the new concept of developing the multicomponent oxide electrodes.

Throughout the whole conducted studies, both, traditional and novel approaches have been considered and applied to enhance the properties of the oxygen electrodes based on the Cu-containing complex perovskites, making the performed characterizations more interesting and comprehensive. The main outcome of this study, as presented in the chapter 13, can be summarized that the development of the functional oxygen electrodes for IT-SOCs can be effectively realized with the usage of novel, proposed and optimized materials, in which Co can be either partially or fully replaced by the copper element. This indicates a bright future for the similar, Cu-based materials concerning usage in the IT-SOCs technology.

Streszczenie

Tytuł rozprawy w języku polskim: „*Funkcjonalne elektrody tlenowe dla stałotlenkowych ogniw Solid Oxide Cells bazujące na zawierających Cu tlenkach typu perowskitu*”

Niniejsza rozprawa poświęcona jest badaniom i rozwojowi funkcjonalnych elektrod tlenowych dla ogniw stałotlenkowych typu SOC (ang. Solid Oxide Cells) opartych na materiałach typu perowskitu, w których drogi i toksyczny kobalt został częściowo lub całkowicie zastąpiony poprzez miedź. Możliwość takiego domieszkowania analizowana jest szczególnie w odniesieniu do zastosowania w zakresie temperatur pośrednich, 600-800 °C, w tzw. ogniwach IT-SOC (ang. Intermediate Temperature SOC).

Praca składa się z trzech głównych części, przy czym w pierwszych trzech rozdziałach omówiono zasoby energetyczne i poprzednie transformacje energetyczne, rolę energii elektrycznej we współczesnym społeczeństwie oraz pojawienie się wodoru jako nowego nośnika energii. Następnie, w rozdziale 4, przedstawiono ogniwa paliwowe, ze szczególnym uwzględnieniem ogniw SOC i elektrod tlenowych stosowanych w ich konstrukcji. Na koniec wprowadzono miedź jako potencjalną domieszkę w tlenkach typu perowskitu. Przegląd przedstawiony we *Wprowadzeniu* w rozdziałach 1-4 wyraźnie pokazuje, że istnieje ogromne zapotrzebowanie na zieloną energię, które dalej będzie rosło w przyszłości. Technologia IT-SOC, która może zapewnić odwracalne i efektywne przekształcanie energii między (nadmiarową) energią elektryczną a wodorem, może być uważana za jedną z najbardziej obiecujących opcji zielonej energetyki. Oczekuje się, że odegra ona kluczową rolę w trwającej transformacji energetycznej w kierunku odnawialnych źródeł energii i powinna pomóc w osiągnięciu celu zerowej emisji netto (ang. Net Zero Emission). Jednakże, zajęcie się obecnymi wadami ogniw IT-SOC jest niezwykle ważne, a różne problemy związane z materiałami elektrod tlenowych wydają się głównymi przeszkodami dla takich ogniw, uniemożliwiając im osiągnięcie wysokiej efektywności, stabilności oraz niższych kosztów produkcji. Można stwierdzić, że jednym z fundamentalnych problemów, który należy rozwiązać, jest zbyt duże wykorzystanie kobaltu w obecnych elektrodach tlenowych. Miedź, jako powszechny i tańszy pierwiastek chemiczny, może być potencjalnie użyta do zastąpienia w różnym stopniu kobaltu, ponieważ posiada odpowiednie właściwości i może prowadzić do wytworzenia materiałów domieszkowanych o porównywalnych parametrach elektrokatalitycznych (rozdział 5).

Na podstawie przedstawionych rozważań, główna idea i początkowa motywacja związana z przeprowadzonymi badaniami została zawarta w rozdziale 6, z konkretnym celem opracowania nowych typów złożonych tlenków perowskitowych, o ograniczonej lub całkowicie wyeliminowanej zawartości Co, które posiadają odpowiedni zestaw właściwości fizykochemicznych i wykazują zadowalające cechy elektrokatalityczne, aby mogły być zastosowane do przygotowania elektrod tlenowych dla ogniw IT-SOC. Wybrano trzy różne grupy potencjalnych materiałów na elektrody tlenowe, w tym wolny od Co $La_{1,5}Ba_{1,5}Cu_3O_{7\pm\delta}$, domieszkowane miedzią $GdBa_{0,5}Sr_{0,5}Co_{2-x}Cu_xO_{5+\delta}$, a także

$La_{0,6}Sr_{0,4}Ni_{0,15}Mn_{0,15}Fe_{0,15}Cu_xCo_{0,55-x}O_{3-\delta}$ z wieloskładnikowym obsadzeniem w podsieci B.

Informacje dotyczące metod syntezy (w tym metody zol-żel, metody w stanie stałym i techniki elektroprzędzenia) oraz technik charakterystyki przedstawiono w sekcji *Metody eksperymentalne* (rozdział 7). Zawarto szczegóły dotyczące przeprowadzonych badań dyfrakcji rentgenowskiej w temperaturze pokojowej i temperaturach wysokich, pomiarów mikrostrukturalnych, określenia niestechiometrii tlenowej, analizy termograwimetrycznej, pomiarów spektroskopii Ramana, obliczeń metodą funkcjonału gęstości DFT (ang. Density Functional Theory), pomiarów przewodności elektrycznej oraz testów kompatybilności chemicznej. Ponadto, przedstawiono obszerne dane dotyczące produkcji symetrycznych i pełnych ogniw z elektrodami tlenowymi opartymi o wybrane materiały zawierające Cu. Rozdział ten został również uzupełniony o opis sposobu oceny wydajności elektrokatalitycznej, w tym, odnośnie określenia oporu polaryzacyjnego elektrod wraz z zaawansowaną analizą metodą dystrybucji czasów relaksacji (ang. Distribution of Relaxation Times).

Uzyskane dane eksperymentalne omówiono w sekcji *Wyniki i dyskusja*, obejmującej rozdziały 8-10 z właściwościami fizykochemicznymi trzech badanych układów, oraz rozdziały 11 i 12, które prezentują dane elektrochemiczne dla wytworzonych ogniw. Po pierwsze, szczegółowo scharakteryzowano tlenek $La_{1,5}Ba_{1,5}Cu_3O_{7\pm\delta}$ (rozdział 8). Materiał ten można przygotować metodami syntezy zol-żel i w stanie stałym w temperaturach poniżej 1000 °C w powietrzu. Wykazuje on interesującą strukturę typu perowskitu potrójnego, ze specyficznym obsadzeniem podsieci La/Ba oraz tlenu. Cechuje się również dobrą stabilnością termiczną do 900 °C, co jest wystarczające dla pracy ogniw IT-SOC. $La_{1,5}Ba_{1,5}Cu_3O_{7\pm\delta}$ wykazuje odpowiednią kompatybilność chemiczną z powszechnie stosowanym materiałem elektrolitowym $La_{0,8}Sr_{0,2}Ga_{0,8}Mg_{0,2}O_{3-\delta}$ (LSGM), co wskazuje na możliwość otrzymania warstw elektrodowych. Potwierdzają to także zadowalające wartości całkowitego przewodnictwa elektrycznego i umiarkowany współczynnik rozszerzalności cieplnej, w porównaniu z materiałami perowskitowymi na bazie Co. Temperatura spiekania warstw elektrodowych jest niska i może być dalej optymalizowana (800 °C). Charakterystyka właściwości elektrochemicznych elektrody tlenowej $La_{1,5}Ba_{1,5}Cu_3O_{7\pm\delta}$ na elektrolicie LSGM wskazuje na niskie wartości oporu polaryzacji, np. 0,019 Ω cm^2 w 750 °C. Wyniki testów dla tzw. ogniwa pełnego pokazują, że można uzyskać szczytową gęstość mocy powyżej 530 mW cm^{-2} w 800 °C, ale, co także istotne, przy niższych temperaturach można uzyskać ponad 160 mW cm^{-2} oraz 250 mW cm^{-2} odpowiednio w 600 °C i 650 °C. Elektroda wykazuje również dobrą wydajność w trybie elektrolizy. Ogólnie rzecz biorąc, wyniki potwierdzają, że możliwe jest opracowanie niezawierającego kobaltu materiału elektrody tlenowej, który może zapewnić doskonałą wydajność elektrokatalityczną w temperaturach pośrednich.

W drugim badanym systemie (rozdział 9) zaproponowano serię tlenków $GdBa_{0,5}Sr_{0,5}Co_{2-x}Cu_xO_{5+\delta}$. Materiały te wykazują strukturę krystaliczną podwójnego perowskitu i można je przygotować metodą zol-żel. Jednak wyższa zawartość Cu powoduje problemy z syntezą, i jak potwierdzają wyniki dyfrakcji rentgenowskiej, próbki czyste fazowo można otrzymać, gdy x jest równe lub mniejsze niż 1,15. Jednocześnie, ponieważ zmniejszenie zawartości kobaltu jest istotne, ostatecznie wybrane składy

mieszczą się w zakresie $1 \leq x \leq 1{,}15$. Jak wykazano w charakterystyce właściwości fizykochemicznych, tlenki $GdBa_{0,5}Sr_{0,5}Co_{2-x}Cu_xO_{5+\delta}$ zachowują symetrię tetragonalną w powietrzu od temperatury pokojowej do 1000 °C. Co istotne, ich współczynniki rozszerzalności cieplnej są poniżej $20 \cdot 10^{-6}$ K^{-1} w wysokich temperaturach, co jest warte podkreślenia dla tego typu tlenków zawierających Co. Wykazują one również odpowiednie wartości całkowitej przewodności elektrycznej oraz dobrą kompatybilność chemiczną z materiałami elektrolitowymi LSGM i $Ce_{0,9}Gd_{0,1}O_{2-\delta}$ (GDC). W charakterystyce właściwości elektrochemicznych, skład o stosunkowo wysokiej zawartości miedzi, $GdBa_{0,5}Sr_{0,5}Co_{0,9}Cu_{1,1}O_{5+\delta}$, cechuje się najniższą wartością oporu polaryzacji, wynoszącą 0,017 Ω cm^2 w 850 °C, co potwierdza skuteczność podjętej strategii zastąpienia kobaltu miedzią. Ponadto, przy zastosowaniu analizy rozkładu czasów relaksacji (ang. Distribution of Relaxation Times), zidentyfikowano etap ograniczający szybkość działania elektrody $GdBa_{0,5}Sr_{0,5}Co_{0,9}Cu_{1,1}O_{5+\delta}$ jako redukcję wcześniej zaadsorbowanego i zdysocjowanego tlenu. Umożliwiło to również badanie wpływu kolektora prądowego i elektrolitu na wydajność. W efekcie, można było pokazać właściwy kierunek poprawy dla tego typu materiałów elektrodowych w przyszłości. Co ciekawe, właściwości elektrokatalityczne elektrody tlenowej $GdBa_{0,5}Sr_{0,5}Co_{0,9}Cu_{1,1}O_{5+\delta}$ można ulepszyć poprzez zastosowanie metody elektroprzędzenia do przygotowania materiału w formie nano-włóknistej. Po odpowiednim spiekaniu, unikalna morfologia może ułatwić reakcję redukcji tlenu. Ponadto, elektroda $GdBa_{0,5}Sr_{0,5}Co_{0,9}Cu_{1,1}O_{5+\delta}$ oraz jej odpowiednik o wyższej zawartości Co, $GdBa_{0,5}Sr_{0,5}CoCuO_{5+\delta}$, wykazują wyjątkową wydajność w ogniwach pełnych, z maksymalną gęstością mocy przekraczającą 1200 mW cm^{-2} w 850 °C, a także dobrą wydajność w trybie odwracalnym. To dowodzi, że funkcjonalne elektrody tlenowe mogą być uzyskane na bazie perowskitów podwójnych o zmniejszonej zawartości Co.

Biorąc pod uwagę interesujące cechy nowo wytwarzanych tlenków o wysokiej entropii, można uwzględnić nie tylko modyfikację stosunku Cu/Co, ale także wprowadzenie wielu pierwiastków metali 3*d*, takich jak Ni, Mn i Fe. Zaproponowano tlenki typu perowskitu pojedynczego z wieloskładnikowym obsadzeniem w podsieci B, $La_{0,6}Sr_{0,4}Ni_{0,15}Mn_{0,15}Fe_{0,15}Cu_xCo_{0,55-x}O_{3-\delta}$, przy czym wyniki strukturalne sugerują, że próbki czyste fazowo można uzyskać w zakresie $0{,}05 \leq x \leq 0{,}2$. Zapewnia to również ograniczenie zawartości Co. Próbki rozważanych tlenków wykazują romboedryczną symetrię *R*-3*c*, która jest zachowana do 900 °C w powietrzu. Cała seria cechuje się bardzo wysokimi wartościami całkowitej przewodności elektrycznej, powyżej 200 S cm^{-1}. Biorąc pod uwagę dobrą stabilność chemiczną z LSGM i GDC, warstwy $La_{0,6}Sr_{0,4}Ni_{0,15}Mn_{0,15}Fe_{0,15}Cu_xCo_{0,55-x}O_{3-\delta}$ mogą być wytwarzane na obu powszechnie używanych materiałach elektrolitowych. Chociaż w testach elektrochemicznych elektroda $La_{0,6}Sr_{0,4}Ni_{0,15}Mn_{0,15}Fe_{0,15}Cu_{0,20}Co_{0,35}O_{3-\delta}$ działała gorzej niż materiał o najwyższej zawartości Co, to zastosowanie metody elektroprzędzenia może znacząco poprawić wartości oporu polaryzacji takiej elektrody, zmniejszając je np. do 0,014 Ω cm^2 w 850 °C. Co więcej, pełne ogniwo oparte na $La_{0,6}Sr_{0,4}Ni_{0,15}Mn_{0,15}Fe_{0,15}Cu_{0,20}Co_{0,35}O_{3-\delta}$ pozwala osiągnąć maksymalną gęstość mocy powyżej 1100 mW cm^{-2} w 850 °C i wykazuje również obiecującą wydajność w trybie elektrolizy. Ogólnie rzecz biorąc,

potwierdza to zasadność użycia nowej koncepcji rozwoju wieloskładnikowych elektrod tlenowych.

W trakcie przeprowadzonych badań zastosowano zarówno tradycyjne, jak i nowoczesne podejścia w celu poprawy właściwości elektrod tlenowych opartych na złożonych perowskitach zawierających Cu, co sprawia, że wykonane pomiary są bardziej interesujące i wszechstronne. Główne wyniki uzyskane w ramach niniejszej pracy, przedstawione w rozdziale 13, można podsumować stwierdzeniem, że rozwój funkcjonalnych elektrod tlenowych dla ogniw IT-SOC można skutecznie prowadzić dzięki zastosowaniu nowych, zaproponowanych i zoptymalizowanych materiałów, w których Co może być częściowo lub całkowicie zastąpiony przez miedź. Wskazuje to na obiecującą przyszłość dla podobnych materiałów opartych na Cu, w kontekście ich zastosowania w technologii IT-SOC.

Lists of abbreviations and symbols

Abbreviations

AC	alternating current
AFC	Alkaline Fuel Cell
ASC	anode-supported cell
BWR	boiling-water reactor
BZY	yttrium-doped $BaZrO_3$
CCUS	carbon capture, utilization and storage technology
CHP	combined heat and power generation
DC	direct current
DFT	Density Functional Theory
DMF	dimethylformamide
DMFC	Direct Methanol Fuel Cell
DOS	density of states
DRI	direct reduced iron
DRT	Distribution of Relaxation Times
EDS	Energy-dispersive X-ray Spectroscopy
EDTA	ethylenediaminetetraacetic acid
EIS	Electrochemical Impedance Spectroscopy
EM	entropy metric
ES	electrospinning method
ESC	electrolyte-supported cell
FFT	fast Fourier transform
GDC	gadolinium-doped ceria
GE	General Electric company
HEO	high entropy oxide
HF	high frequency
HRSG	heat recovery steam generator
HT	high temperature
IGCC	integrated gasification combined-cycle system
IGFC	integrated gasification fuel cell system
IT	intermediate temperature
LDC	lanthanum-doped ceria
LF	low frequency
LNG	liquefied natural gas
LOHC	liquid organic hydrogen carriers
LT	low temperature
MCFC	Molten Carbonate Fuel Cell
MF	middle frequency
MIEC	mixed ionic and electronic conductor
NZE	Net Zero Emissions by 2050 Scenario

OCV	open circuit voltage
OER	oxygen evolution reaction
ORR	oxygen reduction reaction
PAFC	Phosphoric Acid Fuel Cell
PCEC	Protonic Ceramic Electrolyzer Cell
PCFC	Protonic Ceramic Fuel Cell
PEMFC	Polymer Electrolyte Membrane Fuel Cell
PV	photovoltaic
PVB	poly(vinyl butyral-*co*-vinyl alcohol-*co*-vinyl acetate)
PVP	polyvinylpyrrolidone
RT	room temperature
SAED	Selected Area Electron Diffraction
ScSZ	scandium-stabilized zirconia
SEM	Scanning Electron Microscopy
SG	sol-gel method
SOC	Solid Oxide Cell
SOEC	Solid Oxide Electrolyzer Cell
SOFC	Solid Oxide Fuel Cell
SR	steam reforming
SS	solid-state method
STEM	Scanning TEM
TEC	thermal expansion coefficient
TEM	Transmission Electron Microscopy
TG	Thermogravimetry
TPB	Triple Phase Boundary
VASP	Vienna Ab Initio Simulation Package
XRD	X-ray diffraction
YSZ	yttrium-stabilized zirconia

Symbols

a	*a* parameter of the unit cell
a^S	number of sites in the S sublattice
b	*b* parameter of the unit cell
c	*c* parameter of the unit cell
δ	oxygen nonstoichiometry
ΔE_{O2}	energy of O_2 molecule
$\Delta_f H_{298}^{\ominus}$	enthalpy of formation at standard conditions
Δl	change of the initial dimension
ΔT	change of temperature
E_a	activation energy
E_{DFT}	total energy of the unit cell from VASP
E_F	Fermi level
E_{final}	total energy of the formula with the oxygen vacancy formed
$E_{initial}$	initial energy of the formula before the vacancy formation
$E_{ox.vac.}$	energy of the oxygen vacancy formation
f_p	weighting factor of a series of histograms
$\gamma(\tau)$	distribution function of relaxation times
I_c	calculated intensity with background and scale factors included
I_o	intensity of the normalized profile
l	initial dimension
L	number of sublattices in the particular corresponding structure
L_{ind}	inductance of the transmission line
m	characteristic indicator of a particular step of the electrode reaction
N_{obs}	total observations in the histogram
N_{var}	variables of the least squares refinement
X^2	goodness of fit
X_i^B	fraction of the element i distributed in the B sublattice
X_i^S	fraction of the element i distributed in the S sublattice
pO_2	oxygen partial pressure
R	ideal gas constant
r_A	ionic radius of the element at the A-site in ABO_3
r_B	ionic radius of the element at the B-site in ABO_3
r_O	ionic radius of oxygen in ABO_3
R_{ohm}	ohmic resistance
R_p	total polarization resistance of the electrode
RQ	parallel connection of the resistor with constant phase element
R_{wp}	weighted profile R-factor
S_B^{config}	configurational entropy for the B-site cations
S_{SL}^{config}	configurational entropy of the total number of atoms in sublattices
σ	electrical conductivity

t	Goldschmidt tolerance factor
τ	relaxation time
U_{iso}	isotropic atomic displacement
V	volume of the unit cell
V_O	oxygen vacancy
w	separate weights
$Z(\omega)$	impedance as the function of frequency
$Z_{Pol}(\omega)$	polarization resistance of the impedance data

Introduction

1. Energy resources and transitions - historical perspective

Unquestionably, availability of different energy resources is crucial in terms of development of human society. Nowadays people rely almost entirely on electricity in their daily life, which is used for lighting, cooking, house heating and cooling, electronic device charging, internet access, as well as for transport in trains and electric cars. Gaseous and liquid fuels are crucial as well, and are used for heating, for fueling of combustion engines, as well as are indispensable in various industrial processes and in manufacturing of commercial goods. It is very hard to imagine living nowadays without electricity, air conditioning, elevators, airplanes, etc. Those basic examples concern contemporary society, however, similar observations can be made analyzing historical data. In fact, a successful practical implementation of a new energy resource has been always connected with a major breakthrough regarding technological advancement.

When tracing back to 200 years ago, energy resources had already played a vital role in the running of human society. Obviously, the difference is that humans at that time used different resources. As presented in Fig. 1-1 [1], before roughly 1850, the woodfuel was at the dominant position of the global energy consumption. As the first industrial revolution took place in U.K., coal gradually replaced wood, and accounted for the biggest share as the power source. This can be regarded as the first energy transition. It is worth noticing that while usage of coal started as early as at the beginning of the 18^{th} century, it took over 150 years for dominance of this new energy resource [2]. In the next revolutionary change, the global energy supply was taken over by oil around the beginning of the 20^{th} century. This coal-to-oil transition could be largely attributed to the invention and commercialization of an internal combustion engine, which boosted growth of the automobile industry in Europe and USA [3]. Later on, issues related to the climate change and global warming have risen over the past decades, mainly because of coal- and oil-related human activities, including transportation and industrial production. Due to the increasing industrialization in the world, a significant rise of demand for coal and oil consumption could be seen, resulting in the vast volume emissions of greenhouse and harmful gases, including CO_2, SO_x, and NO_x [4–7]. Hence, in order to alleviate the climate changes and achieve the sustainable development goal, natural gas has also drawn great attention globally. As a cleaner energy resource, combustion of natural gas emits less carbon dioxide and sulfur dioxide, making it the perspective new choice in the human energy consumption portfolio. It can be stated that emergence of the natural gas was the third important energy transition. Interestingly, almost at the same time in history, clean energy options (e.g. renewables and nuclear) have appeared, and gradually become more and more widespread.

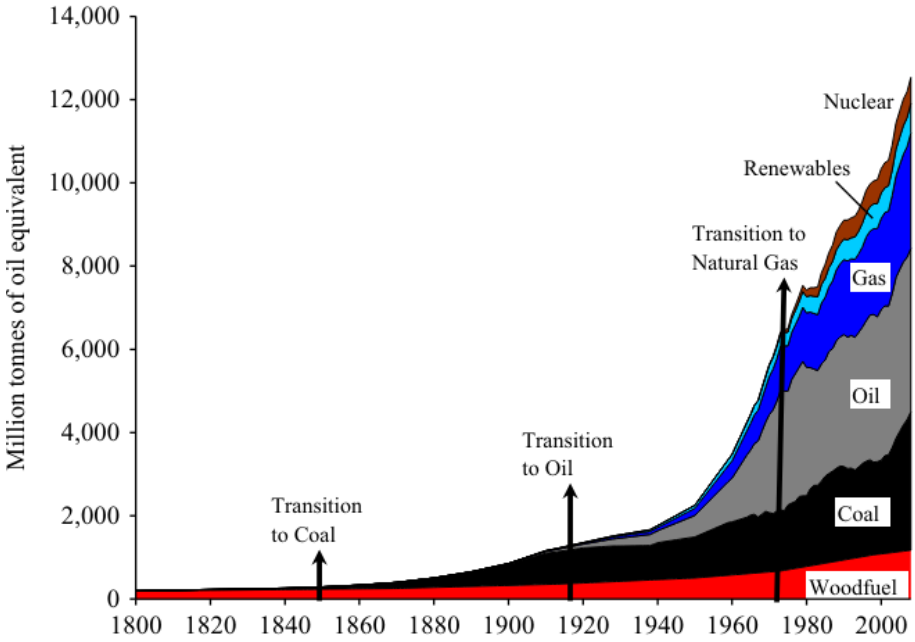

Fig. 1-1. Global energy consumption and energy transitions in years 1800-2010 [1].

As it can be demonstrated, plenty of different energy sources have been exploited in the human history, and some of them are already replaced by others, which stems from reserve levels, and also, available exploitation technology. Nevertheless, choice of a particular energy resource is interesting in itself, and always was important to human's life.

Fire, with which people are very familiar for a long time, is a process that transfers chemical energy from matter (fuel and oxidizer) into physical energy, like light and heat. Obviously, chemical products of the combustion are also generated. Primitive people who had lived more than 200 000 years ago were able to harness fire [8]. In ancient times, when people had limited or even no knowledge of science, they could only drill wood to make fire [9]. However, they still could keep warm, have light, cook hunted meat, and even protect themselves from beast attacks [8]. Back then, fire became useful in pottery making [10], which greatly enhanced the food storage technology. Also, human beings couldn't proceed with metal smelting without fire, which facilitated establishing civilization and human society [11]. From what is mentioned above, it can be easily concluded that wood was actually the most important fuel resource to humankind throughout most of the history. It should be also mentioned that regarding availability, people living at those times had rather easy access to forests or other wild environments, and had little difficulty in chopping wood and transporting it to their residence or to a place where they needed it.

Meanwhile, as a fundamental life necessity to humans, water has always played quite an important role in the energy utilization development. When dating back to classical antiquity, people in the Middle East and Asia have started applying gravity irrigation in the early agricultural production, which was relying on the energy of water [12]. As it can

be seen in Fig. 1-2, a water wheel is an essential device that exploits the potential energy of water, transforming it into mechanical energy that is further useful in various applications, including grain milling (watermill), paper milling and hammer forging [13]. Hence, even before the first industrial revolution, after which people could get power from steam engines, water power has been always regarded highly, and utilized for quite a long time. It could be also proven that rivers or even steams were quite crucial when people managed to build a village, town or city, no matter what was the initial intention behind it, agricultural production or industrial manufacturing, as in case of e.g. Rhine, Thames or Seine river. Currently, pumped hydro energy storage is still the most dominant one concerning global storage power capacity [14].

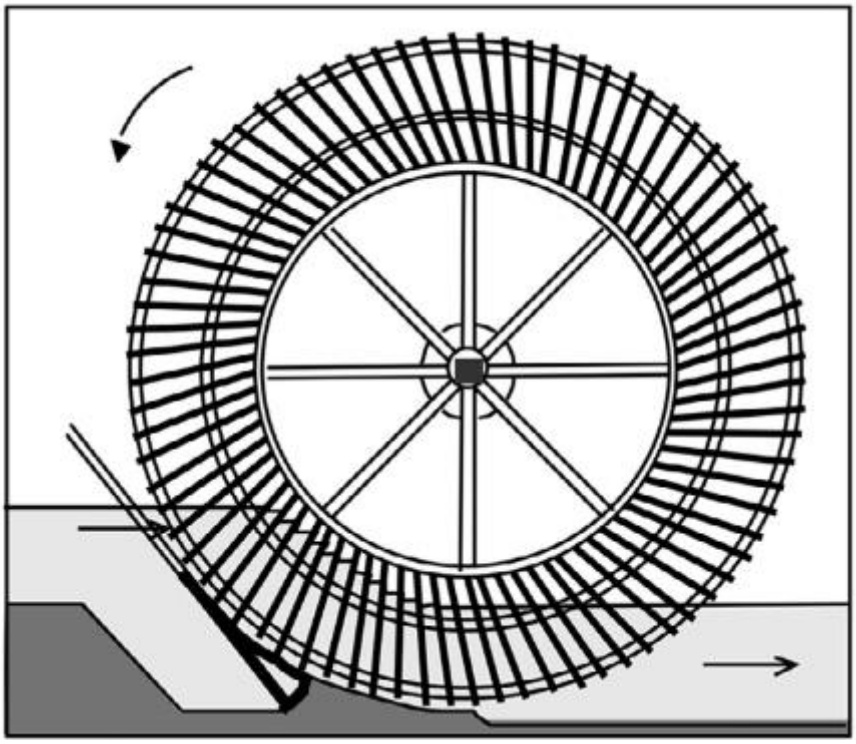

Fig. 1-2. A water wheel design from 19th century. Based on [12].

When it comes to the point of people of ancient times exploiting the natural powers, wind cannot be ignored. Wind phenomenon is actually derived from an inhomogeneous heating of the Earth by the Sun [15], which further arouses pressure differences between land and land and/or land and ocean. Then, the airflow starts at different speeds and intensity. Similarly to water, human beings have noticed the available resource, and thought about how to utilize it and make it serve their life and work better. An exact instance of such usage would undoubtedly be a ship. Long before a steamship was invented, ancient Egyptians started sailing on Nile river, which relied on boats with installed sails [16]. Later, the sailboat greatly facilitated the "Great Geographical Discoveries" period of the 15th century [17]. Apart from that, wind power was also adopted in food production in the Middle Ages [18]. Later, the application of wind power has been broadened to lumber sawing, oil extraction, and mine ventilation. Interestingly,

there is still a great number of windmills working in the world (i.e. in USA and Netherlands) [19]. As one of crucial renewable energy resources, it can be stated that wind power has its renaissance, with wind farms, including offshore ones, becoming more and more common sights in many places [20].

Coal has been and still is regarded as the one of the most important energy sources in the world. Studies proved that the first use of coal took place in China, ca. 1000 B.C. [21]. It seems that Chinese were able to smelt iron ore, which was prior to its similar use in Europe by 1500 years or so [22]. In Europe, the first usage of coal may be traced in Greece and Italy, and it was for metal-related processing purposes, like forging and casting. Nevertheless, initially coal did not get much attention in terms of energy exploitation, likely due to the availability of wood, which at that time still contributed as the prime energy source for humankind. Thus, for quite a long period of time coal has served only as a minor energy choice in Europe. With the time progressing, several reasons have greatly boosted usage of coal: 1. Improved water and sea transportation, accompanied by shipbuilding industry and voyage development, which decreased transport costs of coal; 2. Increasing scarcity of wood, which had been heavily relied on by humans for the purposes of construction and energy use; 3. Growing energy demands, resulted from advancements in metallurgical industry and expanding population, e.g. in Europe; 4. Abundant coal reserves found in Europe and Asia. Eventually, coal became the heart of the Industrial Revolution [21,23]. Until now it has been continuously used around the world, still making major contribution to the power generation and heating, which are essential for human society. It cannot be neglected, however, that overall the history of coal usage has aroused a series of major, negative issues, mainly related to the increasing air and water pollution [24].

As widely-perceived in the world, oil is currently playing an extremely prominent role in the industrial societies. Interestingly, when dating back to the ancient times, oil was applied as asphalt in buildings, roads, ships, and even was used for medical treatment in the Middle East [25]. Oil did not get much attention until the mid-19th century, when cheaper illuminating fuel was needed in Europe and USA. In 1859 (Pennsylvania, USA), oil was successfully extracted from the underground by a drilling prototype machine. That time can be regarded as the beginning of the modern oil industry, following by the flourish of oil refining and transportation. For example, as early as 1856, the first oil refinery was built by famous Polish inventor Ignacy Łukasiewicz.

Ever since the internal combustion engine was invented in Europe in the late 19th century, three-wheel or four-wheel cars were assembled and tried in seeking for a more efficient and comfortable way of transportation. Those cares were fueled by gasoline or diesel engines. Later, owing to the massive commercialization and spreading of the automobile industry in USA, a car has become affordable for a typical household, which largely boosted oil demand in the world [26]. Moreover, during the First and Second World War, as novel types of trucks, tanks, battleships, and even planes were designed and introduced, oil started being regarded as a strategic factor in the battlefield. This is mainly because of relatively easy transportation and high thermal efficiency, which further highlighted its importance in the global energy market. In postwar times and virtually until now, due to the vast development of various industries and different

technologies, including aviation, automobile, construction, heating, and so on, oil has taken the prime place in the energy resources mix since 1960s [25]. Despite the oil-shock of 1970s, it has been playing important role in the global energy market and daily life of humans, and what cannot be completely ignored, it produces lower greenhouse emissions, as compared to coal [27].

In the 21st century, or even a little earlier, it started to be widely perceived that economic growth is not the only concern for human society. This is because of the increasing environmental issues, resulted from the long history (200 years) of fossil fuels consumption, mainly, coal and then, oil. Given that a substantial development still seems to be quite a crucial and urgent target for humankind, and considering the whole world needs, natural gas, as the cleaner burning fossil fuel (compared to coal and oil), has drawn much attention. Its usage has grown dramatically in the global energy market [28,29]. Basically, there is no fixed composition of natural gas, but it consists mostly of methane, with much lower content of other hydrocarbons, like ethane, propane, etc. Minor amounts of nitrogen, carbon dioxide, and other gases are also present [29,30]. Nowadays, natural gas is mainly adopted in heating, industrial manufacturing, and power generation [29]. Thus, it plays an important role in the current energy market in the world.

Overall, it can be summarized that the great achievements made by human beings in terms of industry and technology are usually connected with different energy resources and their consumption, and are often accompanied by the energy transition. Development does not mean that the environmental concerns can be ignored or put aside, as they have been brought about by humankind as well. Maintaining a good balance between a series of factors, including economic efficiency, reserve of resources, and environmental protection, is the main driving force and incentive for humans to keep optimizing the energy solutions from the start to the end. However, it would be ignorant not to notice that different countries have different policies in that matter, and not only scientific reasons are considered. A good example for it is nuclear power, about which often contradictory policies can be found throughout the world.

2. Electricity and its production

In the modern society, electricity is one of the most important and useful energy forms that people are well aware of, and deal with practically every day, which can be easily understood by the household bills paid monthly, which consist of mainly water, gas and electricity. Apart from the massive scale of electrical energy demand in various industries, it is inevitably necessary to care about electricity supply in both households and working places. The power supply for the households, from which the illumination system, domestic appliances including television, air conditioning, washing machine, electrical and microwave ovens etc., could work on, as well as for the commercial places, involving elevators, internet servers, ventilation systems, street illumination and so on, are indispensably important to maintain normal functioning in society. This can also be proven from a common sense which people feel anxious and helpless when the outage suddenly takes place, particularly when an important online business meeting is underway or massive transactions are being processed in a stock exchange. As shown in Fig. 2-1a, the global electricity consumption reached 22848 TWh in 2019, with the industry, commercial and public services, as well as residential components sharing majority of the usage [31]. Nevertheless, the electricity consumption had grown more obviously in 2010-2019 in transportation domain than in sectors of industry, commercial and public services (Fig. 2-1b).

a)

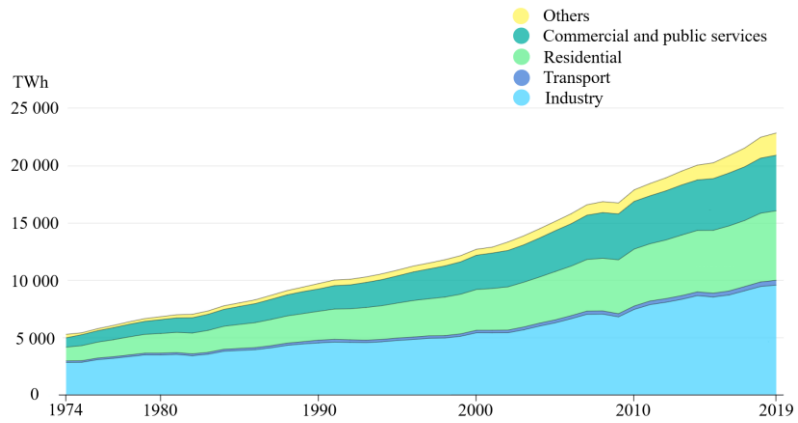

b)

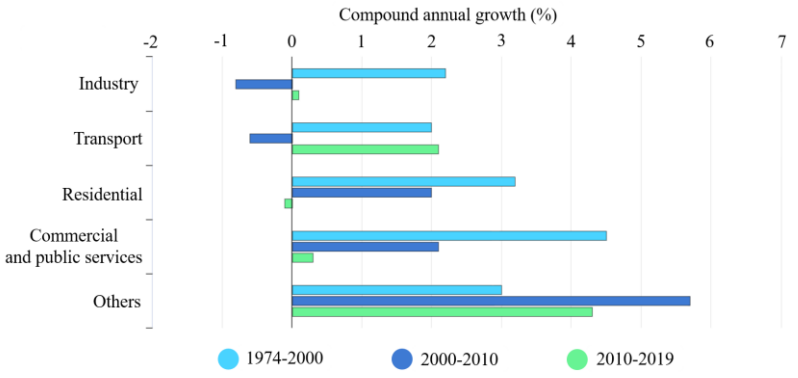

Fig. 2-1. a) World electricity final consumption, and b) compound annual growth of the global electricity consumption by sectors in years of 1974-2019. Based on [31].

This increase can be accounted by the growing number of electrical vehicles in the world, especially in Europe during that period of time, which is surely making a great contribution to mitigating greenhouse gas emissions, as compared to traditional transportation tools powered by fossil fuels. It can be easily expected that the electricity demand worldwide would experience an obvious rise in the foreseeable future as electricity plays a unique role in searching for green and sustainable development for the human society.

Although people have been getting used to electricity for long, it was quite mysterious and frightful for human living in ancient times, in which thunder and lightning were the initial impression among humankind. Powerful, since it destroyed woods, broke rocks and even killed life, and fascinating when it lighted up the sky were another perspectives that motivated people to search and get better understanding on this unknown natural power.

It seems that the earliest endeavors towards electricity in human history could be dated back to 600 B.C., Thales of Miletus, a Greek scientist, obtained the very initial observation of attraction phenomena of rubbed amber when it was close to light objects (e.g. feathers, as can be seen in Fig. 2-2). Afterwards, Theophrastus in 300 B.C., also noticed the similar attraction phenomenon for the material currently known as tourmaline [32,33]. Nevertheless, at that very early stage in history, people had very limited knowledge in explaining and understanding this fantastic phenomenon scientifically.

a)

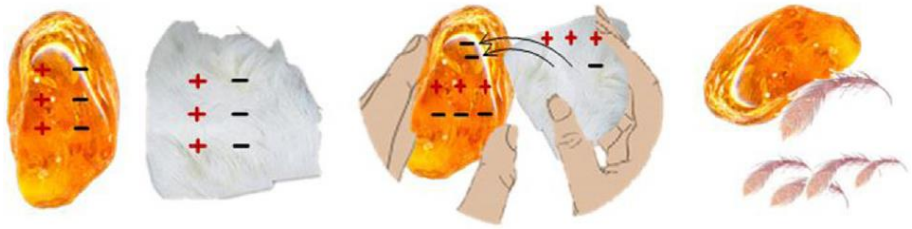

Fig. 2-2. Schematic diagram of electricity experiment with amber and cloth [32].

Quite a long time after that, William Gilbert, a physician, published his work *De Magnete* in 1600, summarizing the attraction would take place in rubbed objects, like amber, diamond and sapphire, as well as the repulsion that occurred in the same poles of two lodestones. It is worth noting that Gilbert coined the term "*electrics*" from ancient Greek language [32–35]. Afterward, Stephen Gray in 1729, found the difference of ability of the electric conduction varied when the respective materials were different [34,35]. Another work that couldn't be ignored was done by Charles Francois Du Fay. Du Fay used "*vitreous*" and "*resinous*" to define two "*electricities*" that could be generated by two group of substances including glass, rock-crystal, precious stones, etc., and amber, copal, silk and paper, etc., respectively. This finding would be regarded as difference of "positive" and "negative" signs of electricity. Still, there was another famous discovery by Pieter van Musschenbroek, called "Leyden phial", in which electricity could be accumulated. Afterward, William Watson improved the phial as "Leyden jar" that could

be the prototype of a capacitor today, which marked the cornerstone that scientists could store the electricity from decaying in the air [32–35].

In 1752, American scientist, Benjamin Franklin, carried out the famous "kite" experiment, in which he used a kite connected by wet hemp as a string and a key hung at the end of the string so that he could collect the lightning from the cloud. He concluded that lightening was derived from electricity in clouds (Fig. 2-3). Additionally, Franklin drew conclusion based on his rubbing experiment that rubbing couldn't generate electricity but just transferred electricity from one object to another. It is worth noting that Franklin regarded the electricity as an "elastic fluid" that could penetrate objects [32–35]. Compared to electricity present in nature, "animal electricity" also drew a great attention from scientists. In 18th century, Italian scientist, Luigi Eliseo Galvani observed a response of a frog's leg when he applied electricity to the muscle on its leg. Thus, Galvani thought that there was a form of electricity existing in animal that could be called "animal electricity" [32–34]. Afterward, another outstanding Italian physicist, Alessandro Volta made a further experiment based on Galvani's "frog's leg", in which he tried to use two types of metals separated by wetted pasteboard to generate current flow. He also found that increasing the number of units in the configuration would improve the potential between the top and down sides. Later, a higher efficiency could be obtained when the pasteboards were infiltrated in salt water or acid (Fig. 2-4). This prominent alternatively arranged configuration was called "Volta pile", which was capable to generate a continuous current flow, could be considered as the earliest battery [32–34,36]. The unit "volt" is consequently named after Alessandro Volta.

Fig. 2-3. Franklin's kite experiment, identifying the lightning and electricity [37].

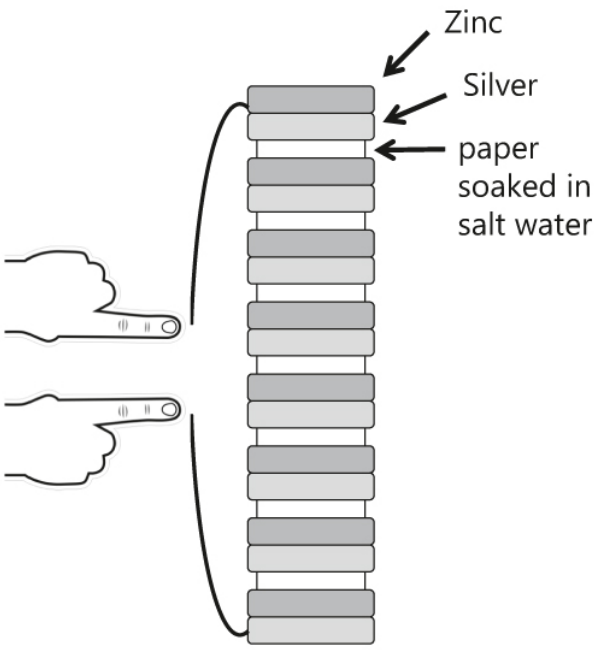

Fig. 2-4. A simplified schematic diagram of Volta's configuration [36].

Interestingly, scientists found that electricity seemed to have impact on other domain that was magnetism in particular, which shaped the important discipline of electromagnetism. A Danish scientist, Hans Christian Ørsted, identified an impact of the electric current on a magnetic needle in his lecture in 1820, which he called "conflict of electricity" [38]. Later, Andre-Marie Ampere stated that "two conductors carrying currents in the same direction attract each other", and he also coined the term "electrodynamics" [32,34,39]. The unit of current "ampere" was named after him. The profound correlation between electricity and magnetism was identified and proven by the English scientist, Michael Faraday. In 1831, he prepared a ring made of bar-iron, wound in two parts with helices (copper wire), called helix A and B. The helix B was connected with a galvanometer while the helix A was connected to a battery. The galvanometer was instantly affected when the current was turned on upon helix A. But soon the effect was gone, even though the circuit of helix A was still connected. The needle of galvanometer responded immediately when he broke the circuit on helix A. That was the first time Faraday found the phenomenon of "induction of electric current from magnetism". Similarly, Faraday recorded this phenomenon in anther experiment, in which he set a hollow helix wound by copper wire. Again the needle of galvanometer deflected when a cylindrical magnet was suddenly pushed in or withdrawn from the helix [40]. Thus, Faraday indicated that the varying magnetism could induce electric current in a circuit. That effect was called "electromagnetic induction". In fact, this discovery would become incredibly crucial in the humans' life in terms of power generation, electricity transportation and so on. Notably, James Clerk Maxwell, an outstanding English scientist, summarized and explained Faraday's electromagnetic induction in a mathematical way of Maxwell's equations, making a great contribution to the development of

electromagnetic domain. Maxwell also pointed out that light is actually a form of electromagnetic wave [41].

It is not surprising that an enormous application range could be expected ascribed to the great development in both, electromagnetism and electricity. In 1830s, current pulse could be transferred via wire by means of electromagnetic technology, that was a telegraph. It meant that a signal or information could be transmitted instantaneously in a long distance. Samuel Finley Breese Morse and his colleague designed a combination of short and long pulses of the current, which could represent the designated English letters or numbers, so called Morse code. Later in 1844, Morse sent the first telegraph message successfully from Washington to Baltimore [32,42,43]. After that, Thomas Alva Edison patented his carbon-filament lamp, which could potentially bring affordable illumination option for every household in the late 19th century [44]. Since the electricity began being popular in the world, particularly in the industry and people's daily life (e.g. lighting), a problem appeared regarding effective electric power transmission covering big area, due to the low and unchanged (constant) voltage level of a generation station, as well as the huge resistance along the conduction wires. Thus, an urgent demand for an effective electricity transmission system was not surprising in terms of the larger scale of electricity application. Later on, Nikola Tesla, patented his famous system of alternating current motors (Fig. 2-5) and transformers, which presented a feasibility of a high-voltage transmission of electricity. That were critical parts of alternating current supply system that have been widely applied in different places. For example, based on Tesla's patterns, the generators of a polyphase system were installed in Niagara Falls, USA, successfully delivering electricity to Buffalo in 1896 [45]. It is well-known that Tesla's idea is still widely adopted around the world, facilitating the power plants to transmit electricity to the places where it is needed.

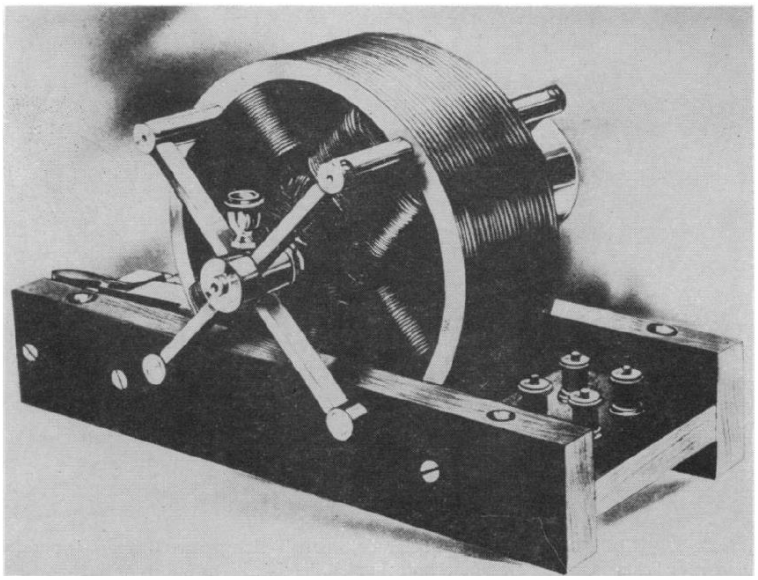

Fig. 2-5. One of the Tesla's original induction motors [45].

As can be derived from the aforementioned brief history of electricity and related scientific and technical progress, the role electricity has been playing is increasingly important for humankind, and it will remain so in the foreseeable future. Therefore, it is worth describing the mainstream energy resources, which are currently used to produce the electricity.

2.1. Coal

Even though the recent energy transition to renewable energy resources is actually taking place, in the domain of electricity generation in the world, coal is still predominantly accounting for the biggest share in the world [46]. This may be attributed to the reliable and durable coal-fueled power generation technology, as well as the quite abundant coal reserves around the world, effectively lowering the capital costs of this energy source [47]. As it is shown in Fig. 2-6, more than 10000 TWh of electricity (over one-third of the total electricity generation) were produced by coal, apparently outnumbering gas that contributed around 6400 TWh in 2022. Typically, a coal-fueled power plant is a basic facility that converts energy from coal to electricity. The general schematic procedures are illustrated in Fig. 2-7a. Firstly, coal is pulverized before fed in the boiler. Then, water is heated up and turned into steam by the thermal energy from the combustion of coal. Secondly, the high-temperature and high-pressure steam would go to a turbine, which blades are rotated by the steam. Finally, the mechanic energy will be transferred to a generator (Fig. 2-7b), so that the electricity is produced and sent to a transformer, and then further to the transmission lines [47]. The steam at outlet of the turbine is condensed and fed to a boiler for circulating afterward. In general, this type of power plant could yield an efficiency of around 30-40%. Typically, the capacity of a coal power plant ranges in 100-4000 MW_e. Additionally, higher efficiency could be reached when improvements like integrated gasification combined cycle or fluidized bed are adopted [47,48] or when the waste heat is recycled and reused in other aspects. More details about the combined heat and power (CHP) generation are presented in the subchapter of 2.8.

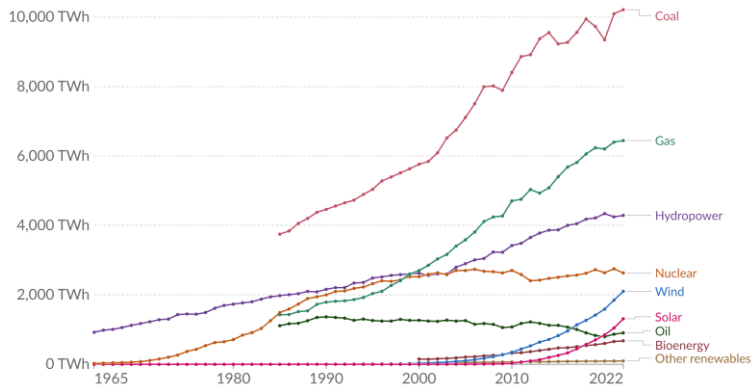

Fig. 2-6. Global electricity production by source. Based on [46]. Note that data for coal, gas, and oil are presented only from 1985, and for wind and bioenergy from 2000.

a)

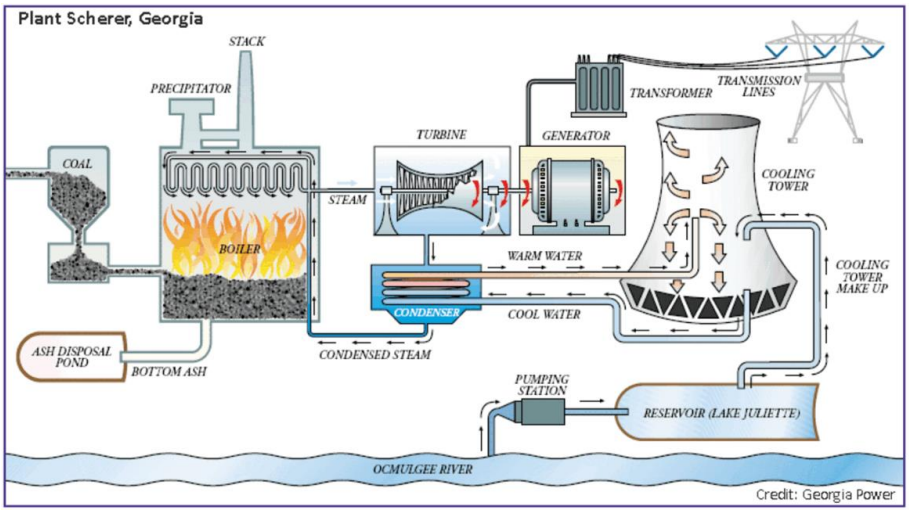

b)

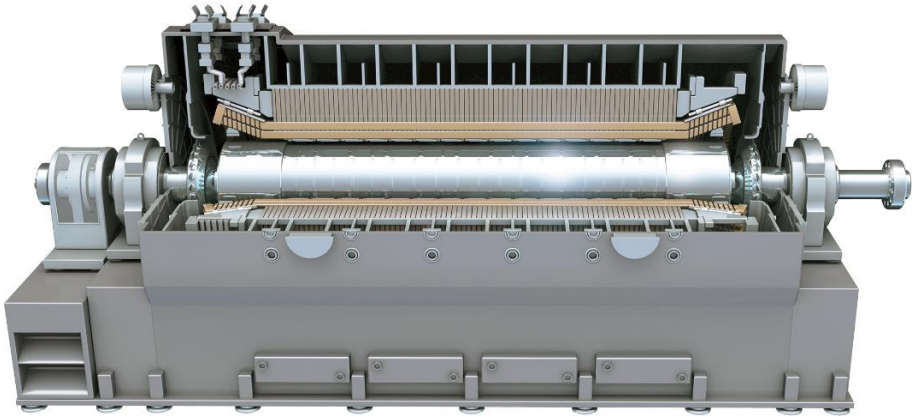

Fig. 2-7. Schematic diagrams of a) a coal-fueled power plant, and b) a typical AC generator with 408 MVA apparent power, produced by GE [49,50].

2.2. Natural gas

As drawn in Fig. 2-6, natural gas (Gas) has been taking the second place in the contribution towards global electricity generation since 2000. There are handful of reasons accounting for that. Firstly, natural gas emits substantially less greenhouse gases than either oil or coal during combustion, alleviating (at least partially) air pollution issues. This is also shown in Fig. 2-8 regarding the total greenhouse gases emissions [51,52]. Secondly, other than liquefied natural gas (LNG) shipped by sea, pipeline systems particularly facilitate the gas transportation in the continents so that lower the application cost. From the major natural gas producing areas (e.g. North America, Russia, the Middle East), natural gas was exported to the adjacent areas or countries via pipelines (Fig. 2-9). For instance, Russia and Norway supplied 112.9 and 167 billion cubic meters to Europe in 2021, respectively [53]. Additionally, LNG could alleviate the difference of natural gas reserves between the demand and supply as well. Thirdly, gas-fired power plant could start and stop quickly, consequently making it suitable to meet the demands related to the

fluctuating electricity usage or support the intermittent wind and solar power [54]. However, due to other reasons, the natural gas supply to Europe has recently changed, which may more or less influence the electricity production in the near future.

When it comes to power generation, the fundamental components of a gas-fired power plant are similar to that of a coal-fueled power plant. A gas turbine is the key equipment in gas-fired power plant, which typically consists of: 1. compressor (of which the role is to compress air and send it to the combustion chamber), 2. combustion chamber (mixing of fuel and compressed air, and then igniting the mixture, which produces high-temperature and high-pressure steam later supplied to the turbine) and 3. turbine (its blades are spun by the steam from the combustion chamber, and in turn, it drives the compressor and rotate the generator to generate electricity). The overall conversion efficiency (single cycle) can reach around 35%. Meanwhile, higher efficiency could be reached when a heat recovery steam generator (HRSG) is adopted, which reuses the exhaust gas from the turbine and heats water in a boiler into steam, so that rotates another steam turbine to generate electricity (so called combined cycle) [55].

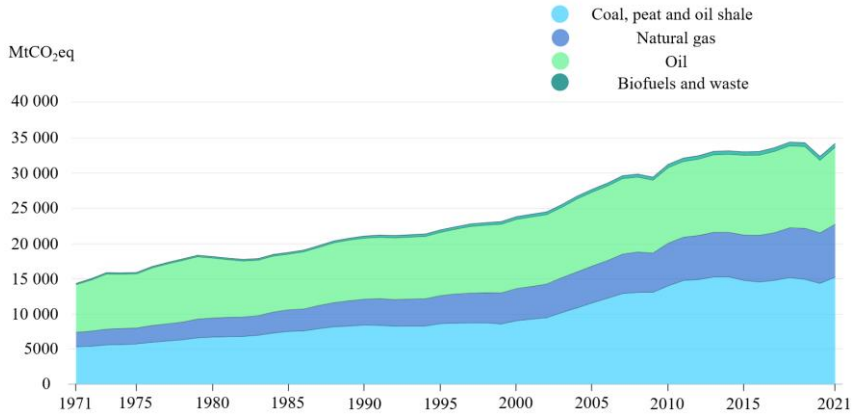

Fig. 2-8. Total greenhouse gas emissions from fuel combustion per product. Based on [51].

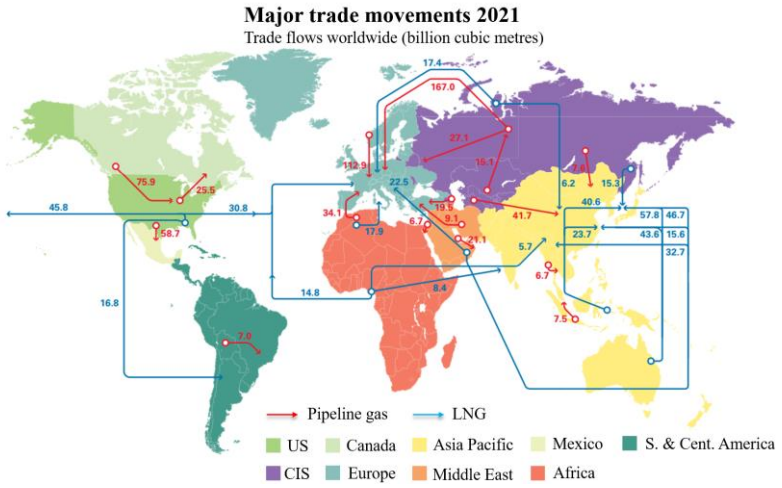

Fig. 2-9. The major trade movements of natural gas via pipeline or LNG. Based on [53].

2.3. Oil

Even though oil is one of the most important fossil fuels on Earth, nevertheless, it cannot compete in the market share in power generation with either coal or gas as, as it is shown in Fig. 2-6. Reasons could be mainly ascribed to the relatively higher price than other fossil fuels, as well as the price fluctuation. Moreover, generation of undesirable residues during combustion and rather outdated generation technology for oil-fired power plants caused this situation. Eventually, combustion of oil is associated with high emissions of greenhouse gases. Those reasons jointly result in a situation that this option can only be considered when peak electricity demand must be met or as backup power supply in office buildings or residential areas (e.g. a diesel generator) [56].

2.4. Hydropower

Holding the third place in world's electricity generation, hydropower contributed more than 4000 TWh in 2016, then reached 4288 TWh in 2022 (Fig. 2-6), marked as the highest among the renewables.

Water has been always considered as the crucial power source, as mentioned in the previous chapter. Later, when it stated to join the modern development for human beings, the term of "hydroelectricity" weighed substantially. The concept is, to exploit the mechanical energy from high-altitude or flowing water to generate electricity [57]. Hydroelectricity has been long known as its features of low-carbon, clean and renewable. Additionally, what should not be underestimated are its flexibility and large storage capacities, as well as for combining wind power and photovoltaic (PV) electricity systems. Since wind and PV systems are prone to be strongly influenced by local weather, in order to maintain stable electrical output, and attributing to quick start-up time, fast ramp rate and flexible storage capability, hydropower plants could efficiently compensate the power gap in the undesirable meteorological condition where deployed with large scale wind or PV systems [58].

There are currently developed few types of hydropower: 1. based on a run of river, generating electricity from the river flow; 2. reservoir hydropower plant with a dam, which is the most common form of hydroelectricity; 3. pumped-storage plants, pumping and storing water in low electricity demand time and release it at high electricity demands.

The run of river is based on a diversion that leads water from the mainstream of a river through a special canal to the turbine and generator. The energy in water flow comes from the declined river bed elevation.

The typical working principle of reservoir plant can be summarized as follow: water stored at a relatively high altitude is released via a penstock, then spins the turbine that in turn rotates the generator to produce electricity (Fig. 2-10). Taking advantage of its massive storage capability, reservoir power plant could store big amount of water in wet season and use water in drought period, consequently enabling this technology to play an unique role in flood control, water supply and irrigation [57]. Interestingly, over 20000

MW_e capacity is installed at the Three Gorges Dam, with DC and AC lines transmitting the produced electricity.

The pumped-storage plants can be regarded as a useful energy storage technology besides electricity generation. Energy can be stored by means of pumping water to the higher elevation. This can be done during the off-peak time of electricity consumption, enabling to effectively use surplus electricity generated by other technologies. Releasing of the stored water can rotate the turbine and then generate electricity during the peak hours of consumption, so that balancing demands of fluctuation of the grid is feasible [59]. Notably, it is the most commonly applied grid energy storage, accounting for over 90% worldwide.

There are still at least half of the potential hydropower resources remaining unexploited. Aiming to achieve the Net Zero Emission goal, recognition of importance, robust support of policy and sufficient financial investments should be made effectively to support development of this technology [58].

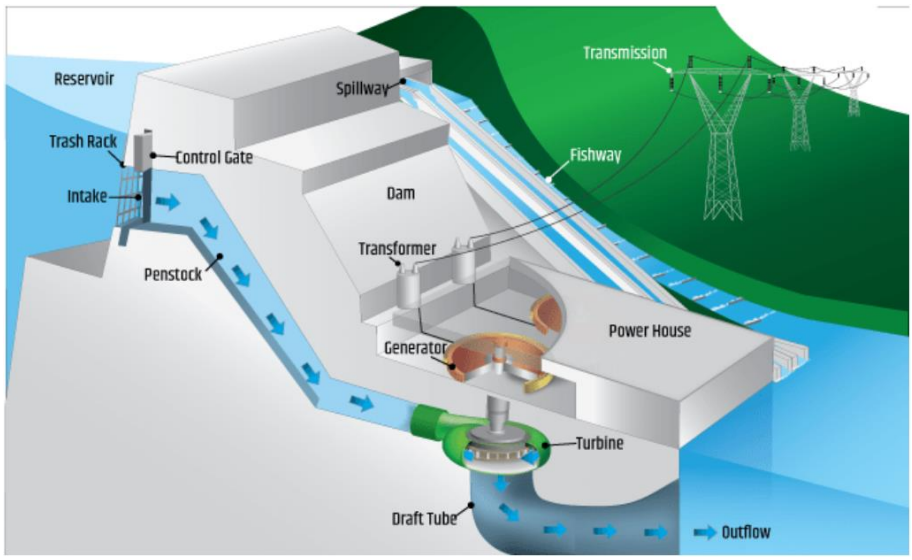

Fig. 2-10. A schematic diagram of a typical reservoir power plant [59].

2.5. Nuclear power

Nuclear energy held the second biggest share among non-fossil fuels in global electricity generation, which accounted for 2632 TWh in 2022. Acting as a vigorous option in supporting the energy transition towards cleaner and sustainable future globally, nuclear power has been thought highly of, due to its advantage of almost no emission of greenhouse gases, which in turn would largely alleviate the electricity reliance on the fossil fuels (but this approach actually varies in different countries).

Nuclear energy is originally derived from the atomic energy during fission or fusion reactions. Setting uranium-235 atom as an example (Fig. 2-11), which is a widely-adopted fuel in nuclear power plants, nucleus of this atom is triggered by a neutron, then it splits

into two smaller nuclei and some additional neutrons that continuously hit nuclei of other uranium-235 atoms, which would eventually repeat increasingly. That is the so called "nuclear chain reaction". Consequently, massive amounts of heat and radiation are released during the fission reaction [60]. When it comes to the nuclear fusion, it is worth noting that bigger amount of energy would be released (fourfold of that of the nuclear fission) when nuclei of deuterium and tritium atoms collide and form a heavier nucleus. Since such a reaction requires extremely high temperature (on the order of 100 million °C) and high pressures to keep the fusion reaction lasting long enough till the net power is generated, enormous and very complex studies and experiments are currently underway to develop eligible materials and technological solutions. Making nuclear fusion practically feasible would indeed realize the ideal and virtually unlimited form of the available energy source (and consequently electricity) [61].

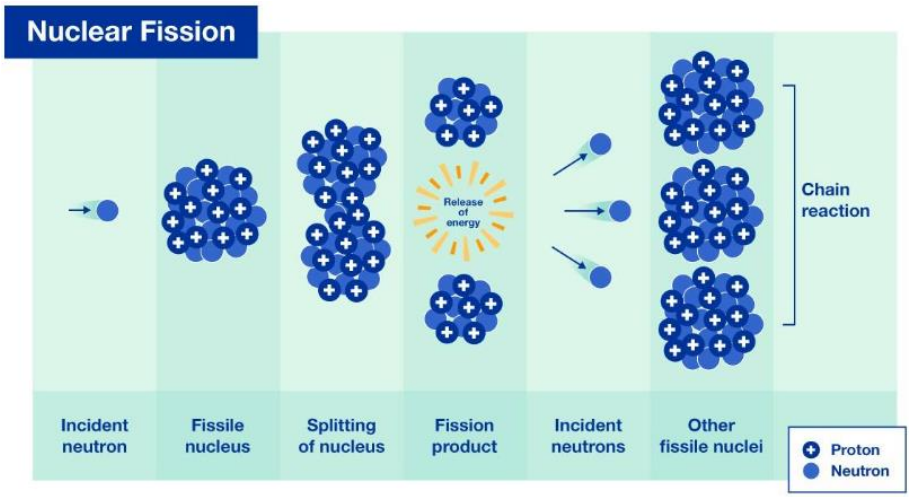

Fig. 2-11. A schematic diagram of the nuclear fission process [60].

Typically, nuclear electricity is generated in a nuclear fission power plant that is fueled by a reactor, which consists of fuel rods of enriched uranium-235. In the reactor, fuel rods are immersed in water as their cooling agent, which is heated up by the reactor into steam to drive the blades of the turbine that further spin a generator to produce electricity. After that, used steam is cooled down and fed to the reactor in a circulation, as demonstrated in Fig. 2-12. In general, the longevity of uranium-235 fuel rods varies in 3-5 years range, after which they have to be recycled or disposed of according to a rigorous procedures, as it also applied to other nuclear waste [60].

Interestingly, apart from electricity, nuclear power plants are able to supply heat and produce hydrogen in the electrolysis process. Since clean hydrogen is desired as an energy carrier in many domains, like the application in fuel cells, synergy of nuclear and hydrogen technologies appears as an interesting, but still not fully-utilized option. Aiming at enlarging the contribution of nuclear energy, some issues should be considered and implemented carefully, like strengthening financial support for new reactors, enacting and improving safety regulations and radioactive waste management, as well as restoring public confidence, particularly after the nuclear accidents [62].

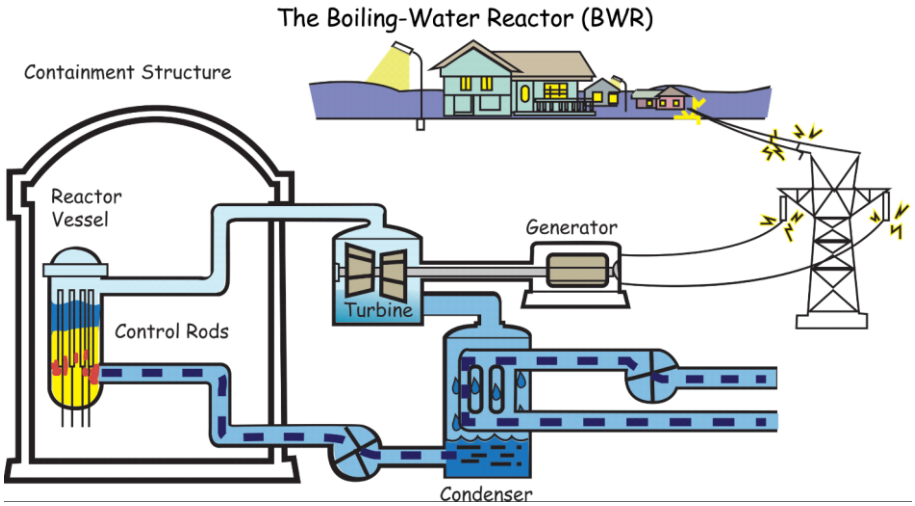

Fig. 2-12. A simplified schematic diagram of a nuclear power plant [63].

2.6. Wind energy

Although still falling behind the nuclear power, wind power is definitely considered as one of the most promising renewables. Electricity produced by wind has grown 5 times since 2010 (data calculated based on [46]), reaching 2098 TWh in 2022. Similar to hydropower, wind power derive from the motion energy of a fluid (wind). While wind has been exploited in ocean voyage and grain milling in ancient times, it is contemporarily be considered as very useful in power generation to human beings.

a) b)

Fig. 2-13. A picture of a typical land-based wind turbines, a) with traditional horizontal-shaft, and b) a smaller size of perpendicular shaft [64].

A wind turbine is the key equipment to turn the energy of wind into electricity, and comprises of giant rotor blades (usually three) and a generator (Fig. 2-13a). When wind flows towards those blades, air pressure difference is generated on both sides of the blades, which propels them to spin. Then the generator is rotated so the electricity is produced. Another type of the wind turbine can be also found, which feature a perpendicular rotation shaft (Fig. 2-13b), contrasting with abovementioned one, which is horizontal. Such turbines are much smaller, and easily installed close to residence communities or buildings, contributing to the localized electricity demand [64]. Typically, a wind farm is favorably located in windy places as onshore wind farm, like the seaside in Netherlands or the U.K. Meanwhile, it can also been installed as offshore wind farm, of which a single turbine can reach a power value of 8 MW_e.

2.7. Solar power

Solar power deriving from sunshine has been regarded as the clean energy resource for quite a long history. People living in ancient society were already able to use sunshine to dehydrate grain or meat in order to extend storage period of food, as well as used it for heating water. Speaking of solar power in terms of power generation, PV technology should be paid attention to, which is based on a photovoltaic cell, made of semiconductor materials (e.g. silicon-based). The cell can absorb photons and then create charge carriers that migrate to current collector of cell and generate current in a circuit (Fig. 2-14).

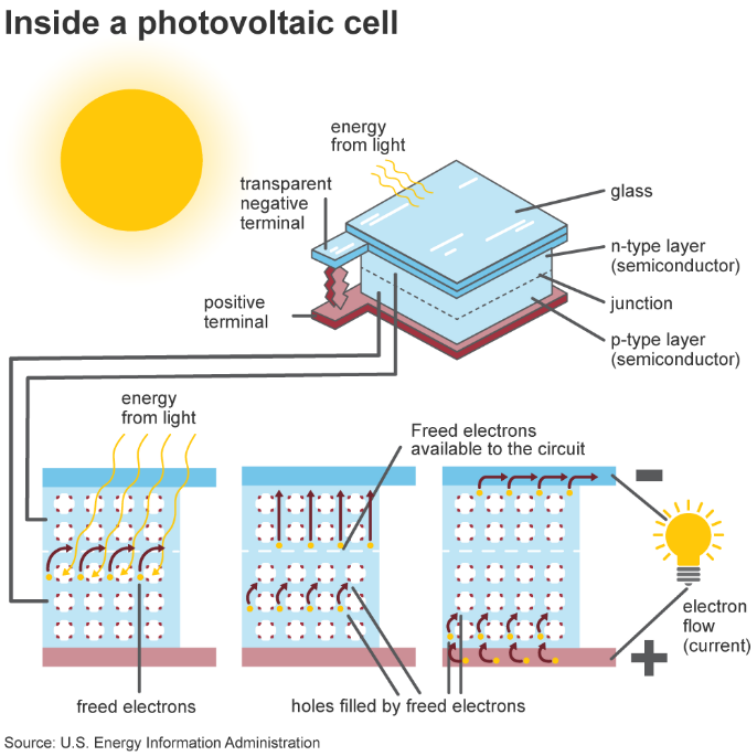

Fig. 2-14. A schematic of the principle of operation of a photovoltaic cell [65].

Such relatively small cells can be connected collectively into a module that can further be combined with other modules, and form an array having a large area. Interestingly, since PV power system generates direct current (DC), which can be converted into alternating current (AC) when inverter is applied, so that electricity produced could be fed to the grid [65]. Obviously, PV systems are preferably suitable to where great amount of sunshine is available, for instance, the Middle East or California, USA. Since its modular installation, a small PV system can also be deployed to rooftop of buildings or houses in urban area. In 2022, electricity produced by solar power reached 1310 TWh, which could be still improved drastically in a bright prospect. Nevertheless, in somewhere in the world (e.g. Poland), related issues about connecting to the grid should be firstly addressed in order to efficiently utilize such a clean energy source.

2.8. Combined heat and power (CHP) generation

Energy efficiency is concerned as one of the main issues when electricity is generated from a power plant that uses generator and turbine primarily driven by hot steam. CHP is a type of technology that allows efficient electricity production, which is enabled by recovering waste heat from a traditional power plant. A significant increase of the energy efficiency can be expected in this case. A typical configuration of the CHP can be seen in Fig. 2-15, in which an additional heat recovery system is used to provide space heating/cooling, and hot water. Unlike the traditional power plant, CHP unit acts more like a distributed power generator that could be deployed at buildings near the end-users [66]. Such smaller installation may have even 75% of total efficiency [67]. Interestingly, in order to apply such solution more easily and conveniently, a packaged micro-CHP has been introduced that uses a reciprocating engine, microturbine, or fuel cell as the main energy converter (Fig. 2-16).

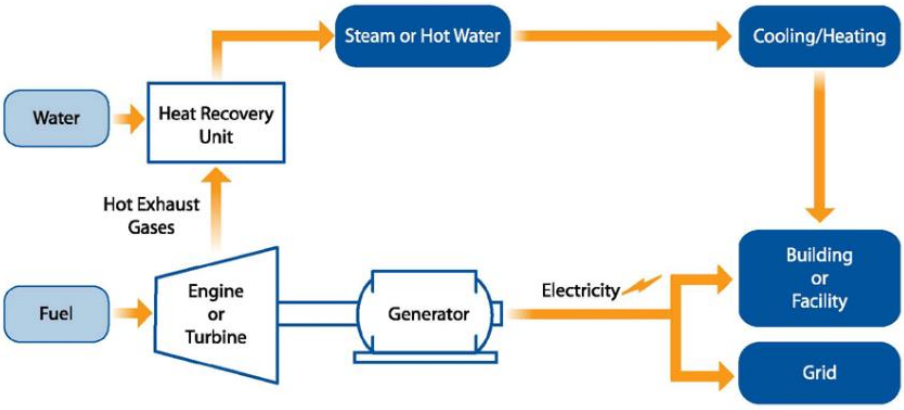

Fig. 2-15. A typical configuration of the CHP generation [66]

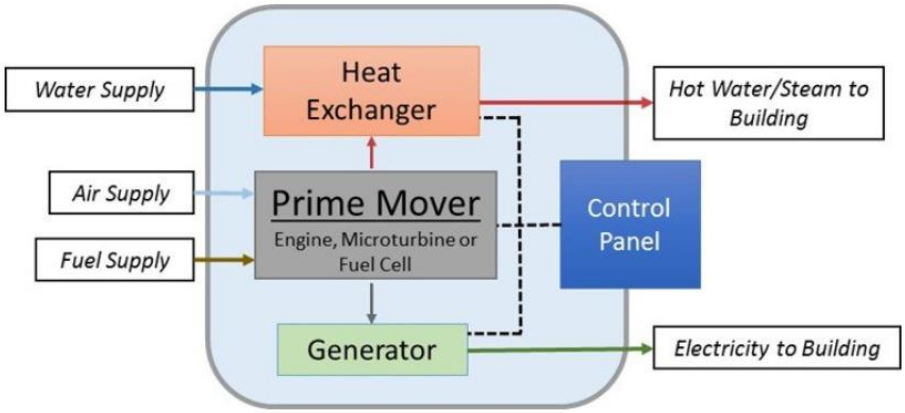

Fig. 2-16. A schematic diagram of a packaged CHP [66]

3. Hydrogen and its role in the energy transition

Speaking of available clean energy solutions needed to achieve the goal of Net Zero Emissions (NZE), hydrogen appears as one of the most promising candidates, so the hydrogen-related new technologies should not be ignored. However, to have a broader perspective, some important facts must be mentioned. First, there is a clear trend observed that the global consumption of hydrogen has increased continuously over the last several years, reaching 95 Mt in 2022, with the forecasted level of about 150 Mt in 2030 (Fig. 3-1) [68]. However, as natural resources of H_2 are rather quite limited (although interesting possibilities are recently considered [69]). hydrogen needs to be produced. As such, H_2 should be rather considered as the energy carrier, which through its specific physicochemical properties may be widely utilized, enabling decarbonization of various industrial sectors [70]. Obviously, it is of importance to relate to the basic properties of hydrogen, so the benefits and shortcomings of its application could be more explicitly stated.

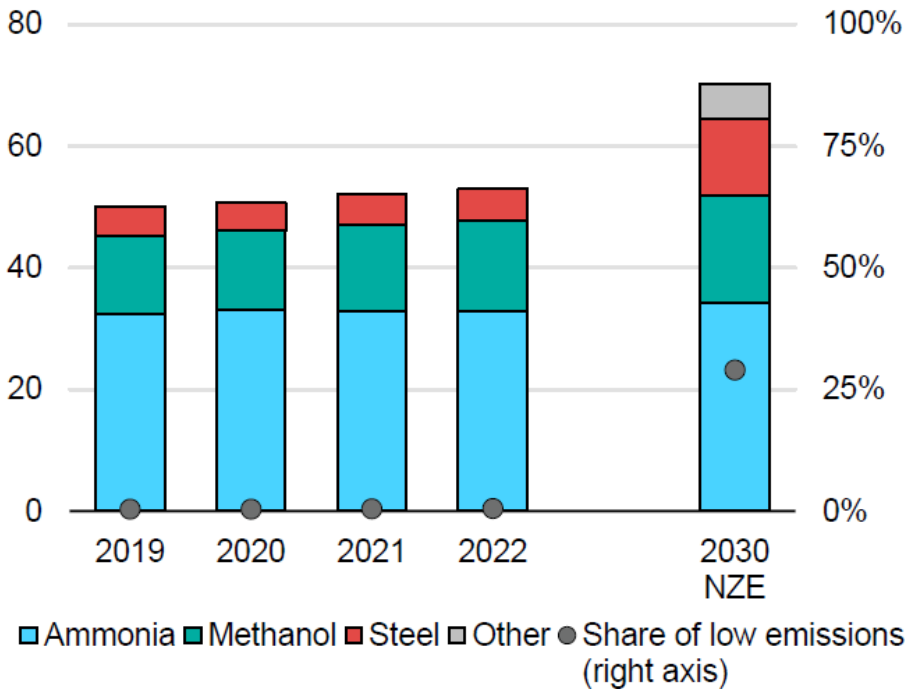

Fig. 3-1. World hydrogen use by sector in 2020-2030 [68]. Note that NZE referred to goal of Net Zero Emissions. And the "New" mainly includes reducing agent in 100%-hydrogen direct reduced iron (DRI), transport and production of hydrogen-based fuels.

3.1. Physicochemical properties of hydrogen

Hydrogen gas is comprised of diatomic molecules, H_2, which consists of the lightest existing element. Three main isotopes of hydrogen are known, stable protium (^1_1H), with the abundance of over 99.98%, stable deuterium (D or ^1_2H), and unstable tritium (T or ^1_3H). It is the most abundant element in the Universe, but on Earth it mostly exists in heterogenous molecules, such as in water or hydrocarbons. Its amount in Earth's crust is relatively low, 0.14 wt.% [71]. Since its boiling point is extremely low, ca. -253 °C, hydrogen is gaseous under normal atmospheric conditions. As gas, pure hydrogen appears as odorless, colorless and tasteless. At room temperature (20 °C) and under normal pressure (1 atm), 1 kg of H_2 takes up the space of 11.9 m^3, which constitutes almost 7% density of air in the same conditions [72].

As a carbon-free fuel, theoretically, only water and heat would be generated after hydrogen combustion in pure oxygen (Eq. 3-1), which is much favored by the mentioned NZE goal in the world. Also, water molecules can be split back relatively easily, making the (chemical) energy storage with utilization of H_2 possible. However, when hydrogen is ignited in air, different NO_x could also be the byproducts [73].

$$H_2(g) + {}^1\!/_2\, O_2(g) \rightarrow H_2O(l),\ \Delta_f H^{\ominus}_{298} = -285.8\ kJ\ mol^{-1} \quad \text{(Eq. 3-1)}$$

It is worth noting that hydrogen possesses the highest energy content by weight (119.9 kJ g^{-1}) among commonly used fuels (as compared in Tab. 3-1). Meanwhile, caution is indispensable as hydrogen gas is flammable in a quite wide range of concentrations (4-75 vol.%), and explosive (15-59 vol.%) when mixed with air [72]. This indicates that careful designs and processing activities must be carried out during the hydrogen production, transportation, storage, and utilization to avoid any leakage or other dangerous situations.

Tab. 3-1. Comparison of heating values between various fuels [72].

Fuel	Higher heating value[a] (at 25 °C and 1 atm) [kJ g^{-1}]	Lower heating value[a] (at 25 °C and 1 atm) [kJ g^{-1}]
Hydrogen	141.86	119.93
Methane	55.53	50.02
Propane	50.36	45.6
Gasoline	47.5	44.5
Diesel	44.8	42.5
Methanol	19.96	18.05

[a]Higher and lower heating values differ by the "heat of vaporization".

3.2. Production of hydrogen

As mentioned above, unlike the well-known fossil fuels, hydrogen is not a primary energy source. This implies that, similarly as for the electricity, hydrogen fuel must be produced by means of other energy sources. It acts as energy carrier that is respectively stored and consumed, depending on the needs [73,74]. Thus, it is very necessary to browse the currently available methods of the hydrogen production.

Steam reforming of natural gas and gasification of coal

Currently, global hydrogen production still predominantly relies on fossil fuels, as can been seen in Fig. 3-2. Reforming of the natural gas, without any coupled carbon capture, utilization and storage (CCUS) technology, accounted for the biggest share in the H_2 production globally in 2022, reaching 62%. This is followed by coal processing (21%), while hydrogen as the by-product (16% share) was mainly produced in refineries, and petrochemical industry [68]. The mentioned CCUS stands for various, but effective carbon dioxide processing technologies, which enable to capture the CO_2 gas emitted (typically) at the fossil fuel consumption site or factory, which is then either reused in other application or stored underground. Obviously, such method enables reducing massive CO_2 emissions into atmosphere [68,75,76]. When natural gas reforming is coupled with CCUS, the exhausted CO_2 can be collected and stored, abating the carbon footprint drastically. However, in 2022 it took up only 0.6% of the industrial H_2 production.

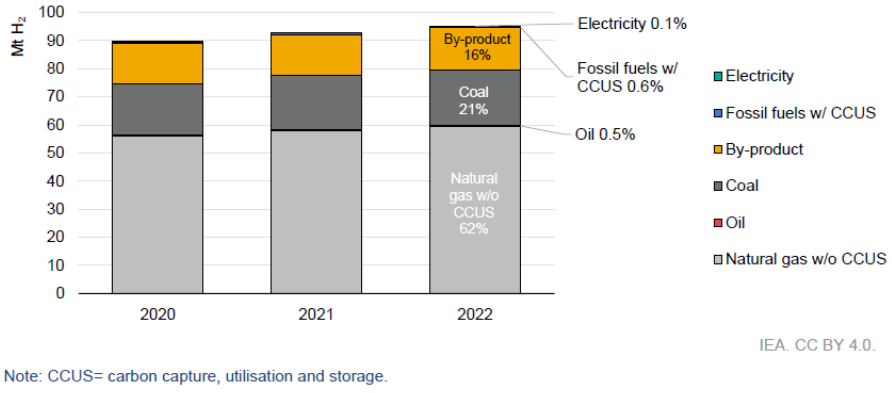

Fig. 3-2. World hydrogen production by technology in 2020-2022 [68].

Hydrogen produced from natural gas can be referred to the steam reforming (SR) of methane. This corresponds basically to mixing of methane with steam at high temperatures, on the order of 800 °C, to allow them reacting. The process is conducted on a dedicated catalyst, while also, an external heat sources is needed. Ideally, it enables producing hydrogen and carbon monoxide, however, the actual process involves other possible reactions, and has to be precisely controlled. The overall SR reaction is illustrated in Eq. 3-2, while chemical reactions are shown in the following Eqs. 3-3 (water-gas-shift reaction increasing the conversion efficiency), 3-4 (methane decomposition), 3-5 (steam-

on-coke reaction), and 3-6 (Boudouard reaction) [73,74,77–80]. Other methods of natural gas reforming (e.g. partial oxidation, autothermal, dry reforming, etc.) can be also used, but SR enables getting the desired high H_2/CO ratio (ca. 3:1).

$$CH_4 + H_2O \rightarrow CO + 3H_2 \text{ (Eq. 3-2)}$$

$$CO + H_2O \rightarrow CO_2 + H_2 \text{ (Eq. 3-3)}$$

$$CH_4 \rightarrow C + 2H_2 \text{ (Eq. 3-4)}$$

$$C + H_2O \rightarrow CO + H_2 \text{ (Eq. 3-5)}$$

$$2CO \rightarrow C + CO_2 \text{ (Eq. 3-6)}$$

Another fossil fuel, coal, can be chosen as the starting source in H_2 production. This technology is realized by the coal gasification process, in which coal is reacted with air/oxygen and steam at elevated temperatures, generating syngas (containing carbon monoxide and hydrogen), as presented in Eq. 3-7:

$$3C + O_2 + H_2O \rightarrow 3CO + H_2 \text{ (Eq. 3-7)}$$

In a similar manner as in SR process, the produced syngas can be treated with steam, yielding more hydrogen [73]. To increase the overall energy efficiency, such gasification could be integrated with a coal-fired power plant or fuel cell-based system. In this case, it would be called the integrated gasification combined-cycle system (IGCC) or integrated gasification fuel cell (IGFC) system [48,73].

Apart from coal, biomass could be used to produce hydrogen by gasification as well. Known as one of the renewable energy resources, biomass is usually formed by plant-based materials that could convert solar power into carbon-related organics by photosynthesis. It constitutes crop wastes, microalgae, forest residues, waste paper, and so on. Hence, it is very desirable that hydrogen could be produced by the gasification process based on biomass usage, but presence of tar by-product hinders development of this technology [73,74,77]. Notably, biomass can be also converted into biofuels, heat, and electricity in order to reuse its stored energy [81].

In general, it can be summarized that fossil fuels have made a great contribution in H_2 production, due to the easy access of the energy feedstock, and more reliable technology. Nevertheless, in the long run, attention should be paid to consider producing hydrogen in a more environmental-friendly way, since the aforementioned fossil fuel-based methods generate large amounts of carbon dioxide. In order to achieve the goal of NZE, renewables should be taken seriously into account.

Water electrolysis

Water, which comprises hydrogen and oxygen elements, is an obvious and very promising source to be adopted as the raw material in hydrogen production. Electrolysis

process allows splitting water molecule into oxygen and hydrogen, when external electricity is supplied to drive the reaction. The overall reaction in this case can be illustrated as in Eq. 3-8:

$$H_2O \rightarrow H_2 + {}^1/_2\, O_2 \text{ (Eq.3-8)}$$

It is evident that no carbon dioxide would be generated and released during the electrolysis process, and water resources are relatively plentiful and easily accessible on Earth. While it can be definitely regarded as the future method with respect to obtaining hydrogen, it just contributed to 0.1% of the global H_2 production in 2022 (Fig. 3-2). An obvious reason for it is related to the costs of electricity. Another issue stems from the fact that electricity itself may come from different sources, and only usage of the renewables ensures that the total emissions are not increased [79,82,83].

The apparatus where the electrolysis reaction takes place is called an electrolyzer. It mainly consists of an anode, cathode, and electrolyte (an example is depicted in Fig. 3-3). There are three main types of electrolyzers, an alkaline electrolyzer, a polymer electrolyte membrane electrolyzer, and a solid oxide electrolyzer, differing in their design, and temperature of operation.

Alkaline electrolyzers account for ca. 60% of the deployed capacity in electrolysis for the hydrogen production in the world [68]. When water is catalytically split, as enforced by the current flow, oxygen and hydrogen are generated at the anode and cathode, respectively. The reactions at the anodic side (Eq. 3-9) and cathodic side (Eq. 3-10) are as follow:

$$2OH^- \rightarrow H_2O + {}^1/_2\, O_2 + 2e^- \text{ (Eq. 3-9)}$$

$$2H_2O + 2e^- \rightarrow H_2 + 2OH^- \text{ (Eq. 3-10)}$$

The hydroxide anions obviously work as ionic charge carriers in the whole reaction, which are provided by the alkaline solution (ca. 30 wt.%) of potassium or sodium hydroxide. During operation, they are conducted in the electrolyte from the cathode to anode. Moreover, solid alkaline exchange membrane is also developed and applied [75]. For the catalysts, nickel- or iron-based materials modified with Pt (at the cathode), and Ni- or Cu-based catalysts modified with selected metal oxides, are economically adopted. Alkaline electrolyzers can work at temperatures below 100 °C, which is relatively cost-friendly regarding commercialization. The general efficiency can reach 60-80% [84], giving as low as ca. 50 kWh of electricity needed for production of 1 kg of H_2. They can also operate for a prolonged time, without any special maintenance needs [83].

Polymer electrolyte membrane (PEM) electrolyzer is another type of the device, which already contributed to about 30% of the H_2 production in the electrolysis process [68]. Unlike in the alkaline electrolyzers, ionic transport in PEM cells is realized by hydrogen cations (in fact, H_3O^+), migrating from the anode to cathode through a polymer

membrane. Still, oxygen would be released from the anode (Eq. 3-11), while hydrogen is generated at the cathode (Eq. 3-12).

$$H_2O \rightarrow {}^{1}/_{2}\, O_2 + 2H^+ + 2e^- \text{ (Eq. 3-11)}$$

$$2H^+ + 2e^- \rightarrow H_2 \text{ (Eq. 3-12)}$$

The internal, good separation of gasses, as well as possibility of production of the pressurized H_2 makes this technology as the especially appealing [83]. Similarly, PEMs work in 70-90 °C range, and may have an efficiency of even 80%. Nonetheless, noble metals are necessarily adopted as catalysts, e.g. platinum black for the cathode and iridium for the anode. This raises the costs of manufacturing, as well as on maintenance in the long-term operation [84,85].

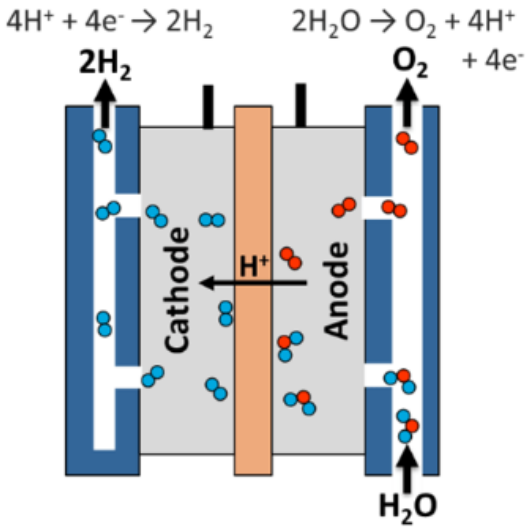

Fig. 3-3. A schematic diagram of the polymer electrolyte membrane electrolyzer [85]. Notice that pure H_2 gas is generated at the cathode during operation.

The third type, Solid Oxide Electrolyzer Cells (SOECs) differs significantly from the other two designs. The notable difference is related not only to all-solid construction (including solid oxide electrolyte), but also much higher operation temperature (on the order of 500-800 °C). This is rather an emerging, but promisingly-popular technology in water electrolysis, since it brings a possibility of reversible operation, i.e. in the fuel cell and electrolysis mode. Such devices are dubbed Solid Oxide Cells (SOCs). Other benefits can be also obtained, as for example, the ability for the co-electrolysis of H_2O and CO_2 [86], and decreased electrical energy demand at high temperatures (Fig. 3-4). In 2022, only less than 1% of the installed capacity for H_2 production by electrolysis was based of SOECs [68]. Since topic of this thesis is closely related to development of oxygen electrodes for SOCs, a separate (next) chapter is prepared, gathering comprehensive information in this matter.

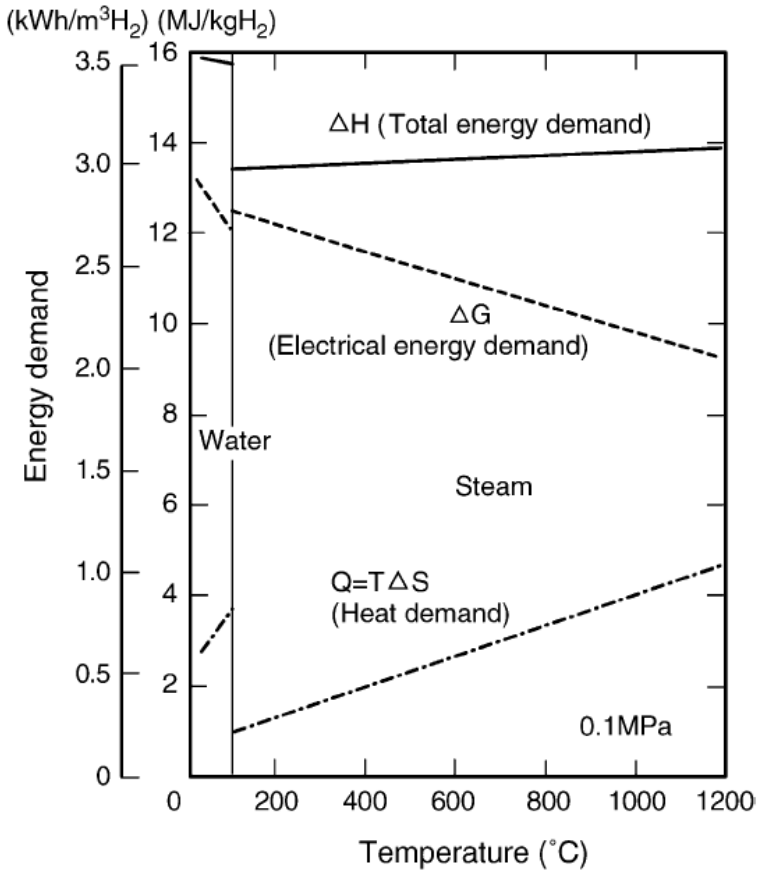

Fig. 3-4. Energy demand as a function of temperature regarding water and steam electrolysis process [87].

In general, water electrolysis indicates a different way of H_2 production in relation to the strictly chemical processes. Since the electrical energy input is necessary to trigger the electrolytic reactions, this technology should be preferably coupled with power generation sites. Also, as discussed in chapter 2, fossil fuels (mostly coal and natural gas) still predominantly contribute to the power generation in the world. Consequently, a simple increase in the installed electrolysis capacity would be rather contradictory to the goal of NZE, due to the increased emissions of greenhouse gases. Based on that it can be stated that renewables and nuclear power resources seem much more suited to be connected with water electrolysis. For example, wind power and photovoltaic technology could be supplemented by the water electrolysis technology (with the coupled H_2 storage) to mitigate their intermittent features caused by the changing weather conditions. In this case, the produced hydrogen would indeed work as the energy carrier that stores the excess of the generated electricity, which later can be released via CHP or fuel cell-based means. Also, the excess of the produced H_2 could be used for different applications, e.g. production of green ammonia or methanol. As for nuclear power, the generated steam and electricity are ideal ingredients for the water electrolysis. It is quite prospective to combine nuclear and water electrolysis technologies in order to yield multiple useful products, and enhance the energy efficiency [73,74,84,85].

Solar power-based alternative methods of H_2 production

When focusing on longer-term perspectives, solar power, which is very crucial to humankind, may be also considered as a good direct source of energy for the H_2 production. Apart from a photovoltaic cell (Fig. 2-14) that can convert solar energy into electricity, and then energize the water electrolysis, there are different means that enable producing hydrogen directly.

Photoelectrochemical water splitting in a photoelectrolytic cell is one of the methods that enables absorbing sunlight energy and directly converting water into hydrogen and oxygen via semiconductor components. As show in Fig. 3-5, when light is directed to a semiconducting anode (*n*-type), it can absorb the photon energy. Both, electrons and holes can be generated, if the absorbed energy is greater than the anode material's band gap energy. Then, water molecules are oxidized into oxygen at such photoelectrode, while the concurrently generated H^+ ions are reduced to the gaseous hydrogen at a metal cathode by the electrons transported via an external circuit [88,89]. Considering the whole water splitting process, different issues should be take into account, which include choosing proper photoelectrode materials that are cost-effective, and could give rise to electron/hole pairs under sufficiently-low overpotential, the recombination of generated electrons and holes should be minimized, and so on [89]. It is no doubt that this direct solar-hydrogen energy conversion technology is carbon-free, and constitutes a very promising method for H_2 production in the future. A large scale commercialization could be realized when the applied photoelectrodes can exhibit high sunlight absorption efficiency, as well as sufficient catalytic activity and good stability [88,89].

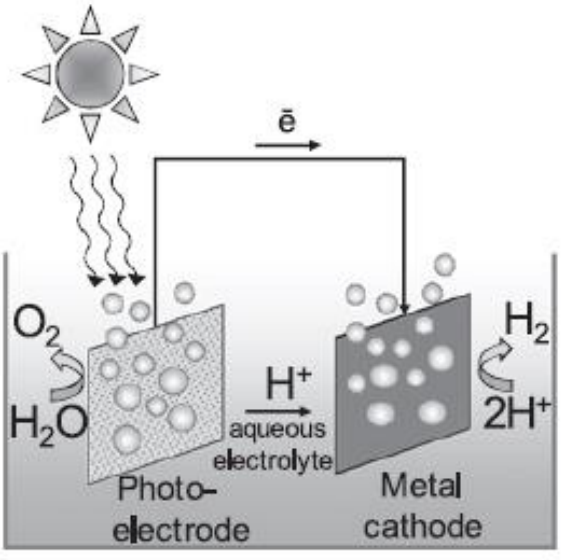

Fig. 3-5. A schematic diagram of a photoelectrochemical water splitting (photoelectrolytic) cell [89].

Photobiological hydrogen production is another noteworthy approach. Obviously, natural photosynthesis is widely-known with respect to generating organic matter. What is worth paying attention is that photosynthesis could be also used for hydrogen

production, which can be mainly realized by two different methods, water biophotolysis, and photofermentative hydrogen production. There are two classes of microorganisms that can be adopted in hydrogen generation, green microalgae and cyanobacteria. Green microalgae produce reduced ferredoxin from the photosynthesis reaction, which could reduce hydrogen cations in water to hydrogen molecules. The process is catalyzed by hydrogenase enzyme. Cyanobacteria, interestingly, are able to carry out hydrogen production and nitrogen fixation at the same time, with the help of hydrogenase and nitrogenase enzymes, respectively. Photosynthetic bacteria (e.g. purple non-sulphur bacteria) are able to break down organic matter, generating hydrogen as by-product when sunlight undoubtedly work as the energy input. That is so-called photofermentative hydrogen production. Overall, it is quite evident that solar power may play a different role in photobiological hydrogen production if different microorganisms are involved in the processes. However, remarkable enhancements in terms of efficiency and yield production should be realized before this technology could be commercialized. So far, it is still at an early stage of research [90].

Summarizing this section, a rather non-technical, but commonly used notation of "hydrogen colors" should be introduced, which not only allows for distinguishing different H_2 production routes, but emphasizes on the related carbon emissions (Fig. 3-6).

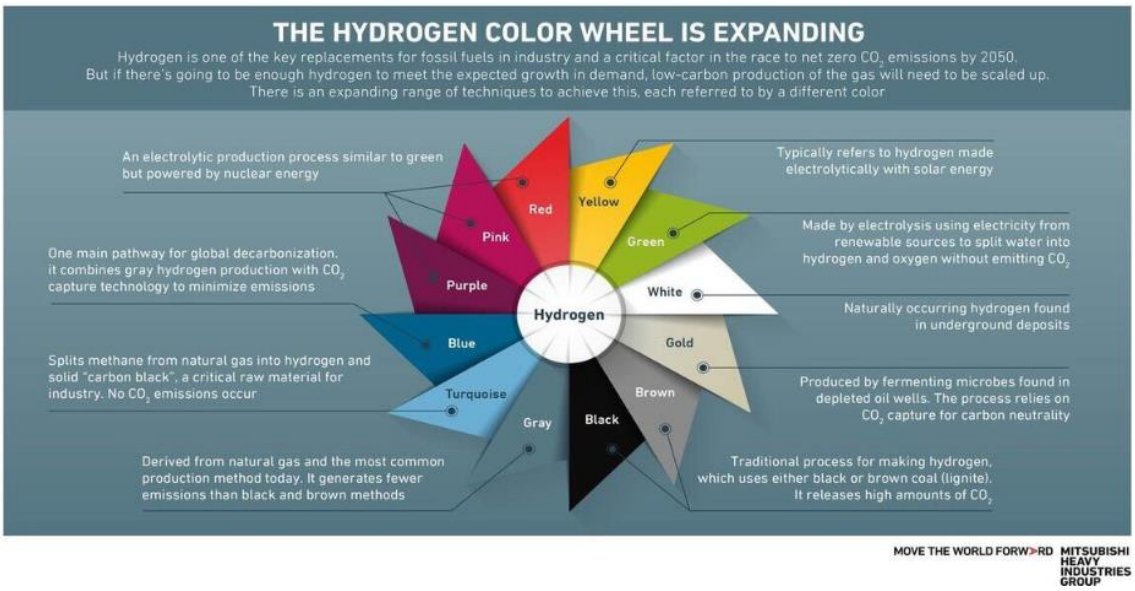

Fig. 3-6. The hydrogen color wheel [91].

3.3. Hydrogen storage

As it is a highly combustible and explosive fuel, great caution should be exercised to properly store hydrogen after its production. According to one of the classification schemes, mainly two types of hydrogen storage, stationary and on-board, should be considered. Speaking of the first one, a larger site can be occupied, and the physical

conditions of the storage (e.g. temperature and pressure) can be tuned in a wider range. Consequently, it is relatively less challenging than the on-board H_2 storage [73,74]. As it can be seen in Tab. 3-2, hydrogen demonstrate the lowest energy density (by volume) among other fuels/chemicals at the same conditions. Thus, in order to store H_2 efficiently and safely when it comes in limited spaces, a specially designed method should be considered. Meanwhile, it should be mentioned that such storage does not bring about much problem with the weight.

Storing hydrogen in the liquid state seems as quite favorable, because other liquid fuels, like gasoline and diesel, have been widely-applied in transportation. This is rather convenient in e.g. a refilling scenario, and also, liquid hydrogen possesses higher energy density than even highly-compressed H_2 gas. Nevertheless, what should be kept in mind is that H_2 boiling point is as low as at -253 °C under 1 bar, creating substantial problems related to safety. A respective container or a vessel should have special insulation characteristics, and low-temperature resistance. Furthermore, the evaporation of liquid hydrogen cannot be neglected, contributing to the short storage time and additional safety issues [73,74,92–94].

Tab. 3-2. Comparison of energy density between fuels, calculated using lower heating values. Based on data from [72]

Fuel	Energy density [MJ m^{-3}]	Conditions
Hydrogen	10.05	1 atm; 15 °C
	1825	206 bar; 15 °C
	4500	689 bar; 15 °C
	8491	liquid
Methane	32.56	1 atm; 15 °C
	6860.30	206 bar; 15 °C
	20920.40	liquid
Propane	86.67	1 atm; 15 °C
	23488.80	liquid
Gasoline	31150	liquid
Diesel	31435.80	liquid
Methanol	15800.1	liquid

Compressing hydrogen is another way for its storage. A remarkable difference can be still made with regard to the energy density (in Tab. 3-2) at the same temperature, when H_2 is stored in the compressed state. For instance, 182 times higher energy density can be achieved at the pressure of 206 bar (15 °C), as compared to that at 1 atm conditions. Further increasing pressure, to the range of 600-1000 bar, can result in a much higher energy density, but advanced materials should be applied to manufacture a suitable cylinder too, e.g. composites based on carbon fibers [73,74]. Nevertheless, compressed hydrogen still cannot reach the same volumetric energy density as gasoline or diesel fuels, which causes problems with its adoption in portable applications. On the other hand, if

e.g. salt caverns or similar underground geological structures are available, storage of H_2 can be realized at the elevated pressures (ca. 20 MPa), with some promising results already documented [95,96].

Alternatively, physisorption and chemisorption are also considered as prospective hydrogen storage methods, and while the former one is about adsorbing hydrogen molecules on the surface of different (solid) materials, the latter one refers to chemical absorption of hydrogen [74,97]. Speaking of physisorption, carbonaceous materials are one of the most promising candidates. For example, activated carbon that features a high surface area and suitable porosity could deliver a storage capacity of 5 wt.%, but at very low temperatures [98]. Zeolite-like carbon may show even a higher capacity of 6.9 wt.% [99], while nickel-impregnated carbon nanotubes demonstrate a considerable capacity of 0.87 wt.% at room temperature, but at high pressures [100].

When it comes to chemisorption, metal hydrides are the well-known candidates. Unlike the compression and liquefication, metal hydrides are able to absorb hydrogen at moderate temperature and pressure conditions. In this case, hydrogen molecules would be disassociated into atoms, then incorporated into the metal lattice, forming respective metal hydrides. The process is illustrated by Eq. 3-13, in which *M* represents a metal element (or an alloy) [101].

$$M + {}^{x}/_{2}\, H_2 \leftrightarrow MH_x \quad \text{(Eq. 3-13)}$$

Basically, the successful candidates should meet the requirements of high H_2 storage capacity, moderate temperatures in both, H_2 absorption and release processes, as well as ability for reversible cycling in prolonged operation. Still, in order to minimize the weight burden in e.g. transport applications, light (metal) elements or alloys are in favor, like Li, Mg, B, and Al. Among hydrides, $NaAlH_4$ has been regarded as one the most promising candidates for practical application, since it is known to reversibly store hydrogen, reaching a capacity of up to 4.5 wt.%, when it is modified, e.g. by nanocrystalline TiO_2 embedded in carbon (TiO_2@C-doped $NaAlH_4$) [102]. The achievable H_2 storage capacity values for selected materials are summarized in Tab. 3-3. Obviously, in-depth studies are still needed that should be dedicated to further adjustments of the absorption/release temperature, improvements in reversibility, as well as kinetics of the reactions [101].

Alternatively to solids, H_2 can be also stored (and transported) with the use of liquids, and in fact, ammonia appears as an obvious choice, due to the developed infrastructure (ammonia is produced commercially by the Haber-Bosch process from hydrogen and nitrogen). However, liquid ammonia is toxic, and the released hydrogen is somewhat contaminated by traces of ammonia [103]. Last but not least, liquid organic hydrogen carriers (LOHC) can be also regarded as a promising H_2 storage/transportation method. Among candidate chemicals, *N*-ethylcarbazole appears as particularly suitable, as a catalytic dehydrogenation process of dodecahydro-*N*-ethylcarbazole can be effectively conducted, and the liquid carrier can be recycled. Theoretically, LOHC systems could be implemented based on the current infrastructure constructed for fossil fuels. Such storage has also other advantages, including high energy density, it is efficient and safe [104].

Tab. 3-3. Comparison of hydrogen storage capacity in different type of materials.

Materials	Hydrogen storage capacity [wt.%]	Conditions	Reference
Activated carbon	5	20 bar; -196 °C	[98]
Zeolite-like carbon	6.9	20 bar; -196 °C	[99]
Nickel-impregnated carbon nanotubes	0.87	100 bar; 25 °C	[100]
TiO_2@C-doped $NaAlH_4$	4.5	100 bar; 50 °C	[102]
N-ethylcarbazole (LOHC)	5.8	70 bar; 130-160 °C	[104]

3.4. Contemporary and future hydrogen applications

In order to create a prosperous future of the hydrogen economy, it is necessary to discuss contemporary situation in hydrogen usage on the commercial scale. In 2022, the biggest share of the global H_2 usage was as ascribed to industry, followed by refining at the second place (Fig. 3-1). In the industry, as depicted in Fig. 3-7, the ammonia production took up the largest share of the hydrogen consumption (60%), while methanol accounted for 30%. It was followed by the steel industry for making direct reduced iron (10%).

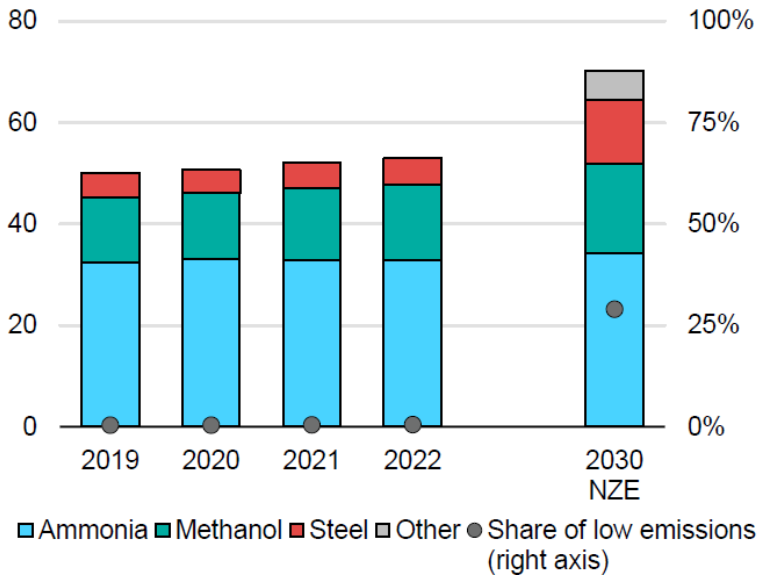

Fig. 3-7. Hydrogen consumption in industry by sector [68]

Although all other applications do not contribute considerably, it can be expected that e.g. hydrogen can be admixed to the gaseous fuel used in the abovementioned CHP units. Later, pure H_2 can be used as well, so the renewable hydrogen can serve as fuel to provide both, electricity and heat at the same time. This should be very beneficial in enhancement of the energy efficiency, when deployed in domestic communities or office buildings. As already briefly mentioned, one of the most prospective applications of hydrogen is for fueling the fuel cells. This is undoubtedly an energy conversion technology featuring high efficiency and clean low emissions (more information about it constitutes the main part of the next chapter). Advantages are also apparent when various fuel cell-based vehicles (cars, trucks, trains, etc.) are fueled with hydrogen, however, hydrogen storage, as well as lack of fueling stations, still bring about serious challenges to the practical, massive commercialization of such solutions. It should be mentioned here that traditional internal combustion engines can also be fueled by hydrogen, after limited modifications [73,83,105,106].

Finally, looking for the possible future growth of the hydrogen economy, with the novel technologies realized, it is reasonable to envision a large scale application of (low emission or clean) hydrogen for the benefits of human society. Such hydrogen can be used to couple and decarbonize various industrial sectors (Fig. 3-8).

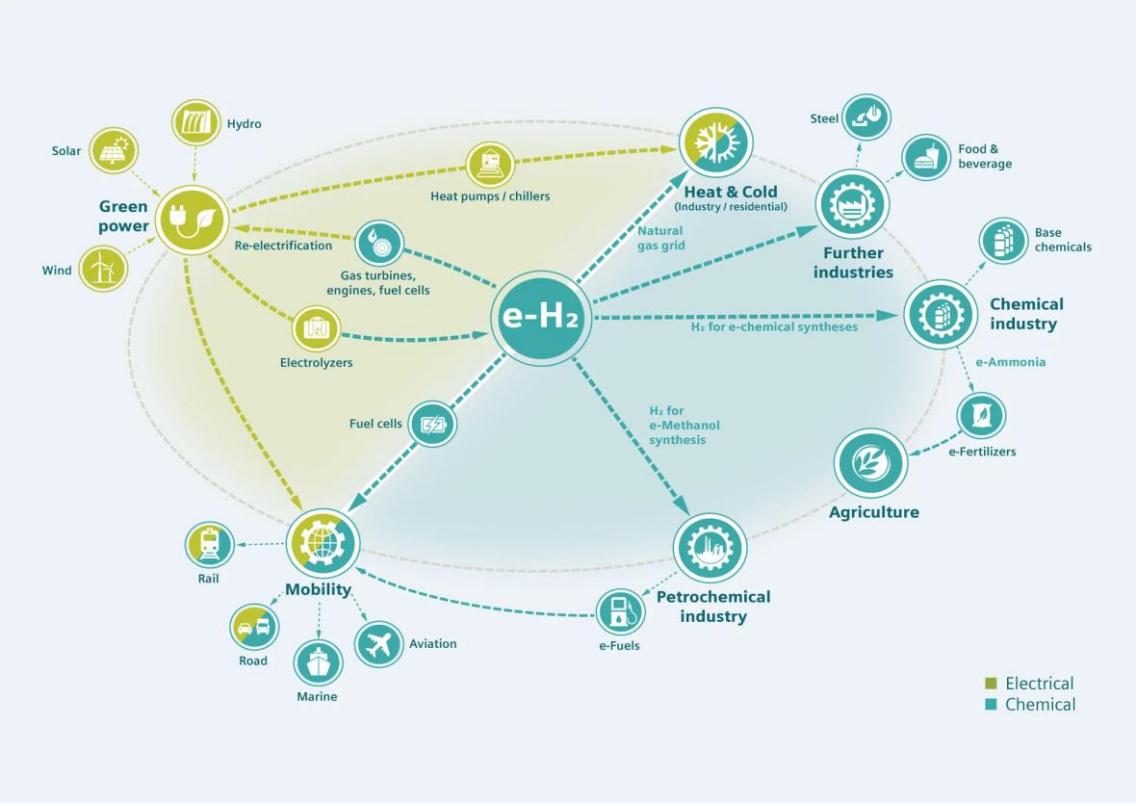

Fig. 3-8. Sector coupling with the usage of clean hydrogen originating from electrolysis (e-H_2). It is considered crucial to decarbonization of different industrial sectors [107].

4. Introduction of fuel cells, with an emphasis on Solid Oxide cells and oxygen electrode materials

Fuel cells are electrochemical devices capable of converting chemical energy of fuel and oxidizer directly into electrical energy and heat. Typically, hydrogen is used as the fuel, but in some types of the cells, also carbon monoxide or even (reformed) methane can be utilized. They are known for their remarkable efficiency, which can be linked with a lack of intermediate energy conversion steps. Also, some of the designs allow for reversible operation, i.e. electricity can be used to split water into hydrogen and oxygen, and the cell works as the electrolyzer [108,109].

Fundamental working principle of a typical fuel cell would be as follow: fuel is catalytically oxidized on an anode, while oxygen (pure or coming from air) is catalytically reduced at a cathode. Formation of the reaction product may take place at either of the electrodes, depending on the type of charge carriers transferred via an electrolyte. To balance the reaction, released electrons are transported via an external circuit. A schematic diagram of fuel cells with O^{2-}- and H^{+}-conducting electrolytes is shown in Figs. 4-1a and b. The typical reaction formulas are described in the equations presented in the graphs as well (setting hydrogen as the fuel).

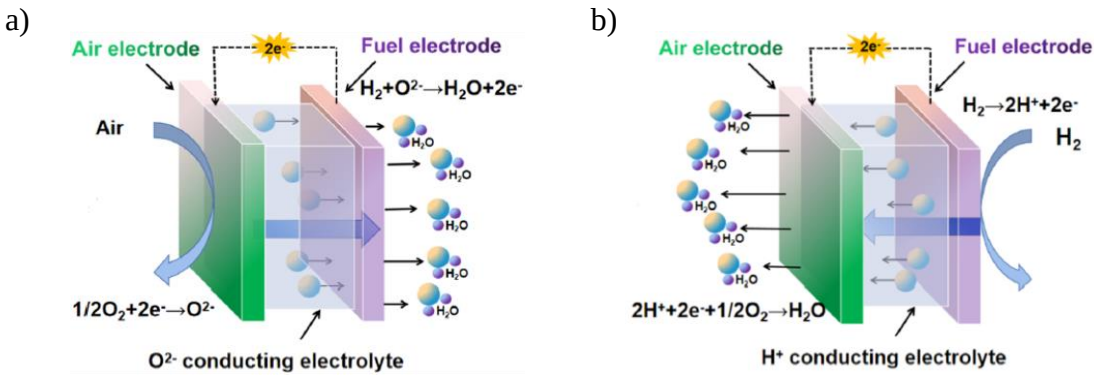

Fig. 4-1. A schematic diagram of a fuel cell with the electrolyte conducting by a) oxygen anions, b) hydrogen cations [110].

Accompanying the great research that has been conducted in previous and also recent years toward development of the hydrogen economy, fuel cells and their application have been considered as the main mean of bringing H_2 utilization to daily life of humankind. It is no doubt that fuel cells technology is one of the most popular approaches, in which the advantages of hydrogen can be utilized. However, trials in history were indispensable in this process. It was not until William Grove, who invented the prototype of a fuel cell in 1839, that gases, such as ethylene and carbon monoxide, were selected as a fuel to generate electricity. The design was later called a gaseous voltaic cell [111]. An array of attempts have been done by followers, including Mond and Langer, who applied porous structure of an electrode and platinum black as a catalyst. Also, trials by Bacon, who

intended to implement ordinary materials, like nickel as electrodes, as well as hydrogen and pure oxygen as fuel and oxidant, respectively, were of importance [111,112]. Those enhancements greatly helped bringing fuel cells to the point, with which people are familiar at present. Many years of development resulted in numerous designs. Nowadays, there are several types of technologically-developed fuel cells (Fig. 4-2), and some of them have been successfully utilized in terms of power generation [113].

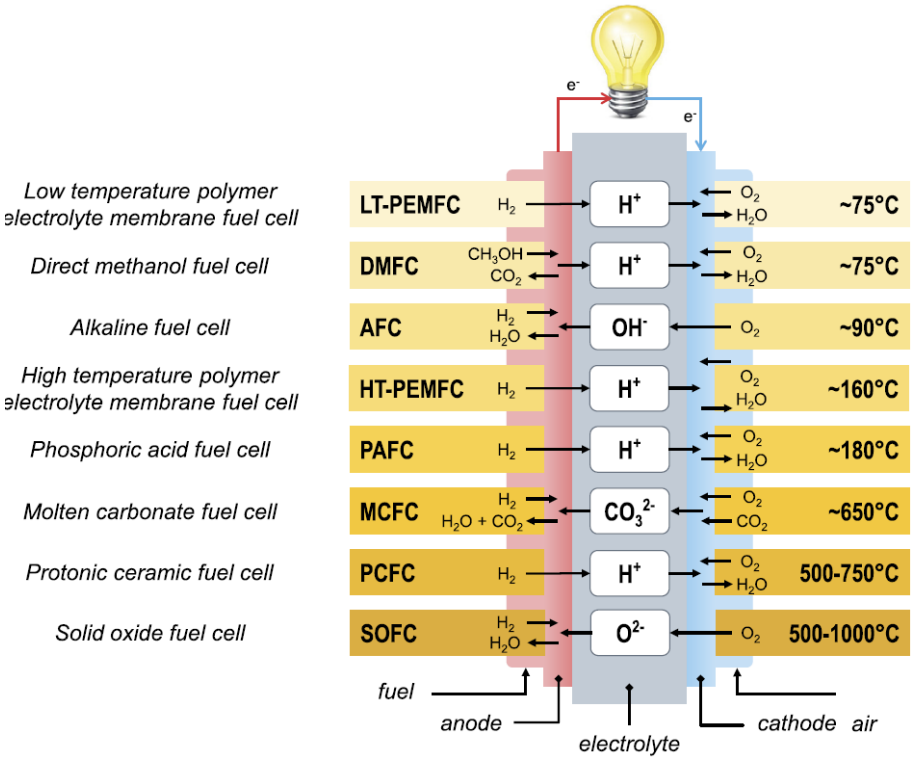

Fig. 4-2. Main types of fuel cell. Notice the used abbreviations, ionic charge carrier in the electrolyte, as well as arrows pointing direction of the electrochemical processes, with reactants and products marked as well [113].

Some of the fuel cell designs have proven to be particularly useful, with larger-scale stacks developed as well (up to MW_e scale), and high efficiency obtained (even 60%). The provided Tab. 4-1 summarizes data on five main fuel cell types, with an emphasis on the applications, advantages, as well as challenges [114]. More details are also given in the text below for selected types of the cells. An observation can be also made that in different literature references the reported values of the efficiency, working temperature, stack power, and other characteristics may vary somewhat, which stems from the constant development process, as well as some differences in the definition of the actual parameters.

Tab. 4-1. Selected data on main five types of fuel cells, with the emphasis on the stack size, efficiency, applications, as well as advantages and disadvantages [114].

Fuel Cell Type	**Polymer Electrolyte Membrane (PEMFC)**	**Alkaline (AFC)**	**Phosphoric Acid (PAFC)**	**Molten Carbonate (MCFC)**	**Solid Oxide (SOFC)**
Fuel	H_2	H_2	H_2	H_2/CO/reformate	CO, H_2
Oxidizer	O_2, air	O_2, air	O_2, air	CO_2,O_2, air	O_2, air
Common Electrolyte	Hydrated Polymeric Ion Exchange Membranes	Mobilized or Immobilized Potassium Hydroxide in asbestos matrix	Immobilized Liquid Phosphoric Acid in SiC	Immobilized Liquid Molten Carbonate in $LiAlO_2$	Perovskites (Ceramics)
Operating Temperature	40 – 80 °C	65 – 220 °C	205 °C	650 °C	600 -1000 °C
Typical Stack Size	1kW-250kW	10-100kW	400W	300kW-3MW	1kW-2MW
Efficiency	60% (Transportation) 35% (Stationary)	60%	40%	50-60%	50-60%
Applications	-Backup power -Portable power -Distributed generation -Transportation -Specialty vehicle	-Military -Space	Distributed generation	-Electric utility -Distributed generation	-Auxiliary power -Electric utility -Distributed generation
Advantages	-Solid electrolyte reduce corrosion & electrolyte management problems -Low temperature -Quick start-up	-Cathode reaction faster in alkaline electrolyte, leads to high performance -Low cost component	-High temperature enable -Increase tolerance to full impurities	-High efficiency -Fuel flexibility -Can use variety of catalyst -Suitable for CHP	-High efficiency -Fuel flexibility -Can use variety of catalyst -Solid electrolyte -Suitable for CHP&CHHP -Hybrid/GT cycle
Challenges	-Expensive catalyst -Sensitive to fuel impurities	Electrolyte management	-Pt catalyst -Long start up time	-High temperature corrosion and breakdown of cell components -Long start up time -Low power density	High temperature corrosion and breakdown of cell components

Polymer Electrolyte Membrane Fuel Cells

PEMFCs are also referred as Proton Exchange Membrane Fuel Cells, emphasizing on the ionic charge carrier in the electrolyte. In a PEMFC, a perfluorinated sulfonated polymer membrane is usually adopted as the electrolyte that transports protons from the anode to the cathode. Typical reactions occurring at these electrodes are shown in Eqs. 4-1 and 4-2, respectively:

$$H_2 \rightarrow 2H^+ + 2e^-$$ (Eq. 4-1)

$$^1/_2\, O_2 + 2H^+ + 2e^- \rightarrow H_2O$$ (Eq. 4-2)

Apart from the membrane, platinum or its alloys are necessary to be used, acting as catalysts. This creates problems, as such materials are easily poisoned by carbon monoxide, if for example, the used hydrogen is produced by fuel reforming. Another issue is related to an increase in the manufacturing costs. It is worth noting that most PEMFCs work at low temperatures, e.g. under 100 °C, which also means a short start-up time and limited degradation of components. PEMFCs can reach a high electrical efficiency of 40-60%. At present, a particular usage of PEMFCs should be mentioned, as they can be installed in transportation vehicles, so called fuel cell vehicles (e.g. Toyota Mirai) [115–118].

Alkaline Fuel Cells

AFCs feature in their construction alkaline electrolytes, typically, potassium hydroxide solutions, which is favorable to the oxygen reduction reaction (ORR). Reactions on both electrodes are shown as Eq. 4-3 (anode) and 4-4 (cathode).

$$H_2 + 2OH^- \rightarrow 2H_2O + 2e^-$$ (Eq. 4-3)

$$^1/_2\, O_2 + H_2O + 2e^- \rightarrow 2OH^-$$ (Eq. 4-4)

Nonetheless, the mentioned KOH solution can be easily affected by carbon dioxide, which suggests using carbon-free reactants on both, the anode and cathode. This is because hydroxyl ions, which act as the charge carriers, react with carbon dioxide, generating carbonates. While the operating temperature range is broader (Tab. 4-1), AFCs can also work in a low temperature range of 23-90 °C, which makes them suitable for transportation or even space applications. Additionally, since nickel is usually chosen as the catalyst for AFCs, this lowers the costs [112,115]. It should be also mentioned that basically, an electrical efficiency of 60% could be reached by the AFC [116].

Phosphoric Acid Fuel Cells

With the liquid phosphoric acid adopted as the electrolyte, hydrogen ions work as charge carriers in PAFCs, migrating to the cathode and reacting with oxygen ions to form water molecules. Due to the higher operating temperature of PAFCs (150-200 °C), the generated water on the cathode can be used for heating applications. Reactions on the anode and cathode are illustrated in Eq. 4-5 and 4-6, respectively:

$$H_2 \rightarrow 2H^+ + 2e^-$$ (Eq. 4-5)

$$^1/_2\, O_2 + 2H^+ + 2e^- \rightarrow H_2O$$ (Eq. 4-6)

Although PAFCs are not subjected to the negative influence of carbon dioxide like AFCs, disadvantages of this design are also noticeable, which are mainly related to the applied platinum catalyst, and relatively lower electrical efficiency (around 37-42%). However, a much higher efficiency could be obtained, even as high as 85%, when the PAFC is used in the CHP system [115–117]. After all, PAFCs are regarded as one of the most mature fuel cell technologies, and were commercialized quite early [118].

Molten Carbonate Fuel Cells

MCFCs are classified as high temperature fuel cells, since they generally operate at relatively high temperatures, on the order of 600-700 °C, in which molten lithium and sodium carbonates act as the electrolyte. Owing to the high operating temperature, MCFCs have fuel flexibility, so for example, natural gas and biogas can be fed as fuel. The hydrocarbons can be internally reformed on the anode, yielding hydrogen and carbon monoxide. Carbonate ions, a specific feature of MCFCs, combine with hydrogen forming water and carbon dioxide, while oxygen reacts with carbon dioxide to generate carbonate ions. The respective reactions on the anode (Eqs. 4-7 and 4-8) and cathode (Eq. 4-9) are provided as follow:

$$H_2 + CO_3^{2-} \rightarrow H_2O + CO_2 + 2e^- \text{ (Eq. 4-7)}$$

$$CO + CO_3^{2-} \rightarrow 2CO_2 + 2e^- \text{ (Eq. 4-8)}$$

$$^1/_2\, O_2 + CO_2 + 2e^- \rightarrow CO_3^{2-} \text{ (Eq. 4-9)}$$

The mentioned high temperature of the operation is desirable, as the use of noble metals as catalysts is not needed, and the cells can reach high efficiency when applied with a CHP. Nevertheless, the relatively poor longevity has been a major concern, since components corrosion and degradation occur at such temperatures relatively fast [112,115,117].

4.1. Solid Oxide (Fuel) Cells

Solid Oxide (Fuel) Cells (SOFCs) feature all solid state configuration, which is beneficial, as there is no need to immobilize a molten electrolyte. Initially, the devices have been develop with the aim to work in the fuel cell mode. However, since the reversed mode of operation became of broader interest for the hydrogen production (see previous chapter), the high temperature Solid Oxide Electrolyzer Cells (SOECs), as well as Solid Oxide Cells (SOCs) names started to be used. While designs of the SOECs are essentially the same as that of the SOFCs, the mode of operation is of course changed. In the literature, shortened name also became popular, and SOCs are considered as the devices capable for the FC and EC operation. To further emphasize on this possibility, a word “reversible” is also added before the SOC, with the rSOCs abbreviation used as well [119,120]. It should

be also stated that in order to avoid confusion, “oxygen electrode” and “fuel electrode” names should be used in this case.

SOFCs, or more broader, SOCs are among the most widely used fuel cell technologies in the world, and their further development (in terms of materials, designs, integration into energy grid, etc.) is quite an active research topic in the academia. The mentioned main feature of SOCs is related to the transportation of either oxygen ions or protons through the dense, solid electrolyte at elevated temperatures. It occurs effectively at 600-1000 °C for the oxygen-conducting electrolytes, while at ca. 500-700 °C for the proton-conducting electrolytes. In the latter case, the Protonic Ceramic Fuel Cells (PCFCs) name is also used, and of importance, such devices can also work as Protonic Ceramic Electrolyzer Cells (PCECs) [121].

In the case of a standard SOFC (oxygen ions as charge carriers), oxidation and reduction reactions occurring on the anode and cathode can be described with Eqs. 4-10 and 4-11, respectively:

$$H_2 + O^{2-} \rightarrow H_2O + 2e^- \text{ (Eq. 4-10)}$$

$$^1/_2\, O_2 + 2e^- \rightarrow O^{2-} \text{ (Eq. 4-11)}$$

Similar to MCFCs, also operating at high temperatures, SOFCs show good fuel flexibility, which means that both, natural gas and gaseous fuel made from coal can be fed to the cell [117]. In the case of carbon monoxide, the anodic reaction can be written as presented in Eq. 4-12:

$$CO + O^{2-} \rightarrow CO_2 + 2e^- \text{ (Eq. 4-12)}$$

High temperature operation also brings about downsides, including slow start-up and cool-down, thermomechanical compatibility issues between components, and decreased longevity due to corrosion and degradation [112,117]. Consequently, such drawbacks potentially hinder SOCs from being applied for portable purposes, e.g. in vehicles. On the other hand, high operating temperature opens other application scenarios, including distributed power generation, auxiliary power option for community, and also CHP usage, since the waste heat from (larger) SOCs can be reused in power generation as well, increasing efficiency up to 60-80% [115,117].

As mentioned, most of the cells can work reversibly as SOECs, producing hydrogen. In this case, surplus electricity (as the power source) and steam (as the feedstock) are required. Nevertheless, the installed capacity of SOECs was far more less, as compared to alkaline electrolyzers (data from 2022) [68]. When steam is fed to cathode, water molecule is reduced into hydrogen and oxygen anion that later is transported through solid electrolyte to the anode and oxidized into oxygen. Related reactions on the oxygen electrode and the fuel electrode are demonstrated in Eq. 4-13 and 4-14, respectively [84]:

$$O^{2-} \rightarrow {}^1/_2\, O_2 + 2e^- \text{ (Eq. 4-13)}$$

$$H_2O + 2e^- \rightarrow H_2 + O^{2-}$$ (Eq. 4-14)

Despite low adoption in the market, such devices are still regarded as very promising and flexible energy conversion units. Again, the possibility for reversing the mode of operation in SOCs should be mentioned, but importantly, carbon dioxide can be also electrolyzed (reversed Eq. 4-12), which is regarded as another important advantage of SOCs [122,123]. Overall, it can be stated that SOCs enable linking electricity, hydrogen, and also, carbon dioxide utilization, and thus are facilitating prosperity of the hydrogen economy, as well may (partially) help with the CO_2-related environmental issues.

Considering enlarging the application of SOCs, an evident trend can be observed throughout the research domain, which specifically aims at lowering the operating temperature to the intermediate-temperature (600-800 °C, so called IT-SOCs) or even low-temperature range (400-500 °C, LT-SOCs) [112,117,118]. Advantages are obvious behind it, which would not only broaden the range of candidate materials for components, particularly for sealants and interconnect materials, but should enable alleviating the aforementioned drawbacks [112,124]. However, the main concern should lie in keeping a good balance between the general performance and operating temperature. In order to achieve this goal, it is quite necessary to have better understanding of the applied materials for SOCs components, primarily including the fuel electrode, electrolyte and oxygen electrode. This is crucial to make the direction of studying and developing novel materials more accurate and efficient.

Fuel electrodes for SOCs

As it is the reaction site where fuel oxidation takes place, the sufficient catalytic activity is the one of the key characteristics that SOFC anode candidates are supposed to possess. Apart from that, other requirements should be taken into account as well, including high electrical conductivity, thermomechanical compatibility, chemical stability, and also, proper porosity for a good contact with the gas atmosphere [125,126]. Given that fuel electrode works in reducing atmospheres, metals would be favorably chosen, like Pt, Co, Ni, and so on. However, platinum is too expansive, and also, usage of metals directly on the oxide electrolyte is problematic, due to different thermal expansion. Importantly, this would also strongly limit the length of the Triple Phase Boundary (TPB), at which the electrochemical reaction takes place. Consequently, in order to extend the TPB, at present, the most widely employed fuel electrodes are made of the cermet-based materials [124–126]. Nickel combined with the yttria-stabilized zirconia (Ni-YSZ, typically 8YSZ or 3YSZ) is the most popular cermet that has been broadly applied in either commercial cells or for the laboratory use. Relatively low cost and adequate catalytic activity make nickel a good option. YSZ is also an important electrolyte material in SOCs (see below), featuring sufficient oxygen ion conductivity and excellent chemical stability. Furthermore, porous skeleton of YSZ decorated with Ni particles provides close thermal expansion behavior to that of the dense YSZ electrolyte. During operation, nickel oxide particles (used to for preparation of the cermet) will be reduced to metallic particles, dispersed in the YSZ skeleton, creating desirable number of

reaction sites (long TPB), as well as desired porosity (ca. 30 vol.%) for the effective contact with the gas atmosphere [125,127].

Similar approach, i.e. formation of a cermet with electrolyte material can be done for other candidates. Also used as the common electrolyte, gadolinium-doped ceria (GDC, typically with 10 or 20 at% of Gd) can be employed as a skeleton of the SOFC anode, due to its high oxygen ion conductivity at intermediate temperatures (ca. 0.01 S cm^{-1} at 500 °C for $Ce_{0.9}Gd_{0.1}O_{2-\delta}$) [125], consequently making Ni-GDC as another popular anode for SOCs [125,126,128].

Nevertheless, nickel is susceptible to unfavorable processes, e.g. sulfur poisoning and carbon deposition, since it facilitates decomposition of hydrocarbons, if they are fed as the fuel [124–126,128]. Copper, on the other hand, is considered as promising to replace nickel, because of its contribution of pure and very high electronic conductivity, enhanced tolerance for sulfur poisoning, as well as inactivity toward carbon deposition. Consequently, Cu-ceria and Cu-YSZ fuel electrode materials are of interest [124–126]. Similarly, both, cobalt and ruthenium have been also considered as replacements for nickel, but their high cost is the main obstacle for possible application [127,128].

Another type of the SOFC anodes should be also mentioned, which comprises perovskite-type oxides. Given that many of such oxides can relatively easily release or accept oxygen into their lattice, as well as that numerous perovskites exhibit mixed ionic-electronic conductivity with a relatively high oxygen ion component, they appear as an attractive alternative. In this case, the presence of the second phase (e.g. YSZ) is not needed. Moreover, compositional flexibility of perovskites and ability to accept dopants at different crystal sites enable, for example, substitution with elements that may easily change their charge state (e.g. Ti, Ni, Co, Mn and Fe). In this case, desirable level of electronic conductivity can be also expected [125]. However, because of the reducing conditions and high temperature of operation, higher concentration of easily-reducible elements is problematic, as the material may decompose.

Lanthanum-doped strontium titanate ($La_xSr_{1-x}TiO_3$) is one of the typical perovskite oxides that possess high electrical conductivity and similar thermal expansion coefficient to that of YSZ in reducing conditions [129]. Additionally, cobalt can also be (partially) substituted at the Ti sites, enhancing the ionic and electronic conductivity [130]. Apart from lanthanum, yttrium can be also selected as a dopant element for strontium at an optimized content, which can strongly promote the electrical conductivity [131]. Lanthanum chromite ($LaCrO_3$) is considered as a potential SOFC anode candidate as well, with a number of works devoted to enhancing its catalytic activity toward different fuels. The works show possibilities of Ca or Sr doping at the La sites, and Ni, Fe, Mn or Co doping at the Cr sites [132,133].

At the same time, oxides with a double perovskite structure have also been studied as fuel electrode candidates. For example, $Sr_2MgMoO_{6-\delta}$ was proven as a prospective anode candidate, due to a series of advantages, including mixed ionic-electronic conductivity and tolerance towards sulfur poisoning [134]. Additionally, related chemical substitution has been also studied in order to improve different properties of the material, and e.g. Co-, Al- and Fe-doping are known to enhance its electrical conductivity [135–137]. Finally, more complex approaches for development of the catalytically-active materials are also

reported, for example, concerning exsolution of the metallic particles from the perovskite backbone [138].

Electrolytes for SOCs

As mentioned above, the capability of using the solid electrolyte exhibiting ionic conduction makes SOCs distinct from other fuel/electrolyzer cell types. It is worth noting that oxygen ions migration in an electrolyte is a thermally activated process, resulting in a strong temperature dependence [124]. Hence, many efforts have been devoted to developing suitable electrolyte materials, especially for IT-SOCs. All electrolyte candidates should meet critical requirements, involving high ionic conductivity, as well as very low electronic conductivity, excellent chemical stability in reducing and oxidizing conditions, chemical and thermomechanical compatibility with other components, sufficient density (gas tightness). It is also beneficial if the material is low cost and environmentally benign [124,139,140]. The most widely-known and commercialized electrolytes are certainly the zirconia-based materials.

Pure zirconium oxide, ZrO_2, demonstrates the cubic fluorite structure, but at high temperatures, and its electrical conductivity is very low. In order to stabilize its structure down to low temperatures and induce presence of ionic conductivity, a proper doping and subsequent introduction of the oxygen vacancies is necessary [124,139]. Different elements can be considered as dopants at the Zr-site, which however must exhibit fixed and lower valence than Zr^{4+}. In case of Y^{3+} doping, the following defect formation equation can be written:

$$Y_2O_3 \xrightarrow{ZrO_2} 2Y'_{Zr} + 3O_O^X + V_O^{\bullet\bullet} \quad \text{(Eq. 4-15)}$$

8 mol% of yttrium oxide used to stabilize zirconia gives so called 8YSZ material ($Zr_{0.84}Y_{0.16}O_{2-\delta}$), which is one of the most popular zirconia-based electrolytes. The properly adjusted dopant content of yttria can fully stabilize the cubic structure, as well as permits obtaining high oxygen ion conductivity at high temperatures [124,139]. Apart from yttria, scandium oxide is also considered as a promising dopant in stabilizing zirconium oxide (abbreviated as ScSZ), which is due to a fact that it can yield higher ionic conductivity, as compared to YSZ. Ionic conductivity dependence on temperature for such electrolytes is illustrated in Fig. 4-3. However, doping with scandia brings about negative issues, e.g. decreased long-term stability, and increased costs [124,139,140].

As commonly used electrolyte, YSZ has been implemented in either electrolyte-supported cells working at high temperatures or since it forms Ni-YSZ cermet, it can be applied successfully in anode-supported cells. In this case, thinner electrolyte layer enables operation at lower temperatures (see Fig. 4-3 for the compared areas specific resistances for 100 μm and 10 μm thin electrolyte layers). Nevertheless, traditional zirconia-based materials might not be an ideal option for IT-SOCs, since either too low oxygen ion conductivity and/or aging issues over the long-term operation [141,142].

Another crucial group of electrolytes comprises ceria-based materials. Similarly as discussed above, Ce^{4+} has to be partially substituted by other metal elements having lower

and not changeable valence state, like gadolinium and samarium. If so, oxygen vacancies are favorably created. As it is also shown in Fig. 4-3, the typical ceria oxide doped with 10 mol% of gadolinium (abbreviated as 10GCO or also as GDC) demonstrates higher ionic conductivity, especially at the temperature range of 500-800 °C, if compared to different zirconia-based electrolytes (except 10ScSZ). Inevitably, disadvantages can be still found in this type of electrolytes. The Ce^{4+} will undergo partial reduction in low oxygen partial pressures at high temperatures (from the fuel electrode side), which results in an emergence of the electronic conductivity and consequently reduces the open circuit voltage (OCV) [124,140–142]. On the other hand, such a disadvantage can be reverted as an advantage, when GDC is combined with nickel oxide (abovementioned Ni-GDC), equipping the fuel electrode with ionic and electronic conductivity.

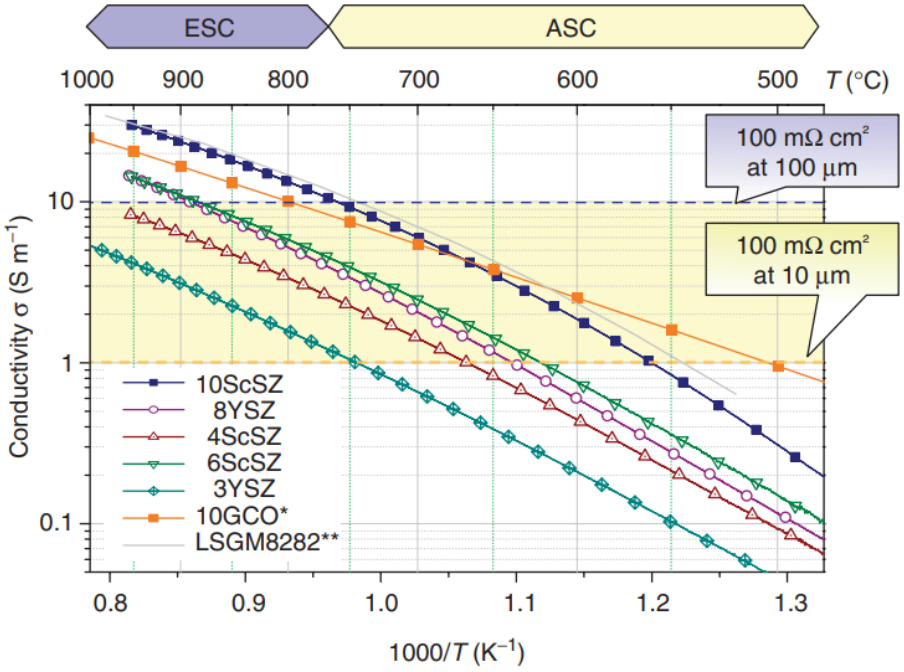

Fig. 4-3. Comparison of oxygen ion conductivity between common electrolytes [142]. Numbers prefixing the ScSZ or YSZ represent the x mol% of the dopant content, 10GCO refers to $Ce_{0.9}Gd_{0.1}O_{2-\delta}$ and LSGM8282 represents $La_{0.8}Sr_{0.2}Ga_{0.8}Mg_{0.2}O_{3-\delta}$.

When it comes to perovskite-type materials, $LaGaO_3$-based oxides are known and are widely used as the solid electrolytes as well, particularly when La- and Ga-site are doped with Sr and Mg, respectively (LSGM). Studies suggested that the optimal doping composition should be $La_{0.8}Sr_{0.2}Ga_{0.83}Mg_{0.17}O_{3-\delta}$ [139], which is very close to the often used, also in this work, composition ($La_{0.8}Sr_{0.2}Ga_{0.8}Mg_{0.2}O_{3-\delta}$). As compared in Fig. 4-3, LSGM8282 shows higher oxygen ion conductivity than GDC and zirconia-based candidates at the temperature range of 600-800 °C, implying that it can be suitable for application in IT-SOCs. Additionally, very low electronic conductivity component can be confirmed in LSGM, making it distinct from GDC [124,139]. Nonetheless, undesirable issues of such electrolytes are also worth paying attention to. First would be the lanthanum

element migration, which results in formation of $LaSrGa_3O_7$ that blocks oxygen ion conductivity [143]. Second is ascribed to the reaction between LSGM and nickel oxide at high temperatures, forming $LaNiO_3$ phase, which is not conducting oxygen anions [139,144]. This is certainly an obstacle, when the nickel-containing ceria-based fuel electrode (e.g. Ni-GDC) is applied. Therefore, for example, $La_{0.4}Ce_{0.6}O_{2-\delta}$ (LDC) must be applied as a buffer layer between the LSGM electrolyte and Ni-GDC electrode. It can effectively prevent the abovementioned issues, due to the similar lanthanum concentration in both, LSGM and LDC, as well as the fact that no reaction between NiO and LDC occurs [139,144]. Summarizing this section it should be also mentioned that unfortunately there are significant problems with making anode-supported designs, which are based on LSGM electrolytes.

Apart from optimizing oxygen ion conductivity in solid electrolytes, protonic conduction appears as another direction for development of the effective electrolytes for fuel cells. Setting Y-doped $BaZrO_3$-based (BZY) electrolytes as an example, an excellent bulk proton conductivity must be mentioned, as compared to the ionic conductivity of the abovementioned oxygen ion conductors, which also appears at the lower temperature range (e.g. below 700 °C). This is very favorable to the design of a particular type of IT-SOCs, named as PCFCs (Fig. 4.2) [145].

Oxygen electrodes for SOCs

An oxygen electrode plays a paramount role in the oxygen reduction reaction (ORR), as it was already aforementioned. Specifically, the functional oxygen electrode should be able to conduct (participate in) the following steps of the reaction: oxygen diffusion in the gaseous phase through the porous structure of the electrode, oxygen adsorption on the electrode's surface, dissociation of oxygen molecules, catalytical reduction of the adsorbed oxygen atoms with electrons collected from an external circuit, transportation of the oxygen anions to the electrolyte, either at the TPB and/or through the bulk of the electrode (Fig. 4-4) [124,140,146].

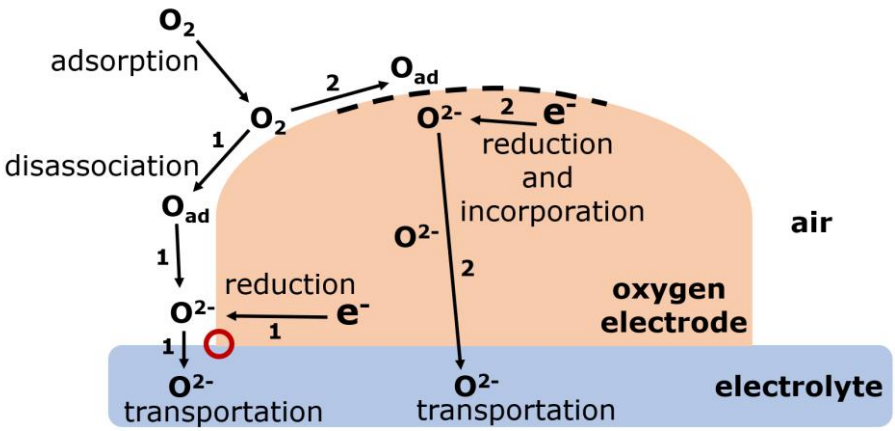

Fig. 4-4. A schematic diagram of the oxygen electrode reaction routes. Route 1 represents situation if the electrode material is a pure electronic conductor. The TPB as the main reaction site is marked with a red circle. Route 2 means that the material shows also ionic conductivity, so oxygen can be incorporated to the bulk of the electrode.

Consequently, an array of requirements has been necessarily summarized over the past decades of studies of the candidate oxygen electrode materials, which involves: sufficiently-high electrical conductivity (on the order of 100 S cm^{-1}) with oxygen ionic conductivity, possibility of manufacturing porous sinters, mild thermal expansion (comparable to that of the solid electrolytes) with a limited chemical expansion effect, good chemical stability, chemical and thermomechanical compatibility with other components, and obviously, sufficiently-high catalytic activity toward the ORR. Also, low costs in manufacturing and limited usage of toxin elements are also positive features [140,146]. It should be mentioned that if the oxygen electrode should work in the reversible SOC, sufficiently-high catalytic activity toward the oxygen evolution reaction (OER), as well as stability in atmospheres with high oxygen partial pressure are also of importance [147].

Basically, the main step of the electrochemical reaction on the oxygen electrode would take place at the triple phase boundary, which provides the junction of the gas phase, electronic electronically conducting phase, and oxygen ionic conducting phase [118,124,128,140,146]. However, as it was previously mentioned, introduction of the high performing IT-SOCs would create a bright future for further adoption of the technology, as the lowered operating temperature broadens choice of the materials and increases the application scenarios. Nonetheless, at lower temperatures a much higher overpotential (as compared to the behavior of the fuel electrode) would make the oxygen electrode the strongly hindering element in the operation. This is due to much lower ORR kinetics in the intermediate temperature range [124,140,146]. Thus, it is imperative to focus on the development of new oxygen electrode materials that can carry out ORR efficiently at the reduced temperatures. An obvious direction is an introduction of the mixed conductors, as in this case the bulk diffusion of the reduced oxygen anions is possible (route 2 in Fig. 4-4), which speeds up the reaction [148].

4.2. Perovskite oxides for SOCs oxygen electrodes

By far, the most well-known and also commercially-applied material for the oxygen electrode is the strontium doped $LaMnO_3$-based oxide (LSM). The material shows single perovskite structure (formulated generally as ABO_3), in which larger La cations occupy the A-site, and are twelve-coordinated with oxygen anions. Smaller Mn ions are present at the B-site, and six-coordinated with oxygen anions, forming corner-sharing network of octahedra, as can be seen in Fig. 4-5. Oxygen nonstoichiometry can be neglected in LSM.

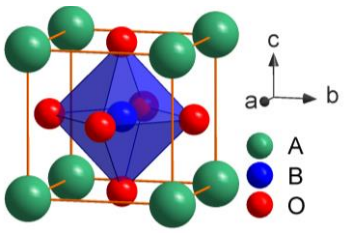

Fig. 4-5. A unit cell of a single (cubic) perovskite structure with ABO_3 formula.

Bearing in mind that majority of the actual perovskite-type materials do not crystallize in the perfect cubic ($Pm-3m$) symmetry, the famous factor called Goldschmidt tolerance factor (t) has been widely used to characterize the extent of the structural deviation. Its calculation method is illustrated in Eq. 4-16, in which r_A, r_B and r_O respectively represent the ionic radii (in the proper coordination) of the A- and B-site elements, as well oxygen [146,149,150].

$$t = \frac{(r_A + r_B)}{\sqrt{2}(r_B + r_O)} \text{ (Eq. 4-16)}$$

Worth mentioning is that while values of t close to 1 usually indicate favorable structural conditions for the perovskite structure formation, and for larger discrepancy from the unity, usually stronger distortions are present. it is not possible to predict the actual symmetry based on the value of the parameter itself [151].

In the mentioned LSM, introduction of strontium plays an important role regarding electronic transport properties. Increasing strontium doping content (even up to 50 mol%) should improve the electrical conductivity, since it increases concentration of the electronic holes, as depicted in Eq. 4-17 [146,150,152]:

$$SrO \xrightarrow{LaMnO_3} Sr'_{La} + Mn^{\bullet}_{Mn} + O^{x}_{O} \text{ (Eq. 4-17)}$$

Creation of holes, which can be associated with Mn^{4+} cations, results in the possible electron hopping between manganese cations. Also, since MO_6 octahedra are sharing corners, the hopping takes place with the participation of oxygen, which can be written as -Mn^{3+}-O-Mn^{4+}- → -Mn^{4+}-O-Mn^{3+}-, representing double exchange (Zener mechanism) [153]. It is also of importance to realize that interaction of 3*d* metal and oxygen in the octahedra generates a complex set of energy levels, as presented in Fig. 4-6. The most important states for the perovskites are the (antibonding) t_{2g} and e_g states, filling of which has determinative role on the electronic transport [154].

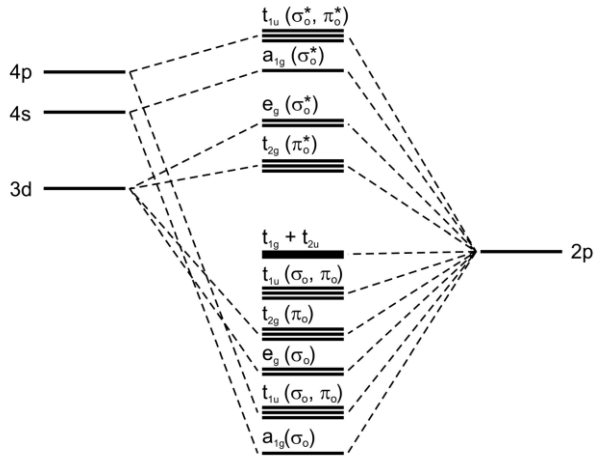

Fig. 4-6. Energy levels of the 3*d* metal MO_6 octahedron [154].

Talking back about the LSM, however, an attention should be paid to its poor oxygen ion conductivity, which restricts the ORR to take place only at the TPB, as highlighted by the red circle in Fig. 4-4 [146,152]. On the other hand, given that LSM shows good chemical compatibility with YSZ electrolyte when the strontium doping content is lower than 30 mol%, it is feasible to introduce YSZ as the ionic conductor to prepare LSM/YSZ composite oxygen electrodes [124,140,146,150,152]. For instance, an anode-supported full cell with LSM/YSZ used as the oxygen electrode reached a maximum power density of 1.8 W cm^{-2} at 800 °C [155]. Nonetheless, aiming at developing effective and efficient oxygen electrodes for IT-SOCs, and considering the poor performance of LSM at reduced temperatures, materials possessing mixed ionic and electronic conduction (MIEC), which allow extending the oxygen reduction to the whole surface of the electrode, as drawn in black-dash line in Fig. 4-4, would be highly-favorable [124,146,149,152].

Owing to the better ionic and electronic conduction, as compared with LSM, cobalt-based perovskite materials are typical MIECs applied in IT-SOC oxygen electrodes [146]. For example, Sr-doped $LaCoO_{3-\delta}$ shows high electrical conductivity and good oxygen (bulk) diffusivity, as well as good catalytic activity toward O_2 dissociation, which together contribute to the excellent electrocatalytic activity. This in consequence results in very low electrode polarization resistance (R_p) values [156,157].

The intrinsic MIEC behavior of $La_{1-x}Sr_xCoO_{3-\delta}$ (LSC) comes from a difference in how the doping with strontium influences properties of LSC. The difference can be presented in the following Eq. 4-18:

$$SrO \xrightarrow{LaCoO_3} Sr'_{La} + (1-n)Co^{\bullet}_{Co} + n/2V_O^{\bullet\bullet} + n/2O_2 \uparrow \quad \text{(Eq. 4-18)}$$

In other words, not all cobalt is oxidized, and the charge balance partially comes from an emergence of the oxygen vacancies. Obviously, depending on the doping level, temperature and the oxygen partial pressure, the respective amounts of the ionic and electronic defects vary. The formed oxygen vacancies are crucial for the ionic conduction, in which the jumping oxygen has to cross a saddle point, as depicted in Fig. 4-7 [158].

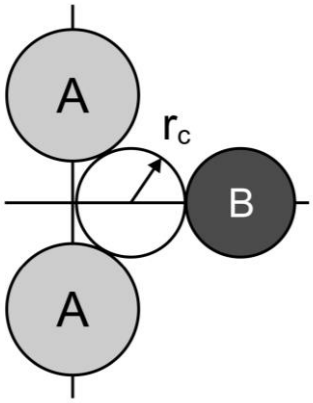

Fig. 4-7. The middle point for the oxygen jump in the $ABO_{3-\delta}$ perovskite structure, r_c stands for the critical radius. Based on [158].

Nevertheless, ascribed to the spin states transition of Co (from $t_{2g}^6 e_g^0$ to $t_{2g}^4 e_g^2$), relatively weak Co-O bonds, and chemical expansion due to the oxygen release at high temperatures, the observed very high thermal expansion coefficient (TEC) is the undeniable downside of such materials. It can exceed $20 \cdot 10^{-6}$ K^{-1}, about twice if compared to LSGM or GDC ($10\text{-}12 \cdot 10^{-6}$ K^{-1}). Replacing La by other lanthanides, like Pr, Nd, Sm and Gd may partially alleviate this issue, due to the decreased concentration of the oxygen vacancies, as well as the limited reduction of Co^{4+} [146,159–161]. It is also possible to prepare composite electrodes based on LSC. For example, the R_p of $La_{0.4}Sr_{0.6}CoO_{3-\delta}$-$Ce_{0.9}Gd_{0.1}O_{2-\delta}$ made with a weight ratio of 3:2 reached a very low value of 0.052 Ω cm^2 at 600 °C, enabling to achieve a peak power density of 1.34 W cm^{-2} for a SOFC at the same temperature [162].

Another effective method to alleviate the downsides of Co-based perovskite materials is doping with other transition metals at the Co-site, which corresponds to lowering of the Co content. If done properly, it also enables maintaining reasonable electrochemical properties at the same time. $La_{0.6}Sr_{0.4}Co_{0.2}Fe_{0.8}O_{3-\delta}$ (LSCF6428) electrode could reach a low R_p value of 0.103 Ω cm^2 at 750 °C, and a peak power density of 572 mW cm^{-2} at 700 °C of the SOFC was reached [163]. This type of material also features the high electrical conductivity and fast oxygen exchange and diffusion ability on its surface and bulk, respectively [146,149,160]. Additionally, with lower Sr-substitution, LSCF exhibit a closer TEC to solid electrolytes, which is due to the lower oxygen vacancy concentration and its changes with temperature. Although LSCF oxides demonstrate good chemical compatibility with ceria-based electrolytes, they cannot be applied directly on YSZ, because of the interfacial reaction [140,146]. Furthermore, replacing La with Ba can also yield excellent performance, and $Ba_{1-x}Sr_xCo_{1-y}Fe_yO_{3-\delta}$ (BSCF) are considered as outstanding oxygen electrode materials. For instance, a very low value of R_p (0.055-0.071 Ω cm^2 at 600 °C) was obtained with $Ba_{0.5}Sr_{0.5}Co_{0.8}Fe_{0.2}O_{3-\delta}$ (BSCF5582) electrode [164]. Besides that, the B-site substitution with transition metal elements like Ni, Mn, and Cu is also regarded as an effective solution toward addressing the problems of Co-containing perovskites, and their introduction causes an emergence of interesting physicochemical properties, and even possibly, results in better electrochemical properties than for the unmodified composition [146,160].

Apart from single perovskites, layered perovskite materials are also well-known as candidates for oxygen electrodes for IT-SOCs. Among them, oxides with K_2NiF_4-type structure are an interesting group of materials. As the representative material, $La_2NiO_{4+\delta}$ (LNO) has been intensively studied, due to its high oxygen diffusivity that, unlike LSCF, results from presence of the interstitial oxygen. The diffusivity is characterized as being higher than that of LSCF ($La_{0.6}Sr_{0.4}Co_{0.2}Fe_{0.8}O_{3-\delta}$), but lower than observed for LSC ($La_{0.3}Sr_{0.7}CoO_{3-\delta}$) [165]. Furthermore, it features the mild thermal expansion behavior that is close to either YSZ and GDC, making it a good candidate for usage in IT-SOCs [146,160].

Meanwhile, double perovskite oxides, formulated as $LnBaB_2O_{5+\delta}$, in which Ln usually refers to different lanthanides or yttrium, and B means the transition metal elements, have been a hot topic over the past decades. $LnBaB_2O_{5+\delta}$ compounds (less

commonly written as $LnBaB_2O_{6-\delta}$) have a distinct feature of alternating arrangement of LnO_δ and BaO layers along the c-axis, as shown in Fig. 4-8, which is favored by the radii difference between Ln^{3+} and Ba^{2+} cations. In this case the oxygen vacancies are preferentially located in LnO_δ layers [166]. This layered structure, in consequence, generates fast oxygen anions diffusion channels, enabling such materials to exhibit very good, but anisotropic oxygen conduction capability [167].

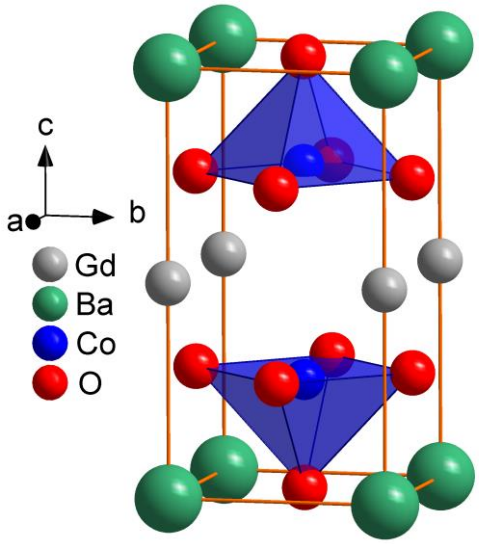

Fig. 4-8. A unit cell of a double perovskite structure of $GdBaCo_2O_5$. Please notice that the Gd-related layer is completely empty ($\delta = 0$) in this model.

In this group of materials, $LnBaCo_2O_{5+\delta}$ are undoubtedly the most widely-studied candidates. Kim et al. conducted work showing that the power density of (identically-constructed) LSGM-supported full cells decreased with the decreasing radii from La^{3+} to Gd^{3+}, when $LnBaCo_2O_{5+\delta}$ were evaluated as oxygen electrode materials [168]. Also, partial substitution with Sr at the Ba-site improves the power density of a single cell, due to the possible enhanced oxygen transport ability [169]. Apart from very good oxygen transport ability, $LnBaCo_2O_{5+\delta}$ also demonstrate excellent electronic component of the conductivity, with values above 100 S cm^{-1} up to 900 °C in air. This can be ascribed to the effective small polaron hopping mechanism based on the good overlapping in the -Co-O-Co- conduction chains, making $LnBaCo_2O_{5+\delta}$ excellent MIEC materials [168–171].

As mentioned above, cobalt-based perovskite materials, also $LnBaCo_2O_{5+\delta}$, with full occupancy of the B-site by Co, suffer from the negative issues like high TEC values, unwanted cobalt diffusion, and all environmental and cost-related issues associated with using of Co element [172–174]. A clear trend can be seen with respect to the development of novel oxygen electrode material, which is aimed at partial or even complete replacement Co with other transition metal elements, but at the same time, maintaining comparable electrochemical properties. Yang et al. explored the possibility of using material with only manganese at the B-sites, and obtained a low value of R_p of only 0.066

Ω cm^2 at 900 °C [175]. Also, mixed Co/Mn-containing samples yielded a desirable catalytic activity, with R_p of 0.081 Ω cm^2 at 900 °C [176]. At the same time, Choi et al. studied the Fe as a candidate substitution element at the Co-site, and obtained R_p = 0.056 Ω cm^2 at 600 °C for the $PrBa_{0.5}Sr_{0.5}Co_{1.5}Fe_{0.5}O_{5+\delta}$ oxygen electrode material [167]. Similarly, favorable results could be also gained from Ni-doped perovskites, for which the R_p value was found as 0.056 Ω cm^2 at 700 °C if $PrBaCo_{1.6}Ni_{0.4}O_{5+\delta}$ was used [177].

In the meantime, a new concept of high entropy oxides (HEO) has been introduced. If applied to perovskite-type materials, the multicomponent occupancy is typically present at either the A- or B-site, generating a high configuration entropy. This may correspondingly give rise to enhancements with regard to the electrochemical or various physicochemical properties. For example, Dąbrowa et al. explored the possibility of using $La_{1-x}Sr_x(Co,Cr,Fe,Mn,Ni)O_{3-\delta}$ and $(La,Pr,Nd,Sm,Gd)BaCo_2O_{5+\delta}$ as oxygen electrodes, and obtained desirable cell performance [178,179]. Single perovskite-type oxides, as for instance non-equimolar $Sr(Fe_\alpha Ti_\beta Co_\gamma Mn_\zeta)O_{3-\delta}$ with medium configurational entropy, was also studied, and was proved to show improved structural stability by the suppressed strontium segregation [180]. It seems that this emerging field, and the new materials obtained via introducing multiple elements into the crystal structure, shall be very promising, and it is a useful way to tune the original oxides, and equip them with enhanced or even new features [181]. In a summary to this section, the related information of selected SOCs has been gathered, and can be found in Tab. 4-2.

Tab. 4-2. Comparison of common materials applied in SOCs or related reversible mode.

Oxygen electrode	Electrolyte	Fuel electrode	Power density	Polarization resistance (symmetrical cell)	Reference
LSM/YSZ (50:50 wt.%)	YSZ	Ni/YSZ (anode-supported)	1.8 W cm^{-2}; 800 °C	-	[155]
LSC/GDC (30:20 wt.%)	GDC	Ni/GDC (anode-supported)	1.34 W cm^{-2}; 600 °C	0.052 Ω cm^2; 600 °C	[162]
LSCF	GDC	-	0.57 W cm^{-2}; 700 °C	0.103 Ω cm^2; 750 °C	[163]
LNO	GDC	Ni/GDC (anode-supported)	0.19 W cm^{-2}; 650 °C	-	[182]
LBCO	LSGM (electrolyte-supported)	Ni/GDC	0.52 W cm^{-2}; 800 °C	-	[168]
$Ba_{0.6}La_{0.4}CoO_3$	LSGM (electrolyte-supported)	$La_{0.8}Sr_{0.2}FeO_3$	0.92 A cm^{-2} 1.4 V; 800 °C	-	[183]

5. Copper as the B-site element in perovskite-type oxides

As discussed in the previous chapter, seeking for promising substitution at the B-site has been reckoned as an effective approach to address negative issues associated with the presence of cobalt in the candidate oxygen electrode materials for SOCs. Among the obvious choice dopants, other 3*d* elements are of interest, but until now researchers have rather concentrated on Fe, Mn or Ni, while (surprisingly) substitution with copper has not been studied in this aspect in details. However, it seems that due to its special properties, copper, as one of first row transition metal elements, should be taken into such considerations thoroughly. Pure copper appears as red-orange-like metal, with excellent ductility and malleability. Importantly, copper features a very high electrical conductivity at room temperature, ~$6.0 \cdot 10^5$ S cm^{-1}, and a melting point of 1084.62 °C. There are abundant Cu reserves around the world, and the element is rather environmentally benign, as well as not so expensive. Based on those properties, copper is widely applied in different industrial branches, also in the power generation industry (e.g. electric wires) [184,185].

Regarding copper-based oxides, especially those with complex chemical composition and structural features, interest in the research and development was highly strengthen by the discovery of a new class of high-temperature superconductors from the La-Ba-Cu-O system by J.G. Bednorz and K.A. Müller in 1986 [186]. Extensive research activities have been carried out to fully understand the phenomenon of the superconductivity, which apart from the important basic science results, yielded development of new materials, such as $YBa_2Cu_3O_{7-\delta}$ or $La_{2-x}Sr_xCuO_{4\pm\delta}$ [187–189].

In oxides, Cu is commonly present as Cu^+, Cu^{2+} and Cu^{3+}, which corresponds to the $3d^{10}$, $3d^9$, and $3d^8$ electronic configuration, respectively. Copper cations can be present in different crystal coordination, which is depicted in Fig. 5-1 on an example of $A_2BO_{4\pm\delta}$ series (i.e. perovskite-related oxides having AO and ABO_3-like structural elements) [190]. In the meantime, it is also of importance to describe how different crystal coordination affects the electronic states of copper cations. This is critical considering possible behavior of Cu-containing oxygen electrode materials for SOCs. As shown in Fig. 5-2, if Cu^{2+} ($3d^9$) would be located in the perfect octahedra, the t_{2g} states are fully occupied, while three electrons are present in the e_g levels ($t_{2g}^6 e_g^3$). This results in the net spin S = ½. This explains a very common Jahn-Teller effect present in many case (i.e. for the six-fold coordinated Cu^{2+}), causing elongation of the z-axis (tetragonal distortion, in-plane compression). In the discussed case the x^2-y^2 orbital is occupied by a single electron. However, if Cu^{3+} ($3d^8$) would be present in such coordination, $t_{2g}^6 e_g^2$ configuration may be present, if the splitting of the energy levels between the z^2 and x^2-y^2 orbitals is sufficiently large. Nevertheless, due to large ionization energy needed, it is not a common charge state of copper, but if mixed states are present, x^2-y^2 electron can be mobile [191]. Another stable configuration for Cu^{3+} ($3d^8$) is in the *z*-axis tetragonal pyramid (five-fold). Reducing copper in this situation would be rather difficult, without increasing the coordination number. Similar situation is for the square-planar (four-fold) case [191].

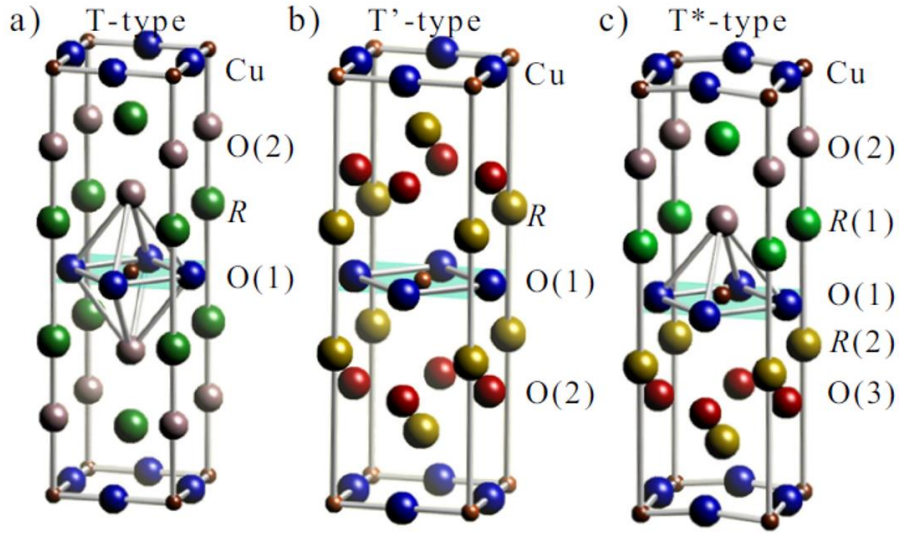

Fig. 5-1. Presence of Cu cations in octahedral, square-planar, and pyramid crystal coordination. Structural models represent the a) T-, b) T'-, and c) T*-type structures of Cu-based $A_2BO_{4\pm\delta}$. Based on [190].

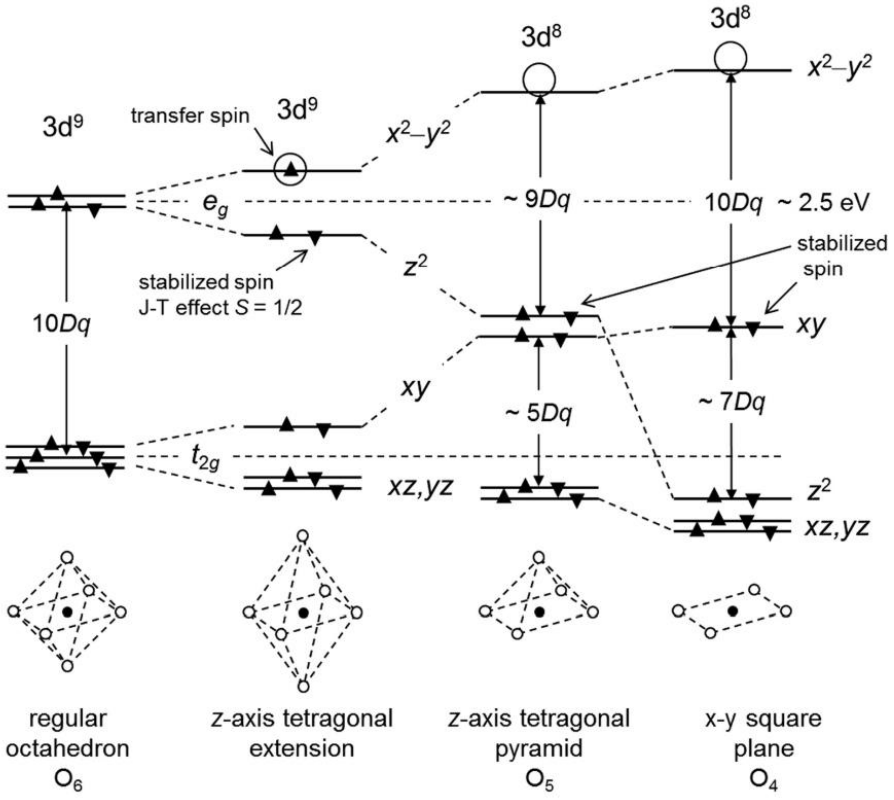

Fig. 5-2. Electronic states (occupation of orbitals) of selected copper cations present in different structural coordination at the ground state [191]. Note that $3d^9$ and $3d^8$ represent Cu^{2+} and Cu^{3+}, respectively.

As it was also mentioned previously, electrocatalytic activity is undeniably recognized as one of the most important properties for SOC oxygen electrode materials. As for the perovskite-type oxides, which feature BO_6 octahedra-based structure, their interaction with gaseous oxygen (e.g. under the oxygen-releasing process) involves formation of structural units with a lower coordination number, especially at the surface. The discussed BO_5 pyramid-like structure is important, as this can be an active site for the oxygen reduction, in particular, at high temperatures [192]. Electronic states occupancy for the selected other 3*d* elements present in the BO_5 pyramids is shown schematically in Fig. 5-3a. As also presented in Fig. 5-2, through the orbitals overlapping and interactions, the 2p atomic levels of oxygen and 3d levels of the transition metal elements are hybridized, in the same way as for CuO_5. However, since different total number of electrons is available, the respective fillings of the e_g and t_{2g} states differ. Again, presence of mixed states of the 3*d* metals may complicate the picture significantly.

It is worth noting that the aqueous ORR activities desirably reach the peak value when the electronic occupation of the (top energy) e_g levels is close to 1, e.g. for Mn^{3+}, Co^{3+}, and Ni^{3+}. It is also known that a similar trend is present for the OER, with the maximum at about 1.2 [193].

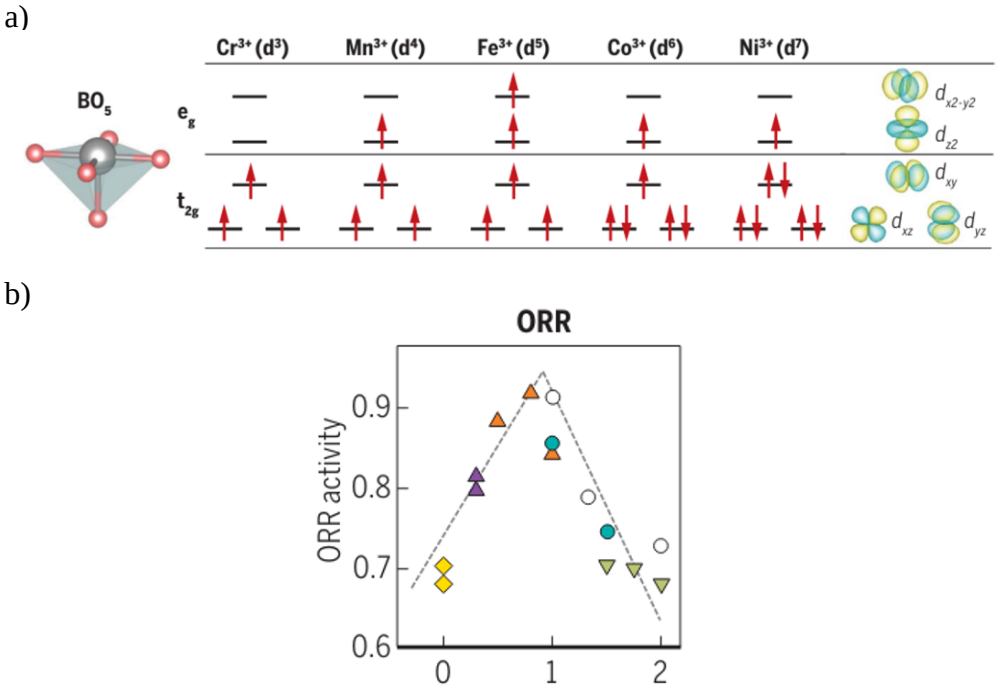

Fig. 5-3. a) Electronic occupation of common transition metal elements in the case of BO_5 coordination. Please notice formal +3 charge state. b) Comparison of related aqueous ORR activities among the discussed elements. Based on [193]. Note that colors of yellow, orange, blue-green, green and white represent Cr, Mn, Co, Fe and Ni, respectively. Pink represents mixed sites.

Regarding Cu-based oxides, the available data on the electrocatalytic activity at low or high temperatures are very limited. This is because the electronic configuration (e_g

filling) for those materials seems as not optimal. Considering for example Cu^{3+} present in the square pyramid ($t_{2g}^6e_g^2$), already two electrons occupy the e_g levels, so the electronic charge transfer during the adsorption, dissociation, and reduction of the oxygen molecules seems as no easy to be described. But it may be speculated that with the electron transfer from another (neighboring) Cu^{2+} site, this may happen, as x^2-y^2 electrons may be mobile and jump between the (octahedral) sites. In other words, oxidation of Cu has to happen at the different than the adsorption site.

For only Cu-based perovskite oxides, rhombohedral $LaCuO_{3-\delta}$ appears as the parent and most interesting example. If close to oxygen stoichiometry ($\delta \approx 0$), it is characterized as an excellent electronic conductor, which can reach a conductivity magnitude of above 10^5 S cm^{-1} at room temperature. It also features other special physicochemical properties, like Pauli-like magnetic susceptibility and metallic properties down to 77 K [194]. Meanwhile, rigorous synthesis conditions are required in order to obtain stoichiometric $LaCuO_3$, for example, it can be synthesized at 1400 °C under a very high oxygen pressure of 5 GPa [195]. Less oxidizing conditions result in a significant decrease of the oxygen content, which strongly affects the properties. Such materials exhibit reduced conductivity and oxygen vacancy ordered structures [196,197]. Also, the stoichiometric material can decompose into La_2CuO_4 and CuO [198].

It is reasonable to set $LaCuO_3$ as an anchor, but chemical modifications must be explored, so derivative perovskite-type candidates can be obtained based on it. For example, in order to keep total Cu occupancy at the B-sites, doping with +2 elements can be done at the A-site at the same time, which would make the synthesis much easier. When a ternary system of $LaCuO_3$-$SrCuO_x$-$BaCuO_x$ is considered, as depicted in Fig. 5-4, it is quite explicit that both, Sr and Ba are favorable dopant elements at the La-site. Accordingly, samples including $La_{0.75}Sr_{0.25}CuO_{3-\delta}$, $La_{0.75}Sr_{0.15}Ba_{0.1}CuO_{3-\delta}$ and $La_{0.8}Ba_{0.2}CuO_{3-\delta}$ could be successfully synthesized via either sol-gel or solid-state synthesis methods. Since the materials exhibit various types of cation- and oxygen vacancy-ordering, their composition is often written in a more complex way, to reflect the structural features. Respectively, the notation can be also presented as $La_3SrCu_4O_{12-\delta}$, $La_3Ba_{0.6}Sr_{0.4}Cu_4O_{12-\delta}$, and $La_4BaCu_5O_{15-\delta}$, respectively. Since copper in such oxides is present in different CuO_x coordination, it implies that complex, but potentially favorable electrocatalytic and mixed ionic-electronic transport properties may be present. As it has been shown in previously work through a series of characterizations, all of those oxides exhibit excellent electrical conductivity (above 300 S cm^{-1} up to 800 °C), as well as show remarkable catalytic activity toward the ORR, $La_{0.8}Ba_{0.2}CuO_{3-\delta}$ in particular. The electrode based on the latter material enabled reaching a peak power density value of 1.05 W cm^{-2} at 900 °C in a LSGM-supported button-type SOFC [199]. Interestingly, in another work focused on doping with Sr at the La-sites, a peak power density of 0.65 W cm^{-2} at 800 °C could be also obtained, with the $La_{0.75}Sr_{0.25}CuO_{2.5-\delta}$ used as the oxygen electrode material [200].

Considering the above, it seems as a very promising direction to explore more possibilities according to the discussed ternary system. For example, as marked in red in Fig. 5-4, $La_{0.5}Ba_{0.5}CuO_{3-\delta}$ composition, in which more Ba was used to stabilize the structure, should be possible to synthesize easily, and can be expected to possess similar

or even better physicochemical and electrochemical properties, as compared to $La_{0.8}Ba_{0.2}CuO_{3-\delta}$. This is due to the complex, and partially oxygen vacancy disordered structure, which was detected in this case [201,202].

Also, the B-site doping can be interesting, if for example other transition metal elements can be introduced, as e.g. with 50 mol.% of Ni doped at the Cu-sites. The resulting $LaNi_{0.5}Cu_{0.5}O_{3-\delta}$ oxide was found to possess a suitable set of physicochemical properties, enabling to reach a peak power density of 0.87 W cm^{-2} at 900 °C, if applied in a lab-scale SOFC [203]. Additionally, the TEC and performance of the single cell having more standard LSCF electrode ($La_{0.6}Sr_{0.4}Co_{0.2}Fe_{0.8}O_{3-\delta}$) can be improved by Cu-doping as well [204].

When it comes to double perovskite structure, copper can also play an important role in improving the thermal expansion behavior, while maintaining excellent electrocatalytic activity. For example, encouraging data were published for $GdBaCo_{2/3}Fe_{2/3}Cu_{2/3}O_{5+\delta}$ oxygen electrode [205]. Overall, it can be therefore stated that considering the enhancements in the economic aspects, environmentally-friendly nature, and encouraging electrochemical data already reported, copper should be undoubtedly thought highly of in order to develop novel oxygen electrode materials for IT-SOCs.

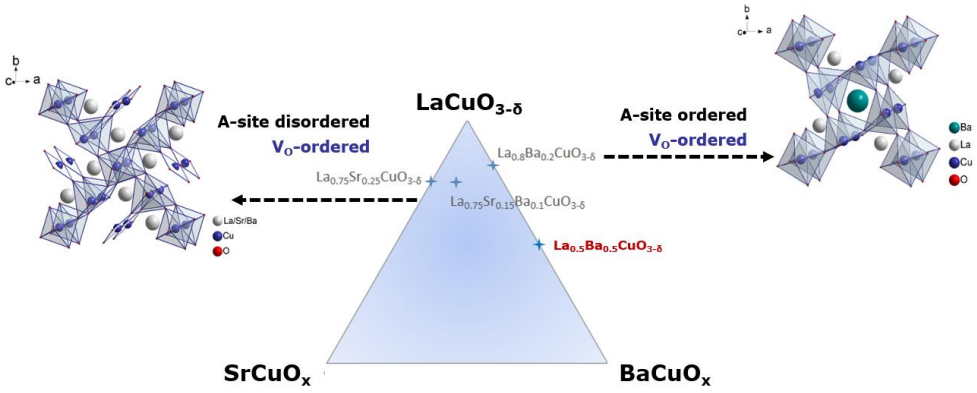

Fig. 5-4. A diagram of $LaCuO_3$-$SrCuO_x$-$BaCuO_x$ ternary system. Selected, already obtained samples materials are highlighted. Also, visualizations of two different unit cells are provided. Based on [199]. Note that a large part of the diagram is not explored yet, with the expected wide ranges of concentrations, for which it is not possible to synthesize phase-pure samples.

6. Aim of the work and initial hypotheses

Considering the abovementioned elaboration of the up-to-date issues concerning the development of oxygen electrode materials for SOCs, it is reasonable to understand the demand for novel compounds, and necessity for their systematic studies, especially regarding the intermediate temperature range of the application. Perovskite-type oxides are certainly the most promising option to start with, but the widely-used cobalt in such candidate oxygen electrode materials can be identified as a double-edged sword, with strong downsides involving its toxic nature, environmental pollution, questionable policies regarding its extraction, high costs of manufacturing, as well as unresolved problems of the chemical expansion effect in the Co-rich perovskite oxides. Thus, the basic intention of this work is to develop new types of the complex oxides, with limited Co content, as well as completely Co-free alternatives, which possess suitable set of the physicochemical characteristics, as well as exhibit good electrocatalytic properties, making them excellent candidates for manufacturing of the oxygen electrodes for IT-SOCs. Importantly, the previous works have shown that copper can be a very prospective element, which can be successfully doped at the B-site of the basic $ABO_{3-\delta}$ structure, partially replacing or fully substituting cobalt. However, depending on the dedicated application, the exact combinations of the substitutions at the A- and B-sites still remain unknown.

6.1. Objectives of this thesis

The main scientific aim of this thesis comprises selecting the proper substitution schemes of Cu-doped and Cu-based complex perovskite-type oxides, and systematic studying of their physicochemical and electrochemical properties, which shall enable developing the new generation of oxygen electrodes for IT-SOCs. Specifically, this aim can be regarded as having both, strictly scientific and practical respects. Regarding the scientific studies, the objectives and targets can be stated as follow:

- In the La-Ba-Cu-O system, the $La_{1.5}Ba_{1.5}Cu_3O_{7\pm\delta}$ triple perovskite (denoted also as $La_{0.5}Ba_{0.5}CuO_{3-\delta}$) can be identified as the candidate Co-free oxygen electrode material. Systematic studies of this compound, having partially disordered A-site, as well as exhibiting specific oxygen vacancy-related features, are proposed to confirm it, focusing on the crystal structure, morphology, chemical stability, and transport properties, with the supplementary Density Functional Theory (DFT) computations. The research involves optimization of the synthesis methods, determination of the lattice structure and unit cell parameters at room temperature and high temperatures by X-ray diffraction techniques with Rietveld refinements, evaluation of the surface properties by Raman spectroscopy, microscopy studies of the material's morphology and microstructure, determination of the oxygen content by iodometric titration, and evaluation of its changes at elevated temperatures in varied atmospheres by

thermogravimetric studies, measurements of the thermal expansion behavior, electrical conductivity, as well as chemical compatibility with common solid electrolyte materials.

- $GdBa_{0.5}Sr_{0.5}Co_{2-x}Cu_xO_{5+\delta}$ ($x \geq 1$) system of double perovskite materials appears as especially interesting, as the proper chemical composition at the A-site allows maintaining the layered structure, and at the same time, Cu-doping can be successfully done, replacing at least half of the cobalt at the B-site. Such compounds are expected to possess suitable characteristics as the candidate oxygen electrode materials, and systematic evaluation of their properties is proposed. Similarly as in the first system, the research shall involve optimization of the preparation method, evaluation of the structural features, morphology, chemical stability, and electrical properties, with the additional DFT calculations. Also, modification of the micro-morphology of the selected electrode material is proposed, which can be successfully conducted by the electrospinning technique.

- With the emergence of the so called "high entropy approach", studies of the possible synergistic effects appearing in the multicomponent perovskite-type oxides are of interest concerning development of the oxygen electrode materials. Consequently, the compositionally-complex $La_{0.6}Sr_{0.4}Ni_{0.15}Mn_{0.15}Fe_{0.15}Cu_xCo_{0.55-x}O_{3-\delta}$ ($x = 0.05$-0.2) perovskite-type oxides can be proposed, in which Cu-doping can be realized, limiting the Co content as well. In a similar manner as above, the planned research involves optimization of the synthesis conditions, evaluation of the crystal structure, microstructure, determination of the chemical stability, and transport properties. Also in this case, the morphology of the selected oxide can be performed by the electrospinning technique.

- Studies of the rate determining steps of the reactions occurring on the oxygen electrode are of crucial importance to have a deeper insight into the electrocatalytic activity of the novel candidate compounds. For this, application of the Distribution of Relaxation Times (DRT) analysis is proposed for the most perspective oxygen electrodes manufactured using the developed $GdBa_{0.5}Sr_{0.5}Co_{0.9}Cu_{1.1}O_{5+\delta}$ and $La_{0.6}Sr_{0.4}Ni_{0.15}Mn_{0.15}Fe_{0.15}Cu_{0.2}Co_{0.35}O_{3-\delta}$ perovskites. This, in turn, shall enable proposing further possible modifications.

Considering the practical aspect of the studies, the related targets can be formulated as follow:

- Development of the appropriate manufacturing methodology for the oxygen electrode layers based on the aforementioned materials is necessary. This is crucial in order to prepare and properly test the symmetrical cells to evaluate the electrode polarization resistance.

- Development of the suitable manufacturing methodology for making laboratory-scale full cells with the obtained materials used as the oxygen electrodes is essential to be able to test the actual performance in the fuel cell and electrolysis modes of operation.

- Comparing the feasibility and performance difference between the electrodes prepared by materials from the electrospinning and sol-gel methods should not only concentrate on the power density outputs and other electrochemical characteristics, but has to also involve studies of the micro-morphology and elemental distribution at the oxygen electrodes after measurements. This requires proper preparation of the samples for the microscopy studies. Assessing longer-term performance is also of importance regarding applicability of the developed electrodes.

6.2. Related literature-based hypotheses

The presented in the previous subchapter objectives are proposed according to the following main hypotheses, which are concluded via thorough literature reviewing:

- Despite relatively limited data, substitution of cobalt by copper is feasible in selected perovskite-type oxides, and can be used in the materials development to effectively tackle the problems associated with high cobalt content. The level of the substitution with Cu can be effectively optimized.

- Complete replacement of Co with copper is also possible in selected oxide systems, yielding materials with unique properties. Nevertheless, it can be expected that fully- and partially-substituted candidate oxygen electrode materials can be more suitable for application in different working conditions.

- Designing of materials with high configuration entropy has been already proved as the novel direction of the oxygen electrodes development. Some of those compounds have demonstrated enhanced properties to some extent, with possibility of achieving synergistic effects beyond the rule-of-mixtures.

- DRT method can be effectively used in identifying the rate determining steps of electrochemical reactions occurring on the oxygen electrodes of the SOC cells. This can be also used to provide guidelines for further optimization of the electrode layer design.

- Electrospinning technology can be applied as the novel synthesis method for preparation of the oxygen electrode materials, since it may enable obtaining special

micro-morphology of the electrode layers. Consequently, this can bring about improved electrochemical properties.

Experimental methods

7. Methodology

At the beginning of this section it is necessary to proclaim that if not stated otherwise, all the research activities, data analyses, and interpretation of results reported in this work were carried out by the doctoral student. Some of the work was also done in cooperation with other researchers, and in this case, it is mentioned specifically.

As explained in the previous chapter, critical analysis of the literature data enabled formulating objectives of this work, which concern the proposed three groups of the Cu-containing perovskite-type oxides, as listed below:

1. $La_{1.5}Ba_{1.5}Cu_3O_{7\pm\delta}$
2. $GdBa_{0.5}Sr_{0.5}Co_{2-x}Cu_xO_{5+\delta}$ ($x \geq 1$)
3. $La_{0.6}Sr_{0.4}Ni_{0.15}Mn_{0.15}Fe_{0.15}Cu_xCo_{0.55-x}O_{3-\delta}$ ($x = 0.05$-0.2)

In order to obtain the chosen oxides, proper synthesis method were considered and applied. It is expected that a different preparation route may have significant impact on quality of the samples, and may to some degree influence the physicochemical and electrochemical properties.

7.1. Synthesis methods

Most of the samples were synthesized via a sol-gel method with an auto-combustion step, which ensures good mixing of the relevant elements, and usually yields fine ceramic oxide powders [206]. Some of the samples have been also prepared by using a standard solid-state method (a facile method, but suitable rather only for obtaining a reference material, due to a larger grain size) and electrospinning technique (which enables substantial variation of the material's morphology, as described below).

The sol-gel (SG) route

The adopted sol-gel method, having a final auto-combustion step, is regarded as a liquid approach to the synthesis, because its basic step involves dissolving all the chemical ingredients to form a desired liquid solution. If a proper complexing agent is also added, this step ensures atomic-level homogeneity of the elements. As such, it is typically used method for preparation of perovskite-type oxides (and many other compounds) [207].

In a typical process, firstly, a diluted nitric acid solution is prepared by adding a proper volume of concentrated nitric acid into distilled water. Then, needed chemicals are added stoichiometrically. In this work, the following chemicals were used (all with a purity of 99.9% or 99+%, or having an analytic grade):

- For the preparation of $La_{1.5}Ba_{1.5}Cu_3O_{7\pm\delta}$: lanthanum oxide ($La_2O_3$, pre-annealed at 1000 °C in air to decompose formed $La(OH)_3$), barium nitrate ($Ba(NO_3)_2$), copper(II)

nitrate trihydrate ($Cu(NO_3)_2 \cdot 3H_2O$), citric acid, added in a molar ratio of 1.5:1 to the total amount of the added metal cations, and ethylenediaminetetraacetic acid (EDTA), added at a ratio of 1:1 with regard to the amount of Ba^{2+}.

- For the preparation of $GdBa_{0.5}Sr_{0.5}Co_{2-x}Cu_xO_{5+\delta}$ system: gadolinium nitrate hexahydrate ($Gd(NO_3)_3 \cdot 6H_2O$), $Ba(NO_3)_2$, strontium nitrite $Sr(NO_3)_2$, copper(II) oxide (CuO), cobalt(II) nitrate hexahydrate ($Co(NO_3)_2 \cdot 6H_2O$), citric acid, added in a molar ratio of 1.5:1 to the total amount of the added metal cations, and EDTA, added at a ratio of 1:1 with regard to the total amount of Ba^{2+} and Sr^{2+}.

- For the preparation of $La_{0.6}Sr_{0.4}Ni_{0.15}Mn_{0.15}Fe_{0.15}Cu_xCo_{0.55-x}O_{3-\delta}$ system: La_2O_3 (pre-annealed at 1000 °C in air), $Sr(NO_3)_2$, nickel(II) acetate tetrahydrate ($Ni(OCOCH_3)_2 \cdot 4H_2O$), manganese(II) acetate tetrahydrate ($(CH_3COO)_2Mn \cdot 4H_2O$), iron(III) nitrate nonahydrate ($Fe(NO_3)_3 \cdot 9H_2O$), CuO, $Co(NO_3)_2 \cdot 6H_2O$, citric acid, added in a molar ratio of 2:1 to the total amount of the already added metal cations, and EDTA, added at a ratio of 1:1 with regard to the amount of Sr^{2+}.

Continuous stirring is needed to assure that the added chemicals are dissolved completely, after which a transparent solution can be obtained. Then, the pH value of the solution ought to be adjusted to 7-8 by adding the ammonia solution. After that, the respective solution should be heated to 80-90 °C for water evaporation, with a clear transition from a solution to a sol, then finally to a gel, observed. Subsequently, the dried gel is ignited, when the temperature is increased to 200-300 °C (the mentioned self-combustion process, fueled by the excessive ammonium nitrate), after which dark ash is produced. The obtained ash is then ground thoroughly in an agate mortar.

A following heat treatment (400 °C) and calcination in air are necessary for removal of carbonaceous residues and pre-sintering of the obtained ash precursor. Since $La_{1.5}Ba_{1.5}Cu_3O_{7\pm\delta}$ material was the first studied composition, trials in order to set the proper conditions of the calcination and the final heat treatment have been performed. The main aim was to optimize the conditions with respect to the formation of homogeneous, fine powders. The basic results in this matter could be also applied to other two systems. After the calcination step, crystal structure of the obtained sample was qualitatively checked (see subchapter 7.3.1). Analysis of such result (i.e. determination of the phase composition) allowed modifying the heat treatment temperature. Also, bearing in mind feasibility, all the annealing steps were performed in air. Finally, to mitigate grain growth phenomenon, the final conditions were selected with the lowest temperature and short time enabling synthesis of (practically) phase-pure samples. Related details of regarding the conditions are summarized and presented in Tab. 7-1, with the selected parameters shown in bold font.

In order to carry out further characterizations, pure as-synthesized samples were selected, and depending on the performed studies, were or were not subjected to an additional treatment (as described in the following sections). For a simplified notation, the following abbreviations were used, as provided in Tab. 7-2.

Tab. 7-1. The applied synthesis conditions (the sol-gel method) for the studied samples. Blue color reflects pure materials, which were selected for further studies. The bold data in the last three columns represent the optimized, most suitable preparation conditions.

Composition	Initial heat treatment [°C, hours]	Calcination [°C, hours]	Final heat treatment [°C, hours]
$La_{1.5}Ba_{1.5}Cu_3O_{7\pm\delta}$	400, 2	900, 6	900, 6
	400, 2	900, 6	950, 12
	400, 2	**800, 6**	**975, 6**
	400, 2	-	975, 6
	400, 2	900, 6	975, 12
	400, 2	900, 6	1000, 12
$GdBa_{0.5}Sr_{0.5}CoCuO_{5+\delta}$	**400, 2**	**800, 6**	**1000, 6**
$GdBa_{0.5}Sr_{0.5}Co_{0.95}Cu_{1.05}O_{5+\delta}$	**400, 2**	**800, 6**	**1000, 6**
$GdBa_{0.5}Sr_{0.5}Co_{0.9}Cu_{1.1}O_{5+\delta}$	**400, 2**	**800, 6**	**1000, 6**
$GdBa_{0.5}Sr_{0.5}Co_{0.85}Cu_{1.15}O_{5+\delta}$	**400, 2**	**800, 6**	**1000, 6**
$GdBa_{0.5}Sr_{0.5}Co_{0.8}Cu_{1.2}O_{5+\delta}$	400, 2	800, 6	1000, 6
$GdBa_{0.5}Sr_{0.5}Co_{0.7}Cu_{1.3}O_{5+\delta}$	400, 2	800, 6	1000, 6
$GdBa_{0.5}Sr_{0.5}Co_{0.6}Cu_{1.4}O_{5+\delta}$	400, 2	800, 6	1000, 6
$GdBa_{0.5}Sr_{0.5}Co_{0.4}Cu_{1.6}O_{5+\delta}$	400, 2	800, 6	1000, 6
	400, 2	800, 6	1000, 10
$GdBa_{0.5}Sr_{0.5}Co_{0.1}Cu_{1.9}O_{5+\delta}$	400, 2	800, 6	1000, 6
$GdBa_{0.5}Sr_{0.5}Cu_2O_{5+\delta}$	400, 2	800, 6	1000, 6
$La_{0.6}Sr_{0.4}Ni_{0.15}Mn_{0.15}Fe_{0.15}Cu_{0.30}Co_{0.25}O_{3-\delta}$	400, 4	800, 2	850, 6
	400, 4	800, 2	900, 6
	400, 4	800, 2	1000, 6
$La_{0.6}Sr_{0.4}Ni_{0.15}Mn_{0.15}Fe_{0.15}Cu_{0.20}Co_{0.35}O_{3-\delta}$	**400, 4**	**800, 2**	**900, 6**
$La_{0.6}Sr_{0.4}Ni_{0.15}Mn_{0.15}Fe_{0.15}Cu_{0.15}Co_{0.40}O_{3-\delta}$	**400, 4**	**800, 2**	**900, 6**
$La_{0.6}Sr_{0.4}Ni_{0.15}Mn_{0.15}Fe_{0.15}Cu_{0.10}Co_{0.45}O_{3-\delta}$	**400, 4**	**800, 2**	**900, 6**
$La_{0.6}Sr_{0.4}Ni_{0.15}Mn_{0.15}Fe_{0.15}Cu_{0.05}Co_{0.50}O_{3-\delta}$	**400, 4**	**800, 2**	**900, 6**

Tab. 7-2. Selected pure samples (as marked in blue color in Tab 7-1), with the related abbreviation used in this thesis.

Composition	Abbreviation
$La_{1.5}Ba_{1.5}Cu_3O_{7\pm\delta}$	LBCu
$GdBa_{0.5}Sr_{0.5}CoCuO_{5+\delta}$	GBSCC1010
$GdBa_{0.5}Sr_{0.5}Co_{0.95}Cu_{1.05}O_{5+\delta}$	GBSCC095105
$GdBa_{0.5}Sr_{0.5}Co_{0.9}Cu_{1.1}O_{5+\delta}$	GBSCC0911
$GdBa_{0.5}Sr_{0.5}Co_{0.85}Cu_{1.15}O_{5+\delta}$	GBSCC085115
$La_{0.6}Sr_{0.4}Ni_{0.15}Mn_{0.15}Fe_{0.15}Cu_{0.20}Co_{0.35}O_{3-\delta}$	LSNMFCC2035
$La_{0.6}Sr_{0.4}Ni_{0.15}Mn_{0.15}Fe_{0.15}Cu_{0.15}Co_{0.40}O_{3-\delta}$	LSNMFCC1540
$La_{0.6}Sr_{0.4}Ni_{0.15}Mn_{0.15}Fe_{0.15}Cu_{0.10}Co_{0.45}O_{3-\delta}$	LSNMFCC1045
$La_{0.6}Sr_{0.4}Ni_{0.15}Mn_{0.15}Fe_{0.15}Cu_{0.05}Co_{0.50}O_{3-\delta}$	LSNMFCC0550

Additionally, the SG method was also used to synthesize the $Ce_{0.6}La_{0.4}O_{2-\delta}$ (LDC) oxide, which is a typical buffer layer material used to minimize reactivity between the oxygen electrode and solid electrolyte [208]. The needed chemicals were La_2O_3, $Ce(NO_3)_3{\cdot}6H_2O$, and citric acid (added in a molar ratio of 1.5:1 to the total amount of the added metal cations). The performed basic steps were similar to those mentioned above, and the initial heat treatment, calcination, and the final annealing were respectively 400 °C for 2 h, 800 °C for 6 h, and 1000 °C for 4 h in air.

The solid-state (SS) method

The SS method was used to obtain a reference $La_{1.5}Ba_{1.5}Cu_3O_{7\pm\delta}$ sample. It was done in cooperation with Dr. Anna Niemczyk from the Institute of Power Engineering - National Research Institute, Warsaw, Poland. The procedure involved firstly mixing of CuO and pre-annealed La_2O_3 oxides with barium carbonate ($BaCO_3$), and milling in a high-energy ball mill. Wet milling conditions were applied, with a small amount of propanol added to the mixture. The obtained mixture was then subsequently dried at 90 °C, and ground to obtain homogeneous precursor. The prepared powder was then pressed uniaxially into pellets, with the applied pressure of about 100 MPa. For the heat-treatment, the pressed pellets were sintered at 880 °C for 8 h in air. In this case, a phase-pure sample could be also obtained.

The electrospinning (ES) method

The ES method, a relatively novel synthesis technique for the oxygen electrode materials, was applied to obtain morphologically modified GBSCC0911, as well as LSNMFCC2035 and LSNMFCC0550 precursor samples. Notably, the initial selection of the conditions for electrospinning was conducted within cooperation with Dr. Jie Luo from the Foshan University, Foshan, China.

Electrospinning can be used to generate interesting and desirable morphology types of a sample, like nanofibers or nanotubes, being significantly different in comparison to those obtained from the SG method [209]. Basically, before the electrospinning step, a respective solution should be prepared, which is usually based on dimethylformamide

(DMF). Then, the required chemicals are added stoichiometrically into the DMF solution. For the mentioned samples, details about the used chemicals can be seen as follow (purities of those chemicals are the same as those used in the SG method):

- $Gd(NO_3)_3 \cdot 6H_2O$, $Ba(NO_3)_2$, $Sr(NO_3)_2$, $Co(NO_3)_2 \cdot 6H_2O$, and $Cu(NO_3)_2 \cdot 3H_2O$ for the preparation of the GBSCC0911 precursor.

- Lanthanum nitrate hexahydrate ($La(NO_3)_3 \cdot 6H_2O$), $Sr(NO_3)_2$, $Ni(OCOCH_3)_2 \cdot 4H_2O$, $(CH_3COO)_2Mn \cdot 4H_2O$, $Fe(NO_3)_3 \cdot 9H_2O$, $Co(NO_3)_2 \cdot 6H_2O$, and $Cu(NO_3)_2 \cdot 3H_2O$ for the preparation of LSNMFCC2035 and LSNMFCC0550 precursors.

After all the added chemicals are completely dissolved in DMF, the weighed amount of polyvinylpyrrolidone (PVP) is added subsequently. Alternatively, PVP can be also dissolved in DMF beforehand, as it was done in the case of the GBSCC0911 precursor preparation. It is worth noting that the respective PVP concentrations for the GBSCC0911, and LSNMFCC2035 or LSNMFCC0550 synthesis procedures were different. For the former one it was selected as 10 wt.%, while for the latter two it was 12.5 wt.%. Also, the weight ratios of all added chemicals, PVP, and DMF were different, which was selected according to the initial trials. Respectively, the ratios were 2:1:9 for GBSCC0911, and 1:1:7 for LSNMFCC2035 and LSNMFCC0550.

The prepared solution can be electrospun in the electrospinning device, as depicted in Fig. 7-1. Apart for setting a properly chosen high voltage, numerous other conditions must be adjusted to ensure formation of the elongated fibers [210].

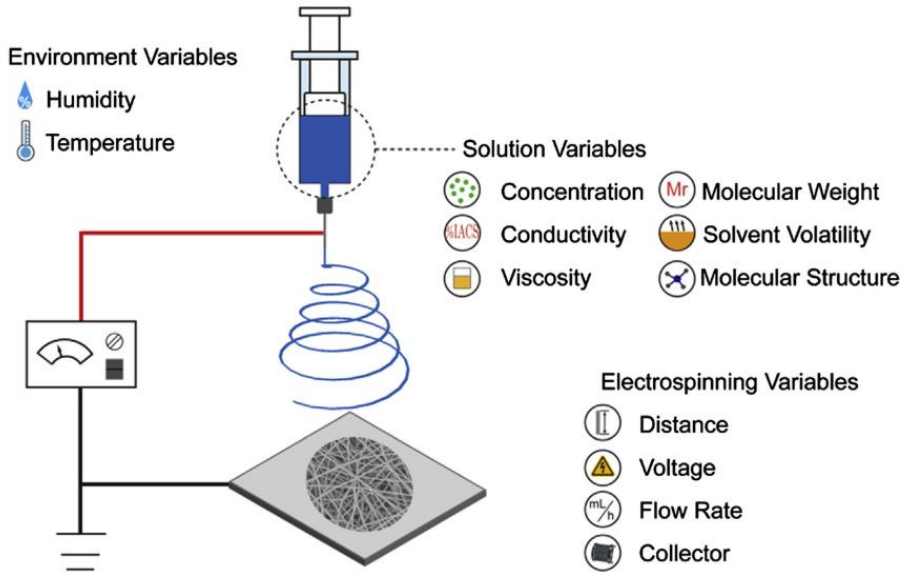

Fig. 7-1. A schematic diagram of the electrospinning technique and relevant variables [210]

In the used Doxa Microfluids Professional equipment, the respective obtained solution was transferred into a syringe, which was installed on a top of a collector, in a distance of about 15 cm. The as-prepared solution was then injected automatically from the syringe, as droplets, toward the collector, by a screw propeller. The flow rate was set in 5-20 ml min^{-1} range, and then, a high voltage (10-20 kV) was applied between the syringe and collector, in order to electrify and elongate droplets into slender fibers. The parameters were adjusted according to the real status of the injection and the fibers formation (controlled by installed inside a chamber a digital camera). Also, a piece of baking paper was spread on the collector, to facilitate collection of the fibers.

When the respective solution was electrospun completely, the fibers clustered as thin, soft and near-transparent membrane-like products that were later peeled and scratched off the paper. To ensure that a proper micro-morphology was formed, microstructure of the precursors was checked by Scanning Electron Microscopy (SEM), as presented in an exemplary Fig. 7-2.

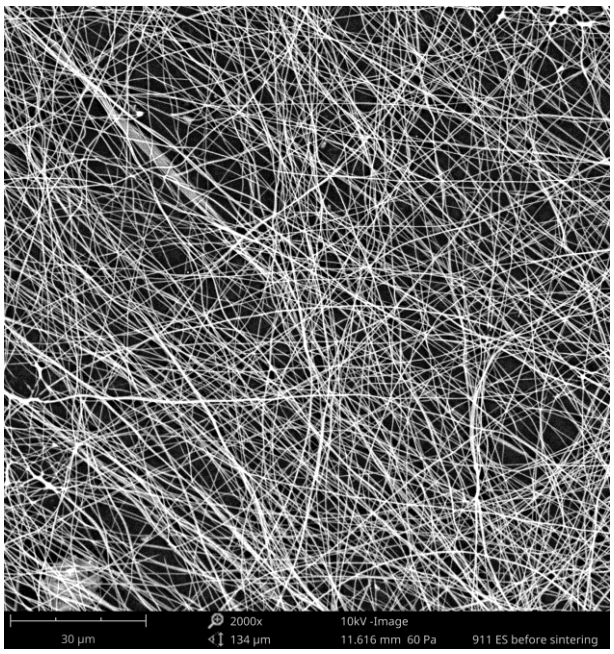

Fig. 7-2. An example of the obtained morphology of GBSCC0911 precursor nanofibers after electrospinning, as observed by SEM.

Obviously, the electrospun precursors require high-temperature sintering, which is needed in order to remove the organic components, as well as to ensure that the synthesis between the inorganic compounds properly takes place. Also, optimizing of the heat treatment must be conducted to obtain phase-pure samples and maintain the desired morphology at the same time. After the conducted initial experiments, the related conditions could be established, as summarized in Tab. 7-3.

Tab. 7-3. The applied sintering conditions for the electrospun samples. The bold data in the last column represent the optimized, most suitable preparation conditions.

Composition with the abbreviation	Sintering [°C, hours]
GBSCC0911 ES	900, 2
	1000, 6
LSNMFCC0550 ES	750, 6
	800, 6
	850, 6
	900, 6
LSNMFCC2035 ES	**900, 6**

As a final comment in this section, it is necessary to remark on the established experimental errors regarding cationic stoichiometry of the discussed samples. In this aspect, considering the purity of used chemicals, accuracy of a balance (±0.0001 g), and other experimental errors involved with the discussed synthesis procedures, it can be estimated that the actual chemical content of metal elements differs less than 0.01 from the one reported in the provided formulas for all of the as-synthesized materials. However, this is of course not related to the phase purity of the materials.

7.2. Calculations of the entropy metric for the multicomponent samples

Since there are multiple transition metal elements co-occupying the B-site in the considered LSNMFCC system, it is of interest and importance to characterize the relevant configurational entropy values. In the simplest approach, only the B-site elements can be taken into account, and the relevant entropy can be calculated using the following equation [180]:

$$S_B^{config} = -R \sum_i X_i^B \ln(X_i^B) \text{ (Eq. 7-1)}$$

where X_i^B refers to the fraction of the element i distributed in the B sublattice. However, the more proper way of implementing such calculations involves the total number of atoms and sublattices in the formula unit. Thus, the related equations can be demonstrated as Eq. 7-2 and 7-3 [211]:

$$S_{SL}^{config} = \frac{-R \sum_S \sum_i a^S X_i^S \ln(X_i^S)}{\sum_S a^S} \text{ (Eq. 7-2)}$$

$$EM = \frac{S_{SL/mol\ atoms}^{config}}{R} \times L \text{ (Eq. 7-3)}$$

In these equations, please note that a^S represents the number of sites in the S sublattice, while X_i^S refers to the fraction of the element i distributed in the S sublattice, L means the

number of sublattices of the particular corresponding structure, and R denotes the ideal gas constant. EM stands for the entropy metric. Hence, calculations of the related S_B^{config}, S_{SL}^{config}, and EM can be summarized in Tab. 7-4.

Tab. 7-4. Entropy values of the LSNMFCC compositions.

Composition	S_B^{config}/R	S_{SL}^{config}/R	EM
LSNMFCC2035	1.543	0.414	1.242
LSNMFCC1540	1.505	0.406	1.219
LSNMFCC1045	1.443	0.394	1.182
LSNMFCC0550	1.350	0.375	1.126

Importantly, since *R*-3*c* structure has one position for the A-site cations, one position for the B-site cations, as well as one structural position, in which the oxygen anions are present, from the structural point of view, all the equations can be used [212]. Nevertheless, taking the obtained values into account, it can be easily concluded that all the compositions in LSNMFCC system should be rather regarded as medium entropy configurations, since EM values are in the 1-1.5 range [211]. However, when only the B-site is counted, that sublattice possesses high configurational entropy in LSNMFCC2035 and LSNMFCC1540 compositions [180].

7.3. Samples characterization

7.3.1. X-ray diffraction

With preparation of new, complex samples, it is of a great importance to get a comprehensive understanding of the structural features, including symmetry, unit cell parameters, and other structural details. X-ray diffraction (XRD) method is regarded as one of the most important techniques for the initial characterization of the samples. In this work, the studies were conducted on Panalytical Empyrean diffractometer equipped with Cu Kα radiation and PIXcel3D detector. A standard measurement at room temperature (RT) took around 51 minutes, with data gathered in a typical range of 10-110 deg for a powdered sample. In the meantime, high temperature XRD (HT-XRD) could be also realized with a specialized module, Anton Paar HTK 1200N oven-chamber installed on the mentioned diffractometer. In the equipment the measurements can be conducted in a temperature range from RT up to 1000 °C, with an interval of 100 °C. Depending on a particular sample, the highest temperature was decreased in some cases. Data were typically registered in two consecutive heating and cooling runs.

A diffractogram is generated as the result of the XRD experiment. In order to identify the phase composition of the measured sample, a qualitative analysis was conducted in HighScore Plus software with the linked PDF-4+ (ICDD) database of crystal structures and experimental results. This allowed to proceed with the basic identification of the

present phases, as well as identify candidate symmetry and space groups for the quantitative structural analyses by Rietveld method.

Rietveld refinements of structural data

Getting deeper understanding of the XRD results requires analysis of the data, with Rietveld method usually utilized, which is based on a least squares approach. The height, width, and position of XRD reflections are refined, and based on it, many aspects of the material's structure can be revealed [213].

Typically, the accuracy of a refinement is revealed via the value of X^2, which can be calculated by Eq. 7-4:

$$X^2 = \frac{M}{N_{obs} - N_{var}} \text{ (Eq. 7-4)}$$

$$M = f_p \sum M_p \text{ (Eq. 7-5)}$$

$$M_p = \sum w(I_o - I_c)^2 \text{ (Eq. 7-6)}$$

Note that N_{obs} stands for the total observations in the histogram, while N_{var} represents the variables of the least squares refinement. And the M can be determined by Eq. 7-5 and Eq. 7-6, in which the f_p refers to a weighting factor when a series of histograms are involved, and w means the separate weights, while I_o and I_c represent the intensity of the normalized profile, and calculated intensity with background and scale factors included, respectively. Last but not least, there is another parameter R_{wp}, which can be calculated by Eq. 7-7:

$$R_{wp} = \sqrt{\frac{M_p}{\sum w I_o^2}} \text{ (Eq. 7-7)}$$

Practically, in order to obtain an acceptable refinement result, R_{wp} should be as low as it can possibly be, but it is worth noting that the actual values of R_{wp} for a typical XRD experiment and a well-refined single-phase material data are in a range of 2-5%.

The used in this work software is GSAS II, which allows for full implementation of the Rietveld analysis [214]. There is an array of parameters, which should be released or constrained, related to the accurate final refinement. The first is the background, for which the applied function is "chebyschev-1" with a number of coefficient equal to 10. Then, the "sample displacement" should be considered as well, which reflects a proper placement of a given sample in the diffractometer. After setting the desired space group and occupancy of all crystal positions by the given atoms, the unit cell parameters can be refined, for the given peak-fitting function, in which various factors are included, such as broadening induced by strain and size. The relative atomic positions in the unit cell can also be taken into account in the refinement, depending on a particular site symmetry. Also, when it comes to the atomic level, it is of great importance that the thermal vibration

U_{iso} factors are refined, but in this case, constraints are usually applied for the specific atomic position. This happens if two different elements occupy the same crystal site (e.g. La and Ba in the LBCu material). In the meantime, all oxygen anions also can have the same U_{iso} parameters constrained for all crystal positions, with site occupancy reflecting the actual stoichiometry.

When a good quality refinement is completed, a final graph can be prepared, as presented in Fig. 7-3. LBCu oxide is taken an example in this case. As it can be seen clearly, the original data and refinement curve are mostly overlapped, while positions of peaks matches those of the allowed reflections Also, the respective intensity of the peaks if reflected very well.

For the refined parameters of the unit cell, a typical magnitude of the measuring error is on the order of 10^{-5}-10^{-4} Å, as can be derived from the diffractometer setup and accuracy. For the errors aroused from the fittings in GSAS II software itself, they are usually less than 10^{-5} Å.

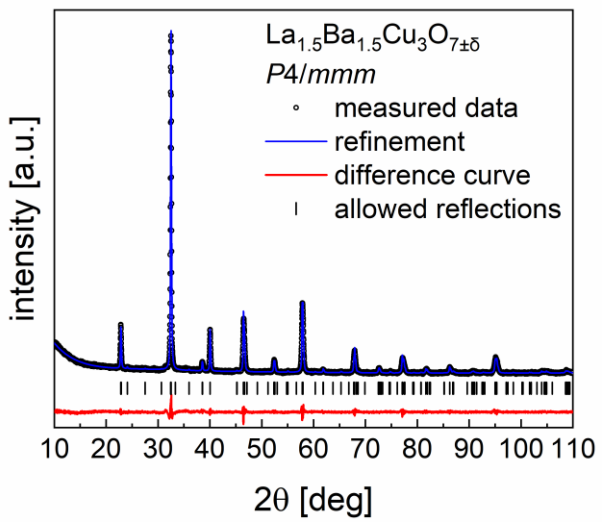

Fig. 7-3. A typical graph showing results of the Rietveld refinement of the XRD data.

If the structural studies are conducted as a function of temperature, HT-XRD can be considered as an effective characterization technique, which can provide more detailed information regarding possible presence of phase transitions, but also thermal expansion data can be obtained. Importantly, structural data from high temperatures reflect the actual situation of the operating conditions of SOCs.

In the case of refinements of the HT-XRD data, the derived unit cell parameters *a*, *b*, and *c*, as well as *V* (the unit cell volume) can be used to calculate the thermal expansion coefficient (TEC) for a given sample. The general dependence is based on Eq. 7-8:

$$TEC = \frac{1}{l}\frac{\Delta l}{\Delta T} \quad \text{(Eq. 7-8)}$$

Where l means the original dimension, calculated by the cube root of V at room temperature, and Δl represents the change of a given dimension upon the change of temperature ΔT. With the plot of $\Delta l/l$ as a function of temperature, the TEC can be derived by slope of the linearly fitted line. Notably, TEC can be calculated along any given crystal axis, which is useful to detect anisotropic behavior. Regarding error values for TEC determination, they were taken as from the linear fitting errors. Their magnitude is on the order of 10^{-8} K^{-1}.

Additionally, in order to have a comparison of the thermal behavior of the studies materials, TEC values for some of the samples were also measured by the dilatometry method, with Linseis L75 Platinum Series dilatometer utilized. The studies required usage of dense sintered specimens. The process of their preparation is discussed below, in the subchapter devoted to electrical conductivity measurements. Similarly as for the HT-XRD, the error of the TEC estimation from dilatometry was taken as that resulting from the linear fitting process.

7.3.2. Oxygen stoichiometry determination

Iodometry

Determination of the oxygen nonstoichiometry is crucial in understanding the crystal structure of the materials, and it is a basis for discussing physicochemical properties of the as-synthesized samples. For evaluation of the oxygen content in materials at RT, the iodometric titration was carried out, which is based on the following reaction equations, as presented in works [215,216].

$$Cu^{3+} + 3I^{-} \rightarrow CuI + I_2 \text{ (Eq. 7-9)}$$

$$Cu^{2+} + 2I^{-} \rightarrow CuI + \frac{1}{2}I_2 \text{ (Eq. 7-10)}$$

In these reactions, the exemplary Cu cations are reduced in the two- and one-electron process, and I_2 is released. For other 3*d* metals (Mn, Fe, Co, and Ni), reduction from +3 or +4 charge state to +2 was considered, in a similar manner. The considered studies were realized in cooperation with Dr. Anna Stępień from AGH University of Krakow.

To ensure proper preparation of a sample for the iodometric titration, it was pre-annealed at 800 °C in air with a heating/cooling rate of 2 °C min^{-1} in order to remove the adsorbed carbon dioxide and water. After dissolution in HCl solution having excess KI added, the iodine anions reduce the 3*d* metal cations, and the I_2 is released. Its amount can be determined by reacting with sodium thiosulfate solution (NaS_2O_3, 0.01 mol/dm^3), in which the produced iodine will be reduced into iodide ions (Eq. 7-11). this occurs with an evident change of a color of the solution.

$$2S_2O_3^{2-} + I_2 \rightarrow S_4O_6^{2-} + 2I^{-} \text{ (Eq. 7-11)}$$

To be specific, in the conducted experiments both, the sample and potassium iodide (KI) are dissolved in hydrochloric acid (HCl) solution with a concentration of 6 mol L^{-1}. The weight of the sample and KI are typically about 0.1 g and 1 g, respectively. Importantly, the dissolution is done in the atmosphere fed with argon (flow rate: 60 mL min^{-1}). The titration starts when the dissolution of the sample and KI is completed, then the sodium thiosulfate solution is added slowly by EM40-BNC Mettler Toledo titrator equipped with a Pt electrode. Notably, while the Pt electrode can detect a potential change in the solution, in this work, the ending point of the titration was adopted as the point of color change in the solution.

Eventually, the average charge state of the 3*d* metal elements, and the, the oxygen content in a particular sample can be calculated by stoichiometry-based calculations of the used volume of the NaS_2O_3 solution. In general, three measurements were conducted, and an average of their results was taken to minimize the experimental error, which was evaluated as not exceeding ±0.01.

Thermogravimetric analysis (TG)

Majority of oxides, especially those used for preparation of the oxygen electrodes for IT-SOCs are known to release oxygen from their structure at high temperatures, which is associated with generation of the oxygen vacancies. Specifically, with an increase of temperature, the weight of a sample will decrease, due to the released oxygen. Thus, by recording the change of the weight as a function of temperature, and taking into account the initial oxygen content evaluated by the iodometric titration, changes of the absolute oxygen content can be derived precisely.

In the conducted thermogravimetric measurements, a given powdered sample with the weight of 60-80 mg was mounted on a platinum pan that is later transferred into the measurement chamber of TA Q5000 IR thermobalance. A program of the whole measurement can be customized, and in the typical settings a target temperature of 800 °C with a heating/cooling rate of 2 °C min^{-1} was selected for one measuring cycle. All the samples were measured at least in two such cycles in order to remove the experimental errors related to the presence of adsorbed species, as well as to standardize the thermal history of all the oxides (i.e. ensure the same heating/cooling rate). Moreover, for the selected materials the measurements could be carried out in different atmospheres, e.g. synthetic air, argon (5N), pure oxygen, and 5 vol.% hydrogen in argon. Gas flow was 100 mL cm^{-3}.

Due to the very high accuracy and precision of the used thermobalance, the errors in TG measurements are accounted as lower than ±0.01%.

7.3.3. Raman spectroscopy

As a supplementary measurement in this work, Raman spectroscopy is also an interesting method to observe surface-related properties of materials [217], but can be also useful in determination of the oxygen vacancies presence in oxides [218]. Similarly as to TG experiments, in order to obtain an equilibrated state of the oxygen content in the

considered samples, it was necessary to apply pre-annealing at 800 °C with a heating/cooling rate of 2 °C min^{-1} beforehand. Then, a powdered specimen was mounted on the Thermo Scientific DXR3 Raman microscope, in which the 532 nm laser beam and 10 X lens were selected. The measurements were done in cooperation with Prof. Wojciech Zając from AGH University of Krakow.

7.3.4. Density Functional Theory (DFT) calculations

Theoretical calculations are of importance to simulate structure data, including unit cell parameters, total crystal energy, and the oxygen vacancy formation, so that deeper insight into the structural features can be gained [219]. The conducted numerical experiments were carried out in cooperation with Dr. Piotr Winiarz from AGH University of Krakow.

To implement a DFT calculation, the VASP 6 package (Vienna Ab Initio Simulation Package) was adopted. Initially, a handful of supercells of 2 × 2 × 1 was built for the formula of $GdBa_{1-y}Sr_yCo_{2-x}Cu_xO_{5+\delta}$, representing a double perovskite structure for the wide range of chemical compositions, as represented by x values equal to 0, 0.5 and 1, and y values of 0, 1, and 2, respectively. Importantly, a range of δ (0, 0.25, 0.5, 0.75, and 1) was set in order to simulate the varying oxygen non-stoichiometry. Subsequently, the calculations of the energy of the oxygen vacancy formation, could be done as denoted by Eq. 7-12:

$$E_{ox.vac.} = E_{final} - (E_{initial} - \frac{1}{2}\Delta E_{O2}) \quad \text{(Eq. 7-12)}$$

where E_{final} represents the total energy of the formula with the oxygen vacancy formed, $E_{initial}$ stands for the formula at the beginning (before vacancy formation), ΔE_{O2} means the energy of an oxygen molecule [220].

Also, DFT method was utilized to calculate possible arrangement of the oxygen vacancies in $La_{1.5}Ba_{1.5}Cu_3O_{7\pm\delta}$, which was done by comparing the refined crystal energy for different possible configurations, and selected values of δ.

7.3.5. Electrical conductivity measurements

The performed electrical conductivity tests were conducted on dense samples having the shape of a cuboid. The measurements were conducted in cooperation with Dr. Marek Zajusz and Dr. Kacper Cichy from AGH University of Krakow.

To obtain a sample in the mentioned shape, a given amount of the precursor powder was mixed with poly(vinyl butyral-*co*-vinyl alcohol-*co*-vinyl acetate) (PVB) in a weight ratio of 99:1, and with added propanol as the solvent for PVB. After ground thoroughly, the obtained mixed powder is dried at about 80 °C in air. Then, a matrix with a diameter of 13 mm can be used to press a pellet with a uniaxial pressure of ca. 100 MPa. After that,

the specimen is sintered at the required temperature (the same or 50-100 °C higher than the respective final heat treatment temperature given in Tab. 7-1), which is required in order to reach a high relative density. When the pellet is sintered, it is then polished into a cuboid (or different) shape by sandpaper. Such samples (after checking their structure) were used in the dilatometry experiments, and in the electrical conductivity studies. For the latter measurements, two terminals were applied on the opposite sides of the sinter with a Pt paste (ESL ElectroScience or FuelCellMaterials), and later were sintered at the required temperature to prepare current collectors.

The applied method of the total electrical conductivity evaluation was a pseudo-4-probe direct current (DC) technique. The related equipment is Keysight 34465A multimeter and Keysight 33210A function/arbitrary waveform generator. Alternatively, Keithley 2000 (Tektronix) multimeter was also utilized. The measured temperature range was typically from RT to either 850 °C or 900 °C. Dimensions of the sinters were taken into account to establish the specific conductivity values. The relative error of the total conductivity measurements was estimated as not exceeding 5%, based on accuracy of the equipment and determination of size of the samples.

7.3.6. Chemical compatibility tests

The compatibility tests with commonly-used electrolyte materials were investigated, as they are necessary in order to evaluate applicability of the considered samples for preparation of the cells. The adopted electrolyte materials are LDC (synthesized by the sol-gel method, only for LBCu oxygen electrode material), $Ce_{0.8}Gd_{0.2}O_{2-\delta}$ (GDC20, FuelCellMaterials, for LBCu and GBSCC system), $La_{0.8}Sr_{0.2}Ga_{0.8}Mg_{0.2}O_{3-\delta}$ (LSGM, FuelCellMaterials) and $Ce_{0.9}Gd_{0.1}O_{2-\delta}$ (GDC, Cerpotech). In the studies, all the considered electrolyte materials were preliminary heated up to high temperatures (1450 °C for LSGM and GDC20, 1450 °C or 1350 °C for GDC, 1400 °C for LDC). In the next step, the powdered electrolyte materials were then respectively mixed with the oxygen electrode material samples (also powders) at a 1:1 wt. ratio, which was followed by pressing in a matrix to form pellets. Then annealing tests at high temperatures were performed, with the relevant scheme summarized in Tab. 7-5. When the respective test was done, a pellet comprising mixture of both materials was crushed and ground thoroughly, and later XRD measurements were conducted to evaluate possible presence of additional phases or significant shift of peaks positions.

Tab. 7-5. Compatibility tests in air of the as-synthesized samples and electrolyte materials.

	Studied materials		
Electrolyte	LBCu	GBSCC	LSNMFCC
LSGM	**900 °C for 2 h**	**950 °C for 2 h**	**850 °C for 2 h**
	800 °C for 100 h		
	HT-XRD up to 975 °C*		
GDC	-	**900 °C for 2 h**	**900 °C for 2 h**
GDC20	800 °C for 100 h	-	-
LDC	800 °C for 100 h	-	-

*Additional experiments were conducted by HT-XRD.

It is also worth noting that for the GBSCC system, two compositions were measured with GDC GBSCC0911 and GBSCC1010. The black-bolded data in Tab. 7-5 indicate good compatibility test outcome, which was adopted in the subsequent cell manufacturing.

7.3.7. Scanning electron microscopy (SEM) studies

It is of great importance to conduct observations of morphology and homogeneity of the as-synthesized powder samples, as well as to study the cross-section of the constructed and measured cells to observe possible reactivity at the interfaces, porosity of the electrodes, adhesion of the electrode layers, etc. The conducted studies in this matter involved SEM experiments. A part of the studies was realized in cooperation with Dr. Juliusz Dąbrowa, Dr. Agnieszka Brzoza-Kos and Dr. Marta Gajewska from AGH University of Krakow.

The microscopic observations were mainly conducted on ThermoFisher Scientific Phenom XL Desktop SEM or JEOL JSM-7100F field emission scanning electron microscope. Observations were done with using the backscatter and secondary electrons. At the same time, the energy-dispersive X-ray spectroscopy (EDS) was also utilized to analyze distribution of selected elements in the samples. For such experiments, the gathering time of the elemental maps was selected as long enough to gather suitable data.

7.3.8. Transmission electron microscopy (TEM) studies

At a higher magnification, TEM allows observing samples at the nano-level. For example, the crystal lattice of the LSNMFCC system can be clearly seen. The performed TEM observations were done in cooperation with Dr. Marta Gajewska from AGH University of Krakow. The applied equipment was FEI Tecnai TF20 X-TWIN (FEG) microscope, working with an accelerating voltage of 200 kV. The preparation of samples for TEM observations was done via depositing powders on the carbon-coated copper TEM grids.

7.4. Preparation and characterization of electrochemical properties of cells

7.4.1. Manufacturing of symmetrical cell

All prepared button-type symmetrical cells studied in this work were based on the electrolyte-support, so it was of importance to obtain proper, dense electrolyte pellets. In order to do so, the LSGM or GDC powder was blended with PVB in a weight ratio of 99:1, with propanol added as the solvent. After the mixture was homogeneously ground, it was dried at 80 °C to remove the residual propanol. Certain amount of the dried mixture was transferred to a 13 mm matrix, and pressed uniaxially under a pressure of ca. 100 MPa, resulting in formation of a disk-shaped specimen with a thickness of around 0.65 mm. After that the disk specimens for LSGM were sintered at 1450 °C for 8 h in air, while for GDC, the temperature was 1350 °C and the time was 6 h (if GBSCC oxygen electrode ware used) or 1450 °C with sintering for 8 h (for LSNMFCC), respectively. When the disk sintering was done, sandpaper was used in order to decrease the thickness of the dense electrolyte pellets to ca. 300 μm for both, LSGM and GDC.

In the second main step, making the electrode slurry is also important, since screen-printing method is adopted to apply a given electrode layer on the electrolyte pellet. The weighed ingredients, involving the selected electrode material powder, pore former (starch) and organic binder (terpineol-based 311237 ink, FuelCellMaterials), were mixed homogeneously with a weight ratio of 20:1:10. Then, the obtained electrode slurry was applied on both sides of the electrolyte pellet (2 layers at each side) by the screen-printing method. It is worth noting that separate drying was necessary after each layer was printed. After that, the cell was transferred to a furnace, and sintered at different temperatures for 2 h. The accordingly used sintering temperatures are gathered in Tab. 7-6. It is worth noting that the actual working area for the electrode layers was ca. 0.28 cm^2. After the sintering of the layers, a given current collector was also applied on top of the electrode layers, in a mesh-like pattern. The adopted current collectors are Ag and Au (both from FuelCellMaterials), as well as Pt (ESL ElectroScience). The related applied schemes of sintering of the current collectors are also summarized in Tab. 7-6.

Tab. 7-6. Applied schemes for sintering of the electrode layers and current collectors in the studied symmetrical cells, also applied for manufacturing of full cells.

Electrode	Sintering temperature of the electrodes [°C], 2 h time	Current collector	Sintering temperature of the current collector [°C], (time of sintering)
LBCu	750	Ag	700 (0.5 h)
	800		
	850		
	900		
GBSCC	900 (LSGM and GDC)	Ag	700 (0.5 h)
		Pt	815 (15 min)
LSNMFCC	850 (LSGM)	Au	750 (1 h)
	900 (GDC)		

7.4.2. Manufacturing of electrolyte- and anode-supported full cells

In the case of electrolyte-supported full cells, the selected electrolyte is LSGM (thickness of 200 μm) or GDC (thickness of 300 μm), depending on different circumstances (e.g. chemical stability). Further reduction of thickness (from 300 μm to 200 μm) of the LSGM electrolyte pellets could be realized by using the polishing machine (Struers Labopol-30 with MD-Piano 220 diamond polishing plate), with the micrometer gauge used as the measuring apparatus.

For the anodes in the full cells, Ni-GDC composite was prepared by mixing nickel oxide (NiO) with GDC (for GBSCC and LSNMFCC) or GDC20 (for LBCu) at a weight ratio of 3:2. Before applying the anode layer, it is of importance to apply a LDC buffer layer on the LSGM electrolyte in advance, in order to prevent elemental mixing, as discussed in chapter 4. The applied method was still screen-printing, similar to that of the electrode layer making in symmetrical cells. The LDC slurry was prepared by mixing the LDC powder and organic binder at a weight ratio of 1:1, and then deposited on the LSGM electrolyte. The sintering was done at 1400 °C for 2 h in air. After the LDC buffer layers are sintered, the Ni-GDC anode slurry could be prepared by mixing NiO-GDC powder, pore former, and organic binder at a weight ratio of 20:1:10. Then, the anode slurry was applied onto the LDC buffer layer by screen-printing (two layers), which was followed by sintering at 1350 °C for 2 h. After the anode part is already applied, the oxygen electrode layer can be prepared on the other side of the LSGM electrolyte pellet. The used method was exactly the same, as described in the chapter related to manufacturing of the symmetrical cells. Also, the same sintering schemes were used. Finally, identical procedures for current collectors were followed as well (Tab. 7-6).

Additionally, for comparison of performance of GBSCC0911 and GBSCC0911 ES oxygen electrode materials, GDC was also selected as the electrolyte support. In this case,

the LDC buffer layer is not needed, so the anode layer could be deposited onto the GDC pellet directly. This is also true for the oxygen electrode layer prepared on another side of the GDC pellet. The related procedures of the preparation are the same as what it is mentioned above.

Another type of a full cell was also studied, which exhibits the anode-supported design with the Ni-YSZ anode and a thin, dense layer of the YSZ electrolyte [221]. Notably, the anode supports were supplied from Dr. Anna Niemczyk from Institute of Power Engineering - National Research Institute, Poland. Still, before applying an oxygen electrode layer on the anode-supported full cell, the GDC buffer layer should be also prepared. The procedure of making GDC slurry was the same as for the LDC layer, but the sintering scheme was 1425 °C for 2 h in air. After that, the oxygen electrode layer could be applied onto the GDC buffer, and was sintered in the same way as in the symmetrical cells.

7.4.3. Measurements of electrochemical properties of cells

It should be emphasized that all measurements of the constructed cells (both, symmetrical and full cells) were realized by using the ProboStat™ device from NORECS, Norway.

For measurements of symmetrical cells, Electrochemical Impedance Spectroscopy (EIS) is considered as the main approach to analyze the electrochemical properties. Firstly, the symmetrical cell is mounted onto the support tube, with electrodes connected by two Pt wires at each side. Each Pt wire is connected by two electrical cables, of which the resistance will not have impact on the final results. Hence, this can be regarded as a typical pseudo-4-probe setup. Those two electrical wires are connected to the measuring equipment, which in the studies were Solartron 1260 frequency response analyzer and Solartron 1287 electrochemical interface. Secondly, the cell is heated up to a given temperature range (600-800 °C or 600-850 °C) for the measurements, with a synthetic air flow fed in a rate of 20 mL min^{-1}.

Notably, the applied perturbation amplitude was 25 mV, with the EIS data recorded in a frequency range of 0.1-10^6 Hz. In order to interpret the data and gain detailed information, the obtained EIS spectra were fitted with a typical equivalent circuit as $L_{ind} - R_{ohm} - (RQ)_{HF} - (RQ)_{MF} - (RQ)_{LF}$, where the L_{ind} derives from the transmission line effects in the electrical wires, and R_{ohm} means the total ohmic resistance of the whole cell, while those (RQ) components simulate the electrochemical processes taking place at high (HF), middle (MF) and low (LF) frequencies (resistance and constant phase element, respectively) [222,223]. The number of the (RQ) parts was not always set as three, and two of them were also applied in some cases (depending on the actual EIS data). ZPlot and ZView (Scribner Associates) software was used in EIS data collecting and fitting, respectively.

The final electrode polarization resistance, R_p, was evaluated as the sum of all the fitted partial resistances in the (RQ) elements. Also, it was recalculated according to the

working area of both electrodes in symmetrical cells (i.e. was divided by two and multiplied by the electrode's surface). As for studies of the full cells, after the whole cell is successfully prepared (either electrolyte-supported or anode-supported), it is necessary to seal the cell between two ceramic cylinders with the same diameter as the support tube of ProboStat™ device. The Ceramabond (AREMCO) was used as the high temperature sealing paste to glue the elements forming a gas-tight connection. It was followed by sintering at ca. 90 °C and 260 °C for 2 h at each step. Later, the formed unit is mounted on the support tube, and sealed in the same procedure.

Similarly, the full cell is heated up to a temperature range of 600-850 °C (in some cases, up to 900 °C) for measuring. At the oxygen electrode side, the synthetic air flow of 20 mL min^{-1} is fed, while the humidified hydrogen gas (3 vol.% H_2O) of 40-60 mL min^{-1} flow is fed to the fuel electrode side. In the studies, the open circuit voltage (OCV) of the full cell was monitored to ensure gas-tightness. Also the voltage-current density curves were recorded by CorreWare (Scribner Associates) software in both, the fuel cell mode and electrolysis mode (measured typically in 600-750 °C range). The later calculations of the output power density were carried out in CView (Scribner Associates), with the final values recalculated according to the working area of the oxygen electrode.

It should be also stated that EIS studies were conducted for the full cells, with the same parameters, as described above for the symmetrical cells. Measurements are done after the fuel electrode was reduced.

7.4.4. Distribution of Relaxation Times (DRT) analysis

Interestingly, apart from the simulation by the equivalent circuit in ZView, DRT is another effective option, which enables extracting details from the measured EIS data. The mathematical background of the method is well-established [224]. In Eq. 13 a relationships is shown between the impedance spectrum $Z(\omega)$ and the DRT $\gamma(\tau)$ parameter:

$$Z(\omega) = R_{ohm} + Z_{pol}(\omega) = R_{ohm} + \int_0^{\infty} \frac{\gamma(\tau)}{1+j\omega\tau} d\tau \quad \text{(Eq. 7-13)}$$

The practical implementation of the DRT method is available for the Matlab software, as an openly available DRTtools code [225]. Briefly, in the DRT approach, EIS spectra are recalculated into the area of separate peaks, presented as a function of relaxation times (frequency). Exemplary data for such recalculation can be seen in Fig. 7-4. It is widely-accepted that those separated peaks represent different reaction steps on an electrode, so therefore, DRT enables a more explicit insight into the EIS results. Further details about the actual implementation of the method are provided in the following chapters presenting the obtained results.

a) b)

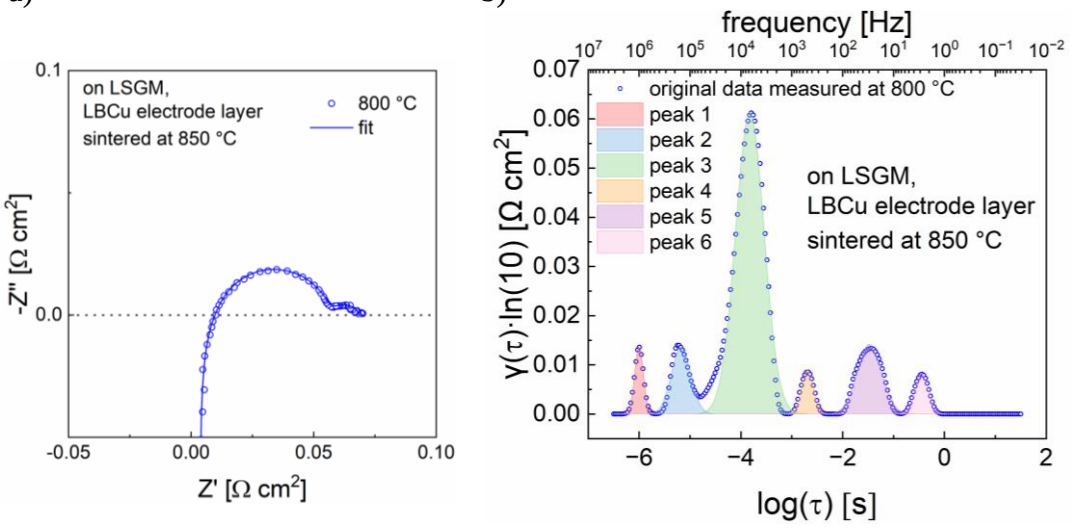

Fig. 7-4. a) Exemplary EIS data presented in a Nyquist plot, with b) resulting graph from the applied DRT analysis method. Please notice that for simplicity of interpretation, some peaks are fitted in a simplified manner.

Results and discussion

Statement on the author's publications

Part of the results presented in the *Results and discussion* section in this dissertation has been published by the author in the following articles:

1. **K. Li**, K. Świerczek, P. Winiarz, A. Brzoza-Kos, A. Stępień, Z. Du, Y. Zhang, K. Zheng, K. Cichy, A. Niemczyk, Y. Naumovich
„*Unveiling the electrocatalytic activity of the* $GdBa_{0.5}Sr_{0.5}Co_{2-x}Cu_xO_{5+\delta}$ *(*$x \geq 1$*) oxygen electrodes for Solid Oxide Cells*"
ACS Applied Materials & Interfaces 15(33) (2023) 39578-39593, **IF (2022) 9.5**

2. **K. Li**, A. Niemczyk, K. Świerczek, A. Stępień, Y. Naumovich, J. Dąbrowa, M. Zajusz, K. Zheng, B. Dabrowski
„*Co-free triple perovskite* $La_{1.5}Ba_{1.5}Cu_3O_{7\pm\delta}$ *as a promising air electrode material for Solid Oxide Fuel Cells*"
Journal of Power Sources 532 (2022) 231371, **IF 9.2**

3. **K. Li**, K. Świerczek, P. Winiarz, A. Brzoza-Kos, A. Stępień, Y. Zhang, K. Zheng, K. Cichy, A. Niemczyk, Y. Naumovich
„*Optimizing the copper content in* $GdBa_{0.5}Sr_{0.5}Co_{2-x}Cu_xO_{5+\delta}$ *double perovskites as the high performance oxygen electrodes for reversible Solid Oxide Cells*"
ECS Transactions 111(6) (2023) 1223-1230, ISSN 1938-5862

The author has also participated in research and preparation of the following papers, which concern the same research field (not discussed in this thesis):

4. Z. Du, L. Shen, Y. Gong, M. Zhang, J. Zhang, J. Feng, **K. Li**, K. Świerczek, H. Zhao
„*Self-assembled perovskite nanocomposite with beneficial lattice tensile strain as high active and durable cathode for low temperature Solid Oxide Fuel Cell*"
Advanced Functional Materials 34(4) (2024) 2310790, **IF (2022) 19.0**

5. A. Niemczyk, S. Jagielski, R. Kluczowski, **K. Li**, K. Świerczek, K. Zheng, Y. Naumovich, J. Kupeck
„*Efficient and economically favorable Co-Free air electrodes for Solid Oxide Cells*"
ECS Transactions 103(1) (2021) 1497-1504, ISSN 1938-5862

8. Physicochemical properties of $La_{1.5}Ba_{1.5}Cu_3O_{7\pm\delta}$

As presented in Tab. 7-1, different annealing conditions were considered to optimize preparation procedure of $La_{1.5}Ba_{1.5}Cu_3O_{7\pm\delta}$ (SG method). In all cases, after the XRD measurements were conducted and the initial identification of the phase composition was performed, the Rietveld refinements were also subsequently carried out in order to characterize structural features. As it is shown in Fig. 8-1a, the optimized LBCu sample (annealed finally at 975 °C in air) fits very well the selected *P*4/*mmm* space group, with all peaks being properly refined. This indicates that the tetragonal symmetry of this material is indeed well selected. Such results are also in accordance with previously published work [226]. At the same time, visualization of the structure is presented in Fig. 8-1b. Due to the complex structural features, 2 × 2 × 1 supercell model is created, with P1 symmetry, in which occupancy of the respective sites is better visible. Apart from the central La-related layer, there are also two mixed La/Ba layers, in which around 25% of the available sites are occupied by La, yielding a final ratio of La to Ba as 1:1. The model can also explicitly demonstrate that there are two types of Cu, which are named as Cu(1) in the octahedra, and Cu(2) in the pyramid, respectively. However, more precise studies show that only around 65% of the oxygen sites in the $Cu(1)O_x$ planes are occupied [202]. Also, a small amount of oxygen anions (several %) is also present in the lanthanum layers, while for simplicity it is not shown in the structural model. Overall, the structure can be identified as the triple perovskite, with the layered structural features along the *c*-axis [227].

In order to make a comparison, structure of LBCu synthesized by the SS method was also analyzed in details, and the refined parameters are summarized in Tab. 8-1. In general, the obtained unit cell parameters from the two synthesis methods are very similar. A little difference the parameter *c* is likely a result from somewhat different oxygen content.

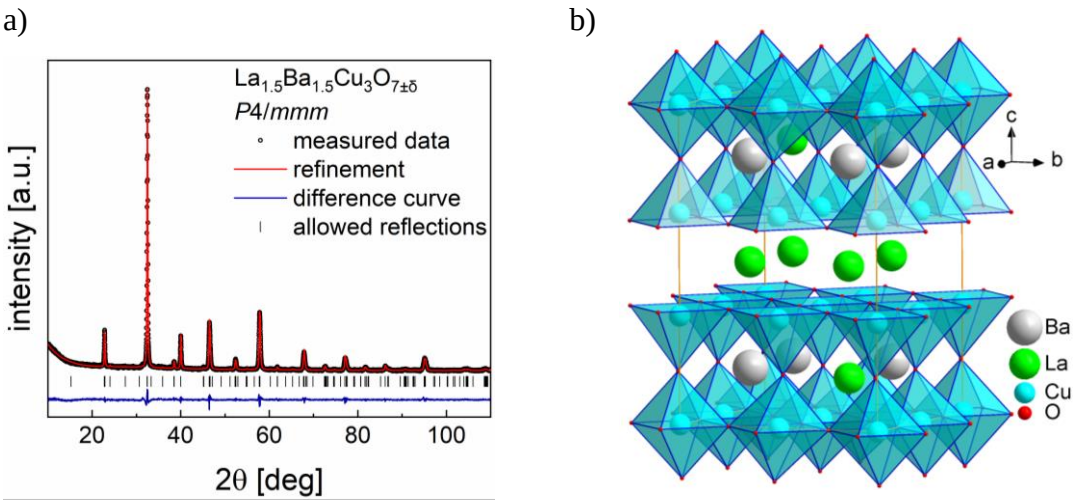

Fig. 8-1. a) The Rietveld refinement results of the obtained LBCu synthesized by the SG method (final annealing at 975 °C), and b) the created superstructure P1 model (2 × 2 × 1) in which δ was assumed as equal to 1. Based on [227].

Tab. 8-1. Summarized data of refined XRD results of LBCu synthesized via SS and SG methods [227].

LBCu synethsized by:	Unit cell parameter *a* [Å]	Unit cell parameter *c* [Å]	Unit cell volume *V* [Å^3]	R_{wp} [%]	Normalized *c*/3*a*
SS	3.9129(1)	11.6921(3)	179.01(1)	3.77	0.996
SG	3.9112(1)	11.7162(5)	179.23(1)	5.49	0.999

Furthermore, in order to have a clearer insight into the crystal structure of LBCu, DFT method was implemented to search for low energy configurations. Beginning with the P1 superstructural model (Fig. 8-1b) with the $La_{1.5}Ba_{1.5}Cu_3O_8$ formula, many possibilities of the optimized supercells having also lower oxygen content can be considered and calculated (Fig. 8-2). The calculated values of the related unit cell parameters and the total DFT energy (of the unit cell) are presented in Tab. 8-2. It is interesting to note that although the case of $La_{1.5}Ba_{1.5}Cu_3O_{7.5}$ I ($\delta = 0.5$) yields a lowest energy of -83.61 eV, the most suitable and probable structure for LBCu can be approximated by the proposed $La_{1.5}Ba_{1.5}Cu_3O_{7.25}$ II model, in which two close $Cu(1)O_5$ pyramids are not linked by the apical oxygen. The reason of this selection can be explained by the experimental oxygen content 7.23(3), as determined by the iodometric titration at RT. Also, for $\delta = 0.25$ the model II gives lower total energy, as compared to the model I (no other simple oxygen arrangements are possible in the Cu(1)-O plane). Notably, when compared with the Rietveld refinement results (Tab. 8-1), the DFT calculated unit cell parameters for the discussed models match the expected values quite well.

Tab. 8-2. Summary of the DFT optimized unit cell parameters and values of the total energy, E_{DFT}. Based on [227].

Composition	*a* [Å]	b [Å]	c [Å]	α [deg]	β [deg]	γ [deg]	E_{DFT} [eV]
$La_{1.5}Ba_{1.5}Cu_3O_{7.5}$ I	3.9282	3.8750	11.6548	90.00	90.11	90.00	-83.61
$La_{1.5}Ba_{1.5}Cu_3O_{7.5}$ II	3.9009	3.8933	11.6867	90.00	90.00	90.00	-83.48
$La_{1.5}Ba_{1.5}Cu_3O_{7.5}$ III	3.9170	3.8977	11.6224	90.00	90.00	90.00	-83.37
$La_{1.5}Ba_{1.5}Cu_3O_{7.25}$ I	3.9238	3.8689	11.6607	90.00	89.94	90.00	-82.22
$La_{1.5}Ba_{1.5}Cu_3O_{7.25}$ II	3.9010	3.8832	11.6963	90.00	89.94	90.00	-82.36
$La_{1.5}Ba_{1.5}Cu_3O_7$ I	3.9337	3.8495	11.6742	90.00	89.99	90.00	-80.93
$La_{1.5}Ba_{1.5}Cu_3O_7$ II	3.9078	3.9078	11.6276	89.70	89.70	89.79	-80.81

To confirm homogeneity of the prepared sample, SEM observations were conducted. As can be seen in Fig. 8-3, the SG method allowed to obtain fine LBCu powder (ground pellet), in which La, Ba, and Cu elements are homogeneously distributed. The visible grains having several up to tens of micrometer in size, comprise small, agglomerated primary particles. Such micromorphology seems as suitable for preparation of the electrode slurry, and further, electrode layers.

a) oxygen content = 7.5 (I)

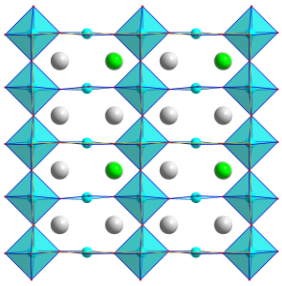

b) oxygen content = 7.5 (II)

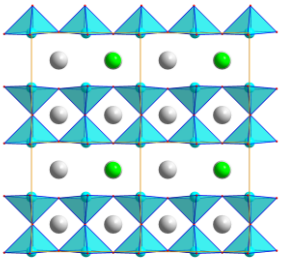

c) oxygen content = 7.5 (III)

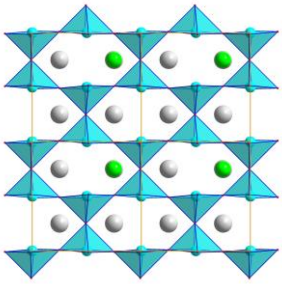

d) oxygen content = 7.25 (I)

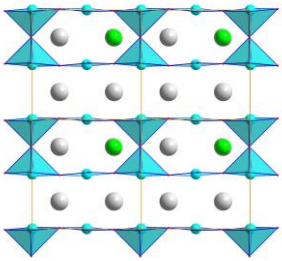

e) oxygen content = 7.25 (II)

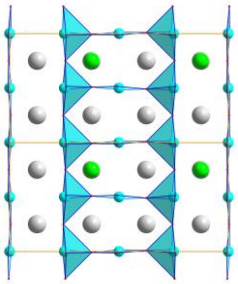

f) oxygen content = 7 (I)

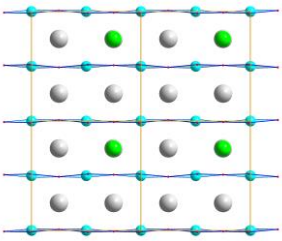

g) oxygen content = 7 (II)

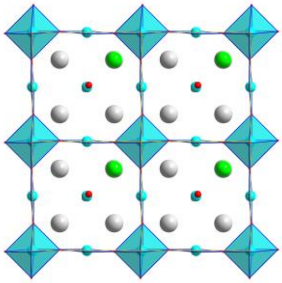

Fig. 8-2. View along *c*-axis on the Cu(1)-O plane with different assumed arrangements of copper and oxygen atoms. This corresponds to the various total oxygen content in the LBCu structure (data visualized for larger, 4 × 4 supercells) [227].

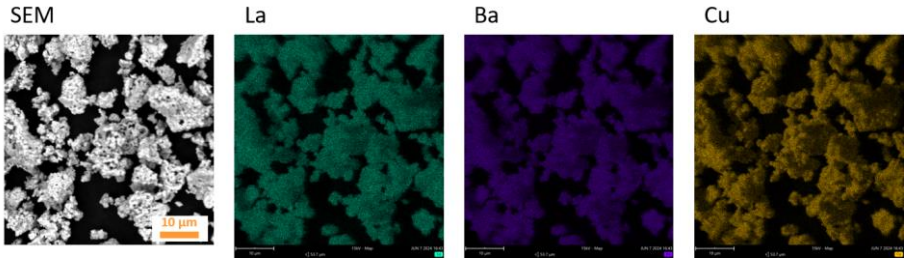

Fig. 8-3. Morphology of the LBCu SG powder together with EDS elemental maps.

In order to characterize the thermal stability of the LBCu material, HT-XRD was conducted and the obtained data were studied in details. As can be seen in Fig. 8-4, the oxide maintains the stable *P*4/*mmm* tetragonal structure up to 900 °C in air, without any impurities detected or phase transitions observed in the whole measurement range. Apparently, the peak positions of the recorded XRD patterns shift to the lower angle area during the heating process, and then move back to the higher angle area on cooling. This is the expected phenomenon, which can be explained by change of the unit cell volume caused by thermal expansion, however, it can also (partially) originate from the oxygen release and the associated chemical expansion in high temperature range. Nevertheless, the observed good thermal stability indicates that the Co-free LBCu material can meet one of the basic requirements as the oxygen electrode in SOCs [228,229].

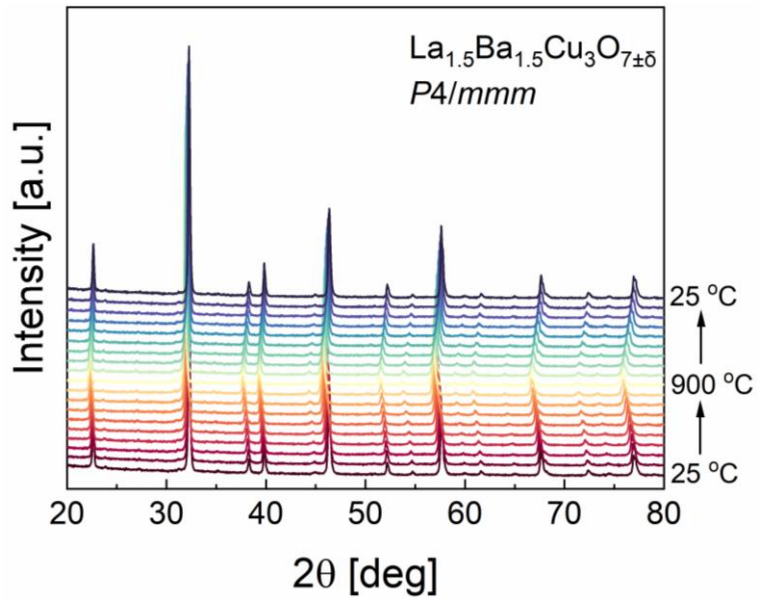

Fig. 8-4. HT-XRD data of LBCu measured in air on heating up to 900 °C and during cooling down to RT [227].

To dig more details from the HT-XRD data, Rietveld refinements can be also conducted upon each of the recorded XRD patterns. With respect to the change of unit cell parameters, both *a* and *c* can be plotted showing their dependence on temperature (Fig. 8-5). A clear linear increase can be seen in the *a* parameter, with only a little bend

at 400 °C. At the same time, parameter *c* shows a more obvious rise after the inflection at 400 °C. This can be ascribed to the mentioned oxygen release and the chemical expansion effect [230]. Accordingly, the more pronounced change along the *c*-axis seems also as a good proof that at elevated temepratures no oxygen is left in the all-lanthanum layers. It can be also stated that the observed anisotropic behavior is expected for the layered-type of the crystal structure.

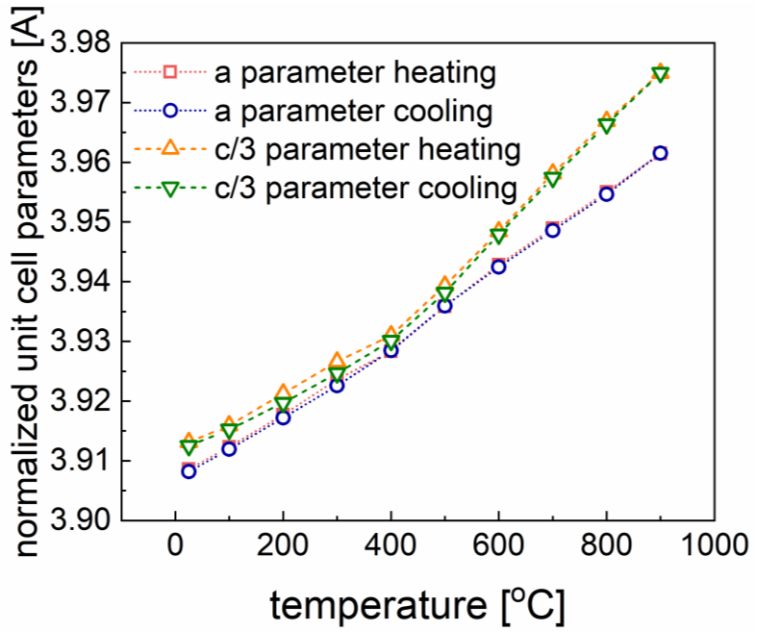

Fig. 8-5. Temperature dependence of the unit cell parameters *a* and *c* in the processes of heating and cooling. Notice normalized (i.e. divided by 3) values of the *c* parameter [227].

Apart from the *a* and *c* parameters, the (linearized) TEC can be derived when the plot of cube root of the relative changes of unit cell volume *V* with the temperature dependence is drawn, as it is shown in Figs. 8-6a and b. In the graphs, the slope of the curve can represent the TEC of the material. It is obvious that during heating and cooling the TEC values are highly comparable. Specifically, the TEC at the low temperature range (RT-400 °C) is about 13.2-13.3·10^{-6} K^{-1}, while at higher temperatures (400-900 °C) is somewhat higher, 18.8·10^{-6} K^{-1}. The values are comparable to other Cu-based oxides [199]. Compared to cobalt-based or cobalt-containing oxides, LBCu shows a big advantage of the mild expansion behavior [231–233]. Additionally, similar value of the average TEC was obtained as equal to 15.5·10^{-6} K^{-1}, up to 900 °C, in the dilatometry measurements. The discrepancy in the values is not surprising, because of different arrangement of the experiment, in which a polycrystalline sinter is tested.

The presented above results suggest that a good thermal match between LBCu and common electrolyte materials, e.g. LSGM and GDC, can be expected, and it should help alleviating the degradation caused by a mismatch in the thermomechanical properties. This may help also with the improved long-term operation [161].

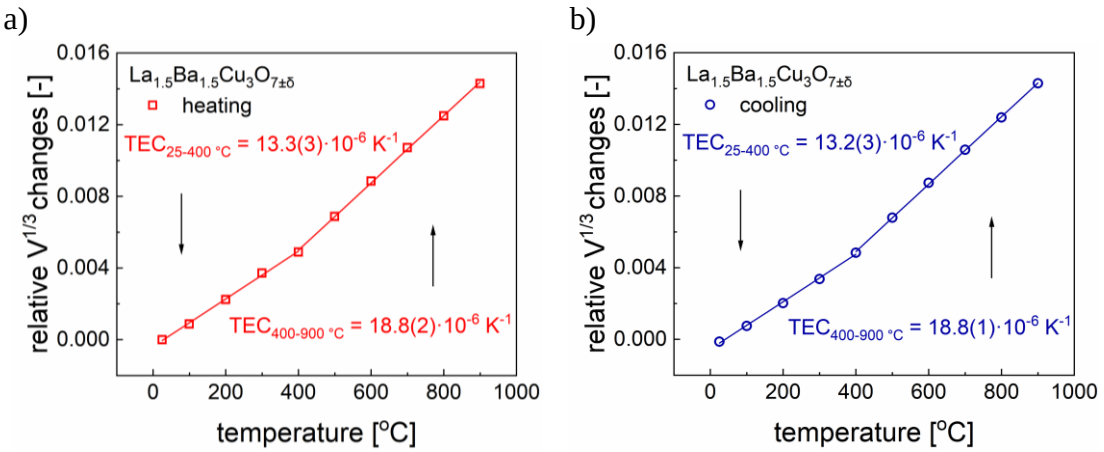

Fig. 8-6. Temperature dependence of the linearized changes of the unit cell volume for LBCu (SG). Data presented on a) heating, and b) cooling.

The characterization of the oxygen content in LBCu is realized via the iodometric titration, from which a value of around 7.23(3) at RT could be established (as mentioned above in the DFT section). From this result, an average oxidation state of copper can be determined as +2.32. Interestingly, when compared to other transition metal elements-based perovskite compositions, e.g. Fe- and Mn-based single perovskite-type oxides, LBCu demonstrate an apparently lower oxygen content, if its formulated in the simplified notation of a single perovskite: $La_{0.5}Ba_{0.5}CuO_{2.41}$ [234,235]. This fact, about the higher oxygen deficiency in LBCu, could potentially facilitate oxygen mobility in the lattice. However, since different oxygen sites are occupied in different manner, the actual improvement cannot be easily predicted.

After that, the thermogravimetric measurements were also carried out in order to obtain more details of the oxygen content change with temperature, also, in different atmospheres (pure oxygen, air, 1 vol.% O_2 in Ar, Ar, and 5 vol.% H_2 in Ar), as it is shown in Fig. 8-7a. In the most reducing conditions of 5 vol.% H_2 in Ar, LBCu decomposes into metallic copper, barium oxide, and lanthanum oxide (as confirmed by the XRD studies). In neutral or oxidizing atmospheres the material exhibits a stable behavior, and a continuous oxygen releasing process is visible above ca. 300 °C. Specifically, the equilibrated oxygen content increases to 7.25, when LBCu is cooled in pure O_2, and decreases to 7.16, if cooled in 1 vol.% O_2 in Ar. This (equilibrated) oxygen content difference between pure O_2 and 1 vol.% O_2 in Ar atmospheres is less pronounced than the oxygen loss in air between RT and 800 °C, which is around 0.33. In fact, the value is comparable to some of Co-containing perovskite materials [236–238], but higher than the changes recorded for $La_4BaCu_5O_{13\pm\delta}$ [199]. Meanwhile, it is necessary to mention that the starting point of the oxygen loss is increased with the decreased oxygen partial pressure (pO_2), e.g. from around 300 °C in pure O_2 to about 335 °C in 1 vol.% O_2 in Ar, and even reaches around 500 °C in Ar. From Fig. 8-7b, it can be easily concluded that the oxygen content decreases more apparently with the increased temperature at the same pO_2 environment, as well as that with the decreased pO_2 at the same temperature. Overall, the behavior can be compared to that of similar Co-based perovskites [239]. However, it

seems that the average charge state of Cu cations may be below +2 at the highest temperature and low pO_2.

Also, as presented in Fig. 8-7c, the slope of curves in the calculated logarithm of relative oxygen vacancies concentration vs. log(pO_2) coordinates can be seen. A rather weak dependence on pO_2 implies that no simple model of the defect formation can be proposed (in agreement with the complex crystal structure), but possibly, some oxygen vacancy disordering may take place, resulting in the enhanced ionic conductivity.

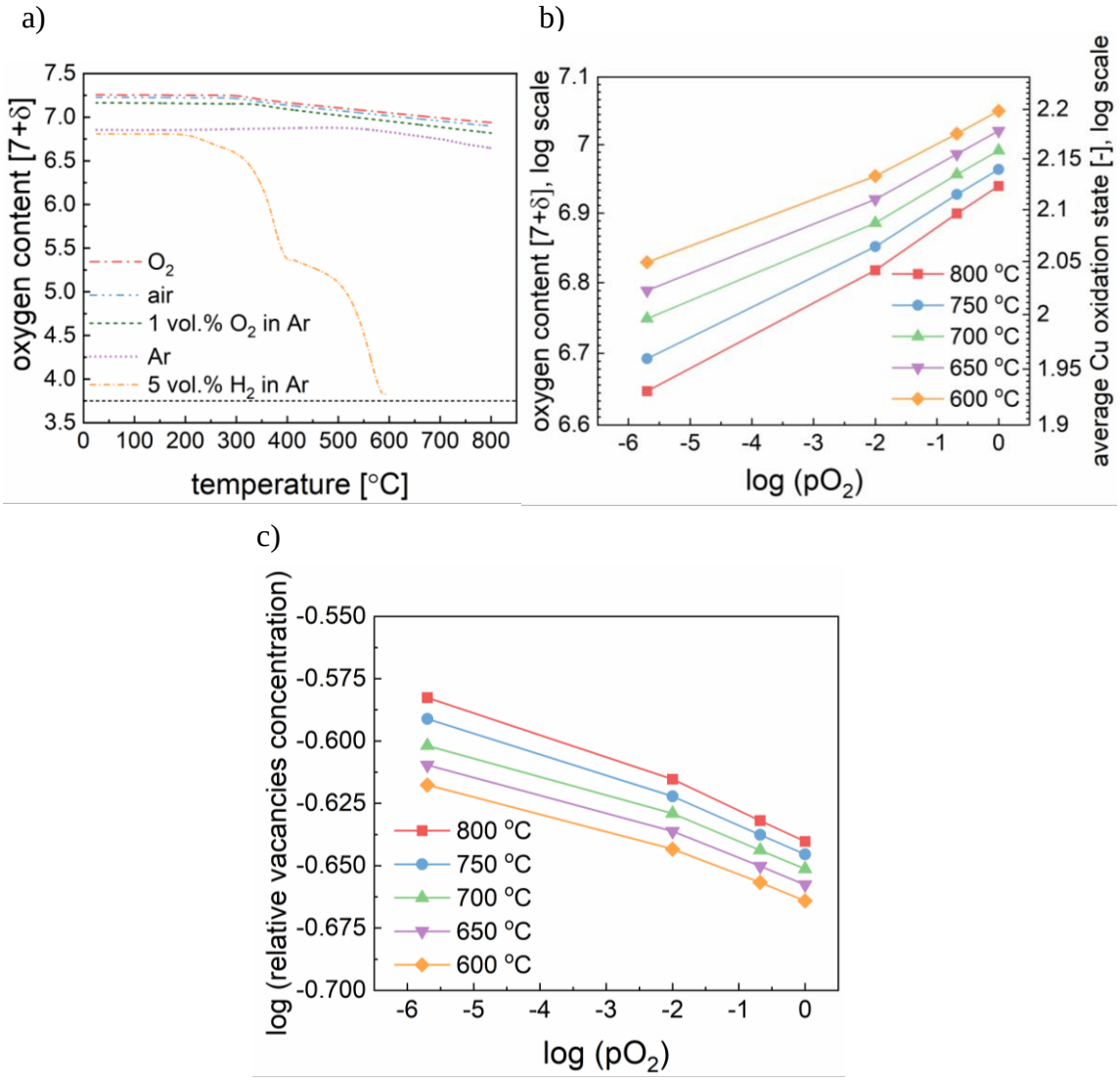

Fig. 8-7. a) Temperature dependence of the oxygen content in LBCu in varied atmospheres (data measured on heating, notice that the initial value at RT is equilibrated), b) the oxygen content as a function of the oxygen partial pressure pO_2 at elevated temperatures, and c) the relative oxygen vacancies concentration as a function of pO_2 at elevated temperatures presented in log-log graph [227].

In addition, Raman spectra were also measured for LBCu samples annealed in air and argon. As it can be seen in Fig. 8-8, there are three peaks identified in the range of 200-

600 cm^{-1} for both samples, which are similar to those reported for $YBa_2Cu_3O_{7-\delta}$ [240]. These three peaks can be attributed to three characteristic modes of vibration, O2+/O3-, O2+/O3+ and O4. More precisely, the modes of O2+/O3- and O2+/O3+ can be attributed to the movement of oxygen alongside the *c*-axis in the Cu-O sheets, while the O4 mode may relate to the apical oxygen present in the pyramids. There is no obvious shift of the peaks after treatment in Ar (more oxygen vacancies), but changes of the intensity of two main peaks are apparent. On one side, it confirms that the structure maintains its stability, but on the other, that the different oxygen content may (to some degree) affect the Raman spectra.

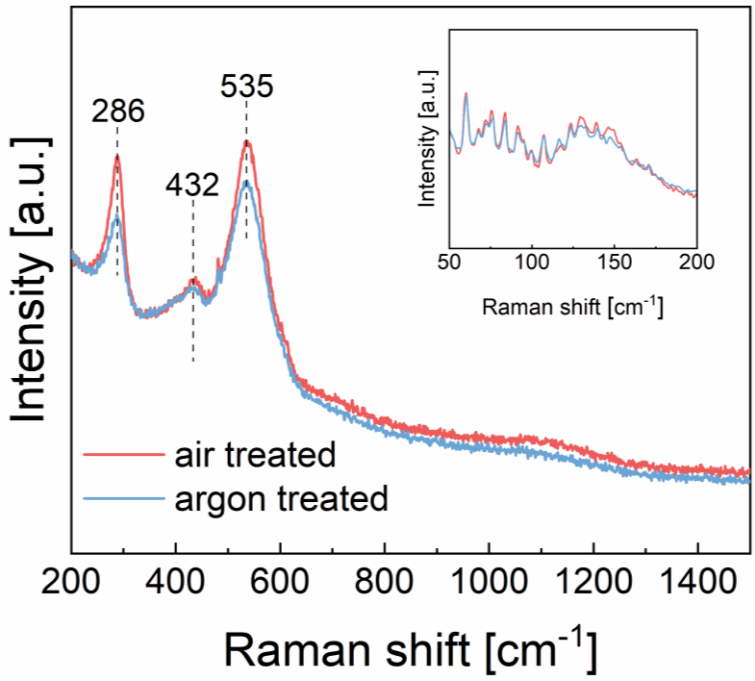

Fig. 8-8. Raman spectroscopy data for LBCu samples annealed in air and in Ar [227].

When it comes to the electrical conductivity measurements (Fig. 8-9a), the it can be noted that values for samples originating from two preparation methods share similar starting and ending points, around 57 S cm^{-1} at RT, and 14 S cm^{-1} at 900 °C, respectively. However, the SG sample reaches a maximum value of 75 S cm^{-1}, while the SS sample reaches only 68 S cm^{-1} at around 300 °C. Such difference may stem from the difference of the microstructure and porosity of samples, which has impact on the rate of the oxygen releasing. For example, fine powder, which can be obtained via the SG method results in a higher relative density during the sample's pressing and sintering. Overall it means that in the measuring conditions at a particular temperature both samples may exhibit somewhat different oxygen content, which affects the recorded values. Nevertheless, the effect is small.

It is also interesting in Fig. 8-9b that an activated-like conductivity behavior can be seen in the lower temperature range, nonetheless, it is not linear in the graph. Taking into account that oxygen starts being released above 300 °C in air (Fig. 8-7a), this phenomena

can be ascribed to the change of the mobility of charge carriers (as opposed to variation of their concentration) [241]. In the temperature rage above 300 °C, the conductivity falls dramatically, which is the consequence of the reduced concentration of the electronic holes (related to Cu^{3+}), as well as the broken conduction chains of -Cu-O-Cu- due to the increased content of the oxygen vacancies. Similar behavior has been found in many mixed ionic-electronic conducting perovskite-type oxides [150,242]. However, it is still worth mentioning that the total conductivity values are above 10 S cm^{-1}, which should be sufficient in practical application of IT-SOCs.

Concerning the ionic component of the conductivity, with the intrinsic partial disorder of the oxygen sublattice, along with the appearing additional oxygen vacancies in the relatively low temperature range (e.g. above 300 °C), the mobility of such ionic defects can be assumed as high at higher temperatures. This is expected to help achieving the desirable catalytic activity level [243].

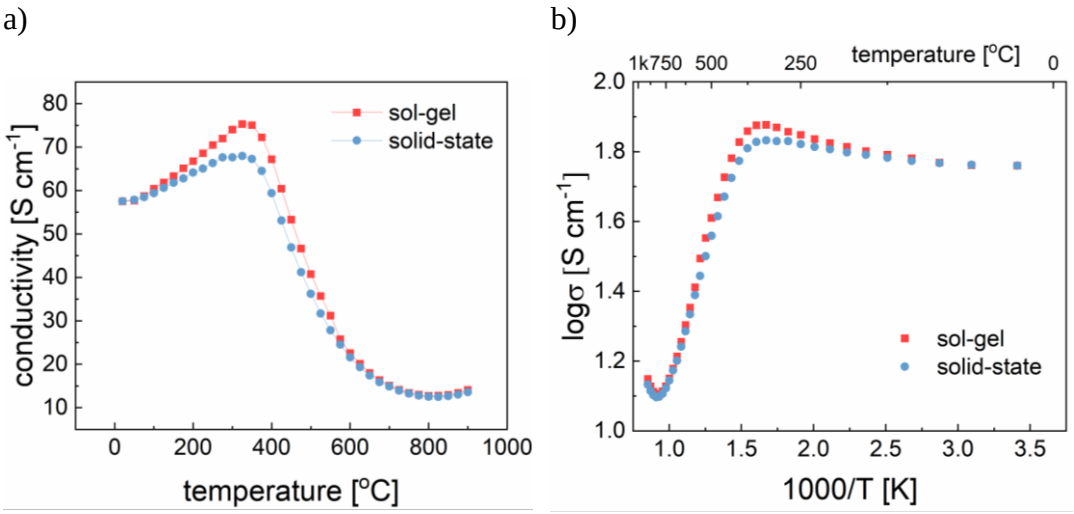

Fig. 8-9. Temperature dependence of the a) total electrical conductivity in air, and b) with data presented in Arrhenius-type coordinates of LBCu synthesized by two methods. Based on [227].

The chemical compatibility is actually very crucial when long-term operation of SOCs is prioritized. As already mentioned, the initially considered and selected electrolyte materials are LSGM, LDC and GDC20 [244–246]. When the LSGM is mixed with LBCu and annealed at 900 °C for 2 h, no additional reflections could be detected in the XRD patterns (Fig. 8-10a), but the two sets of peaks representing crystal lattice of both materials are highly-overlapped and almost undistinguishable. This could either mean strong reactivity or oppositely, may be explained by the very similar unit cell parameters and symmetries, yielding a single-phase like diffractogram. To get a deeper insight of this phenomenon, further XRD measurements were carried out at high temperatures. As it is shown in Fig. 8-10b, emergence of secondary phases can be seen at 975 °C, and this phase still exists after cooling down to RT. However, the XRD patterns of the LBCu/LSGM mixture still appear as a single-phase like material at lower temperatures. When the angular range is magnified to 30-34 deg (Fig. 8-10c), the main peak appears rather as

resulting from highly-overlapped two reflections. Also, the one corresponding to LBCu shifts faster with temperature, from the right shoulder of the overlapped main peak to the left shoulder, analyzing data from RT to 900 °C. This can be interpreted as resulting from a fact that the TEC of LBCu is higher than that of LSGM. Overall, it can be therefore stated that these two materials are chemically compatible up to 900 °C. Also, the data possibly indicate favorable conditions of the interface formation between the phases, which may help with preparation of the electrode layers.

Besides, further evaluation of the chemical stability of LBCu with LSGM are implemented in order to confirm the long-term mutual compatibility at 800 °C for 100 h (Fig. 8-10a). The obtained satisfactory data are comparable to those reported previously for $La_4BaCu_5O_{13\pm\delta}$ [199]. Nevertheless, when it comes to compatibility with LDC and GDC20 (Figs. 8-10d and e, respectively), secondary phases the appearing, which indicates that there is indeed reactivity going on between LBCu and these two electrolyte materials, making them unsuitable in the long run. Notably, the long-term thermal stability experiment for LBCu in highly-oxidizing atmosphere (pure oxygen) was also conducted (Fig. 8-10f), which shows no additional reflections emerging and no changes of other structural features after 100 h annealing at 800 °C. All the abovementioned facts suggest that LBCu possesses good chemical compatibility with LSGM, and sufficient stability in either air or oxygen atmosphere. While the electrode sintering temperature should be limited to 900 °C, stable long-term operation can be expected.

As a summary to this chapter, it can be stated that all the acquired data on the physicochemical properties of $La_{1.5}Ba_{1.5}Cu_3O_{7\pm\delta}$ indicate that the proposed and developed oxide can be a promising oxygen electrode candidate material for IT-SOCs based on LSGM electrolyte, fulfilling typically considered requirements.

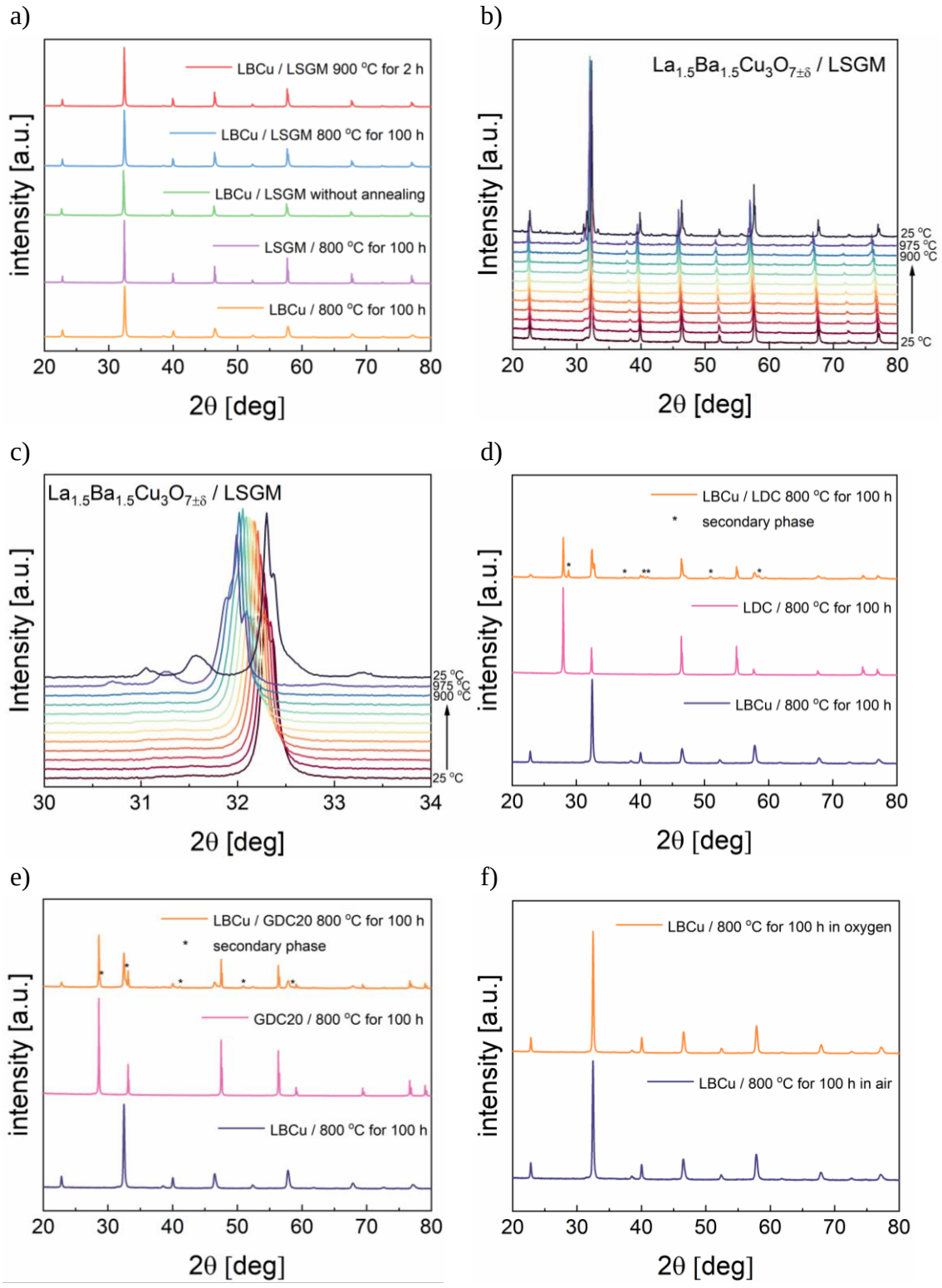

Fig. 8-10. Results of structural studies for the annealed in different conditions mixtures of LBCu and selected solid electrolytes. a) XRD data for LBCu-LSGM, b) HT-XRD data for LBCu-LSGM, c) magnified range of HT-XRD data for LBCu-LSGM, d) XRD data for LBCu-LDC, e) XRD data for LBCu-GDC20, and f) XRD data for LBCu annealed in pure oxygen.

9. Physicochemical properties of $GdBa_{0.5}Sr_{0.5}Co_{2-x}Cu_xO_{5+\delta}$

Regarding the second considered system of the candidate oxygen electrode materials, i.e. $GdBa_{0.5}Sr_{0.5}Co_{2-x}Cu_xO_{5+\delta}$ series, similar measurements, needed to determine physicochemical properties of the materials relevant concerning the application, were conducted. In this work, x values equal to or greater than 1 were considered, as one of the aims is to minimize usage of the toxic and expensive cobalt, however, reference materials with higher cobalt content were also studied in some cases.

Data on the initial crystal structure characterization of the as-synthesized $GdBa_{0.5}Sr_{0.5}Co_{2-x}Cu_xO_{5+\delta}$ ($x \geq 1$), carried out via the XRD studies at RT, are gathered in Fig. 9-1. As can be seen in Figs. 9-1a and b, for the selected four compositions in $1 \leq x \leq 1.15$ doping range, the A-site ordered, layered structure named as the double perovskite-type one, can be positively identified. The respective symmetry is tetragonal *P*4/*mmm*, which is the aristotype structure for such ordered perovskites [151]. Besides, the same symmetry can be also confirmed in the other obtained samples when x ranges up to 1.6. However, the secondary phase that is possibly related to the orthorhombic triple perovskite structure emerges if x is in the range of 1.2-1.6. Further increasing the copper doping results in high amount of impurities, which effect is clearly visible in Fig. 9-1c. Thus, it is worth noting that compositions, which are practically phase-pure, can be obtained in the x range of 1-1.15 (a tiny amount of the contamination detected in GBSCC085115 can be neglected [247]. The observed behavior may be due to the decreased oxygen content with the increased copper substitution (Tab. 9-1), which suggests that the higher copper doping amount may exceed the limit of the solid solution formation. Importantly, single-phase materials are more interesting for evaluation of their physicochemical properties, as in this case it is possible to relate the measured characteristics to the chemical composition and structure.

Tab. 9-1. The evaluated oxygen content in the GBSCC samples at RT. Data from the iodometric titration. The error values do not exceed ±0.01 [248]. GBSCC1505 oxide is given as a reference.

composition	oxygen content (5+δ)
GBSCC1505	5.59
GBSCC1010	5.64
GBSCC095105	5.61
GBSCC0911	5.52
GBSCC085115	5.49

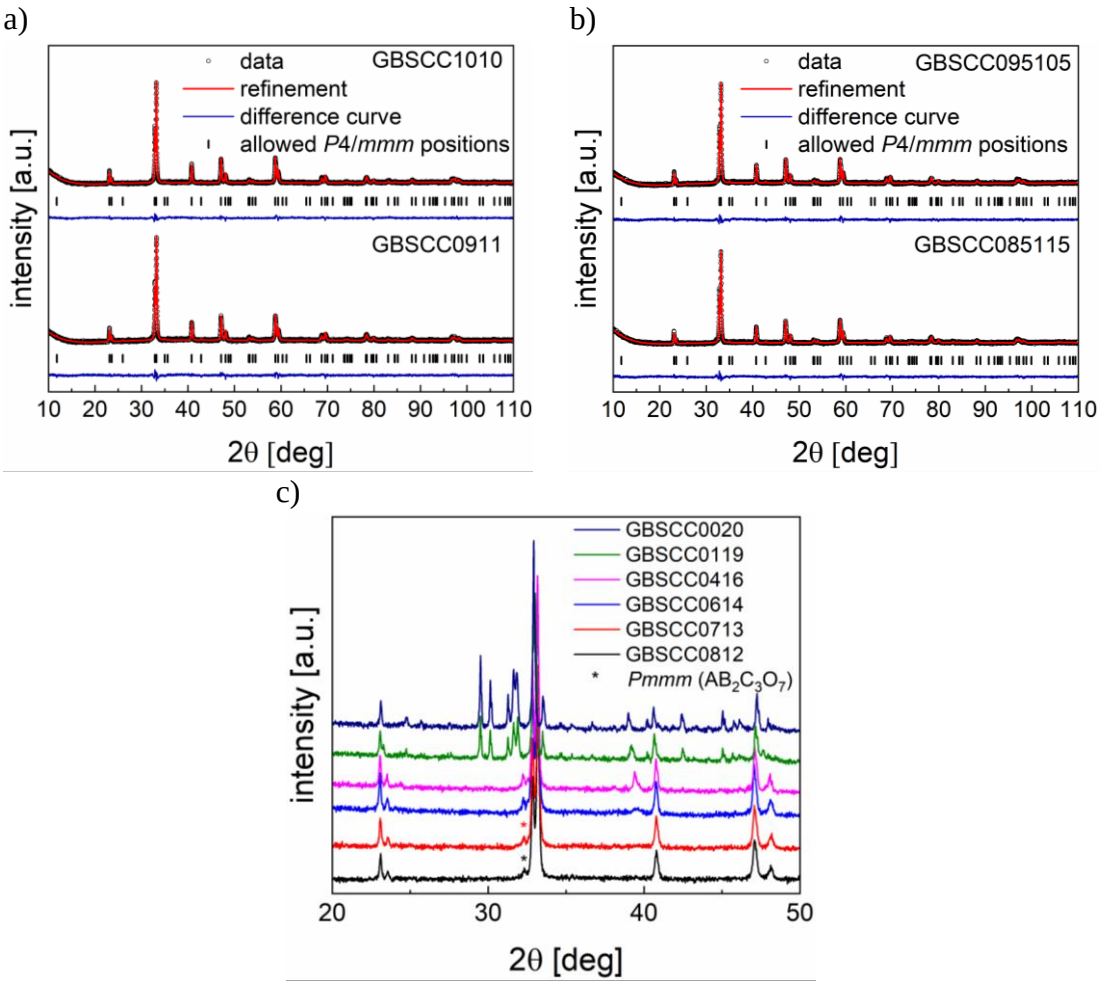

Fig. 9-1. XRD data for a) GBSCC1010 and GBSCC0911, and b) GBSCC095105 and GBSCC085115 samples recorded at RT, together with the respective Rietveld refinements. c) XRD data measured for other GBSCC samples (x = 1.2-2) at RT. Based on [248].

When focusing on the refined values of the unit cell parameters *a* and *c*, their dependencies on the copper doping amount is surprisingly weak (Fig. 9-2a, Tab. 9-2). The changes are less pronounced than for the case of doping with other transition metal elements, e.g. Fe [249,250], Mn [251] or Ni [252]. At the same time, when the ionic radii at the B-site are taken into account, 0.61 Å and 0.53 Å for Co^{3+} and Co^{4+}, respectively (both at the high spin state in 6-fold coordination), as well as 0.73 Å and 0.54 Å for Cu^{2+} and Cu^{3+}, respectively (both in 6-fold coordination) [253], alongside the oxygen content (Tab. 9-1), it can be understood that the couple of Co^{3+}/Co^{4+} is partially replaced by Cu^{2+}/Cu^{3+}.

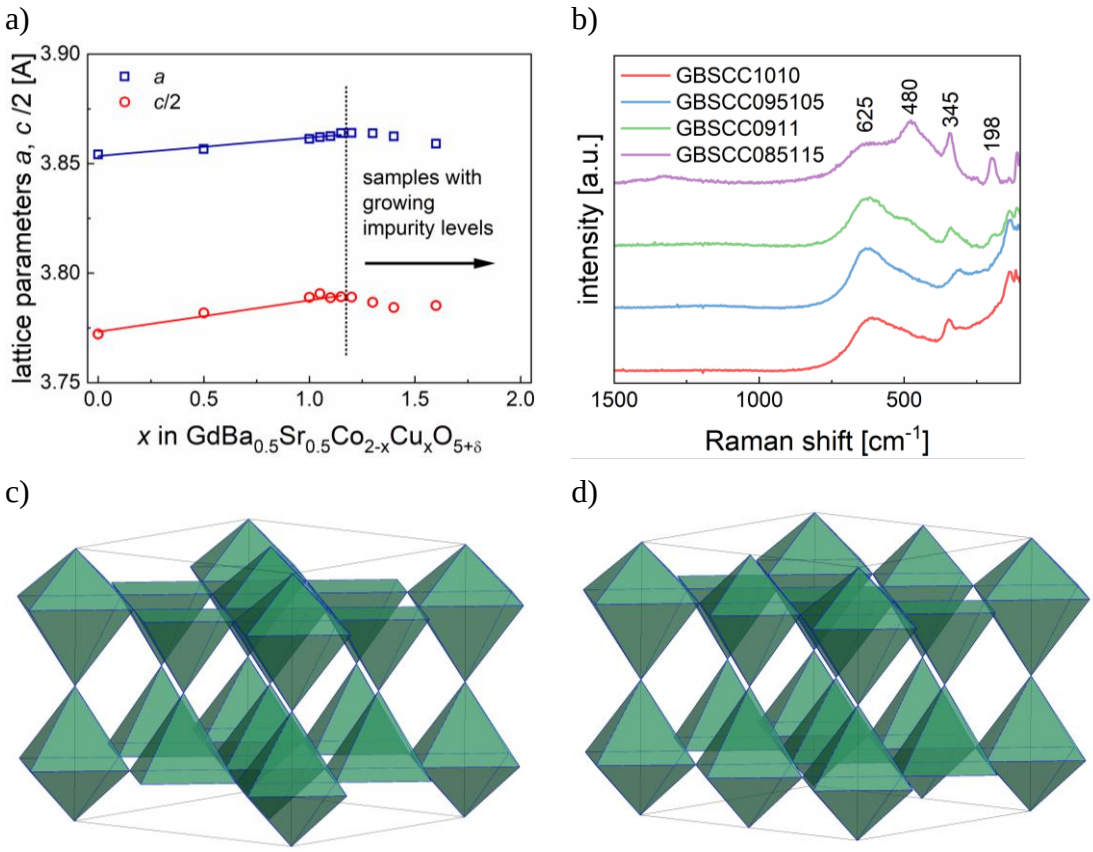

Fig. 9-2. a) Unit cell parameters dependence on the copper doping level in $GdBa_{0.5}Sr_{0.5}Co_{2-x}Cu_xO_{5+\delta}$ series. b) Raman spectroscopy data for the selected GBSCC materials. Simplified models of possible different oxygen arrangements in the *a*-*b* plane associated with Gd, with maintaining $\delta = 0.5$. Only (Co, Cu)O_5 and (Co, Cu)O_6 polyhedra are shown: c) only octahedra-pyramids connections are present in the cell, d) all, pyramids-pyramids, octahedra-octahedra, and mixed connectivities are possible. Based on [248].

Tab. 9-2. The refined structural parameters of the selected GBSCC materials [248].

Composition	Unit cell parameter *a* [Å]	Unit cell parameter *c* [Å]	Unit cell volume *V* [Å^3]	O (0.5,0,*z*) *z* value	R_{wp} [%]
GBSCC1505	3.8566(1)	7.5637(1)	112.50(1)	0.210	1.9
GBSCC1010	3.8625(1)	7.5809(1)	113.10(1)	0.209	2.3
GBSCC095105	3.8629(1)	7.5812(2)	113.13(1)	0.208	2.6
GBSCC0911	3.8633(1)	7.5799(2)	113.13(1)	0.218	2.5
GBSCC085115	3.8640(1)	7.5784(2)	113.15(1)	0.215	2.7
	3.8654(1)[1]	7.5757(2)[1]	113.19(1)[1]	0.217[1]	2.8[1]

[1] GBSCC085115 is sintered twice at the same condition.

The Raman spectroscopy can also unveil more details related to the crystal structure of GBSCC. As shown in Fig. 9-2b, there are 4 peaks identified among the selected

compositions. The main and most obvious peak that appears at 625 cm^{-1} may be understood as the bond stretching movement of the oxygen that is linking the octahedra and pyramids in the *a*-*b* plane, as discussed previously in the literature report [254]. The signal at 480 cm^{-1} seems to related to the oxygen linking only pyramids. As presented in Figs. 9-2c and d, this can be visualized in a form of two simplified models, in which the oxygen vacancies are arranged in a different way. Likely, the assumed structural modification toward the Fig. 9-2d model, as can be inferred by the emergence of the 480 cm^{-1} signal with the increasing Cu content, is the reason why the parameter *c* shows an nonlinear tendency in the considered range of doping (Fig. 9-2a). Additional Raman signal can be also identified, the peak at 345 cm^{-1} is likely related to the vibration of Cu/Co. The signal marked at 198 cm^{-1} remains unclear.

The SEM observations were also done in order to show micro-morphology and homogeneity of the obtained samples, as presented in Figs. 9-3a-d for the considered samples. It is quite clear that all the samples synthesized by the SG method demonstrate good homogeneity in terms of cations distribution, without undesirable segregation observed. Taking the particle size into account, these as-synthesized powers are suitable for making electrode layers for the electrochemical characterization (micrometer size grains comprising agglomerated smaller particles).

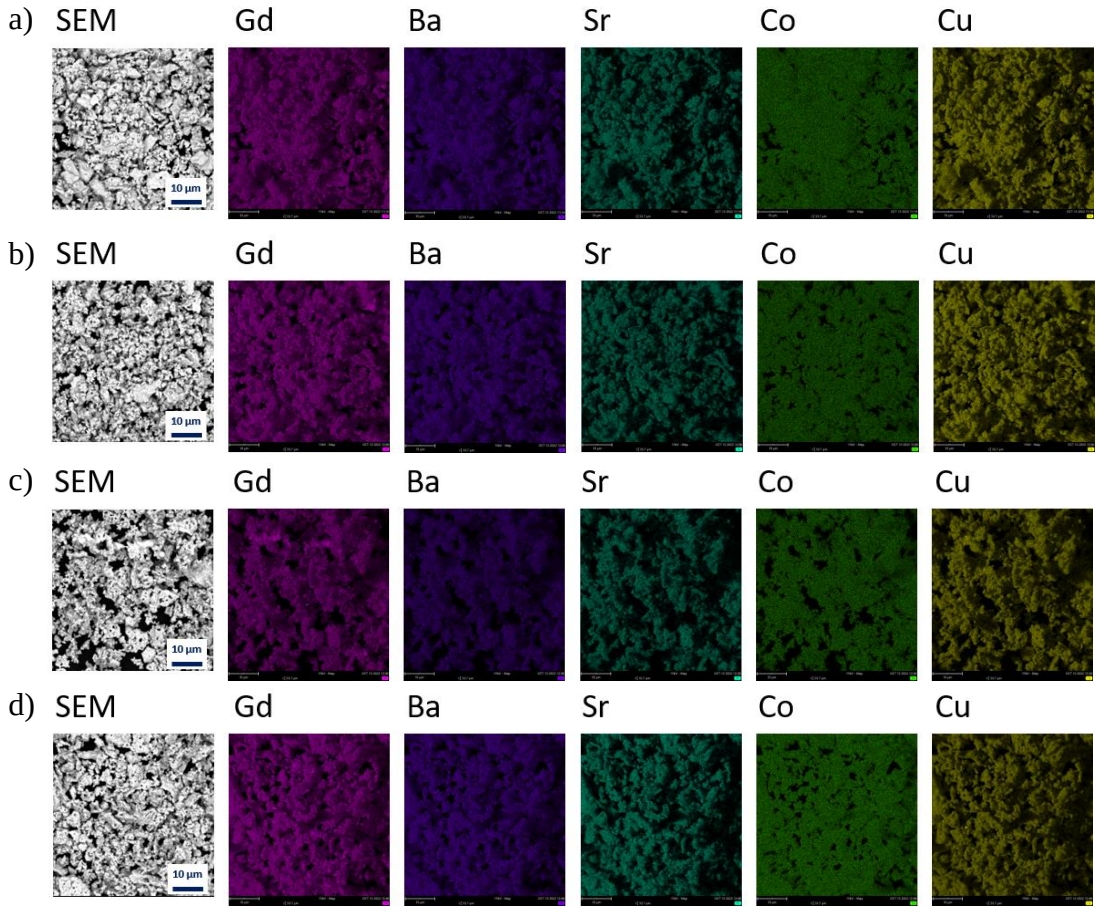

Fig. 9-3. Morphology of the a) GBSCC1010, b) GBSCC095105, c) GBSCC0911, and d) GBSCC085115 powders, together with respective EDS elemental maps.

Regarding thermal stability at high temperatures, as it was already discussed in the previous chapter, HT-XRD technique can provide valuable information. As can be seen in Figs. 9-4a-d, all the samples exhibit stable behavior and maintain tetragonal symmetry up to 1000 °C in air (data measured with an interval of 100 °C). Also, the results obtained on cooling show perfect repeatability down to RT. No secondary phases were observed in any of the measured diffractograms, implying the GBSCC system ($1 \leq x \leq 1.15$) possesses the adequate thermal stability and fulfills the basic requirements regarding the manufacturing of the electrodes and cell operation.

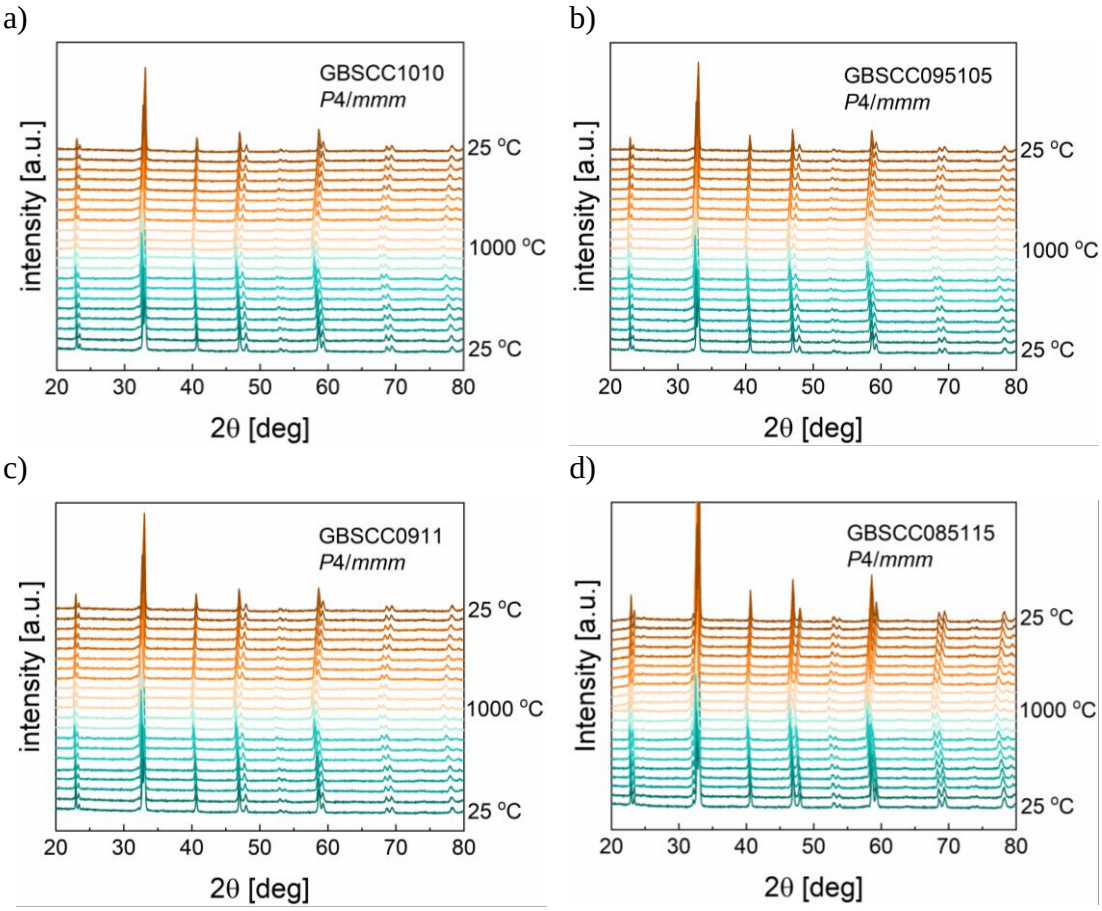

Fig. 9-4. HT-XRD data recorded for a) GBSCC1010, b) GBSCC095105, c) GBSCC0911, and d) GBSCC085115 materials in air on heating and cooling. Based on [247] and [248].

All the obtained diffractograms were analyzed by the Rietveld method, which enabled deriving changes of the unit cell parameters as a function of temperature (Figs. 9-5a-d). Both parameters of *a* and *c* exhibit monotonous and linear-like rising with the increase of temperature in all samples. Although the slopes of either *a* or *c* are not inflecting considerably at higher temperatures, this effect is visible in all the samples. It can be interpreted as originating from the physical (thermal) and chemical expansion [255,256]. It is also clear that these inclined curves of *a* or *c* show similar increase in all four samples, indicating that the TEC values are similar for the considered materials.

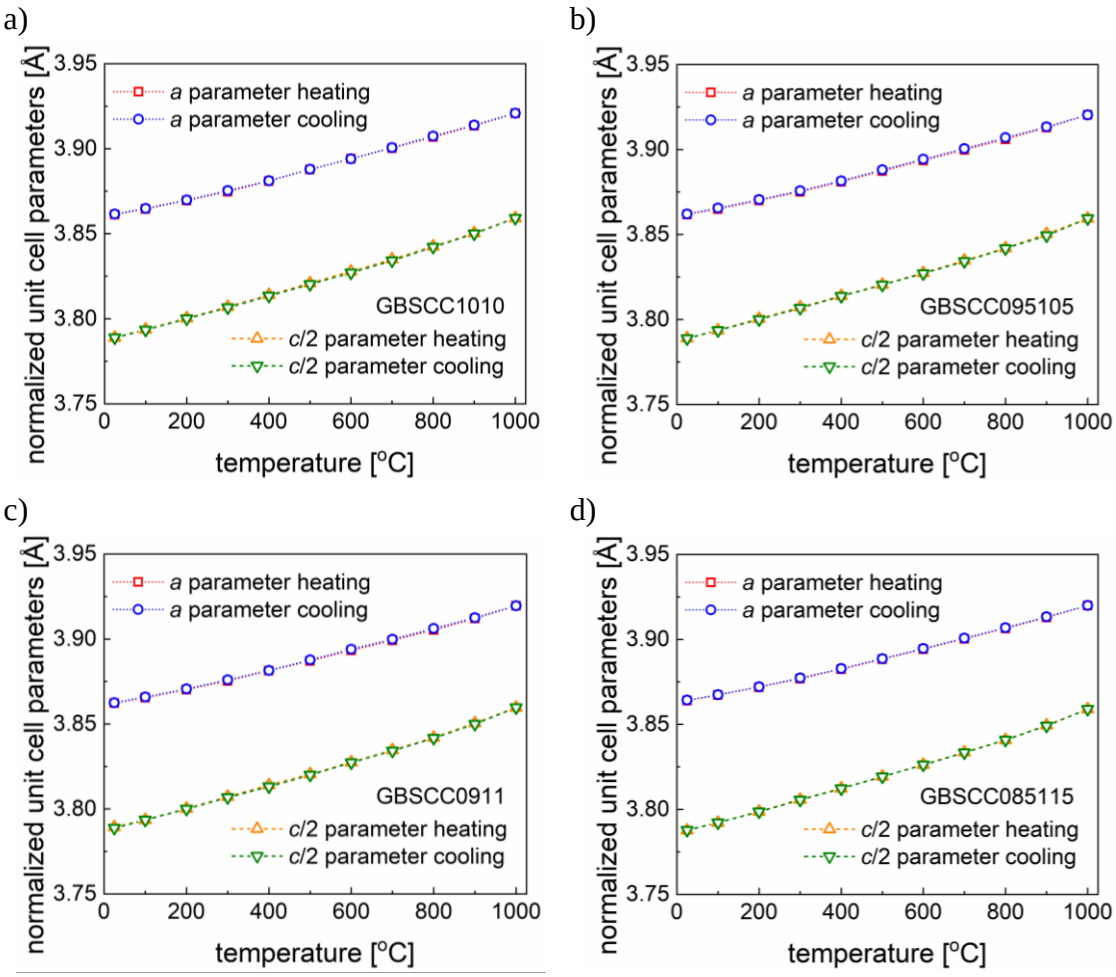

Fig. 9-5. Derived from Rietveld refinements unit cell parameters dependence on temperature for a) GBSCC1010, b) GBSCC095105, c) GBSCC0911 and d) GBSCC085115 samples. Data on heating and cooling based on [247] and [248]. Notice normalized values for the *c* parameter for easier comparison with the *a* parameter.

In Figs. 9-6a-h, the calculated TEC values, separately on heating and cooling are presented for all samples, as derived from the HT-XRD data. As expected, TEC values in both, the low temperature range (RT-300 °C) and the high temperature range (300-1000 °C) are quite comparable among the samples, specifically, showing values of around $14 \cdot 10^{-6}$ K^{-1} and $17\text{-}18 \cdot 10^{-6}$ K^{-1}, respectively. It can be stated that the differences on heating and cooling are negligible. When compared to other Co-based double perovskite-type oxides [250,257], and in the GBSCC system itself, a conclusion can be drawn that copper doping indeed improves the thermal expansion behavior (lowers TEC values, especially ah higher temperatures). This is favorable in cell manufacturing and operation. The behavior is linked with changes of the oxygen content with temperature in the studied perovskites, as shown below.

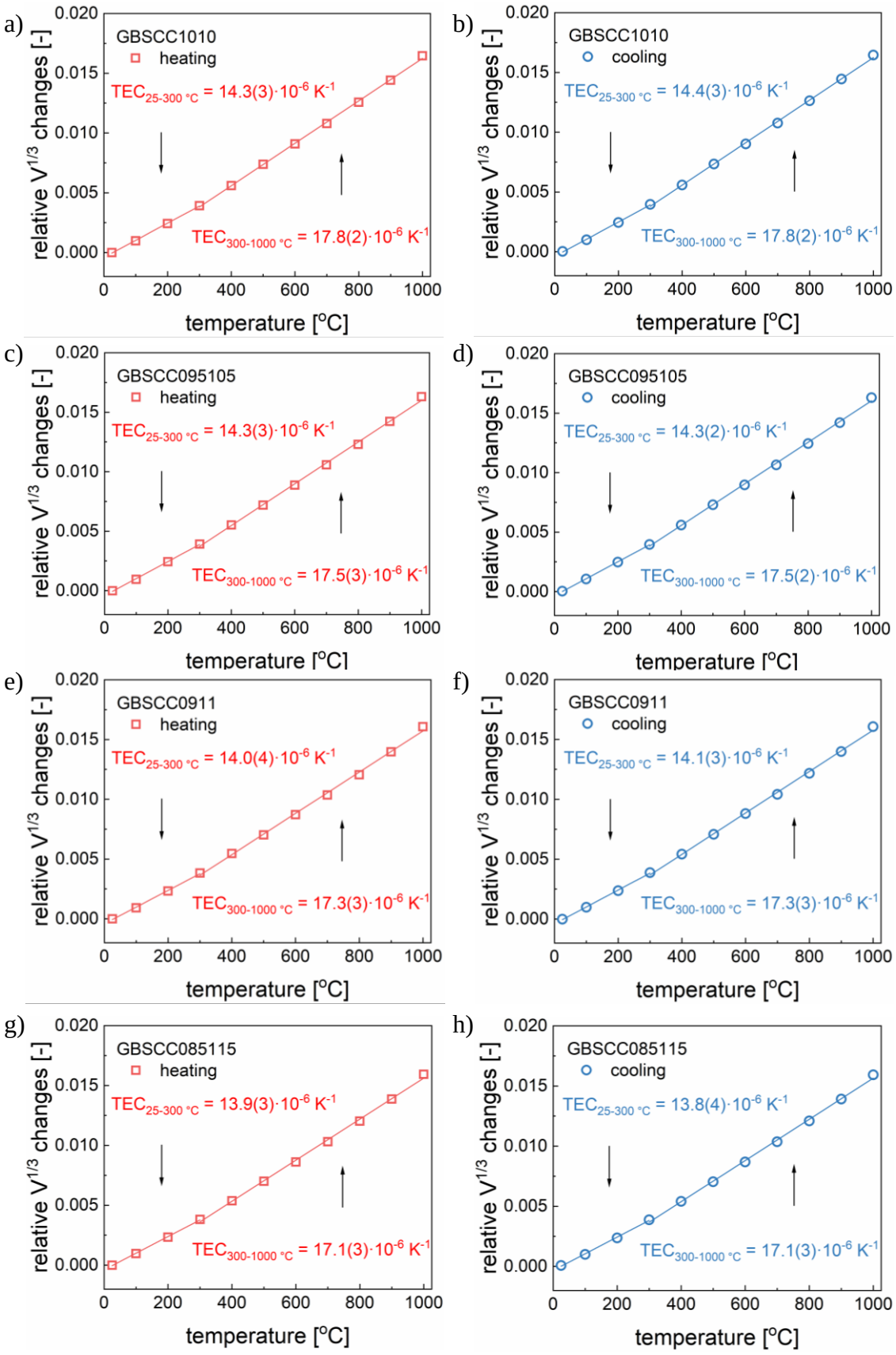

Fig. 9-6. Calculated TEC values of a) and b) GBSCC1010, c) and d) GBSCC095105, e) and f) GBSCC0911, and g) and h) GBSCC085115 samples.

As previously briefly discussed and shown in Tab. 9-1, the equilibrated oxygen content at RT in the series varies with the Cu substitution level. Those results were carried out by the iodometric titration. Measured data indicated a decreasing tendency for the oxygen content with higher copper amount in the materials, if x is in the range of 1-1.15. The information about the oxygen content is crucial, as it enables related discussion of the average oxidation state of Co/Cu present at the B-site. As discussed previously, the average oxidation state of Co (in perovskite type oxides) is more likely to be between +3 and +4, while +2 is preferable in the case of Cu, but +3 state is also possible [189,258]. For example, taken into account the oxygen content in GBSCC1010, the average oxidation state of Co/Cu can be calculated as +3.14, implying therefore presence of the mixed states of $Co^{3+/4+}$ and $Cu^{2+/3+}$. Obviously, the mixed charge states should allow maintaining the electroneutrality in the material. When it comes to GBSCC0911, a lower oxidation state is obtained, +3.02, while it is even under +3 in the case of GBSCC085115 (at RT). The possible conclusion therefore is that the average oxidation state of Co is higher than +3.5, while lower than +2.5 for Cu in the studied GBSCC system. Interestingly (and not fully explained at this stage), a lower oxygen content is obtained in the GBSCC1505 sample, as compared to other high Co-content perovskite counterparts [169].

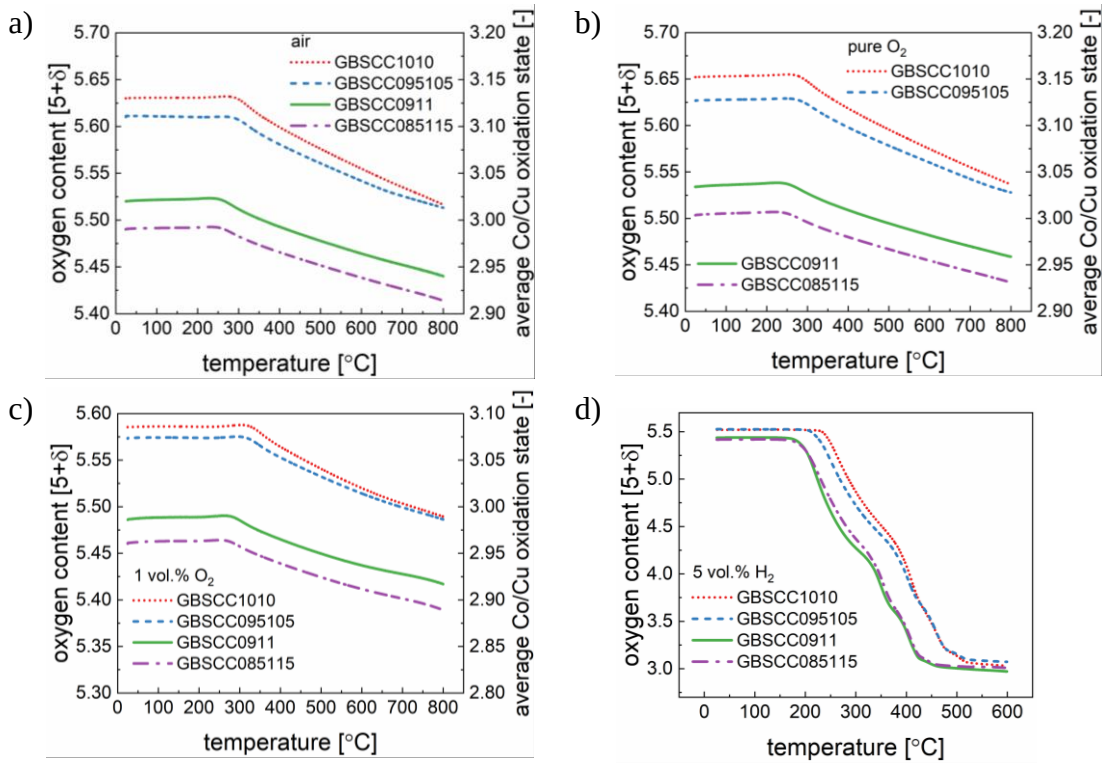

Fig. 9-7. Recalculated from the TG data temperature dependences of the oxygen content in a) air, b) pure oxygen, c) 1 vol.% O_2 in Ar, and d) 5 vol.% H_2 in Ar (decomposition) for the considered GBSCC system. Based on [248].

Because of the importance from a point of view of the application, and aiming at the better understanding of the properties, the oxygen content variation with temperature was also measured by usage of the thermogravimetric analysis. The studies were carried out for the considered for samples in different atmospheres. Data presented in Fig. 9-7a is prepared taking the initial oxygen content (at RT) from results obtained by the iodometric titration. As can be clearly seen, all samples show oxygen release process (additional oxygen vacancies generation), with an interesting tendency that the onset of the oxygen release starts (in most of the cases) at lower temperatures in materials with higher copper doping. Similarly as in air, the oxygen release process can be also observed in both, pure oxygen and 1 vol.% O_2 in Ar (Figs. 9-7b and c). As for the decomposition occurring in 5 vol.% H_2 in Ar, the final products can be detected as mixtures of metallic and oxide phases. The obtained average oxygen content being equal to ca. 3 at 600 °C reflects well the expected value coming from the decomposition process.

Based on the thermogravimetric analyses along with the iodometric titration measurements, it is also interesting to implement the DFT calculations that can simulate the as-built $GdBa_{1-y}Sr_yCo_{2-x}Cu_xO_{5.5}$ models (Fig. 9-8), and refer them to the experimental results.

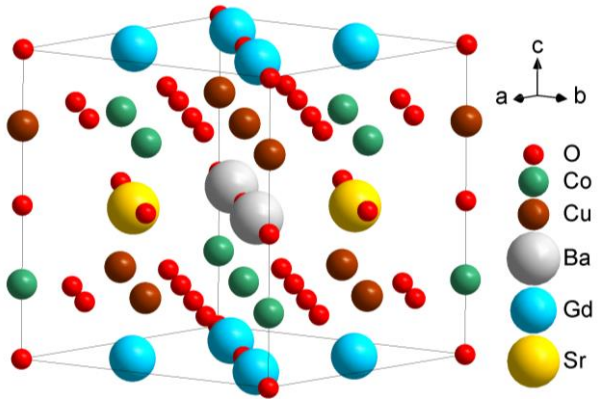

Fig. 9-8. A representative supercell of $GdBa_{0.5}Sr_{0.5}CoCuO_{5.5}$, created by doubling of the *P*4/*mmm* unit cell along the x- and y-axis. The exact formula in the supercell is $Gd_4Ba_2Sr_2Co_2Cu_2O_{22}$. A way of substitution of cobalt (green) by copper (brown) is also presented. Notice vacant sites location, simulating the oxygen vacancies.

As it can be seen in Figs. 9-9a-d, the 2D contour graphs show the related calculated results in terms of unit cell parameters and volume *a*, *c*, *V* and the total VASP energy, respectively. It is worth mentioning that the *x*-axis and *y*-axis in those figures are referred to the strontium and copper doping content, respectively. Colors of red and blue represent the highest and lowest values of a given parameter, correspondingly. In order to proceed the whole calculations in a simpler way, it is reasonable to assume that all the considered $GdBa_{1-y}Sr_yCo_{2-x}Cu_xO_{5.5}$ maintain the same crystal structure and symmetry. As for the parameter *a*, it is found to increase with the higher copper and barium contents, which can be understood by the difference of ionic radii [253].

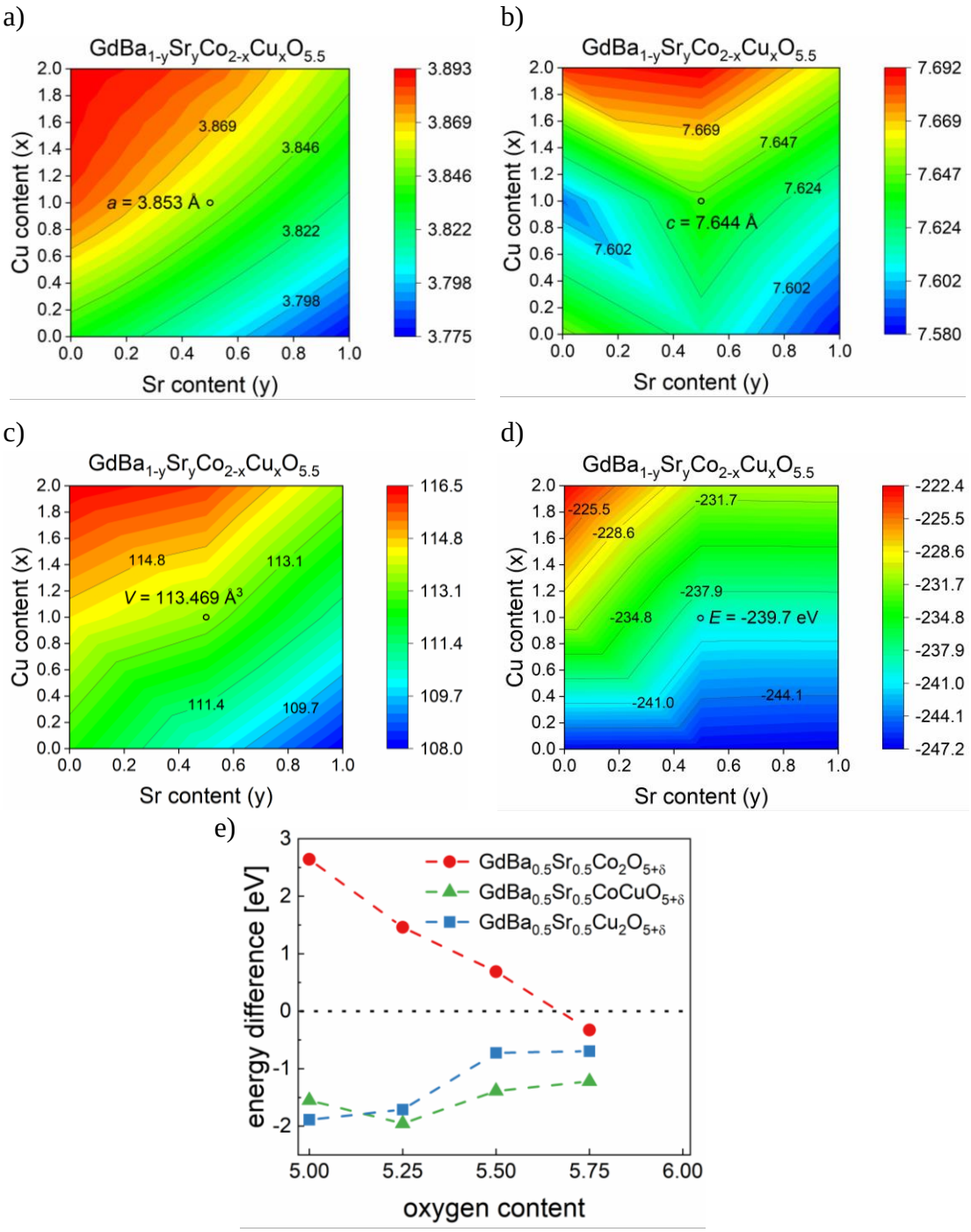

Fig. 9-9. DFT-derived unit cell parameters or volume: a) *a*, b) *c* and c) *V* as a function of Sr and Cu content in $GdBa_{1-y}Sr_yCo_{2-x}Cu_xO_{5.5}$, d) calculated total VASP energy (eV for the unit cell), and e) calculated energy difference between $GdBa_{0.5}Sr_{0.5}Co_{2-x}Cu_xO_{5+\delta}$ and materials with different oxygen content, with the energy of the released oxygen taken into account. The minimum represents the most stable configuration. Please note that the same structural model was used for all calculations, despite the fact that Cu-rich compositions could not be obtained as phase-pure. Based on [248].

The calculated value of *a* equal to 3.853 Å for $GdBa_{0.5}Sr_{0.5}CoCuO_{5.5}$ is in good accordance with that obtained from the experimental data, 3.8625(1) Å for GBSCC1010 (Tab. 9-2). Speaking of the parameter *c*, another low value zone can be seen in the middle copper content area, apart from the expected one in right-side bottom (originating from the ionic radii differences). Also, the obtained value *c* for $GdBa_{0.5}Sr_{0.5}CoCuO_{5.5}$, 7.644 Å, is higher than the experimental one, equal to 7.5809(1) Å. This might be due to the simplified model, which was adopted, especially regarding non-random placement of the oxygen vacancies. Nevertheless, the volume of the unit cell (Fig. 9-9c) shows the similar tendency as that in the experimental data (Tab. 9-2). Importantly, the used DFT method was proven to be quite successful in simulating the actual GBSCC system, when compared to other literature works (Tab. 9-3).

Tab. 9-3. The comparison of structural data for different GBSCC compositions derived from DFT calculations and experiments.

Material	Calculated		Experimental		Reference
	a [Å]	*c* [Å]	*a* [Å]	*c* [Å]	
$GdBaCo_2O_{5.5}$	3.76(1)	7.58(1)	3.8534	7.5318	[259]
	3.8363	7.6497			this work
$GdBaCo_2O_{5.5}$	3.838	7.676	3.88	7.542	[260]
$GdBaCoCuO_5$			3.875(2)	7.587(8)	[261]
	3.8830	7.5934			this work
$GdBa_{0.6}Sr_{0.4}Co_2O_{5.79}$			3.856	7.546	[169]
$GdBa_{0.4}Sr_{0.6}Co_2O_{5.83}$			3.840	7.549	[169]
$GdBaCoCuO_{5.643}$			3.894	7.604	[262]
$GdBa_{0.5}Sr_{0.5}CoCuO_{5.662}$			3.866	7.576	
$GdBa_{0.5}Sr_{0.5}CoCuO_{5.64}$			3.8625(1)	7.5809(1)	this work

As depicted in Fig. 9-9d, the most stable formula (with the lowest energy) should occur from compositions with the high cobalt and strontium content. But this can be somewhat modified by the oxygen content. When it comes to the VASP energy for the unit cell, a lower energy is favored since it means the structure is more stable [263]. Thus, as it is shown in Fig. 9-9e, the composition of $GdBa_{0.5}Sr_{0.5}Co_2O_{5+\delta}$ is less favorable particularly when there is a very high amount of oxygen vacancies in it. As for other two, $GdBa_{0.5}Sr_{0.5}Cu_2O_{5+\delta}$ (although cannot be synthesized) and $GdBa_{0.5}Sr_{0.5}CoCuO_{5+\delta}$, their most favorable structure seem to be with low oxygen content of 5 and 5.25, respectively. This low oxygen content is generally in a good accordance with the trend observed in Tab. 9-1.

Additionally, DFT also allows evaluating the density of states (DOS). For instance, in the models of $GdBa_{0.5}Sr_{0.5}CoCuO_{5.5}$ and $GdBa_{0.5}Sr_{0.5}CoCuO_{5.75}$ (less oxygen vacancies) the contributions to the DOS near the Fermi lever (E_F) were found to be mainly attributed to the 3*d*-states of cobalt and copper, and partially, to the 2*p*-states of oxygen. Considering there is no energy gap near the E_F, the thermally activated behavior in the electrical conductivity (as shown below) can possibility be related to the hopping energy barrier.

Speaking of the total electrical conductivity (σ), on one hand, it is quite apparent that a significant rise occurs in all the selected compositions, when they are heated up to 850 °C, as can be observed from the measured data presented in Fig. 9-10a. On the other hand, the values of conductivity decrease with the increasing copper content at the same temperature. This can be linked with the decreasing oxygen content from GBSCC1010 to GBSCC085115, which has a great impact on the charge transfer process of "-O-Cu-O-" and "-O-Co-O-" [258].

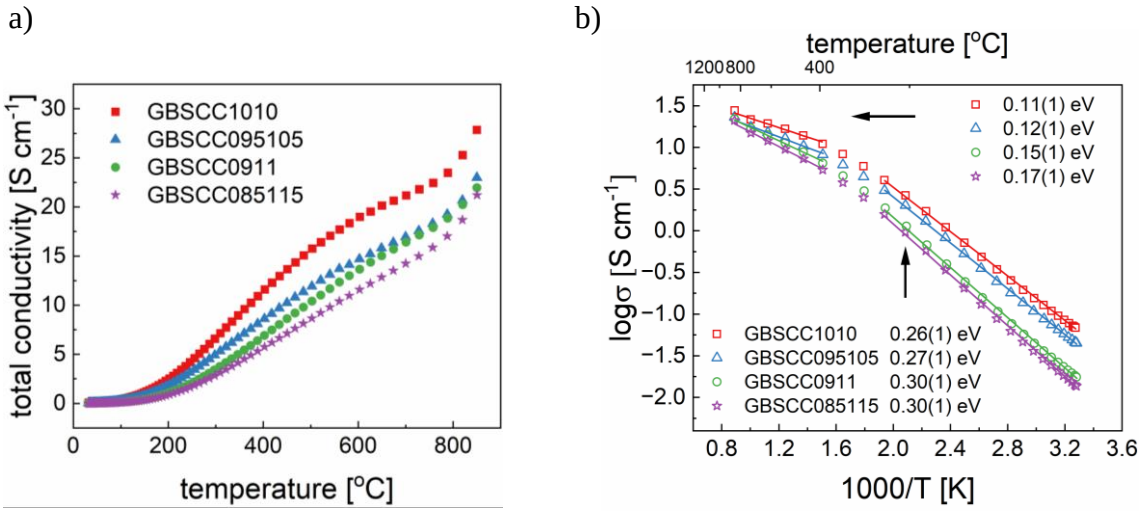

Fig. 9-10. a) Total electrical conductivity for the GBSCC system in air as a function of temperature, and b) conductivity in Arrhenius coordinates [248].

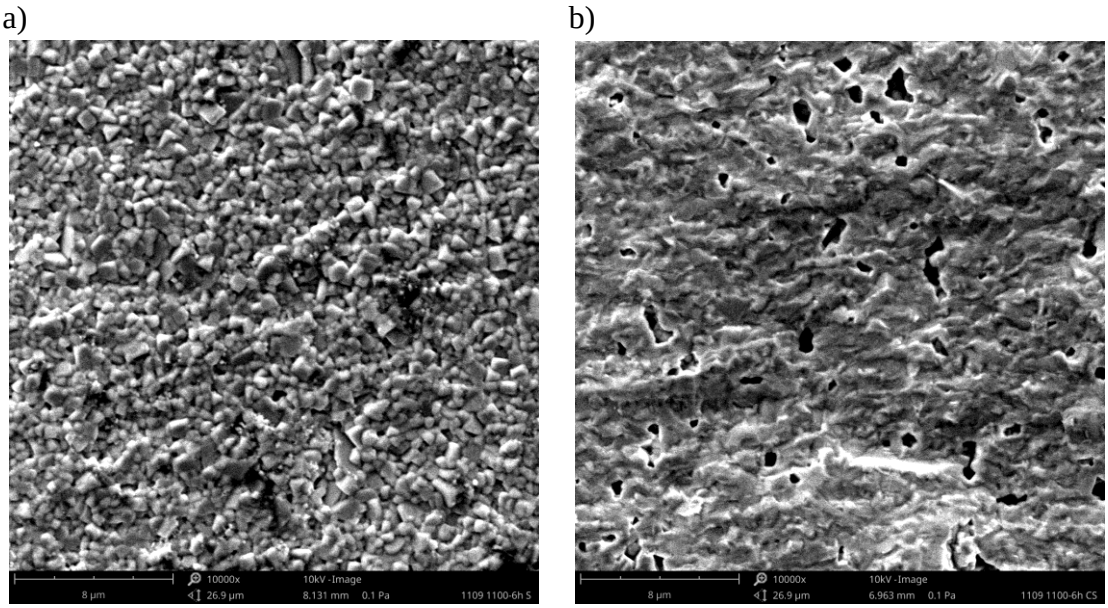

Fig. 9-11. SEM micrographs of a) surface, and b) cross-section of the GBSCC0911 pellet sintered at 1100 °C in air (i.e. the same conditions as the sample used in the electrical conductivity measurements) [248].

When focused on Fig. 9-10b, these plots exhibit straight lines in both, low and high temperature ranges, so that the respective activation energy (E_a) values can be derived. The behavior indicates the thermally-activated process in the conduction mechanism. It is not clear why the activation energy decreases at higher temperatures, but one explanation is that it is a combined effect from the emergence of the attritional amount of the oxygen vacancies. Meanwhile, increasing E_a values can be noticed for samples with the higher Cu content, denoting that the cobalt element can facilitate the total conduction process. Similar phenomenon is discussed in other works as well [264,265].

The relative density of the measured samples is on the order of 90% or a little below (Figs. 9-11a and b), implying the specific conductivity values can be somewhat higher when the correction factor corresponding to the porosity influence (1.2-1.3) is taken into consideration [266]. Nevertheless, even without a correction, the conductivity among all the compositions is above 10 S cm^{-1} in the 600-800 °C range, suggesting the adequate transport properties of GBSCC materials considering application in IT-SOCs.

Similarly as discussed in the previous chapter for LBCu, it is of a great importance to assess the chemical compatibility of the GBSCC system with the selected electrolyte materials, LSGM and GDC, since possibility of cells manufacturing will highly rely on the mutual compatibility of oxygen electrode and electrolyte materials [244,245].

As results are demonstrated in Figs. 9-12a-d and Fig. 9-13, materials from the GBSCC system are chemically compatible with LSGM, as no impurities or secondary phases could be identified in the XRD patterns after annealing at 950 °C for 2 h in air. Furthermore, the GBSCC1010 and GBSCC0911 compositions also exhibit good combability with GDC after annealing at 900 °C for 2 h. Consequently, this fact supports that both, LSGM and GDC can be applied as the solid electrolyte or buffer layer material for not only in the symmetrical cell, but also in the full cell configuration.

As a summary to this chapter, it can be stated that all the results concerning physicochemical properties of $GdBa_{0.5}Sr_{0.5}Co_{2-x}Cu_xO_{5+\delta}$ *indicate that the proposed materials with limited Co content, especially in the* $x = 1\text{-}1.15$ *range are promising candidates for manufacturing the oxygen electrodes for IT-SOCs, fulfilling demanded requirements.*

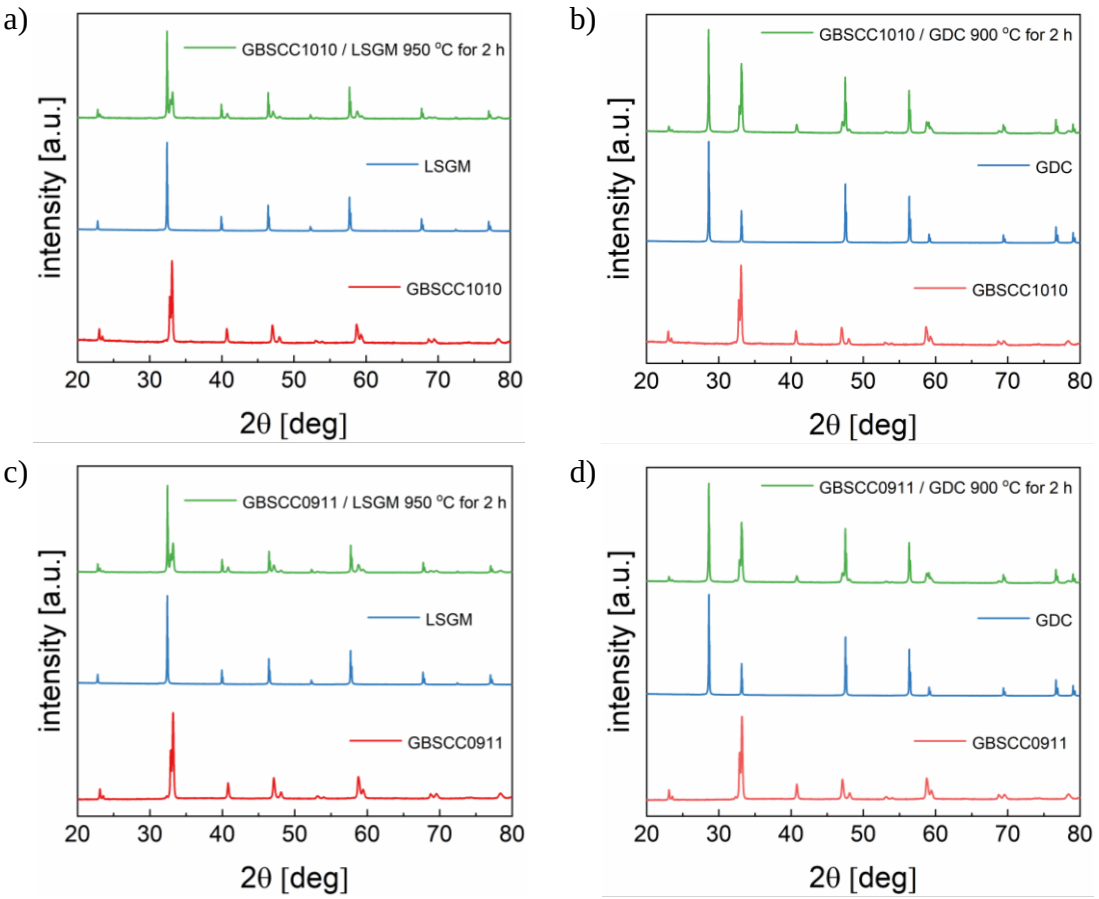

Fig. 9-12. Results of the XRD studies for the annealed mixtures of GBSCC1010 or GBSCC0911 with the selected solid electrolytes. a) Data for GBSCC1010 with LSGM, and b) with GDC. c) Data for GBSCC0911 with LSGM, and d) with GDC.

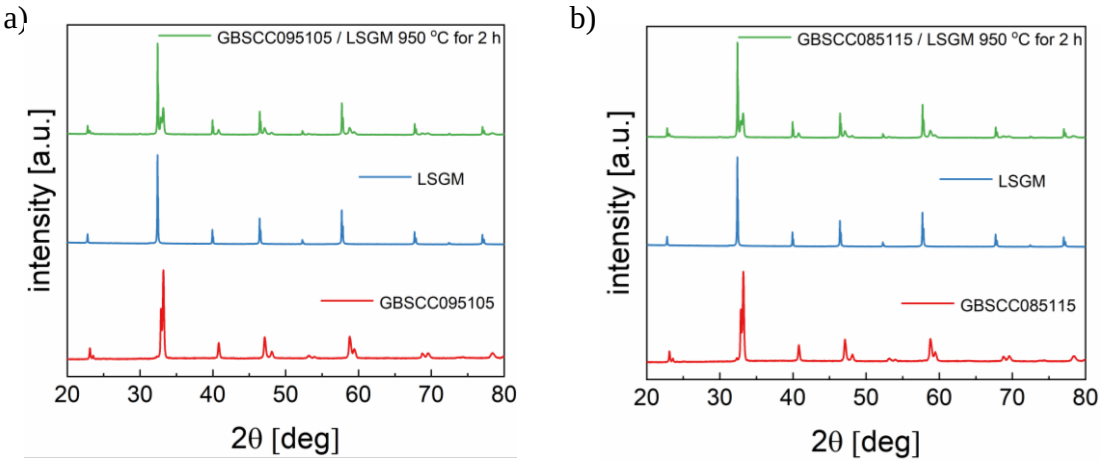

Fig. 9-13. Results of the XRD studies for the annealed mixtures of a) GBSCC095105, and b) GBSCC085115 with LSGM electrolyte material.

10. Physicochemical properties of $La_{0.6}Sr_{0.4}Ni_{0.15}Mn_{0.15}Fe_{0.15}Cu_xCo_{0.55-x}O_{3-\delta}$

Recent interest in the multicomponent and/or high entropy oxides can be related to the fact that behavior outside of a simple rule of mixtures can be expected, if many (five or more) elements in an equimolar or close to such ratio are present in one sublattice, for example, in the oxide. In other words, such materials may have different behavior that the one expected on a basis of properties of the traditional (simple) compounds [267–269]. It should be however emphasized that only a small number of high entropy materials are entropy-stabilized, and the definition itself is still discussed. As presented in Tab. 7-4, the considered $La_{0.6}Sr_{0.4}Ni_{0.15}Mn_{0.15}Fe_{0.15}Cu_xCo_{0.55-x}O_{3-\delta}$, with five elements at the B-site, exhibit entropy metric EM suggesting the medium entropy configuration [211]. The idea behind selection of the compositions was to use LSCF6428, a typical oxygen electrode material, and introduce multicomponent occupancy with a fixed equimolar Ni:Mn:Fe dopant ratio 1:1:1 between these three elements, as well as with introduction of varying Co to Cu ratio, with the aim to see how Cu affects the properties replacing Co. In consequence, the above formula was proposed, and the staring material was selected as $La_{0.6}Sr_{0.4}Ni_{0.15}Mn_{0.15}Fe_{0.15}Cu_{0.05}Co_{0.50}O_{3-\delta}$. At the same time, introduction of more than 0.2 moles of Cu proved to be difficult, yielding precipitation of the secondary phases. Consequently, the x range was limited to 0.05-0.2 range, for which four samples could be obtained (Tab. 7-1).

In a similar manner as discussed in previous two chapters, crystal structure of the samples from the LSNMFCC system should be identified, and the XRD results of such analyses, together with the Rietveld refinement data, are shown in Figs. 10-1a and b. All the samples, including LSNMFCC2035, LSNMFCC1540, LSNMFCC1045, and LSNMFCC0550 are pure-phase after synthesis in air, with the identified *R*-3*c* symmetry for all of them. Additionally, the model of a unit cell with *R*-3*c* crystal structure is also built (Fig. 10-1c), which allows to better understand the actual atomic arrangement of cations and oxygen anions in the considered samples. Both cationic sublattices show random distribution of, respectively, Ni/Mn/Fe/Cu/Co cations in the octahedra, and La/Sr cations between them, in the 12-fold coordinated sites.

The detailed values of the refined unit cell parameters are summarized in Tab. 10-1. It is of interest that the *a* parameter varies only very slightly among the samples, while there is a clear increasing trend in the parameter *c* with the increasing copper doping content (Figs. 10-2a and b). This also results in the increasing values of the unit cell volume *V* for higher Cu content. The reason behind it seems to be the same, as discussed in the previous chapter for the GBSCC series (Co^{3+}/Co^{4+} is partially replaced by Cu^{2+}/Cu^{3+}). Notably, the R_{wp} values for the four XRD data analyses are lower than 3%, indicating a relatively high refinement accuracy. Other data presented in Tab. 10-1 are discussed below.

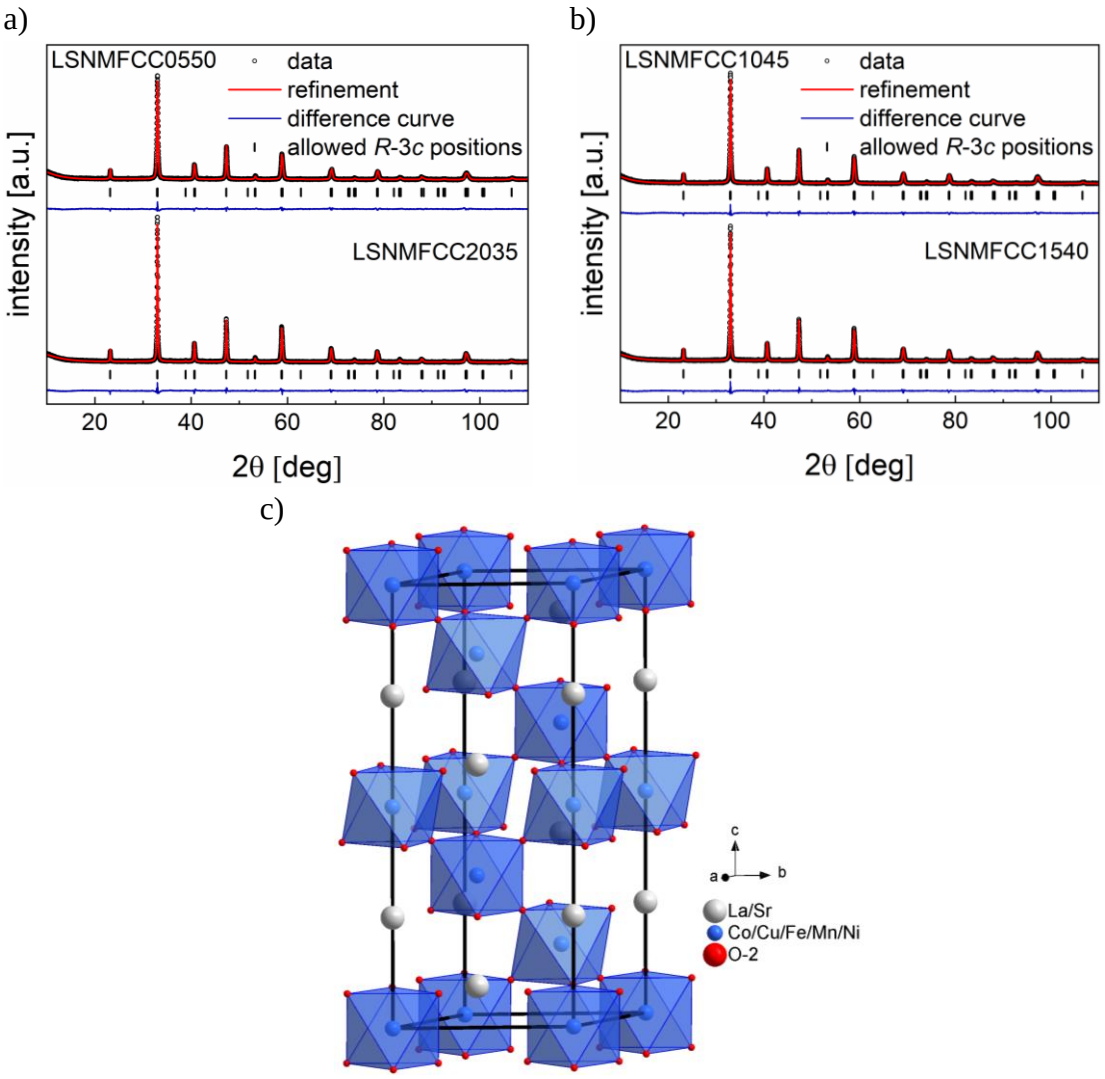

Fig. 10-1. XRD data for a) LSNMFCC0550 and LSNMFCC2035, and b) LSNMFCC1045 and LSNMFCC1540 samples recorded at RT together with respective Rietveld refinements. c) Created model of a unit cell for the rhombohedral *R*-3*c* space group.

Tab. 10-1. The refined structural parameters of the selected LSNMFCC materials.

Composition	*a* [Å]	*c* [Å]	*V* [Å^3]	Size [nm]	R_{wp} [%]	TEC[1]	TEC[2]	3-δ
LSNMFCC0550	5.4441(2)	13.2719(4)	340.65(2)	57	2.4	15.1(3)	20.6(6)	2.87(1)
LSNMFCC1045	5.4444(2)	13.2813(4)	340.93(2)	63	2.7	14.8(3)	20.6(6)	2.88(1)
LSNMFCC1540	5.4439(1)	13.2930(3)	341.17(1)	79	2.7	14.6(3)	20.6(6)	2.87(1)
LSNMFCC2035	5.4430(1)	13.3027(3)	341.31(1)	80	2.8	14.6(3)	20.5(6)	2.86(1)

[1]Note that TEC data are in the range of 25-400 °C in heating process.

[2]Note that TEC data are in the range of 400-900 °C in heating process.

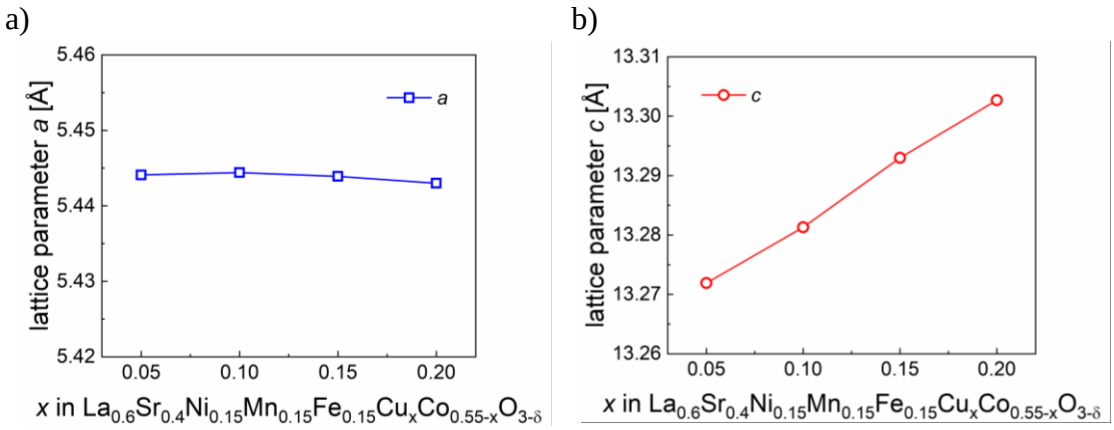

Fig. 10-2. Unit cell parameters: a) *a* and b) *c* depend on the copper doping level in $La_{0.6}Sr_{0.4}Ni_{0.15}Mn_{0.15}Fe_{0.15}Cu_xCo_{0.55-x}O_{3-\delta}$ series.

At the same time, as can be stated from the SEM observations (Figs. 10-3a and b, Figs. 10-4a and b), all LSNMFCC samples exhibit good homogeneity regarding distribution of all metal elements, as well as the grains of the respective powders contain agglomerated primary particles. Notably, if compared with data for the LBCu and GBSCC obtained by the SG route, a similar morphology can be noticed. This is of importance, as preparation and characterization of the electrodes with similar microstructure features is crucial in terms of comparison of the performance between different materials.

To have a deeper insight into the atomic-scale properties of the considered oxides, also TEM/EDS observations were made, to ensure that there are no precipitated phases nor inhomogeneities at the nanoscale. Results of these studies are presented in Figs. 10-5a-c and Figs. 10-6a-c, respectively for the LSNMFCC2035 and LSNMFCC0550 samples. The experiments proved equal distribution of all the cations at the nanoscale as well, further confirming that the obtained materials exhibit excellent structural and microstructural properties. This result is especially noteworthy, as in previous literature data on the multicomponent perovskite oxides some inhomogeneities could be observed [178]. Also, the observed crystallite size in the TEM images generally matches that obtained from the Williamson-Hall analysis implemented in GSAS II software and presented in Tab. 10-1. Finally, selection of the rhombohedral *R*-3*c* space group could be confirmed (Figs. 10-5b and 10-6b), as the visible lattice fringes could be indexed correctly in this case.

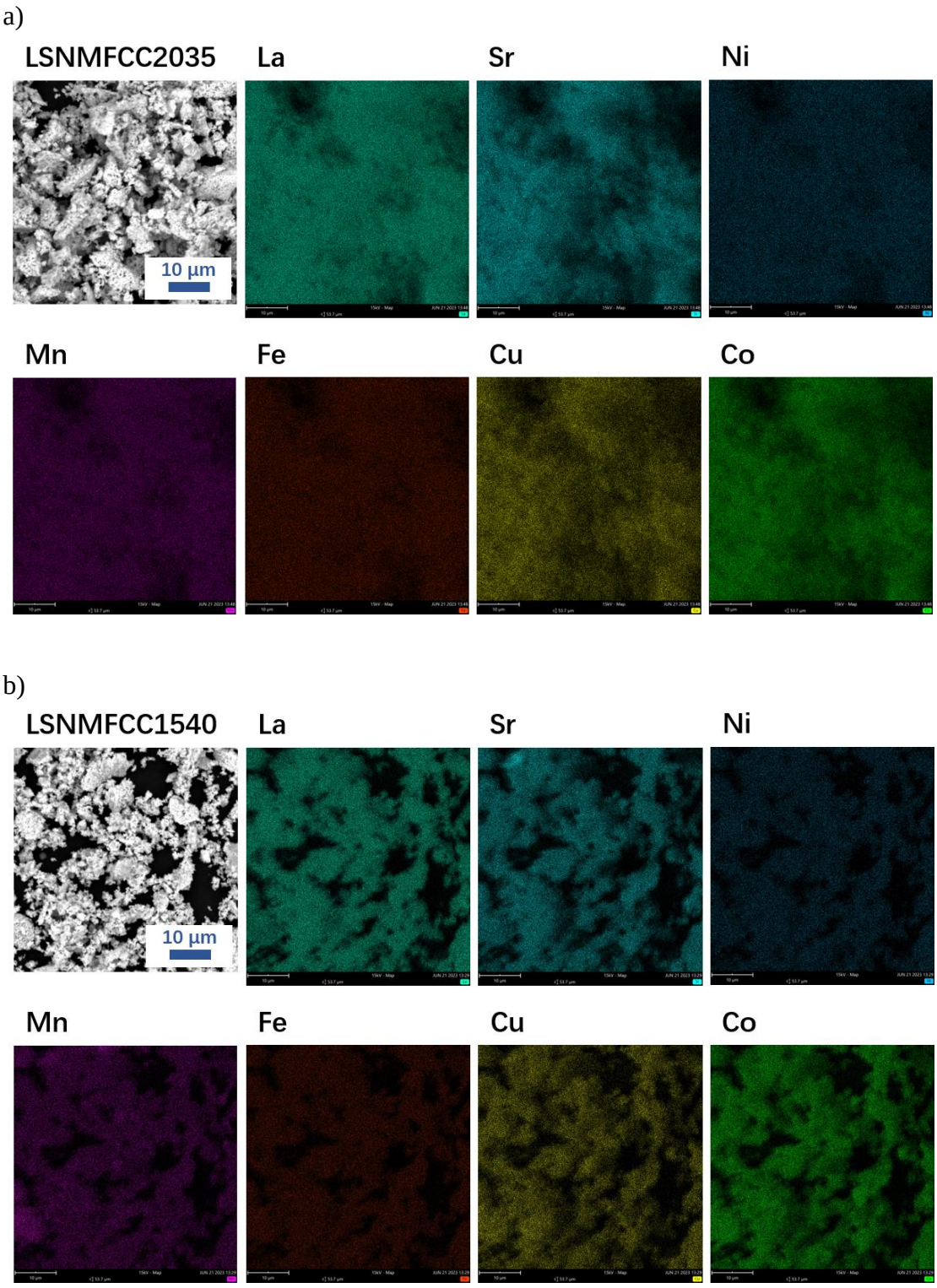

Fig. 10-3. Morphology of the a) LSNMFCC2035, and b) LSNMFCC1540, together with respective EDS elemental maps.

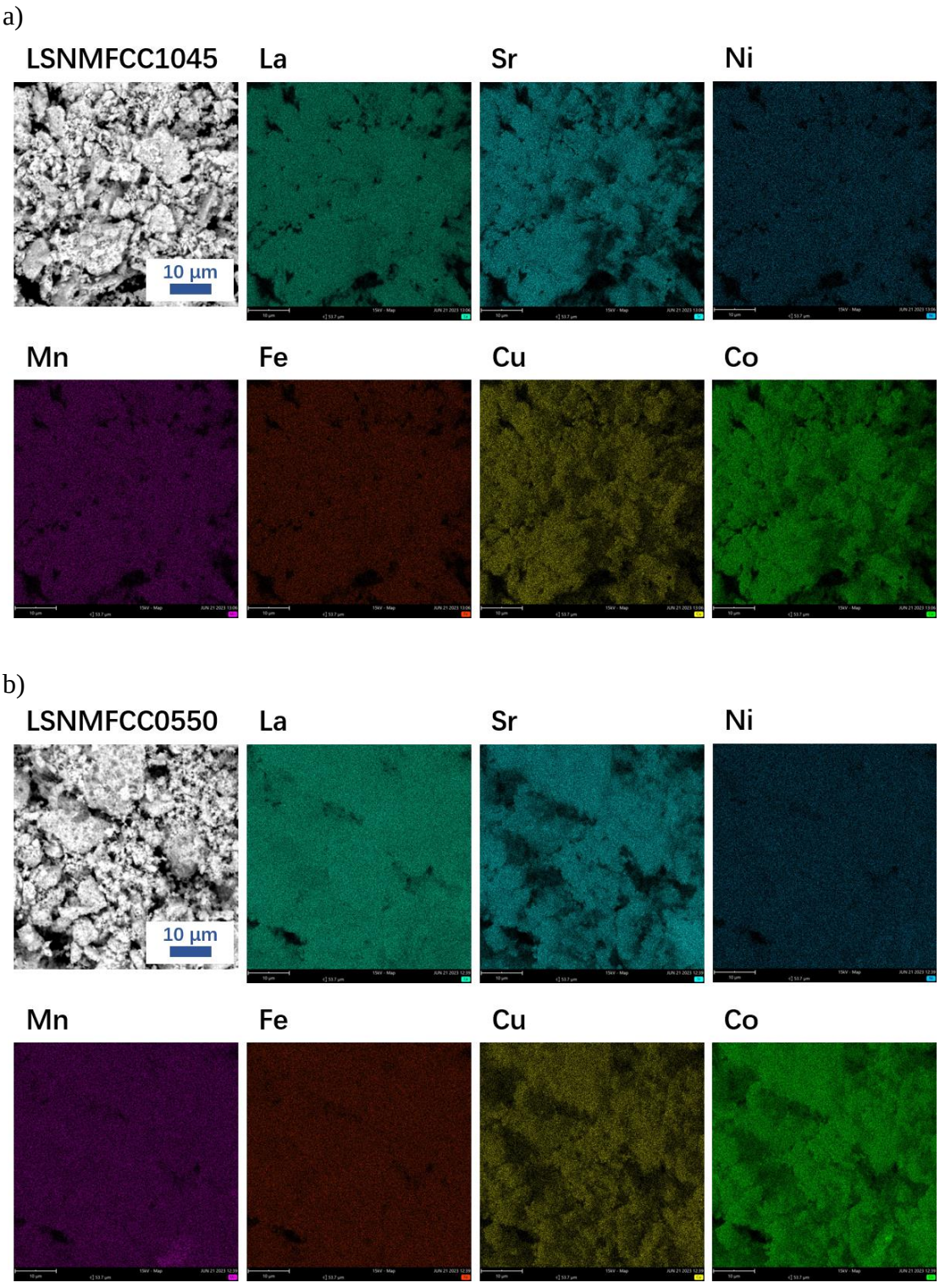

Fig. 10-4. Morphology of the a) LSNMFCC1045, and b) LSNMFCC0550, together with respective EDS elemental maps.

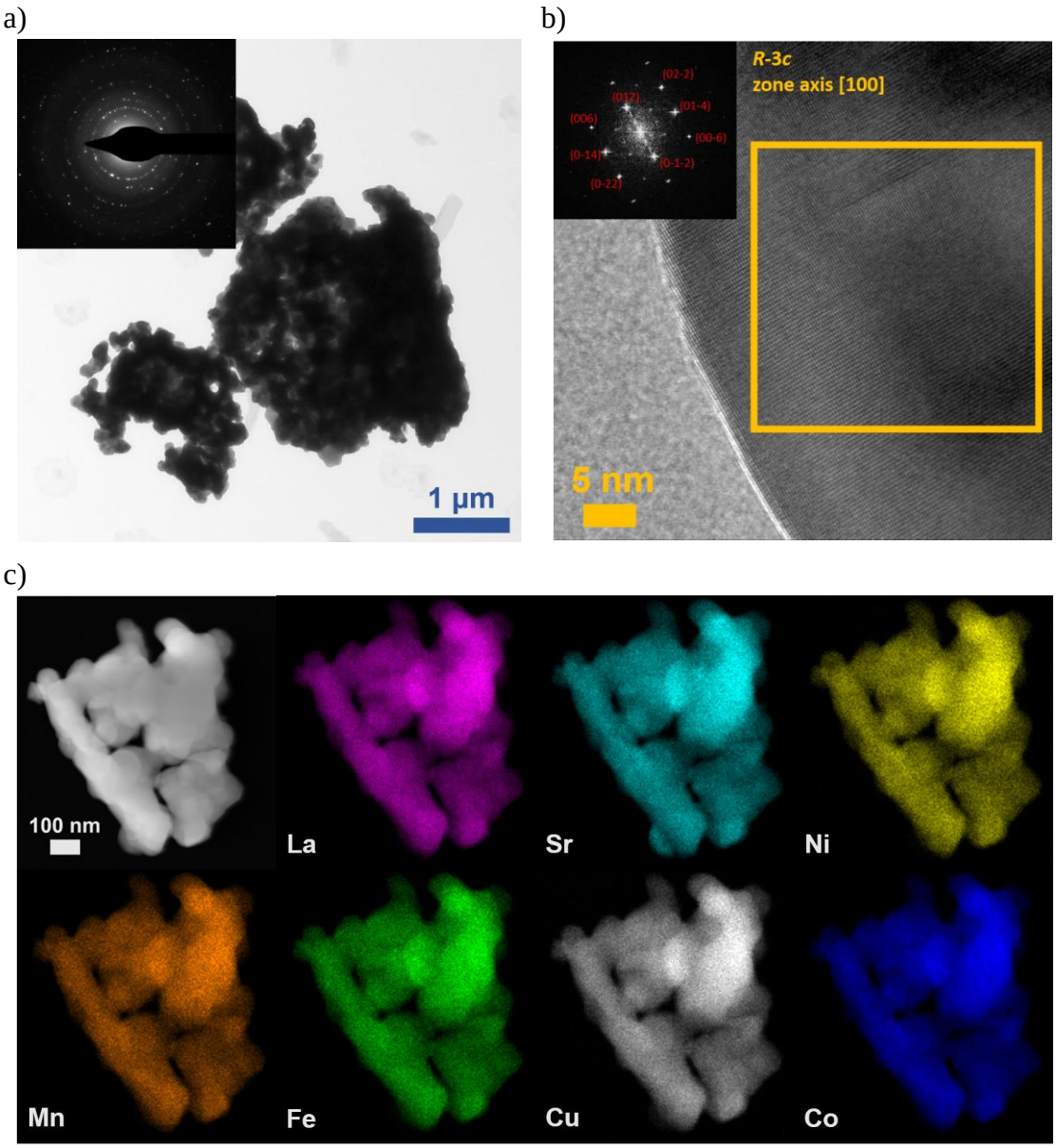

Fig. 10-5. The TEM/EDS observations of the LSNMFCC2035 sample. a) Bright-field TEM image with the corresponding Selected Area Electron Diffraction (SAED) pattern, b) high-resolution (HR) TEM image with the fast Fourier transform (FTT) indexed as the rhombohedral *R*-3*c* phase, and c) scanning TEM (STEM) image with the corresponding EDS maps showing the uniform distribution of elements.

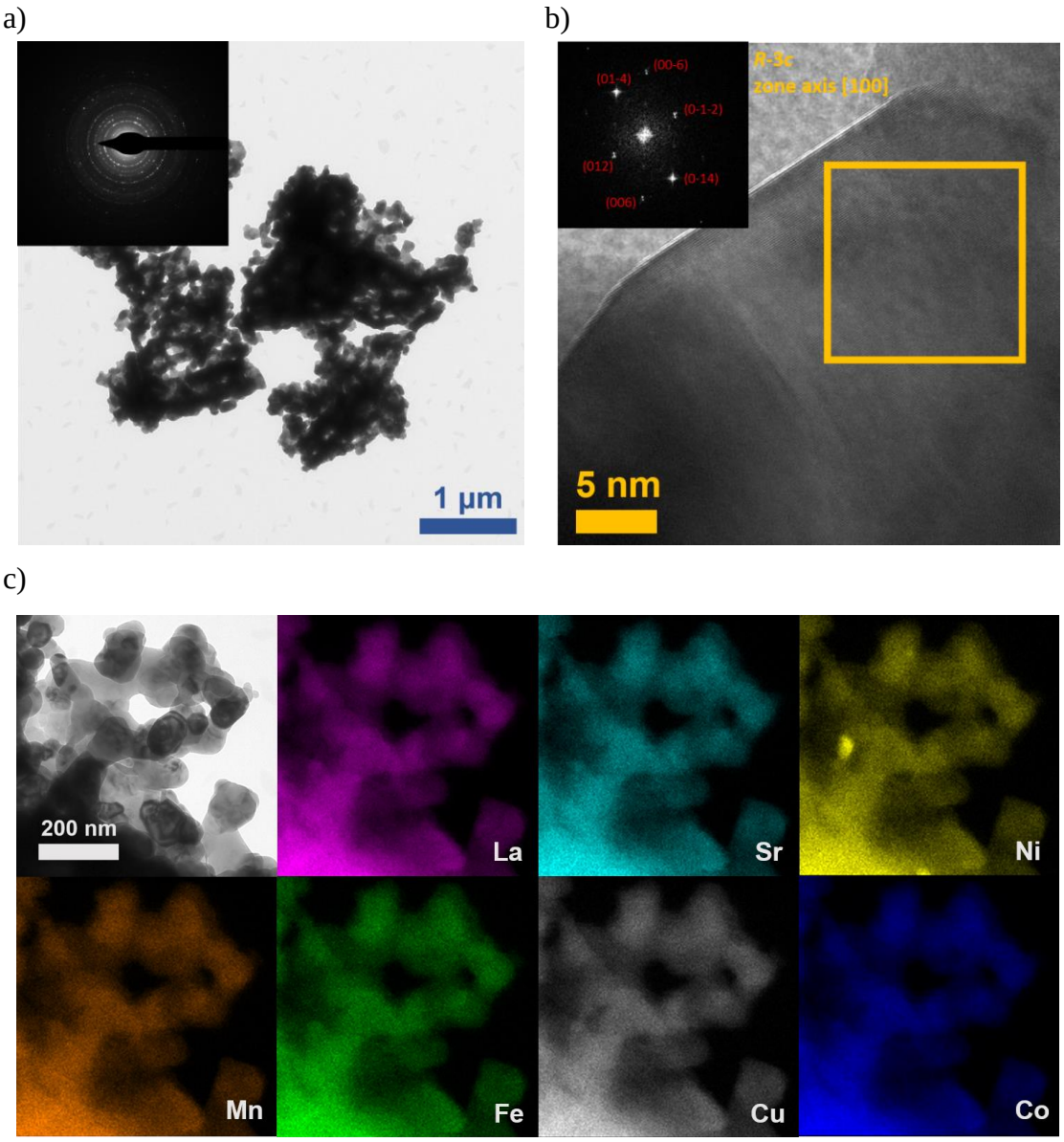

Fig. 10-6. The TEM/EDS observations of the LSNMFCC0550 sample. a) Bright-field TEM image with the corresponding Selected Area Electron Diffraction (SAED) pattern, b) high-resolution (HR) TEM image with the fast Fourier transform (FTT) indexed as the rhombohedral *R*-3*c* phase, and c) scanning TEM (STEM) image with the corresponding EDS maps showing the uniform distribution of elements.

Aiming at characterizing behavior at high temperatures, and consequently to establish thermal stability, the HT-XRD experiments were conducted for the four samples in a temperature range of RT-900 °C in air. As depicted in Figs. 10-7a-d, the as-synthesized LSNMFCC show a good thermal stability during the heating and cooling processes, maintaining the rhombohedral symmetry throughout the whole measurement range. No secondary phases nor phase transitions taking place were detected. Thus, it is easily concluded that the considered LSNMFCC oxides can meet the requirements of the thermal stability in both, electrode layer sintering and cell operating conditions.

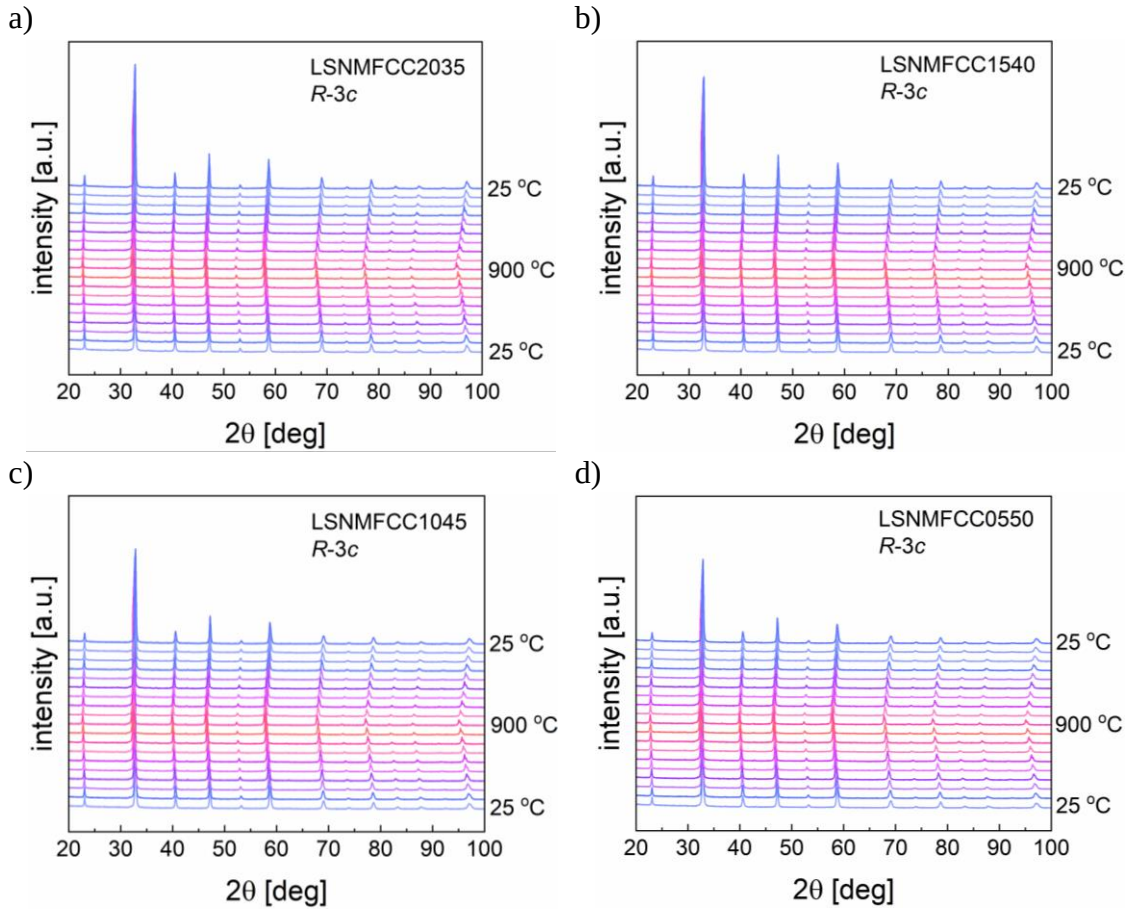

Fig. 10-7. HT-XRD data recorded for a) LSNMFCC2035, b) LSNMFCC1540, c) LSNMFCC1045 and d) LSNMFCC0550 materials in air on heating and cooling.

Similarly as for previous studied systems, more details could be also obtained from the HT-XRD measurements, as it is presented in Figs. 10-8a and b. The derived unit cell parameters *a* and *c* show a monotonous and almost linear increasing trend with the increasing temperature for all the samples. An inflection at ca. 400 °C more pronounced for the *a* parameter, but it is relatively small. Meanwhile, it is worth noting that the data for this parameter are highly overlapped, implying a quite similar expansion route along this axis. It is also in a good accordance with almost unchanged values for the *a* parameter in the whole series at RT (Tab. 10-1). Even though the parameter *c* can be distinguished at RT between the samples (Tab. 10-1 and Fig. 10-8b), the growing behavior is somewhat

different, with smaller slope for materials with larger Cu content. This results in that the data seem to be merged together in the high temperature range. Interestingly, this also indicates that the unit cell volume of all materials at the highest temperatures will be very similar.

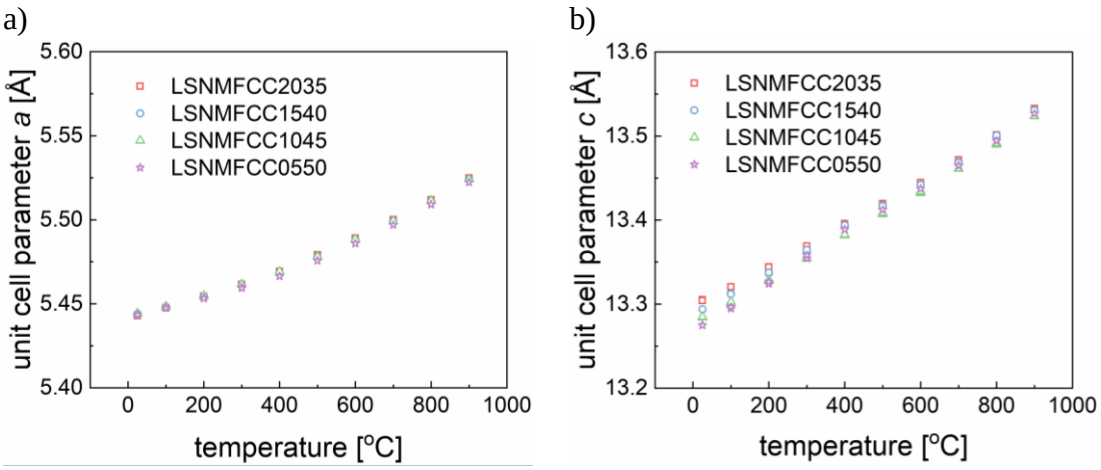

Fig. 10-8. Derived from Rietveld refinements unit cell parameters dependence on temperature for the selected LSNMFCC samples for a) the unit cell parameter *a*, b) the *c* parameter.

Moreover, the TEC data are also accessible through the conducted HT-XRD measurements and Rietveld analyses. As depicted in Fig. 10-9a-h, TEC values obtained on heating and cooling are very analogous to each other, and it is true for all studied samples. Concerning application as electrode layers in the cells, the materials would show a stable expansion behavior in the start-up and cool-down processes. Also, relatively moderate TEC values were obtained for all samples, even at the higher temperature range (400-900 °C). While somewhat higher than for the GBSCC series, the results appear as acceptable, and can be still regarded as better than those for Co-based oxides [250,257]. In the case of LSNMFCC0550, the material with the highest Co content, the values are $15.1 \cdot 10^{-6}$ K^{-1} and $20.6 \cdot 10^{-6}$ K^{-1}, respectively below and above 400 °C. However, a small improvement can be seen for samples with higher Cu content in the lower temperature range (Tab. 10-1), denoting the decreased thermal expansion induced by the copper doping. Surprisingly, at higher temperatures TEC remains almost the same for all materials, as opposite to the GBSCC series.

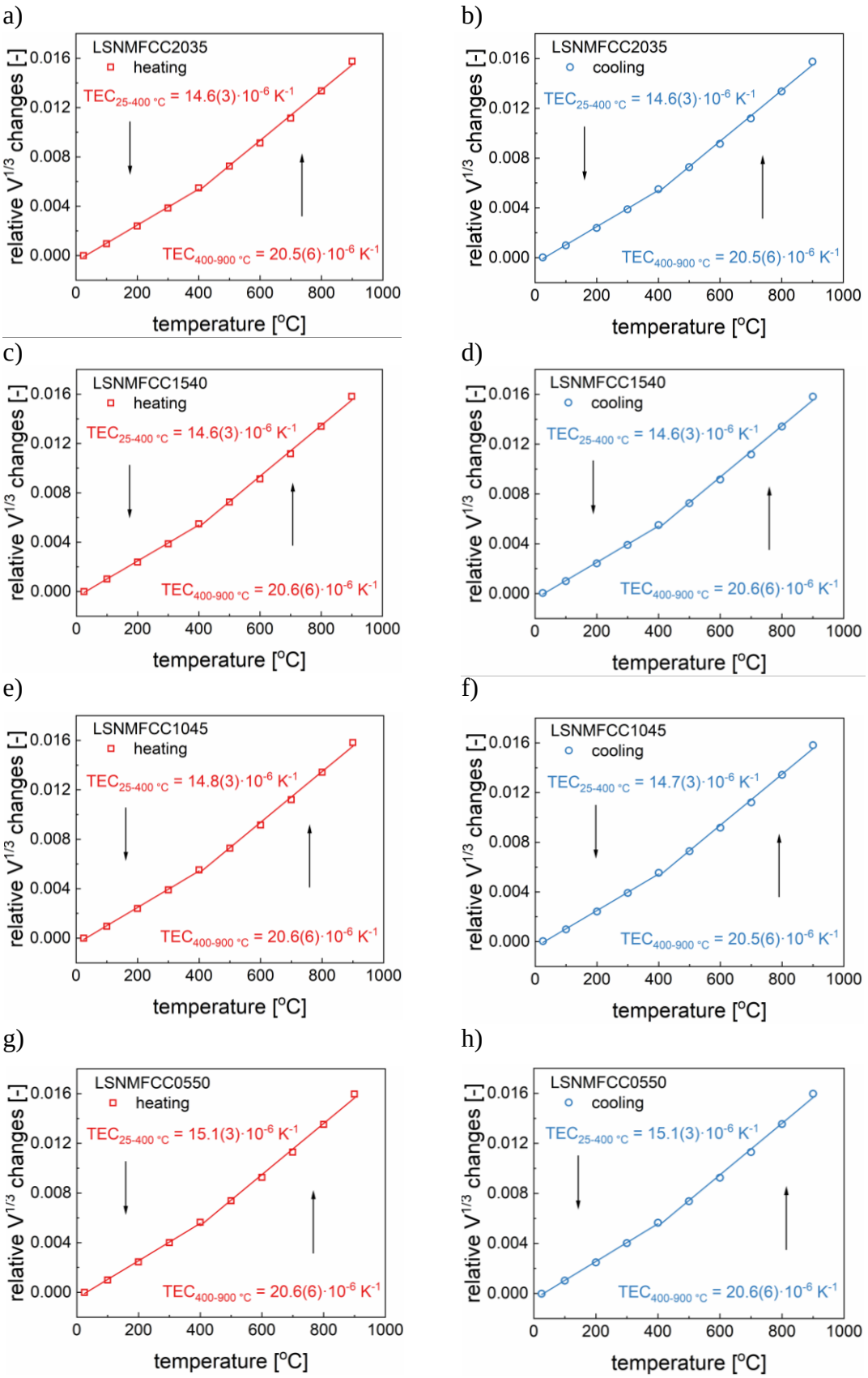

Fig. 10-9. Calculated TEC values of a) and b) LSNMFCC2035, c) and d) LSNMFCC1540, e) and f) LSNMFCC1045, and g) and h) LSNMFCC0550 samples.

The discussed above behavior at high temperatures seems to be linked with the oxygen content and its changes with temperatures, as it is known for many perovskite-type oxides. Considering this, iodometric titration experiments were performed, which enabled determining the average oxidation state of the B-site elements, and therefore, values of δ at RT for all materials. As summarized in Tab. 10-1, the selected LSNMFCC oxides exhibit almost the same oxygen content at RT, indicating very similar oxygen vacancy concentration. This result is surprising, because of differences in doping with Cu and Co, as proved in the GBSCC series. Possibly this is one of the effects, which stems from the high value of the configurational entropy present in the materials.

To fully assess the oxygen content-related properties of the LSNMFCC series, thermogravimetric measurements were carried out in air (Fig. 10-10a). A visible feature of all the recorded curves is that the samples undergo a continuous and smooth oxygen release process up to 800 °C, without any sudden and significant bend occurring. This confirms that there are no phase transitions taking place during the measurements at high temperatures. Furthermore, while data for LSNMFCC2035 start with the lowest oxygen content out of selected compositions at RT, the material shows the largest change of the values, and therefore the highest oxygen vacancies concentration at 800 °C. This implies that the material should be bestowed with a good ionic conductivity at elevated temperatures.

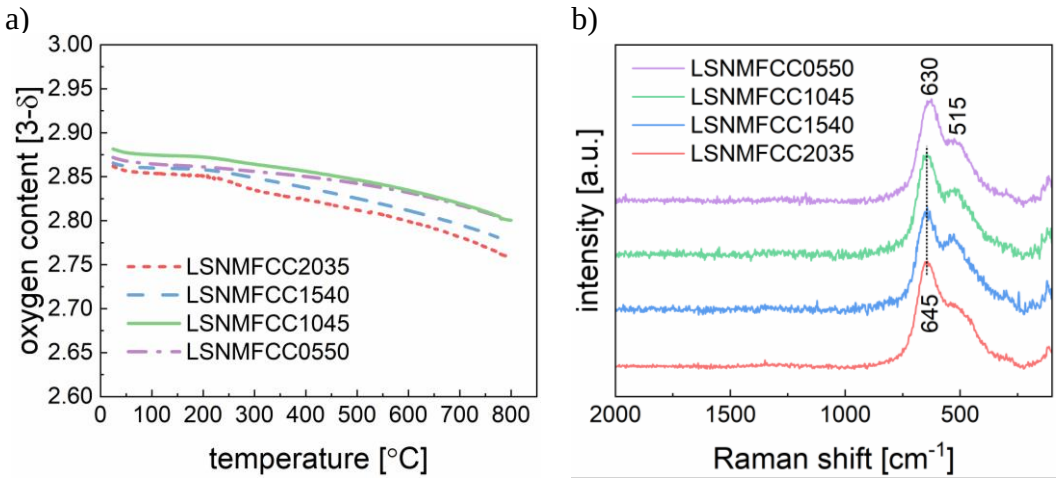

Fig. 10-10. a) Recalculated from the TG data temperature dependences of the oxygen content in LSNMFCC series in air. b) Raman spectroscopy data for the selected LSNMFCC materials.

In addition, it is of interest to implement the Raman spectroscopy measurements, since it may offer information in terms of bonding in the perovskite-type oxides. As it is depicted in Fig. 10-10b, there are two peaks clearly visible, located at ca. 515 cm^{-1} and 645 cm^{-1} (630 cm^{-1} for the case of LSNMFCC0550). These two peaks are normally observed in the LSCF materials, e.g. LSCF6428, in which are described as being related to the characteristic modes in the *R*-3*c* structure [270,271]. Meanwhile, similar peaks are also detected in other high-entropy perovskite-type oxides [178].

It is important also to characterize the total electrical conductivity of the LSNMFCC samples, and the results are shown in Figs. 10-11a and b. Interestingly, all of the materials demonstrate very high, favorable values of the conductivity in air, which are all above 200 S cm^{-1} in the temperature range of RT-850 °C. Particularly, LSNMFCC2035 exhibits the highest conductivity among the series, reaching over 750 S cm^{-1} at around 500 °C, which is followed by data for LSNMFCC1540 with a lower copper content. In the latter case the values still exceed 600 S cm^{-1} at the similar temperature. These results denote two important things, first, the selected multicomponent compositions are suitable to achieve high total conductivity, despite relatively low Co content. Second, the copper doping is beneficial for improving the electrical conduction. Both effects are likely related to the presence of the B-site cations in different charge states, facilitating the electron exchange process. Two more unusual effects are visible. The activation energy that can be calculated in the low temperature range of RT-400 °C is the highest in the case of LSNMFCC2035 material exhibiting the best transport properties (Fig. 10-11b). Also, the supplementary data on the Seebeck coefficient values (Fig. 10-11c) indicate a negative sign of this coefficient, which is rather unusual, as most of the related perovskites are *p*-type conductors [272,273].

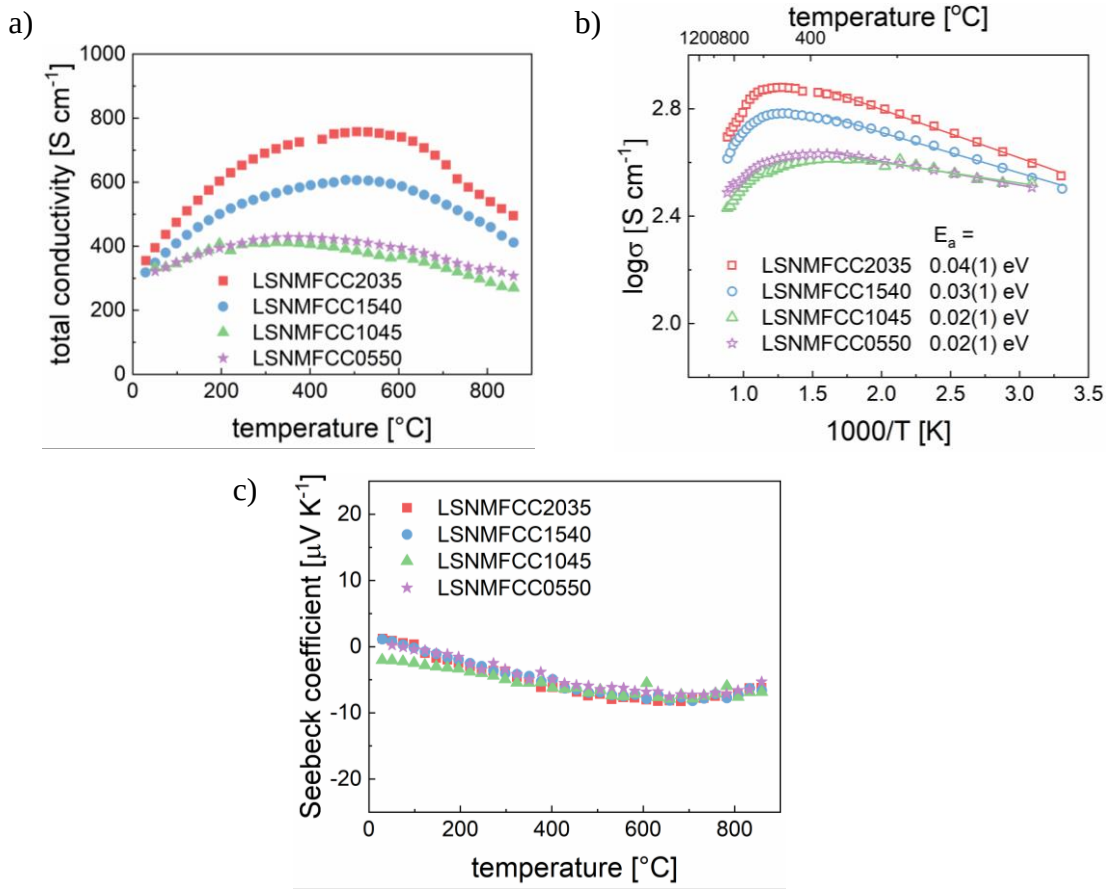

Fig. 10-11. a) Total electrical conductivity for the LSNMFCC series in air as a function of temperature, (b) conductivity in Arrhenius coordinates, and c) temperature dependence of the Seebeck coefficient.

In general, the derived values of the activation energy among selected samples are quite low, which indicates that the conduction mechanism in the crystal lattice is easy, with a large degree of delocalization of the electrons. More studies are needed to confirm if the observed behavior can be explained by the small polaron behavior, or rather, another mechanism is involved. Nevertheless, similarly as the properties regarding the oxygen content, also the transport properties in the series are not standard, and seem to be affected by the multicomponent occupancy at the B-site.

Chemical compatibility of LSNMFCC with the discussed before LSGM and GDC electrolyte materials was also checked, as it is crucial because any reaction between the electrode layer and electrolyte will have a negative impact on the performance of the cell. After initial trials regarding selection of the proper temperature, the compatibility tests were conducted for 2 h at either 850 °C or 900 °C, and the results are demonstrated in Figs. 10-12a-h. Favorably, the whole LSNMFCC series exhibit the good chemical compatibility with LSGM (up to 850 °C) and GDC (up to 900 °C) electrolyte materials. No impurities or secondary phases could be detected after annealing in air at the abovementioned temperatures. Therefore, the results adequately prove that both, LSGM and GDC can be applied as electrolyte materials or buffer layers in the construction of the cells.

Summarizing this chapter, it can be written that the proposed multicomponent oxides, $La_{0.6}Sr_{0.4}Ni_{0.15}Mn_{0.15}Fe_{0.15}Cu_xCo_{0.55-x}O_{3-\delta}$ $(0.05 \leq x \leq 0.20)$ possess physicochemical properties, which are suitable in terms of the possible application as oxygen electrodes for IT-SOCs. Also, the increased configurational entropy likely influences (in a beneficial way) their behavior regarding oxygen content changes at elevated temperatures, related thermal expansion, as well as total electrical conductivity.

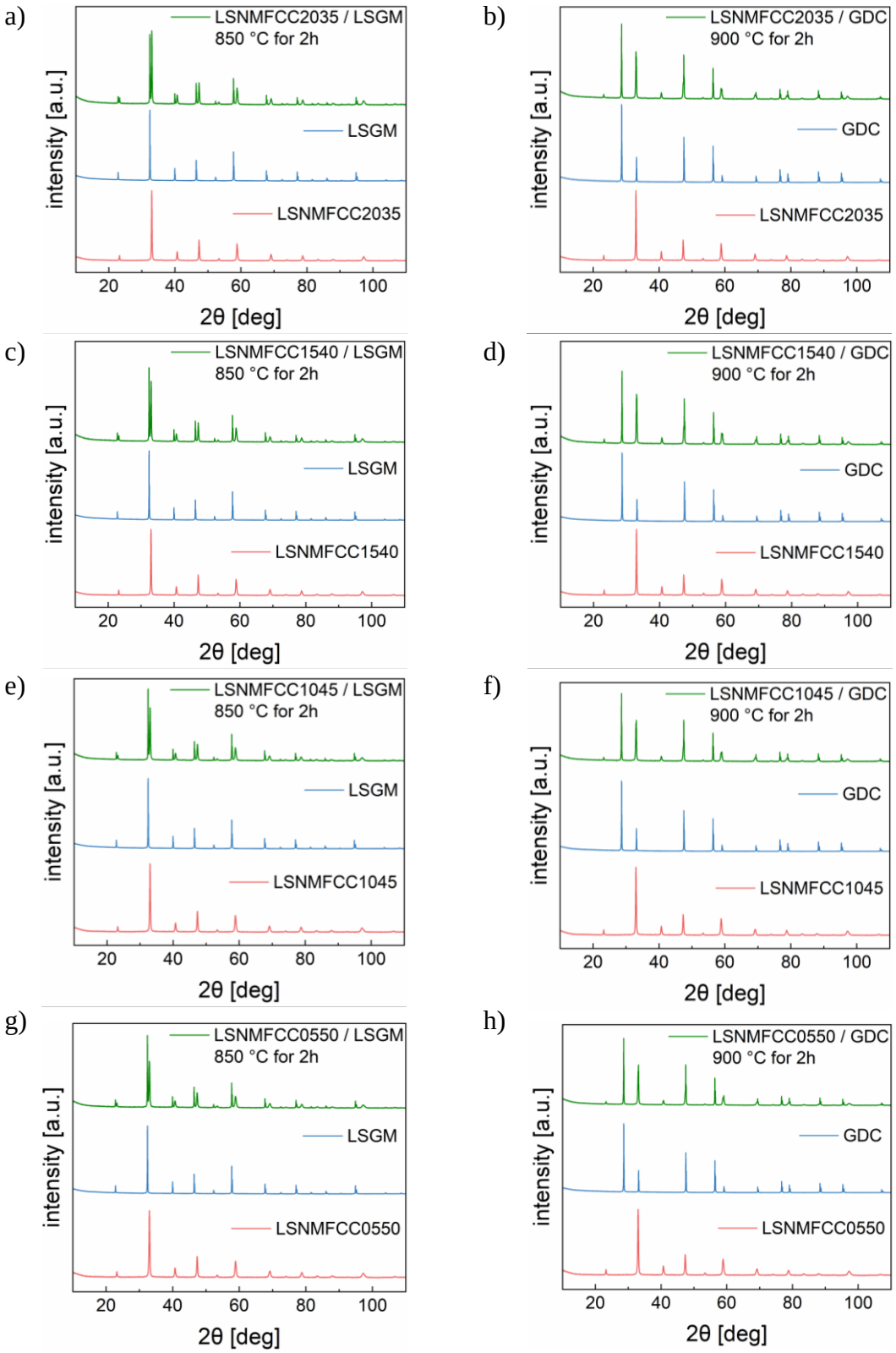

Fig. 10-12. Results of the XRD studies for the annealed mixtures of: LSNMFCC2035 with a) LSGM and b) GDC, LSNMFCC1540 with c) LSGM and d) GDC, LSNMFCC1045 with e) LSGM and f) GDC, and LSNMFCC0550 with g) LSGM and h) GDC electrolyte materials.

11. Electrochemical properties of the developed oxygen electrodes in IT-SOCs

Comprehensive studies of the fundamental physicochemical properties, results of which are reported in chapters 8, 9, and 10, allowed gaining insight into relationships between the chemical composition, structure, oxygen content, thermomechanical characteristics, transport properties, and chemical reactivity with selected solid electrolyte materials. This enabled proposing materials from the three studied groups for manufacturing of the oxygen electrodes, and further evaluation in the cells. Obviously, systematic electrochemical studies are indispensable in characterizing the electrocatalytic activity and output performance. Both, symmetrical and full cells (laboratory-scale, button-type) were prepared and tested, as documented and discussed below. The following three subchapters reflect the three studied perovskite-type systems.

11.1. $La_{1.5}Ba_{1.5}Cu_3O_{7\pm\delta}$ as the oxygen electrode material

It is worth noting that one of the advantages related to application of Cu-based materials as oxygen electrodes in IT-SOCs is the related to the relatively low sintering temperature of such materials, especially if compared to Mn- or Co-based perovskite oxides [274,275]. Thus, this benefit can also be applied in manufacturing of the electrodes, allowing obtaining electrode layers at relatively low temperatures, and at the same time, showing good adhesion to the electrolyte and desirable porosity in their bulk. Taking this into account, several attempts have been undertaken to establish the most proper layer sintering temperature for the selected LBCu material. As can be seen in Figs. 11-1a and b, electrodes sintered in 750-900 °C range exhibit significantly different properties, with large difference in their polarization resistance R_p (data from symmetrical cells tested in air).

As depicted in Fig. 11-1a, there are evidently two arcs visible for all the LBCu oxygen electrodes, but their relative size (at all temperatures) differs considerably depending on the sintering temperature of the electrode layers. The arc visible in the high frequency part (close to zero in the *x*-axis) can be ascribed to reactions taking place at electrode-electrolyte interface, while the one in low frequencies (close to the tail of curve on the right side) can be attributed to reactions happening at the surface of the electrode [222,223]. The optimal LBCu electrode is obtained when it is sintered at 800 °C, as can be clearly seen from data presented in Figs. 11-1a and b. Specifically, the R_p reaches as low as 0.019 Ω cm^2 and 0.041 Ω cm^2 at 750 °C and 700 °C, respectively. Furthermore, such values can be regarded as quite exceptional, when compared to other Cu-based electrode materials (Tab. 11-1). Also, results are much lower than the widely-accepted resistance value threshold of 0.15 Ω cm^2 for SOC oxygen electrodes [276]. Notably, this R_p limit can be even met at ca. 625 °C, as the calculated value at 650 °C yields 0.090 Ω cm^2. The origins of the exceptional catalytic activity most likely stem from the favorable

set of the physicochemical properties, especially, the complex, partially disordered oxygen sublattice, which may facilitate the oxygen migration. This is expected to help with the relatively fast oxygen release/intake at lower temperatures. When it comes to the activation energy, much higher value of 1.82 eV was calculated for the electrode sintered at 900 °C, the electrodes sintered at lower temperatures exhibit lower activation energy, ranging in 1.26-1.37 eV range (as calculated at 600-700 °C). The differences likely are related to the changed morphology and porosity, as well as the possible reactivity and/or modified adhesion at the interface with the electrolyte.

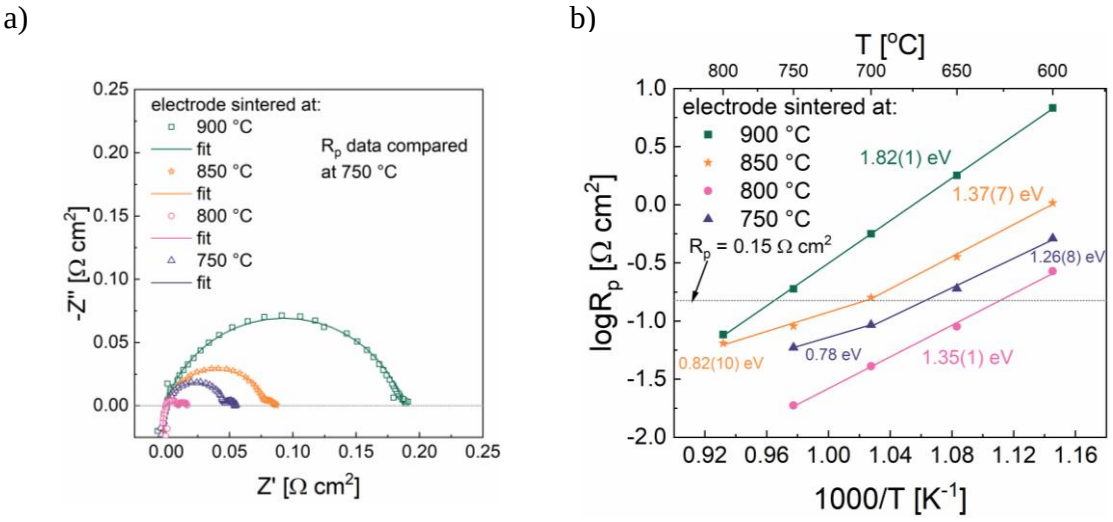

Fig. 11-1. a) Typical Nyquist plots recorded at 750 °C for the LBCu electrodes sintered at different temperatures, together with respective fits, and b) related electrode polarization resistance R_p presented in Arrhenius-type coordinates in the whole studied temperature range (600-800 °C). Data concern cells prepared on LSGM electrolyte with the Ag current collector [227].

Tab. 11-1. Comparison of the electrode polarization resistance values for different Cu-based and Cu-containing perovskite-type and related materials.

Chemical composition	R_p [Ω cm^2]	Reference
$La_{1.5}Ba_{1.5}Cu_3O_{7\pm\delta}$	**0.041 (700 °C)**	**This work**
$La_{1.5}Ba_{1.5}Cu_3O_{7\pm\delta}$	**0.019 (750 °C)**	**This work**
$SrFe_{0.7}Cu_{0.3}O_{3-\delta}$	0.107 (700 °C)	[277]
$NdBaCu_2O_{5+\delta}$	3.18 (700 °C)	[278]
$NdBa_{0.5}Sr_{0.5}Cu_2O_{5+\delta}$	0.20 (700 °C)	[278]
$La_2Cu_{0.8}Co_{0.2}O_4$	0.51 (700 °C)	[279]
$Sr_{0.7}Y_{0.3}CuO_{2+\delta}$	0.054 (750 °C)	[280]
$La_{0.8}Sr_{0.2}Mn_{0.8}Cu_{0.2}O_{3-\delta}$	4.3 (750 °C)	[281]
$La_{0.7}Sr_{0.3}CuO_{2.5}$	0.25 (800 °C)	[274]
$SrFe_{0.7}Cu_{0.2}W_{0.1}O_{3-\delta}$	0.102 (800 °C)	[282]

It can be stated that such low R_p values obtained for the optimized LBCu electrode indicate that as a Co-free material, LBCu can reach desirable electrocatalytic activity if compared to the Co-based electrode materials [146]. Still based on the obtained data, more important details can be uncovered via the DRT analysis.

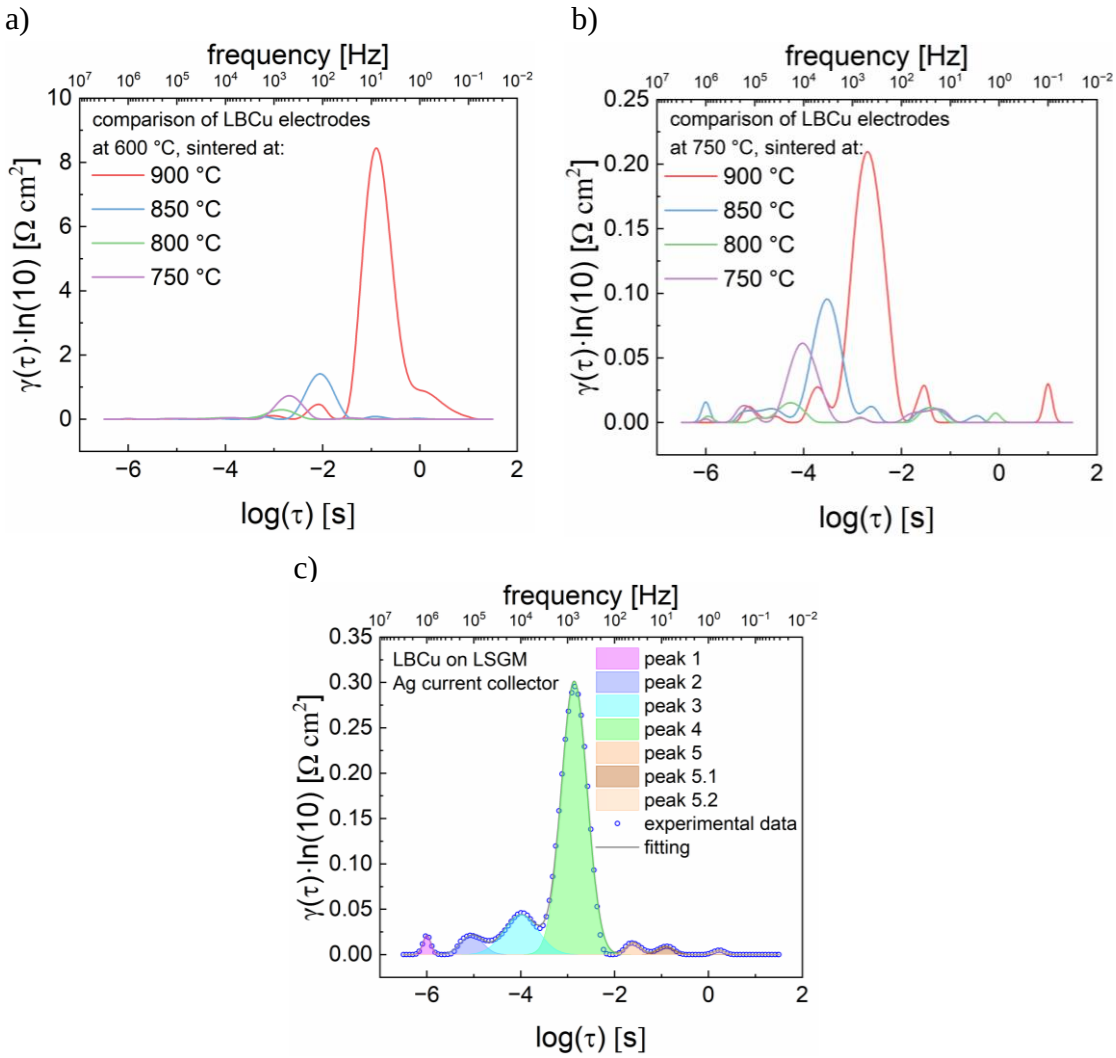

Fig. 11-2. Results of DRT analyses presented as a function of log(τ) for symmetrical cells with LBCu electrodes sintered at different temperatures, compared at a) 600 °C, and b) 750 °C. c) The detailed analysis (with fitting of the respective peaks) of data analyzed at 600 °C for the LBCu electrode sintered at 800 °C.

Figs. 11-2a-c present results of the DRT analyses. It is an obvious characteristic that the biggest in terms of its area (as well as highest) peak can be easily identified in all electrodes at both temperatures, 600 °C and 750 °C. This biggest peak can be attributed to the mentioned previously large arc at the lower frequency zone. As compared at 600 °C (Fig. 11-2a), the respective maxima are at around 10, 100, 400 and 800 Hz for the electrodes sintered at 900, 850, 750 and 800 °C, respectively. Furthermore, when compared at 750 °C (Fig. 11-2b), an evident shift toward higher frequencies can be

detected in all electrodes. Specifically, the main peaks are now at 400, 2000, 10000 and 11000 Hz, keeping the previous order regarding the electrodes. Data for the electrode sintered at the highest temperature indicate problems with the gas diffusion and adsorption of the oxygen molecules at the surface, which likely results from the not sufficient porosity. The results are improved if the sintering temperature was decreased to 850 °C, however, the best performance was reached for the electrode manufactured at 800 °C. As presented in Fig. 11-2c, the peaks for frequencies below 100 Hz ($\tau > 10^{-2}$ s) are negligible, and the rate limiting step appears as related to the reduction of the previously adsorbed and dissociated oxygen [283–286].

It is also of interest to characterize if the obtained low R_p values can remain stable for a prolonged time. For the durability tests, the best performing LBCu electrode was selected (sintered at 800 °C), and the measured data are shown in Fig. 11-3. Temperature of the tests was designated on a basis that the mentioned threshold of 0.15 Ω cm^2 was already matched at 625 °C. On one hand, it can be stated that throughout the span of 120 h measurement time, the R_p behaves relatively stable, yielding a final value of 0.090 Ω cm^2. It is even slightly lower than the beginning one (0.093 Ω cm^2). On the other hand, despite some minor fluctuations, there are neither sudden jumps nor obvious increasing or dropping of R_p in the whole measurement. This result indicates that LBCu electrode sintered at 800 °C exhibits a good long-term stability of the performance.

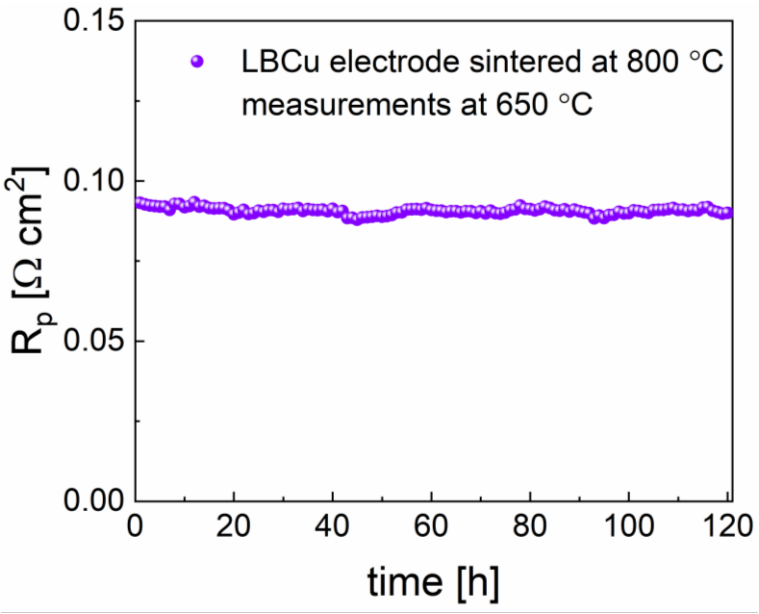

Fig. 11-3. Polarization resistance R_p of the LBCu electrode sintered at 800 °C as a function of time. Measurements conducted in air during 120 h experiment [227].

Moreover, the SEM micrographs were recorded, showing the micromorphology of the cross-section of the symmetrical cell after long-term measurements (Fig. 11-4). It is clearly visible that the LBCu electrode layer has a thickness of around 30 μm, and maintains a good porosity after the 120 h measurements, as well as the good adhesion with the LSGM electrolyte (contributing to the low R_p values). When focusing on the

EDS maps, all elements related exclusively to LBCu, i.e. Ba and Cu are distributed homogeneously on the electrode's part, while Sr, Ga, and Mg are located in the LSGM part. La, which is present in both materials, can be observed at both parts. Importantly, no regions having enrichment in a given element could be observed. Therefore, without any elemental segregation detected, it can be concluded that no interfacial reaction between the LBCu electrode and LSGM electrolyte took place after the measurements This is in good accordance with the results of the chemical compatibility measurements (Figs. 8-10a and b).

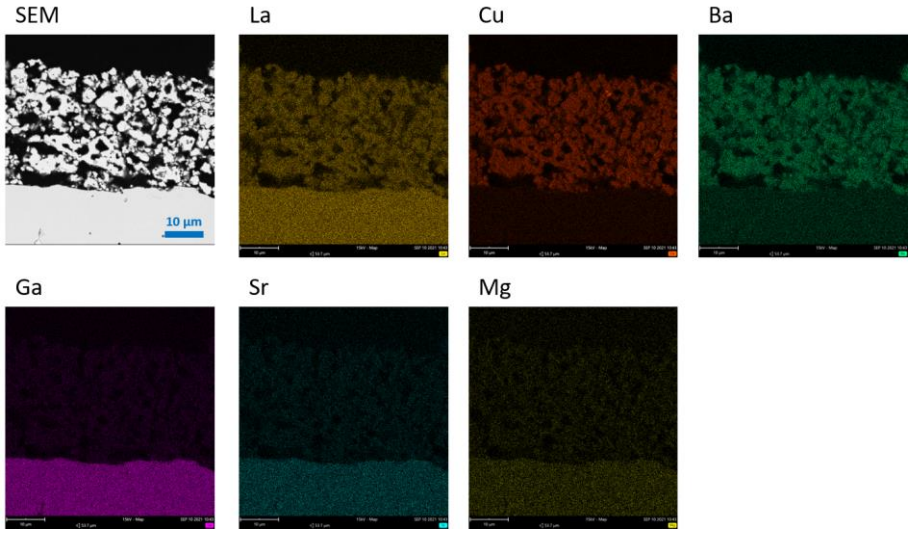

Fig. 11-4. Elemental maps gathered in SEM/EDS experiments for the cross-section of the interface of the LBCu oxygen electrode sintered at 800 °C with the LSGM electrolyte, after testing for 120 h in the symmetrical cell configuration [227].

As excellent electrocatalytic activity of the optimized LBCu electrode was confirmed in the symmetrical cell configuration, as well as it was shown to possess suitable long-term stability, it is of interest to apply and test such electrode on the LSGM electrolyte-supported full cell. Since LDC buffer has to be used on the fuel electrode side, the configuration of the tested cell was Ni-GDC|LDC|LSGM|LBCu, representing the fuel electrode, buffer layer, electrolyte, and oxygen electrode, respectively. The obtained results of tests in the SOFC mode can be seen in Fig. 11-5a. Relatively high power density outputs can be seen, as calculated from the current density-voltage (I-V) curves at each tested temperature. For example, the cell reaches over 160 mW cm^{-2} and 250 mW cm^{-2} at 600 °C and 650 °C, respectively, denoting a good performance in the lower temperature range. Even with the applied thin LSGM electrolyte, all the I-V curves are mostly straight, indicating very limited or negligible effect from the activation polarization part on the total polarization resistance. In general, the obtained output performance is excellent, when compared with data for other Cu-based electrodes, e.g. $NdBa_{0.5}Sr_{0.5}Cu_2O_{5+\delta}$, $PrBa_{0.5}Sr_{0.5}Cu_2O_{5+\delta}$, $La_4BaCu_5O_{13\pm\delta}$, and $LaNi_{0.5}Cu_{0.5}O_{3-\delta}$ at lower temperatures [199,203,287]. Although the performance is lower than for the high Co-content $LaCo_{0.4}Ni_{0.4}Cu_{0.2}O_{3-\delta}$ [288], the optimized LBCu can be still regarded as very promising

electrode. As mentioned, there is also a noticeable improvement over the previously published data for $La_4BaCu_5O_{13\pm\delta}$ oxygen electrode tested in a similar configuration, which allows to say that the intrinsic properties of $La_{1.5}Ba_{1.5}Cu_3O_{7\pm\delta}$ triple perovskite contribute considerably to the enhancement.

Additionally, performance in the reversed mode of the cell (as an electrolyzer) was also characterized for the selected temperature of 800 °C (Fig. 11-5b). Based on the data it can be concluded that LBCu shows also good electrocatalytic activity towards the oxygen evolution reaction (OER), reaching a current density of over 370 mA cm^{-2} at 1.5 V. Meanwhile, the measured Nyquist plots of the full cell are presented in Fig. 11-5c. The recalculated area specific ohmic resistances are less than 1 Ω cm^2 and 0.6 Ω cm^2 at 600 °C and 650 °C, respectively, which contribute effectively to the desirable performance level in the fuel cell mode (Fig. 11-5a). When it comes to the polarization part, two arcs are explicitly visible in the range of 600-750 °C, with the high frequency one obviously diminished at 800 °C.

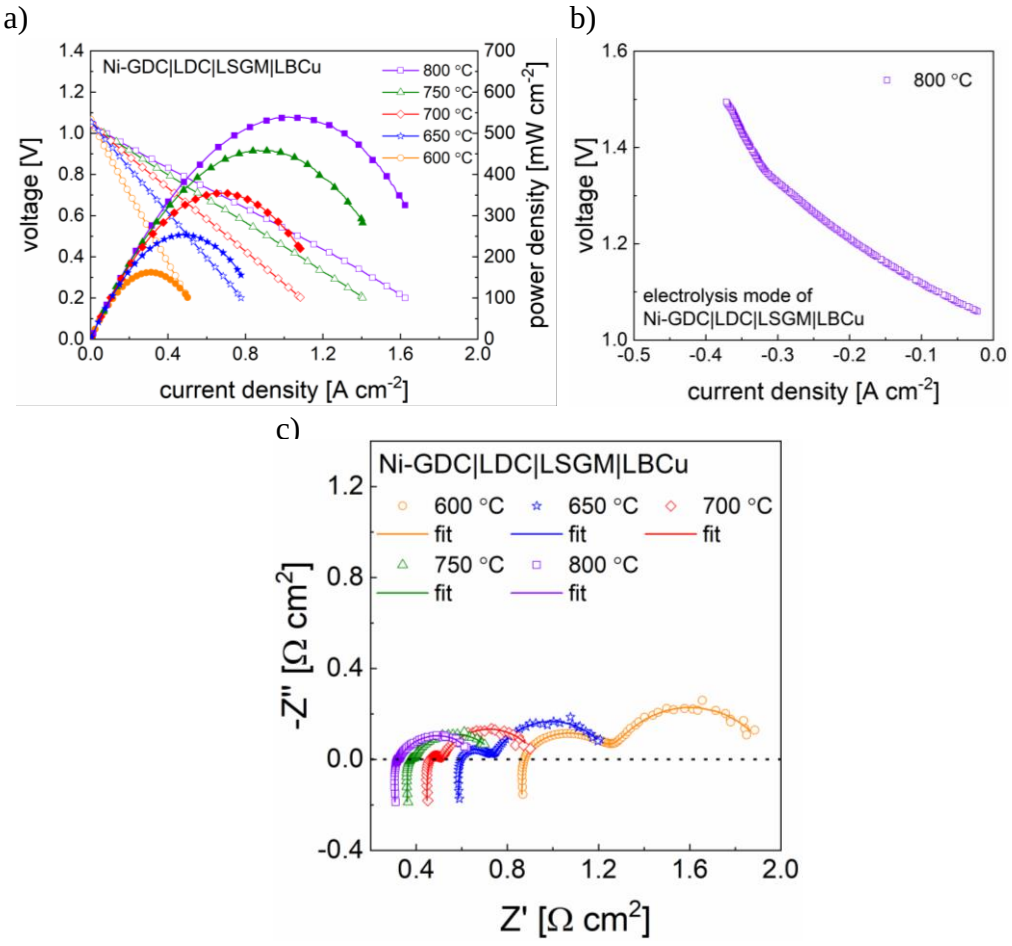

Fig. 11-5. a) Current density-voltage (I-V) curves and the related power density output of the Ni-GDC|LDC|LSGM|LBCu full cell measured in the 600-800 °C range, b) the respective I-V curve of the same cell working in the electrolysis mode at 800 °C. c) EIS data of the measured single cell as a function of temperature with respective fits [227].

11.2. $GdBa_{0.5}Sr_{0.5}Co_{2-x}Cu_xO_{5+\delta}$ as the oxygen electrode materials

The selected $GdBa_{0.5}Sr_{0.5}Co_{2-x}Cu_xO_{5+\delta}$ oxides also benefit from the possible lowered sintering temperature for electrode layers, as they contain a relatively high content of Cu. After a series of initial trials, 900 °C was selected as the most suitable temperature, which is higher than that for the best LBCu electrode, but still relatively low. Initially, the electrochemical tests were done in the same configuration, as described in the previous chapter, i.e. with the LSGM electrolyte and Ag current collector in symmetrical cells. However, suitable chemical stability toward the GDC electrolyte enabled more comprehensive research with that electrolyte used as well.

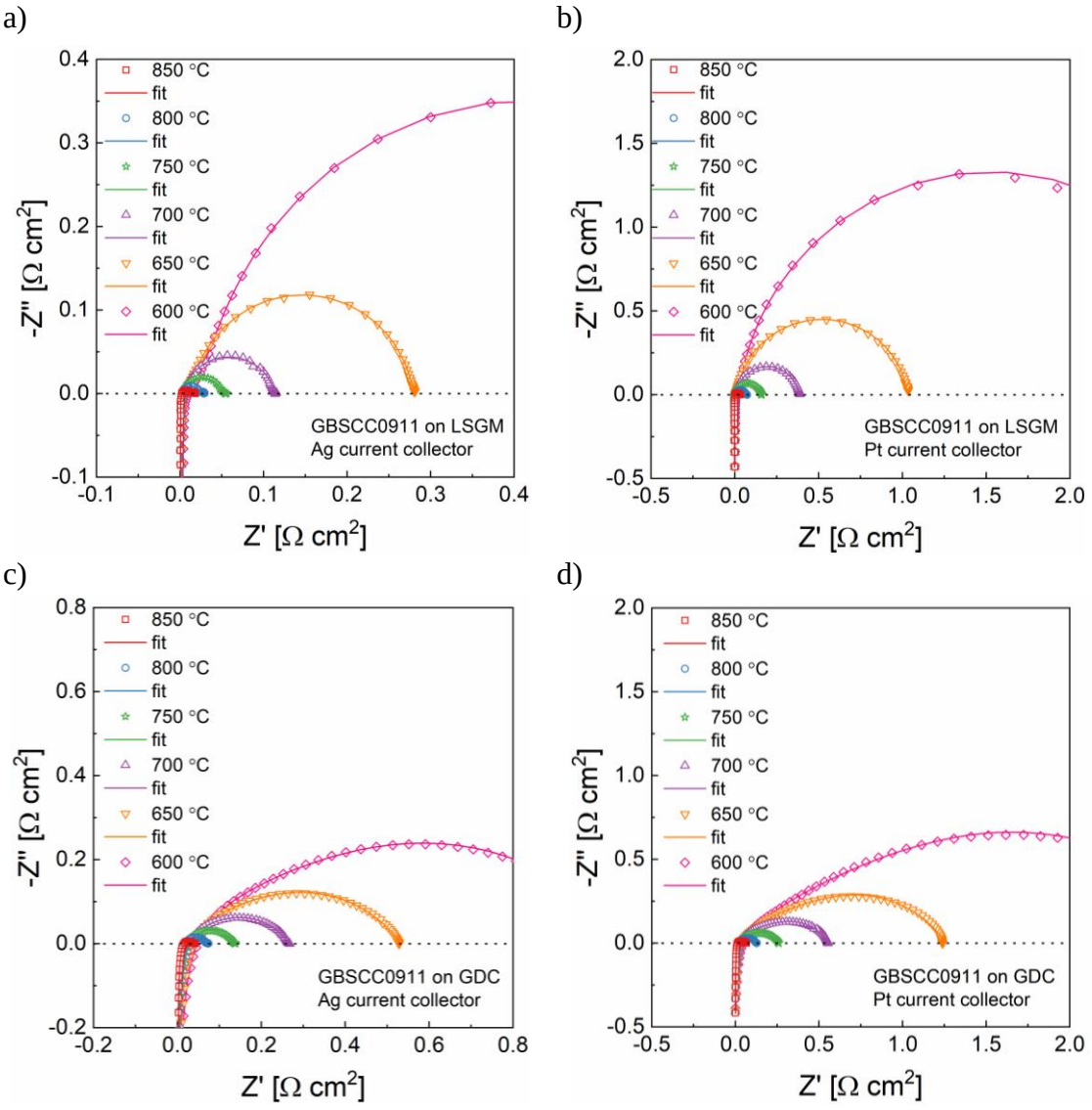

Fig. 11-6. EIS data with the respective fits for the symmetrical cells with GBSCC0911 electrodes: (a) LSGM-based with Ag, (b) LSGM-based with Pt, (c) GDC-based with Ag, and (d) GDC-based with Pt. Data recorded in the 600-850 °C temperature range [248].

However, relatively big differences in performance brought questions about nature of the observed changes, as well as possible role of the current collector as well, so additional studies with the Pt current collector were also performed. All the discussed results are depicted in Figs. 11-6a-d, Figs. 11-7a-d, an Figs. 11-8a and b.

As presented in Fig. 11-6a, arcs in the Nyquist plot show a clear temperature dependence. The GBSCC0911 electrode (on the LSGM electrolyte and with Ag current collector) reaches the lowest polarization resistance at 850 °C, with the R_p value of only 0.017 Ω cm^2. It is apparently better than for the GBSCC1010 electrode in the same conditions, for which the value is 0.026 Ω cm^2 (Fig. 11-7a). This comparison denotes an enhancement of the electrocatalytic activity owed to the higher copper doping content. The same conclusion can be also made at other temperatures (600-800 °C). Nevertheless, this enhancement does not act linearly with the copper content, and for instance, the R_p values of the GBSCC085115 electrode are somewhat higher than those recorded for the GBSCC0911 and GBSCC095105 electrodes on LSGM (Fig. 11-9a). This may stem from the fact that the GBSCC085115 material is at the limit of formation of the solid state solution, above which non negligible amount of the secondary phases appears.

In general, the obtained R_p resistances are comparable or even better than those for the state-of-the-art Co-based double-perovskite counterparts [257,289,290]. However, when the Pt current collector is applied, the relatively worse performance can be observed, especially at lower temperatures, while the differences are less obvious at higher temperatures (Fig. 11-6b, Fig. 11-7b). This effect can be clearly revealed on Arrhenius plots prepared for the GBSCC0911 and GBSCC1010 oxygen electrodes (Figs. 11-9b and c). Notably, the activation energy values of electrodes with the Pt current collector are higher by ca. 0.2 eV, comparing to the electrodes with Ag. This may due to the fact that Ag can possibly contribute to the electrocatalytic activity [291].

The comprehensive research indicates that when the applied electrolyte is changed to GDC, the obtained R_p values are obviously higher than those on LSGM (Fig. 11-6c, Fig. 11-7c). This phenomenon also occurs when Pt is adopted as the current collector (Fig. 11-6d, Fig. 11-7d). However, the calculated values of the activation energy are lower than for the electrodes prepared on LSGM (Figs. 11-9b and c). Similarly, an increase of the activation energy (by ca. 0.17-0.18 eV) also takes place on the GDC electrolyte when the Ag is replaced with Pt for both, GBSCC0911 and GBSCC1010 electrodes. Other trends can also be observed, including slightly lower activation energy for GBSCC0911 than for GBSCC1010 obtained on LSGM, which is reversed for the GDC electrolyte, no matter what current collector is applied. A question may be raised, what is the actual reason for such complicated behavior. In order to reply to this query and to have a comprehensive understanding of the ORR taking place on the considered electrodes, the symmetrical cells with the best performing GBSCC0911 electrode and the different electrolyte and current collector configurations were studied in more details, with the collected in air EIS data analyzed by the DRT method (Figs. 11-10a-d, Figs. 11-11a-d). Also (the most stable) cell with the GDC solid electrolyte and Pt current collector was tested as a function of the changing oxygen partial pressure, with the selected DRT analysis data presented in Figs. 11-12a-d, as well as comprehensive evaluation shown in Figs. 11-13a-c.

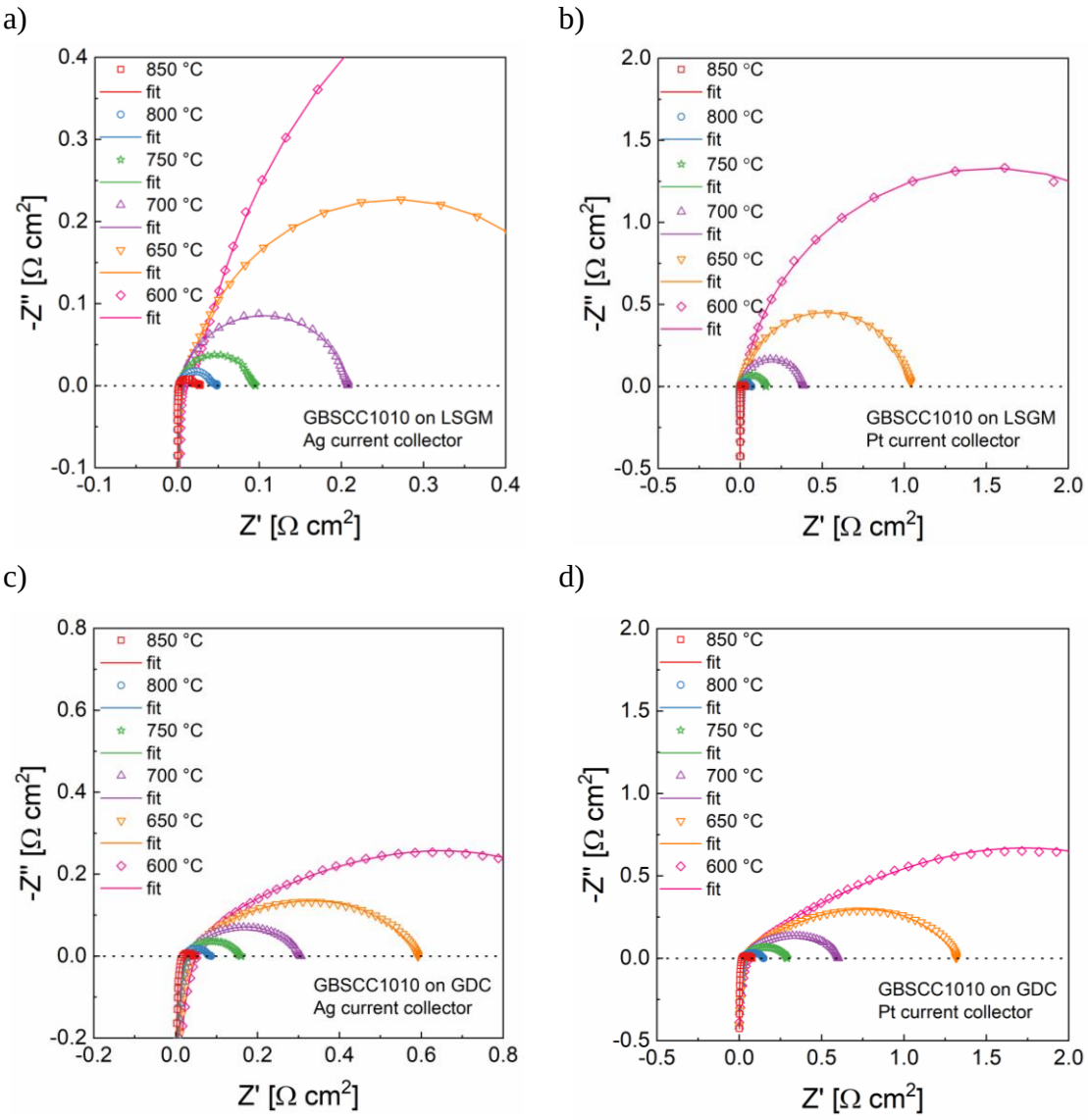

Fig. 11-7. EIS data with respective fits for the symmetrical cells with GBSCC1010 electrodes: (a) LSGM-based with Ag, (b) LSGM-based with Pt, (c) GDC-based with Ag, and (d) GDC-based with Pt. Data recorded in the 600-850 °C temperature range [248].

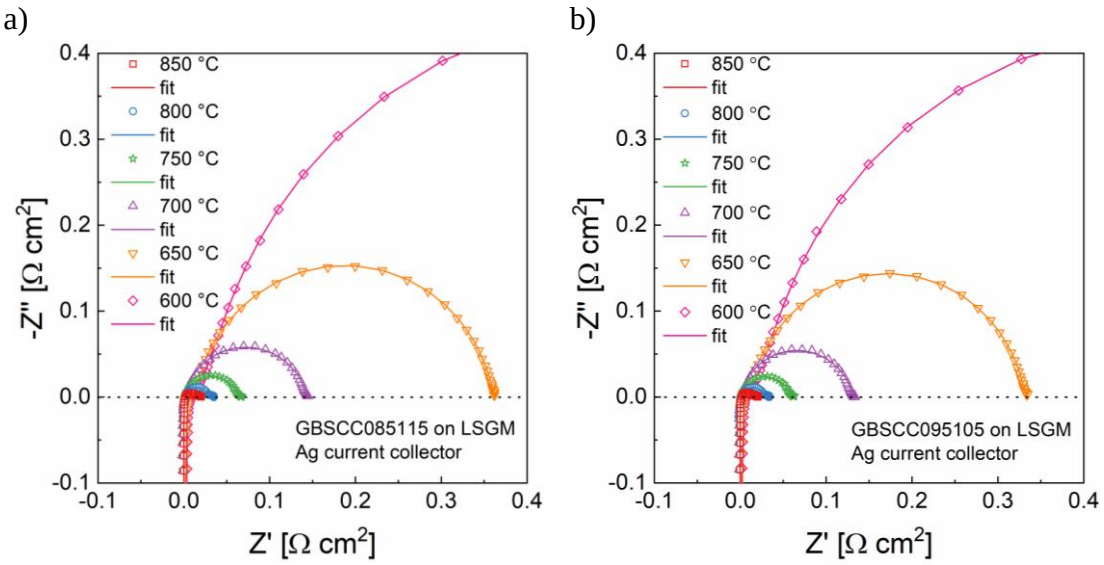

Fig. 11-8. EIS data with respective fits for the symmetrical cells with a) GBSCC085115 electrode, and b) GBSCC095105 electrode on LSGM with Ag current collector, respectively. Based on [247].

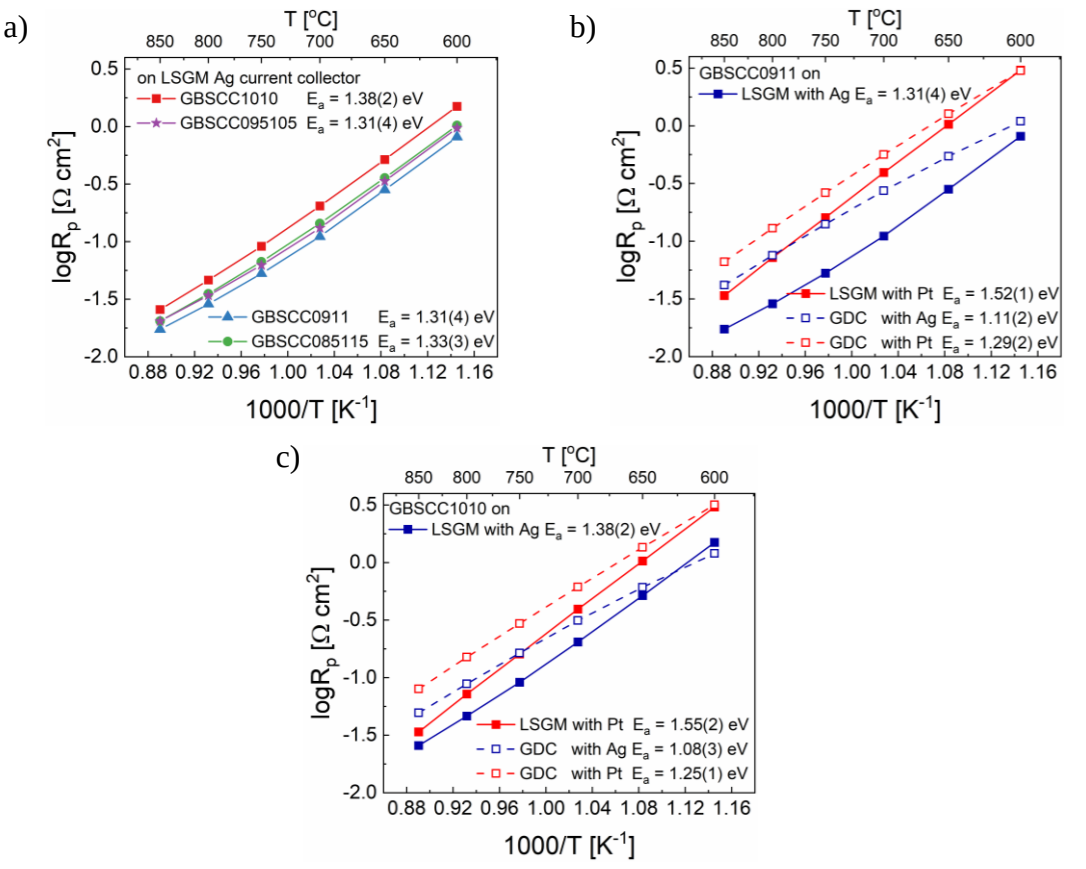

Fig. 11-9. Electrode polarization resistance R_p presented in Arrhenius-type coordinates for: a) all considered GBSCC electrodes on the LSGM electrolyte with the Ag current collector, b) GBSCC0911, and c) GBSCC1010 on the LSGM/GDC electrolyte with the Ag/Pt current collector, respectively [248]

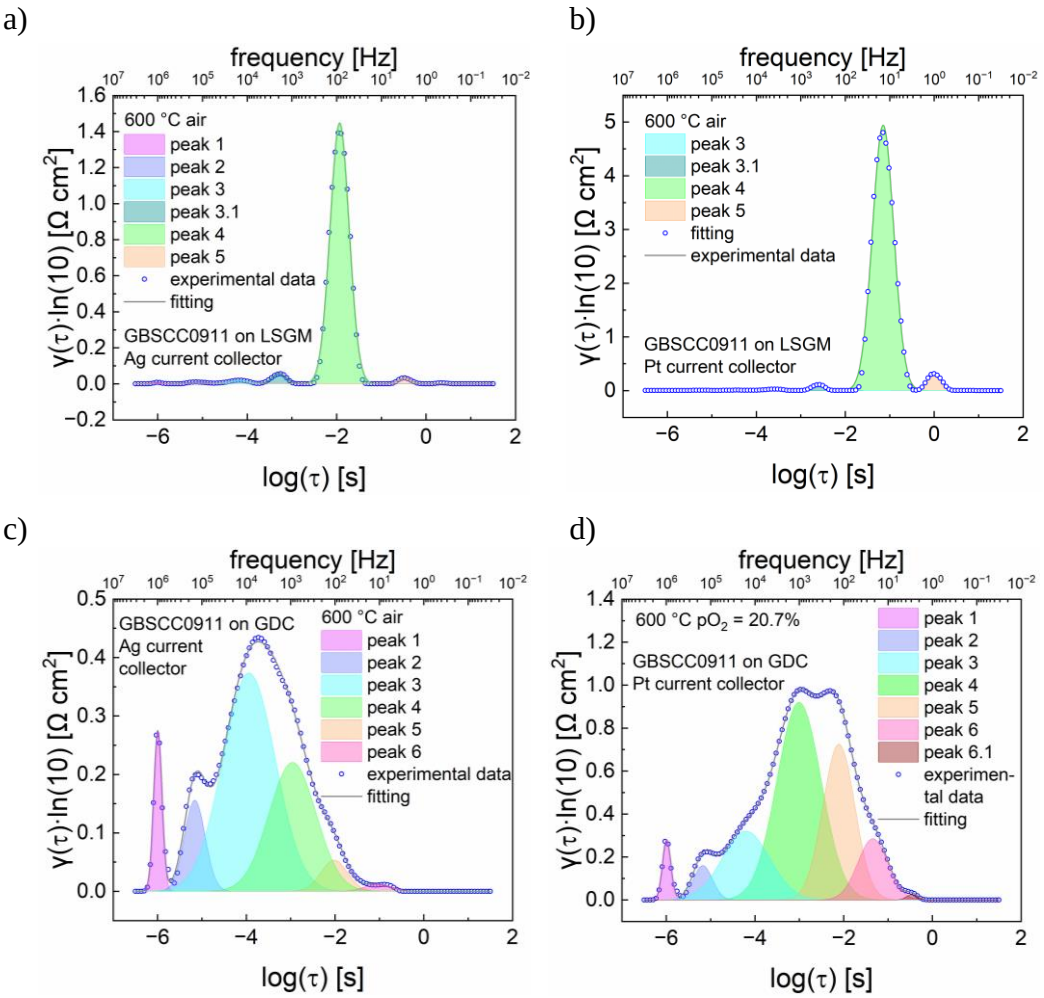

Fig. 11-10. Results of the DRT analysis as a function of τ for different symmetrical cells with GBSCC0911 electrodes. Data recorded at 600 °C for: a) LSGM electrolyte and Ag current collector, b) LSGM and Pt, c) GDC and Ag, and d) GDC and Pt [248].

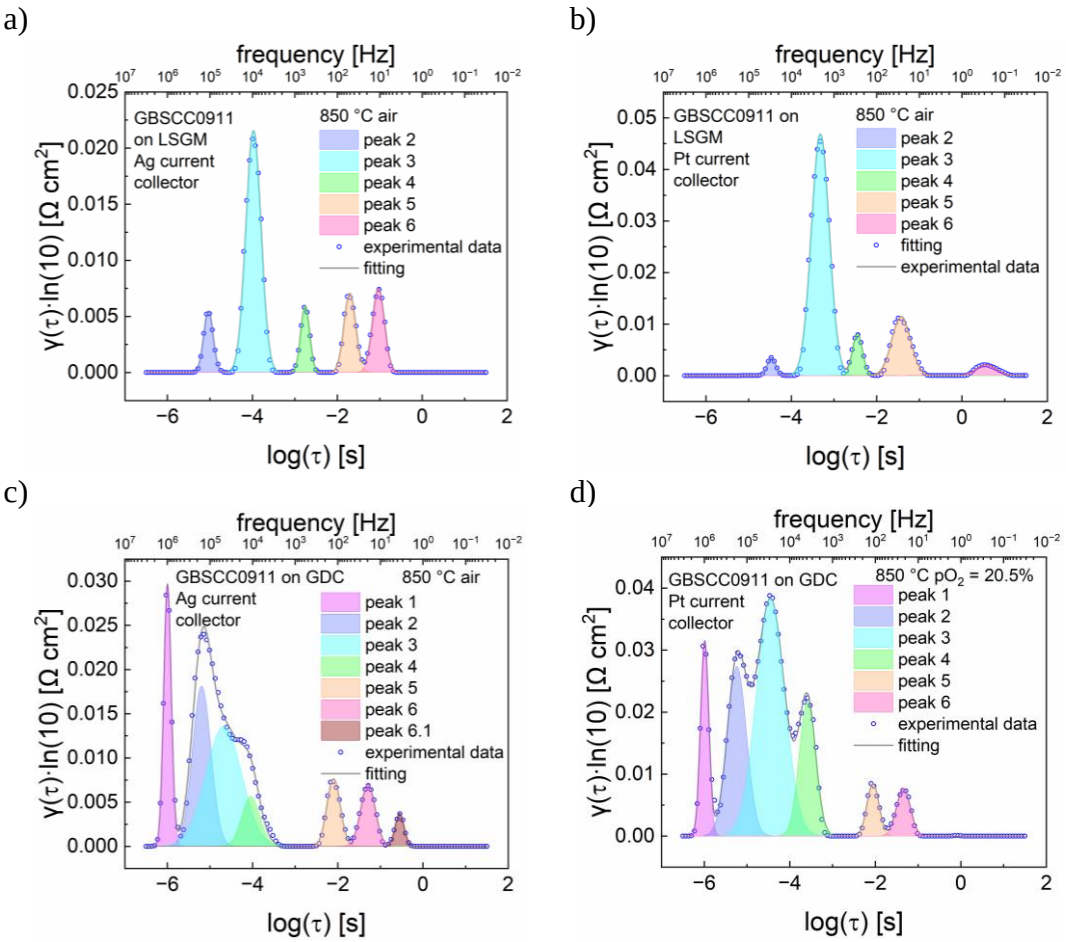

Fig. 11-11. Results of the DRT analysis as a function of τ for different symmetrical cells with GBSCC0911 electrodes. Data recorded at 850 °C for a) LSGM electrolyte and Ag current collector, b) LSGM and Pt, c) GDC and Ag, and d) GDC and Pt [248].

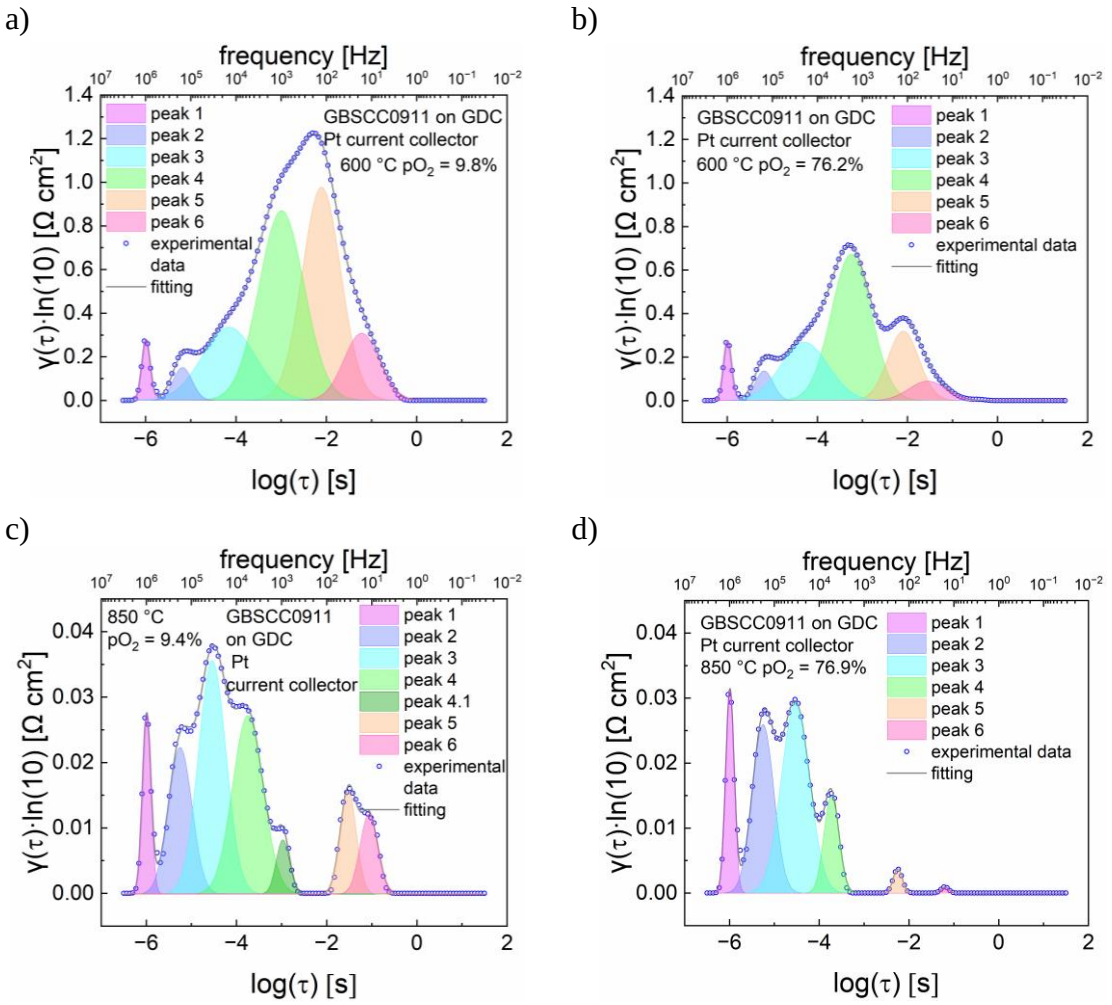

Fig. 11-12. Typical results of the DRT analysis for the selected pO_2 values as a function of τ, measured for the symmetrical cell with GBSCC0911 electrodes on the GDC electrolyte and with Pt current collector: a) and b) data recorded at 600 °C, as well as c) and d) at 850 °C for different pO_2, respectively [248].

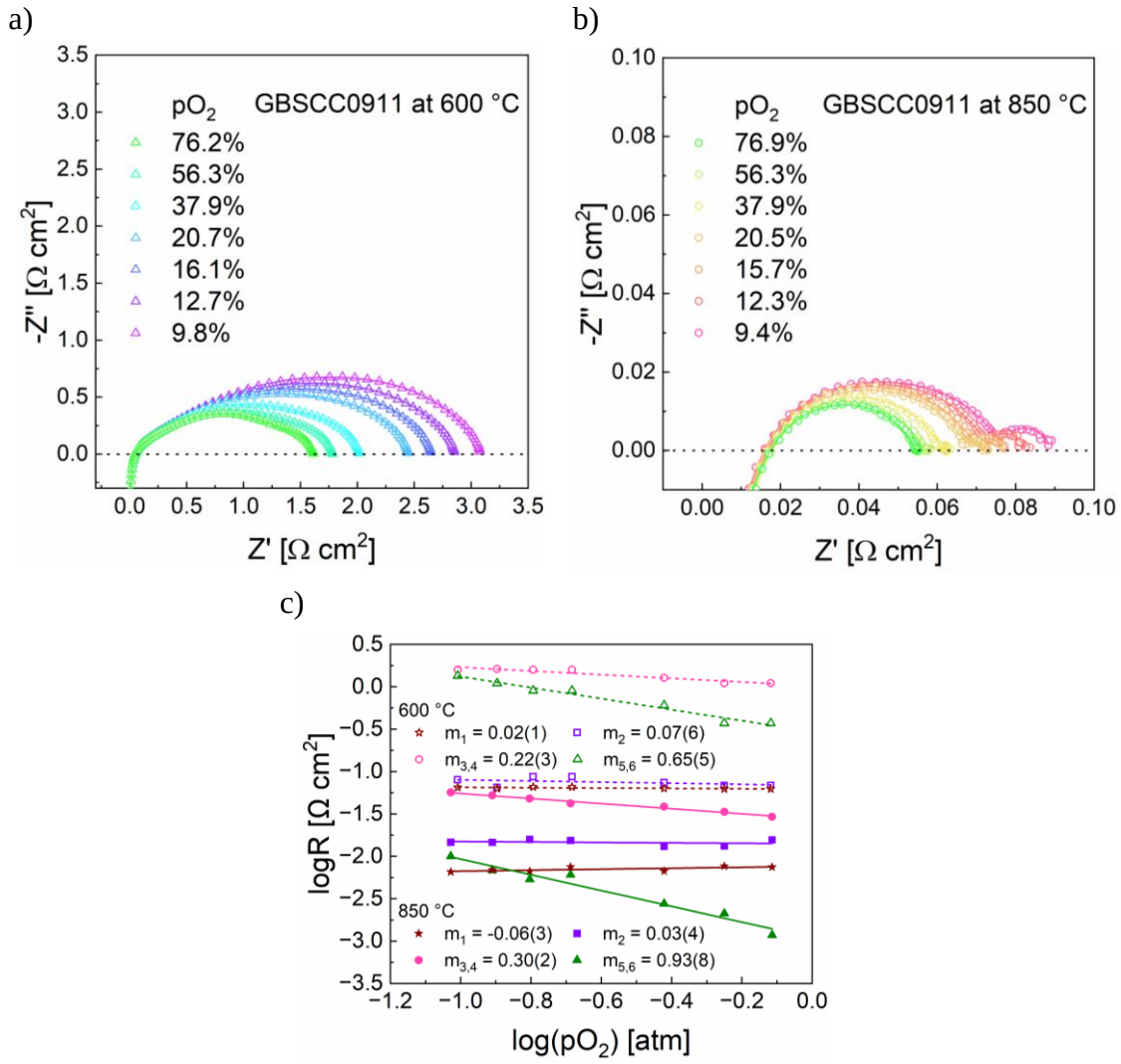

Fig. 11-13. Measured EIS spectra for the symmetrical cell (GBSCC0911 on GDC with Pt) as a function of pO_2 at a) 600, and b) 850 °C. The lines represent standard fits with the equivalent circuit. c) Dependence of the derived partial resistances as a function of pO_2 in log-log coordinates. Note the included slope values *m*, fitted for data registered at 600 and 850 °C [248].

The visible in all the presented DRT graphs numerous peaks correspond to different steps of the electrode reaction, however, depending on the used electrolyte, current collector, and temperature, the peaks may shift, diminish, or appear as merged with their adjacent peaks. This indicates that all these factors indeed have an effect on the electrochemical reactions taking place at the oxygen electrode. Considering theoretical knowledge of the ORR, it is of importance to introduce the characteristic indicator *m*, value of which represents different steps of the total reaction. It is known that the following steps are of importance: adsorption of oxygen molecules (m_{ad} = 1), dissociation of oxygen molecules (m_{dis} = 0.5), two-step reduction of oxygen (m_{red1} = 0.375 and m_{red2} = 0.125), incorporation of the reduced oxygen into lattice (m_{inc} = 0), and migration of oxygen anions through the electrode/electrolyte interface (m_{mig} = 0) [284–286]. In order

to determine which peak correspond to which step, it is necessary to conduct the EIS/DRT experiments as a function of pO_2. Considering time needed for such studies and their complexity, only the best performing GBSCC0911 electrode was selected, together with the GDC electrolyte and Pt current collector, as this configuration ensured the most stable performance (as explained in the next section).

In Figs. 11-13a and b, the EIS curves are presented in Nyquist plots for, as recorded at 600 °C and 850 °C. It is evident that the arcs become larger with the decreasing pO_2 (from around 76% to 9%). Although there are main 6 peaks identified in such varied pO_2 measurements (Figs. 11-12a-d), some of the peaks can be combined together and eventually interpreted as four prime electrochemical processes. As depicted in Fig. 11-13c, the peak 1 can be analyzed separately since it acts quite independently to the varied pO_2, so m_1 at 600 °C = 0.02(1), and m_1 at 850 °C = −0.06(3). Alongside with its highest frequency (10^6 Hz), it can be consequently related to the process of charge transfer through the interface of electrode/electrolyte. As for peak 2 (m_2 at 600 °C = 0.07(6), m_2 at 850 °C = 0.03(4)), it demonstrates the similar independency in relation to the pO_2, and since it occurs at relatively lower frequencies (< 10^5 Hz), thus, it can be regarded as the incorporation of reduced oxygen into the electrode lattice. Then, there are two peaks, peak 3 (also 3.1, if present) and 4 (also 4.1), appearing at the frequency range of 10^3-10^5 Hz and changing considerably in different pO_2 ($m_{3,4}$ at 600 °C = 0.22(3), $m_{3,4}$ at 850 °C = 0.30(2)). Since the combination of these two peaks can be more reasonably interpreted than their separate state, they are, together, assigned to the reduction process of oxygen, with the value of combined $m_{3,4}$ close to 0.25. Additionally, these two peaks jointly show up as the dominant area in all DRT graphs, indicating that the oxygen reduction is actually the rate-limiting step in the ORR on the GBSCC0911 electrode. Speaking of the remaining peaks, peak 5 and 6 (also 6.1) can be integrally considered as well, which allow to observe a strong dependence on the pO_2 values ($m_{5,6}$ at 600 °C = 0.65(5) and $m_{5,6}$ at 850 °C = 0.93(8)). Therefore, their origin can be regarded as the oxygen molecules dissociation at lower temperature ($m_{5,6}$ close to 0.5), while the oxygen adsorption at higher temperature ($m_{5,6}$ close to 1). In general, such behavior of the GBSCC0911 electrode and related interpretation, presented in the author's paper [248], follows closely previously published data for other, highly-efficient oxygen electrode materials [292,293].

As for the comparison with respect to the other electrolyte and current collector types, the calculated partial polarization resistances are summarized in Tab. 11-2. There is an array of conclusions that can be drawn as well. Firstly, as it can be visibly derived, the charge transfer process favors the interface of GBSCC0911 with LSGM (data at 850 °C are actually close to 0). When GDC is adopted as the electrolyte, the polarization resistance at the interface does not contribute obviously to the total R_p at 600 °C, while it indeed has bigger impact at 850 °C, although still not the dominant one. This difference in charge transfer may be explained as due to the similar perovskite-type related crystal structures of both, GBSCC0911 and LSGM. Secondly, the LSGM-supported cells also show an advantage in terms of the incorporation of the reduced oxygen into the lattice. Thirdly, another difference is about the current collector used, and it is obvious that the oxygen reduction can be improved by Ag, with which the cells show much lower $R_{3,4}$ at both temperatures. This fact again proves the catalytic effect aroused by Ag [291]. As it

is shown in the graphs, $R_{3,4}$ undoubtedly takes up the biggest proportion in the total polarization resistance R_p, denoting that the oxygen reduction is indeed the rate-limiting step in the ORR. Last but not least, when focusing on $R_{5,6}$, silver also seems to be beneficial to the adsorption and dissociation of oxygen, which is more evident at lower temperature [248].

Tab. 11-2. Comparison of components of the total polarization resistance of symmetrical cells with GBSCC0911 electrodes and different electrolytes and current collectors. Data were recorded in air or close to air oxygen partial pressure at two different temperatures [248]

Cell	600 °C				850 °C			
	R_1 [Ω cm^2]	R_2 [Ω cm^2]	$R_{3,4}$ [Ω cm^2]	$R_{5,6}$ [Ω cm^2]	R_1 [Ω cm^2]	R_2 [Ω cm^2]	$R_{3,4}$ [Ω cm^2]	$R_{5,6}$ [Ω cm^2]
LSGM Ag	0.002	0.005	0.805	0.012	-	0.002	0.011	0.005
LSGM Pt	-	-	3.010	0.126	-	0.001	0.027	0.008
GDC Ag	0.064	0.091	0.849	0.049	0.006	0.010	0.017	0.007
GDC Pt	0.066	0.087	1.584	0.903	0.008	0.015	0.042	0.016

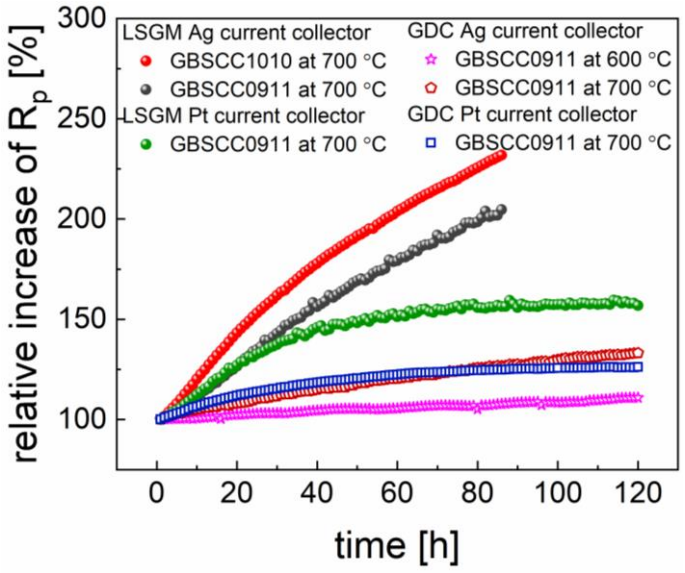

Fig. 11-14. Relative increase with time of the polarization resistance of different cells (on LSGM or GDC electrolyte) with selected GBSCC electrodes and Ag or Pt current collectors [248].

Aiming at evaluation of the long-term stability of the obtained oxygen electrodes and symmetrical cells, changes of the EIS spectra, and therefore in R_p values, were registered for 120 h in experiments performed at 700 °C. The related results are shown combined in Fig. 11-14 in a form of relative changes. Importantly, both electrodes, GBSCC0911 and

GBSCC1010 manufactured on the LSGM with Ag used as the current collector demonstrate an increasing trend of R_p with time. The electrode with lower Cu content shows a higher relative increase of the values, over 225% after 80 h of tests. The reason of this unstable performance can be identified in the SEM results (Figs. 11-15a and b, Figs. 11-16a and b), presented below. As can be seen in Figs. 11-15b, the segregation of the Sr element is clearly detected at the interface between the GBSCC1010 electrode and LSGM electrolyte. Interestingly, such segregation seems to be confined by a higher copper doping content in the GBSCC0911 electrode, although it can be still somehow identified (Fig. 11-16a). Nevertheless, the improvement observed for GBSCC0911 in terms of the R_p increase with time is not satisfactory. At the same time, it is necessary to note that when Ag is replaced with Pt, a stable performance can be obtained on LSGM (represented by green ball points in Fig. 11-14) after 80 h of operation.

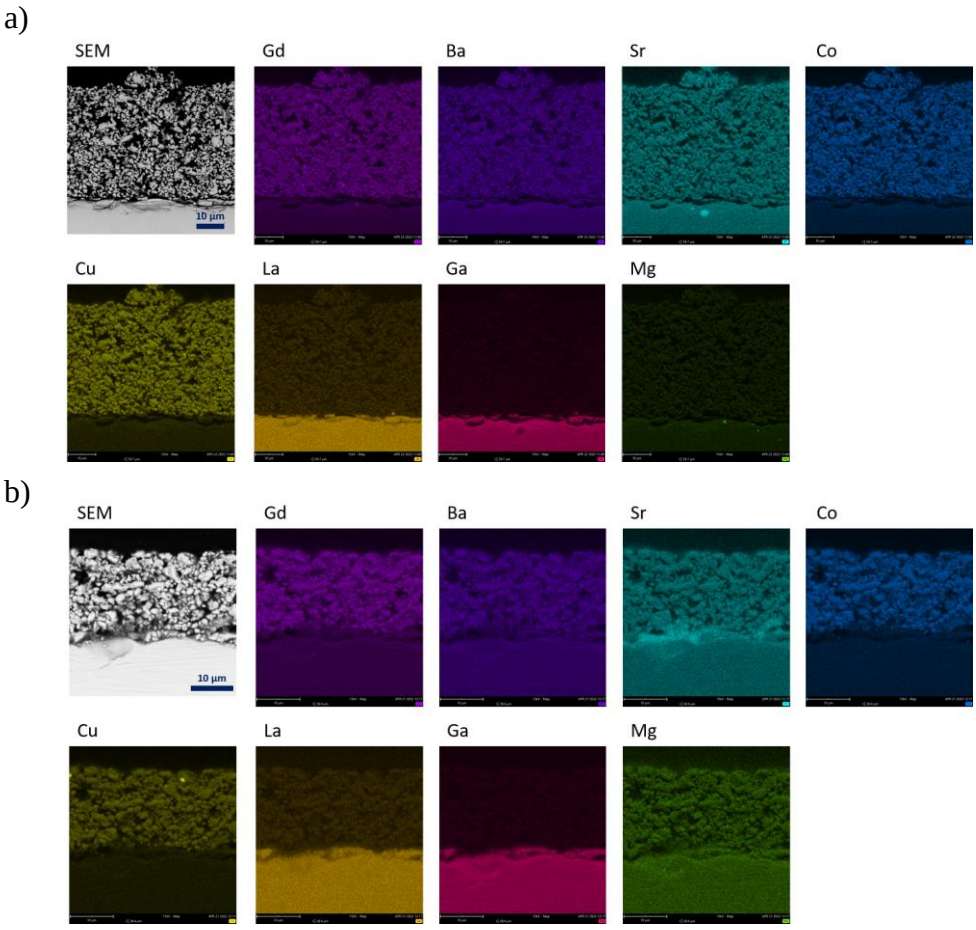

Fig. 11-15. Morphology (cross-section) of the measured oxygen electrode/electrolyte interface together with the corresponding elemental maps obtained by EDS, a) GBSCC0911 after EIS tests in the symmetrical cell (LSGM electrolyte), b) GBSCC1010 after long-term stability measurements in the symmetrical cell (LSGM electrolyte). Notice strontium segregation at the interface [248].

a)

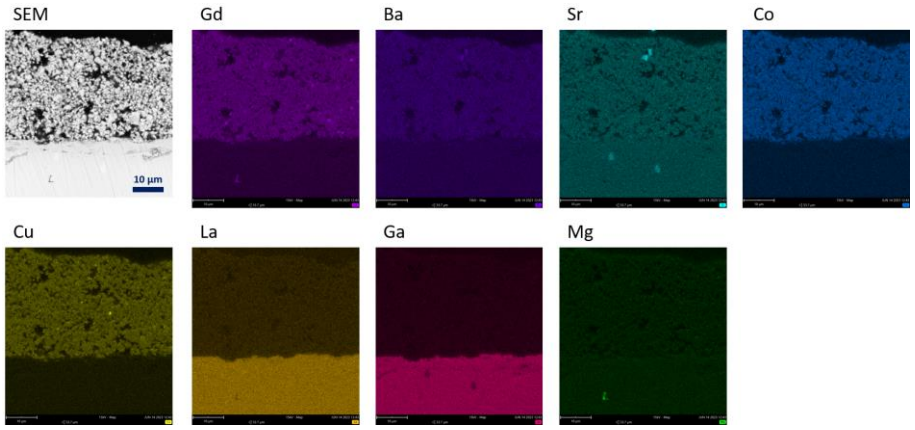

b)

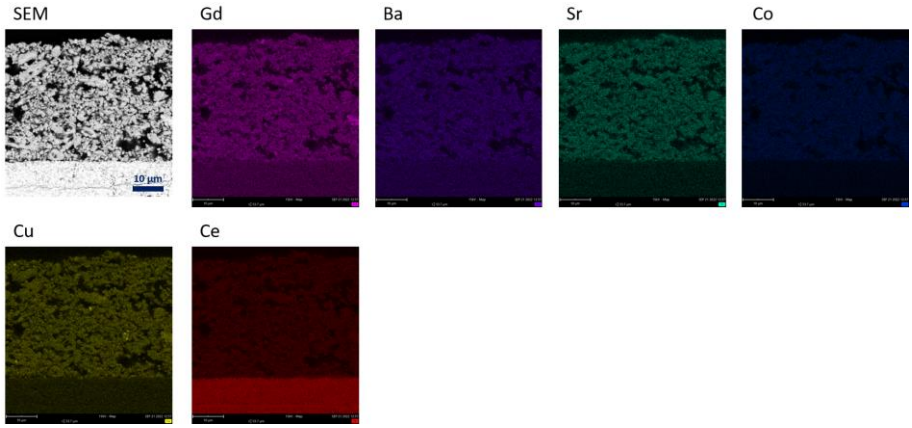

Fig. 11-16 . Morphology (cross-section) of the measured oxygen electrode/electrolyte interface together with the corresponding elemental maps obtained by EDS, a) GBSCC0911 after long-term stability measurements in the symmetrical cell (LSGM electrolyte). Sr segregation is suppressed, b) GBSCC0911 after long-term stability measurements in the symmetrical cell (GDC electrolyte). No Sr segregation occurred [248]

While data for the GDC-based cell with Ag still show the increasing trend (pentagons), it is not as pronounced as for the LSGM-based cells, however, no stabilization can be seen. Furthermore, lowering operation temperature can also bring about a much lower relative increase of R_p (pink stars, ca. 10% increase at the end), but the increasing trend is still visible during whole time of the measurements. Such results indicate that the Ag current collector is not suitable for the long-term operation with GBSCC electrodes, although it can result in the excellent electrochemical performance in the short-term operation (Figs. 11-9b and c). On the other hand, Applying GDC as the electrolyte can prevent Sr segregation at the interface (Fig. 11-16b), and yield a stable performance with Pt used as the current collector (blue squares in Fig. 11-14). Such cell shows a relative increase of R_p by only 0.04 % h^{-1} in the last 40 hours of operation. This value can be regarded as very promising for the laboratory-scale cells, and similar results are also provided in other work [294].

In all the micro-morphology tests of the electrodes after measurements, as observed by SEM, a good adhesion of the electrode layers to both electrolytes is maintained. This can be related to the relatively well-matched thermal expansion of the materials. Despite some Sr segregation for GBSCC1010, it did not cause delamination or cracks formation. In addition, the desirable porosity of all the tested electrode layers can be seen, enabling sufficient gas diffusion and adsorption of oxygen on surface of the electrodes. Overall, it can be stated that favorable morphological feature are not limiting the GBSCC electrodes, but rather, are contributing to the very good electrochemical performance.

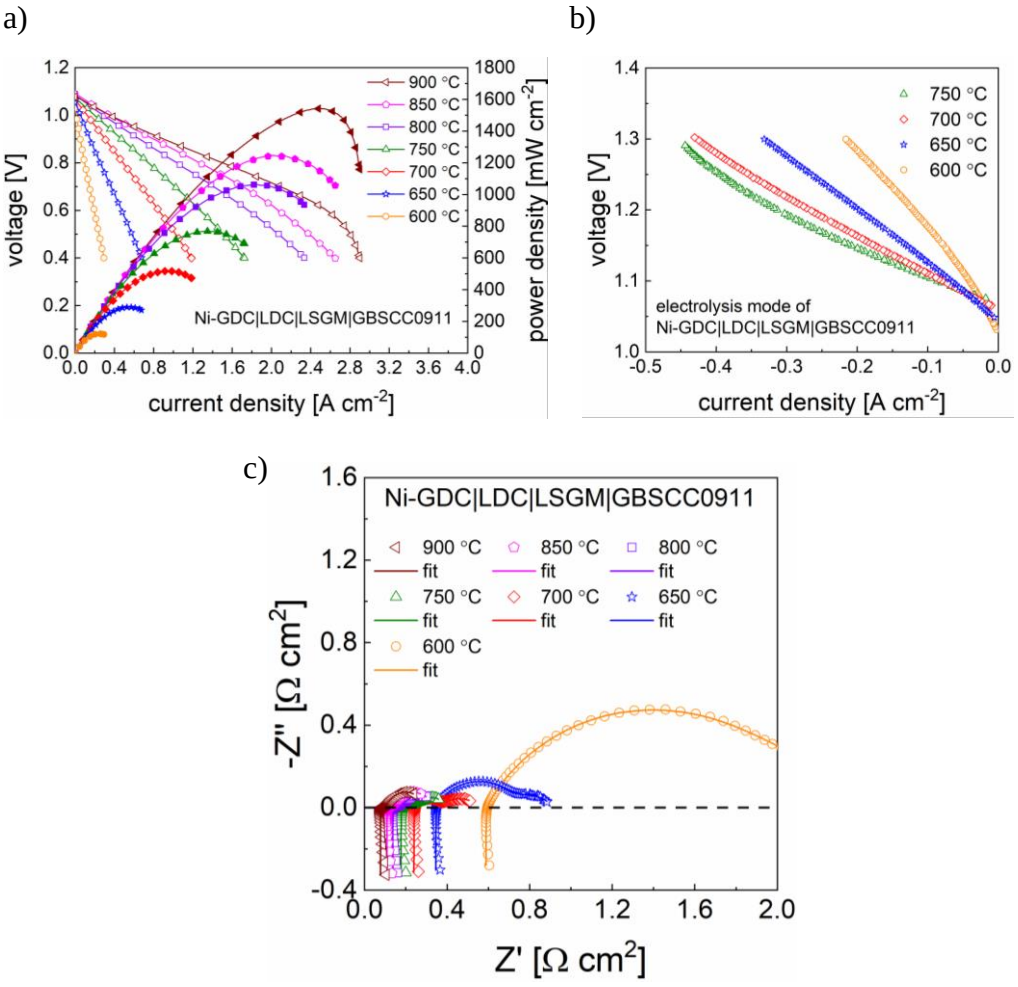

Fig. 11-17. a) Current density-voltage (I-V) curves and the related power density output of the Ni-GDC|LDC|LSGM|GBSCC0911 full cell measured in the 600-800 °C range, b) the respective I-V curve of the same cell working in the electrolysis mode. c) EIS data of the measured single cell as a function of temperature with respective fits [248].

Importantly, applying the developed oxygen electrodes in a full cell is also of interest to evaluate the output power density dependence on temperature, as well as working ability in the reversed mode. While the best performance could be expected for the GBSCC0911, for better comparison, the GBSCC1010 is also selected and applied.

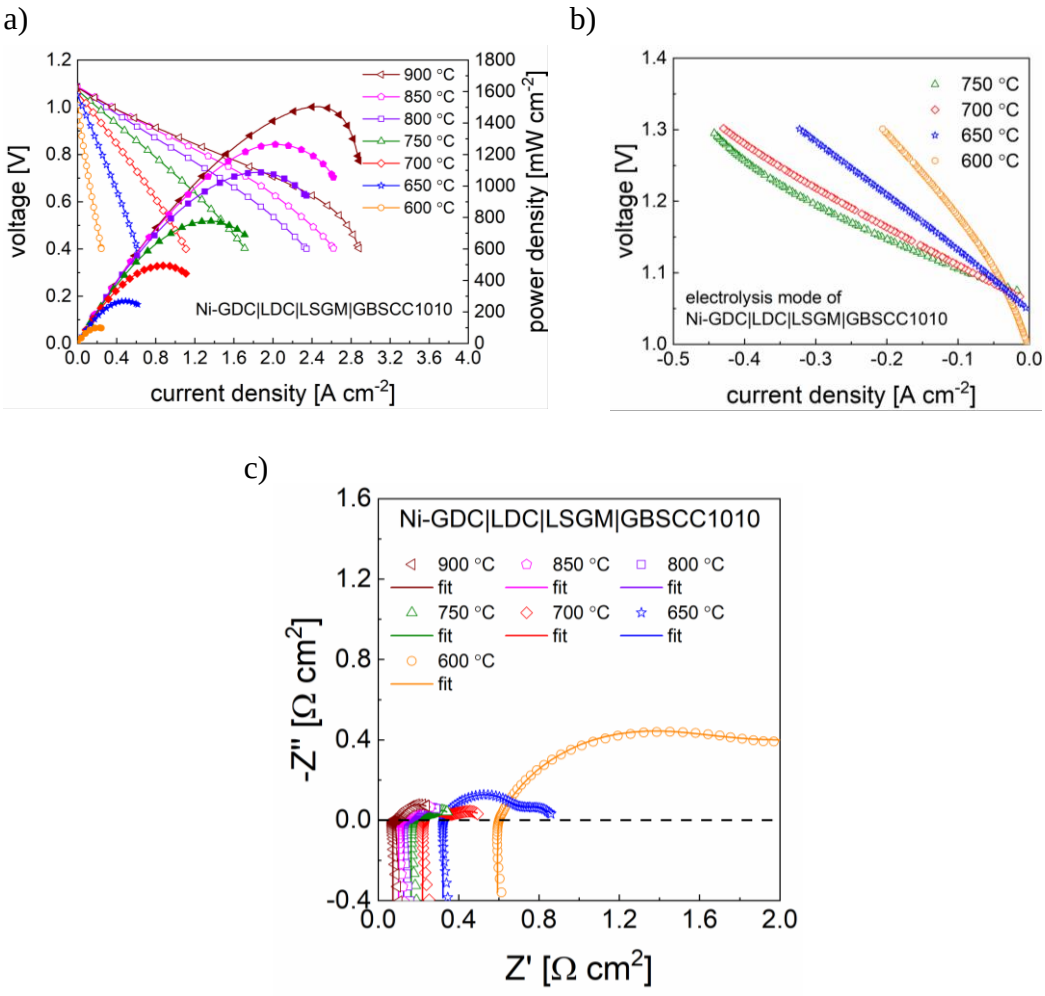

Fig. 11-18. a) Current density-voltage (I-V) curves and the related power density output of the Ni-GDC|LDC|LSGM|GBSCC1010 full cell measured in the 600-800 °C range, b) the respective I-V curve of the same cell working in the electrolysis mode. c) EIS data of the measured single cell as a function of temperature with respective fits [248].

As shown in Fig. 11-17a, the I-V curves demonstrate an expected, increasing maximum specific current density and power with the increasing temperature. Specifically, for the Ni-GDC|LDC|LSGM|GBSCC0911 full cell a peak of output power exceeding 1500 mW cm^{-2} could be measured at 900 °C, followed by around 1240 mW cm^{-2} at 850 °C. Similarly high values were measured for the Ni-GDC|LDC|LSGM|GBSCC1010 full cell (Fig. 11-18a). Such surprisingly high output power densities suggest that both, GBSCC0911 and GBSCC 1010 can potentially work in a practical fuel cell, while the GBSCC0911 electrode with lower Co-content appears as more competitive, as compared to those high Co-containing materials [262,295,296]. Notably, when the cell works at 700 °C or below, GBSCC0911-based full cell shows an improved power density. In general, the obtained performance is obviously better than that for $LnBaCo_2O_{5+\delta}$ (Ln = Pr, Nd and Gd) [250,297]. It is also interesting to compare the performance at 600 °C and 650 °C with the LBCu-based full cell (Fig. 11-5a). While

both GBSCC electrodes perform somewhat better at 650 °C, at the lower temperature still the cell with LBCu oxygen electrode showed higher power output.

Concerning work as an electrolyzer, the Ni-GDC|LDC|LSGM|GBSCC0911 cell reaches a current density of 0.44 A cm^{-2} with the voltage of 1.3 V at 750 °C (Fig. 11-17b). The other electrode also performs in a similar manner (Fig. 11-18b), suggesting that GBSCC oxygen electrodes can also be applied in the SOEC mode. As far as the polarization resistance of the full cells is concerned, the EIS curves in Fig. 11-17c and Fig. 11-18c indicate low values of both, polarization resistance and ohmic component-related parts, which effectively help to achieve the exceptional output performance in the fuel cell mode (Fig. 11-17a and Fig. 11-18a). To be specific, there are three arcs identified in measured temperature ranges, of which the arc at high frequencies gradually merges with the one at middle frequencies at lower temperature.

Additionally, the GBSCC085115 material was also applied as the oxygen electrode in an anode-supported full cell, with Ni-YSZ used as the fuel electrode and YSZ as electrolyte, as well as GDC buffer included. As can be seen in Fig. 11-19a, the cell could reach a peak output power density of over 725 mW cm^{-2} at 850 °C, and 575 mW cm^{-2} at 800 °C. It is also noteworthy that in the electrolysis mode the cell delivered a current density of around 0.33 A cm^{-2} with the voltage of 1.5 V at 800 °C, implying the promising application of GBSCC085115 material for the reversed mode of operation.

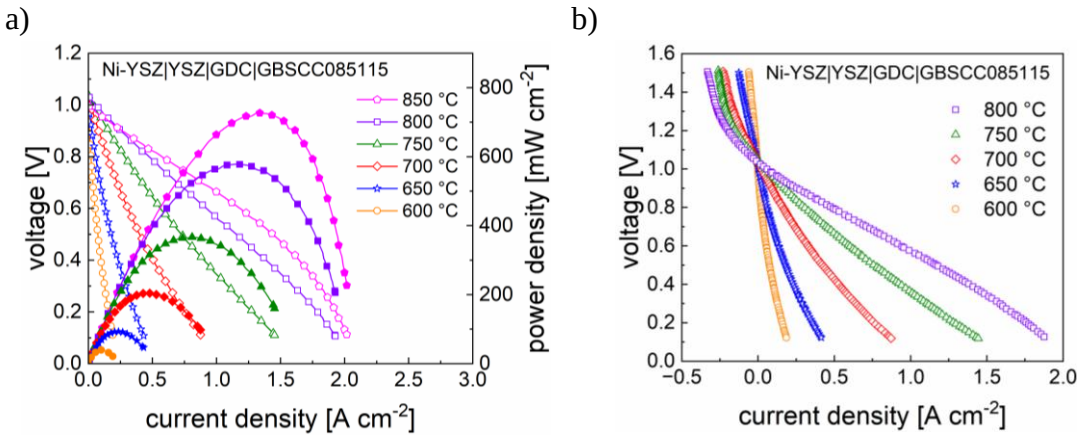

Fig. 11-19. a) Power density output of the Ni-YSZ|YSZ|GDC|GBSCC085115 full cell measured in the 600-800 °C range, b) the respective I-V curve of the same cell working in the fuel cell and electrolysis modes [247].

11.3. $La_{0.6}Sr_{0.4}Ni_{0.15}Mn_{0.15}Fe_{0.15}Cu_xCo_{0.55-x}O_{3-\delta}$ as the oxygen electrode materials

Results presented in this chapter regarding development of the oxygen electrodes from the proposed $La_{0.6}Sr_{0.4}Ni_{0.15}Mn_{0.15}Fe_{0.15}Cu_xCo_{0.55-x}O_{3-\delta}$ system follow the general idea presented in two previous subchapters. However, the initial experiment for the cells manufactured on the GDC electrolyte were conducted during the international internship, which was realized at the Catalonia Institute for Energy Research IREC, Barcelona, Spain. Since the screen-printing equipment at the Laboratory of Nanoionics and Fuel Cells led by Prof. Albert Tarancón is different than the one used at the Department of Hydrogen Energy, Faculty of Energy and Fuels, there are some differences in the initial results, which can be ascribed to the electrodes' morphology.

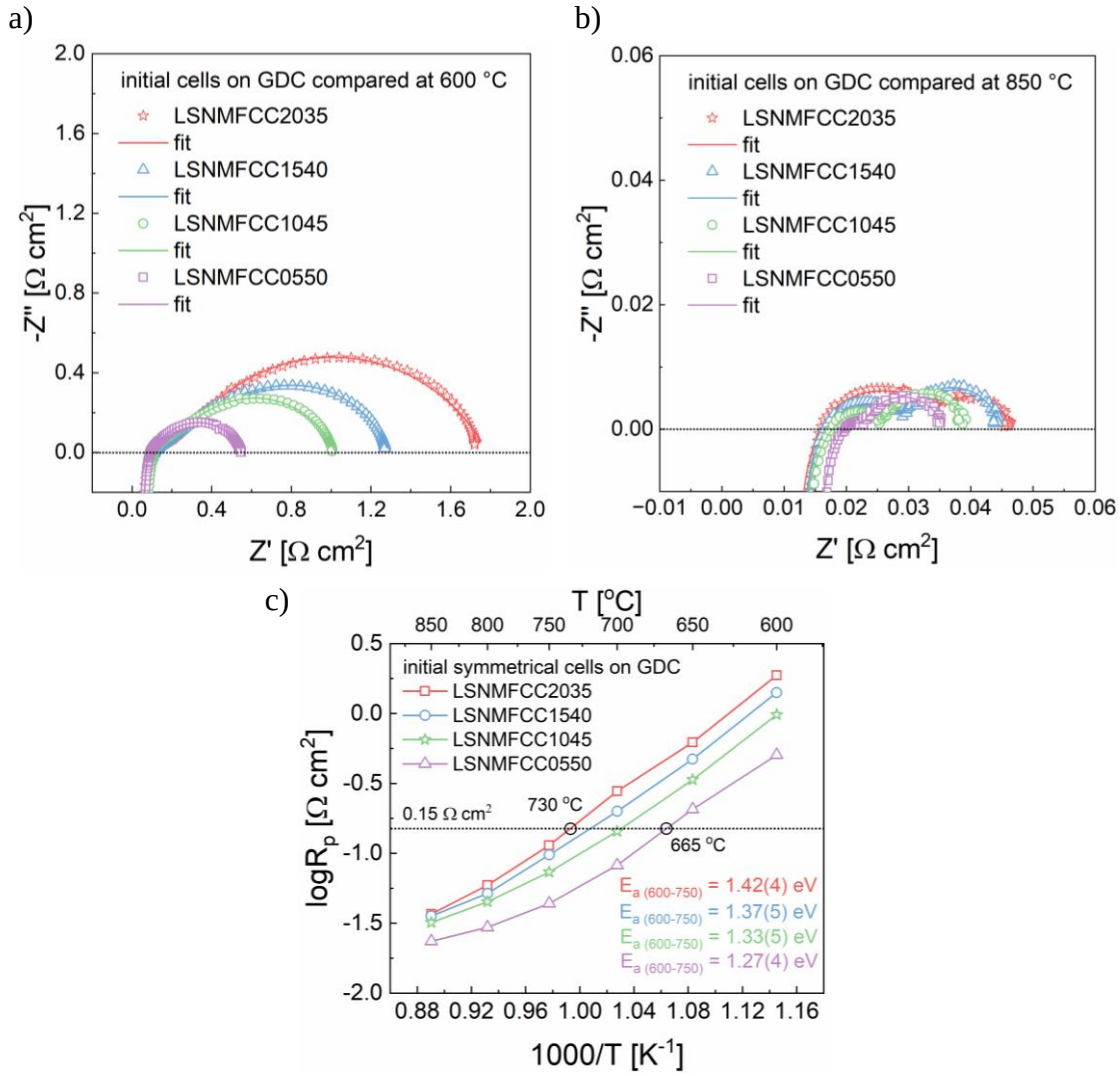

Fig. 11-20. Typical Nyquist plots for the LSNMFCC electrodes (GDC electrolyte) compared at a) 600 °C, and b) 850 °C with their respective fits. c) Related electrode polarization resistance R_p presented in Arrhenius-type coordinates. Notice the included activation energy values.

As the feature of Cu-containing oxides, LSNMFCC-based electrodes can be also sintered at relatively low temperatures (850 °C on LSGM and 900 °C on GDC), which is certainly advantageous in manufacturing of button-type symmetrical and full cells for the electrochemical characterizations. The results of initial measurements based on the GDC electrolyte for four selected electrodes are shown in Figs. 11-20a and b. It can be easily concluded that higher cobalt content in the oxides can yield lower R_p values, e.g. LSNMFCC0550 can meet the requirement of 0.15 Ω cm^2 at around 665 °C, while LSNMFCC2035 meets it at 730 °C (Fig. 11-20c). This fact indicates that Co indeed plays a dominant role in determining the electrocatalytic activity in the LSNMFCC series of electrode materials.

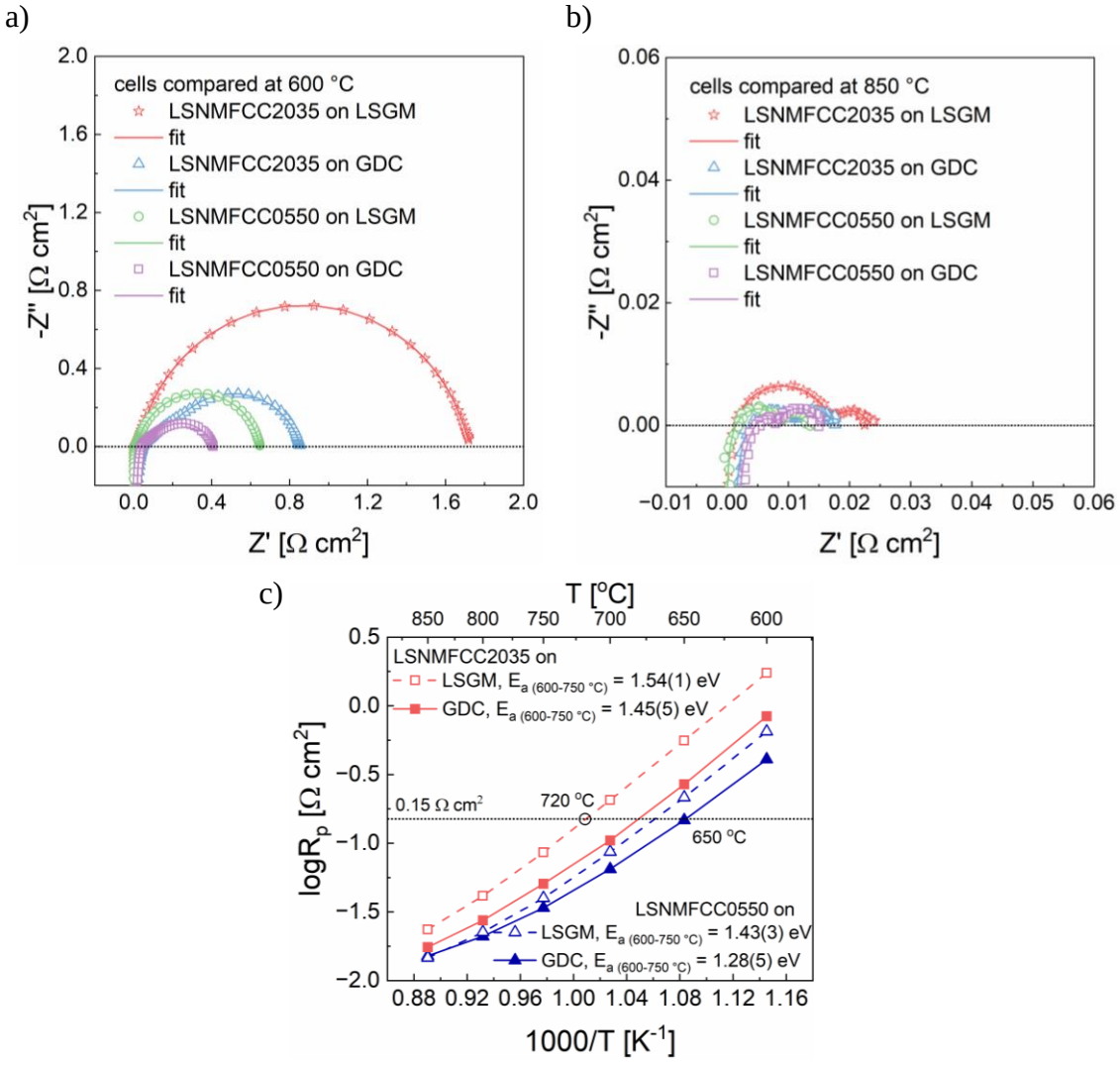

Fig. 11-21. Typical Nyquist plots for the LSNMFCC0550 and LSNMFCC2035 electrodes compared at a) 600 °C, and b) 850 °C with their respective fits. Data for cells based on the LSGM or GDC electrolyte. c) Related electrode polarization resistance R_p presented in Arrhenius-type coordinates.

Given that both, GDC and LSGM are compatible with LSNMFCC series (Figs. 10-12a-h), further characterizations based on the two electrolytes are also implemented in an improved approach in cell manufacturing process (the final procedure was done in the same manner like for the previously discussed systems). Notably, since the observed trend was the same as in the initial measurements, just LSNMFCC0550 and LSNMFCC2035 electrodes were selected for the more detailed studies, which represent the best and the worst electrocatalytic activity, respectively related to the highest and lowest Co-content.

As presented in Fig. 11-21, there are several observations worth paying attention to. Firstly, the improved approach in the cell manufacturing indeed made a positive difference on the R_p values of both cells. To be specific, in Fig. 11-21c, the cell with LSNMFCC0550 on GDC meets the 0.15 Ω cm^2 at 650 °C, yielding a value of R_p as low as 0.015 Ω cm^2 at 850 °C, while cell with LSNMFCC2035 meets the mentioned threshold at around 680 °C, reaching the R_p value as low as 0.018 Ω cm^2 at 850 °C based on the GDC as well. Secondly, in both cases, for LSNMFCC0550 and LSNMFCC2035, the cells based on GDC can yield lower R_p in comparison to those based on the LSGM electrolyte. It is unexpectedly different to the results presented for the GBSCC system. Specifically, LSNMFCC0550 on LSGM reaches 0.65 Ω cm^2 at 600 °C, as compared to 0.41 Ω cm^2 on GDC at the same temperature. This comparison can be also found for LSNMFCC2035, with 1.73 Ω cm^2 and 0.84 Ω cm^2 on LSGM and GDC, respectively. Thirdly, no matter the type of the electrolyte applied, the R_p values of LSNMFCC0550 are always lower than those of LSNMFCC2035, which is in good accordance with the initial cells' measurements and confirms the role of the cobalt element.

In order to have an insight into the reasons of such the improvement in comparison to the initial symmetrical cells, the DRT analysis was again adopted to unveil the details regarding of the electrochemical steps of the ORR. The results are shown in Fig. 11-22, with visible peaks in the respective log(τ) ranges. According to the conclusions from the GBSCC system, those characteristic peaks can be assigned to different electrochemical steps of the ORR. Consequently, the respective peaks were analyzed in a similar manner for the LSNMFCC system.

The peak 1 in both Figs. 11-22a and b, shows an evident improvement when cells are optimized, implying that the charge transfer at the electrode/electrolyte interface is effectively improved. Also, some enhancements, although not as big as for peak 1, can be seen also for peak 2, which corresponds to the enhancement in the reduced oxygen incorporation into the crystal lattice. The peak 4 of the optimized cells is apparently smaller than that of the initial cells, indicating a boosted process of the oxygen reduction on the electrode. Last but not least, although not so significant as for other peaks, some enhancements related to the oxygen adsorption and dissociation can be also seen. Overall, the improved approach of the cell manufacturing can effectively enhance and optimize the performance.

It is noteworthy that although the LSNMFCC0550 demonstrates the best electrochemical performance among the LSNMFCC series, eventually, the material with the highest Cu content (lowest Co amount), LSNMFCC2035, appears as more interesting, as it possesses the highest configurational entropy (Tab. 7-4). In this aspect, some trials

have been performed to improve its properties further, as documented in the next chapter devoted to the application of the electrospinning method.

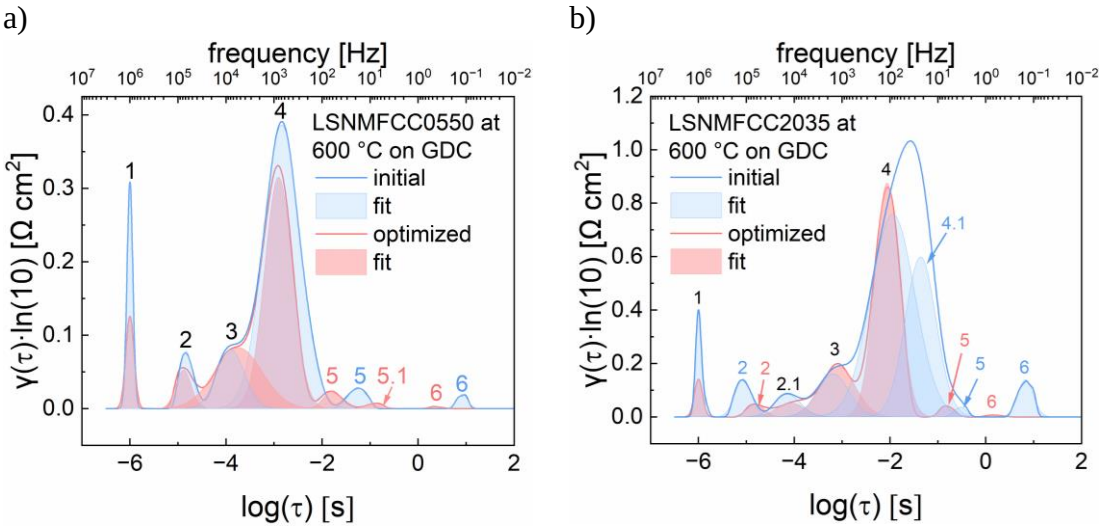

Fig. 11-22. Comparison based on results of the DRT analyses as a function of log(τ) for the initial and optimized symmetrical cells based on the GDC electrolytes, as compared at 600 °C, with the a) LSNMFCC0550, and b) LSNMFCC2035 oxygen electrode, respectively.

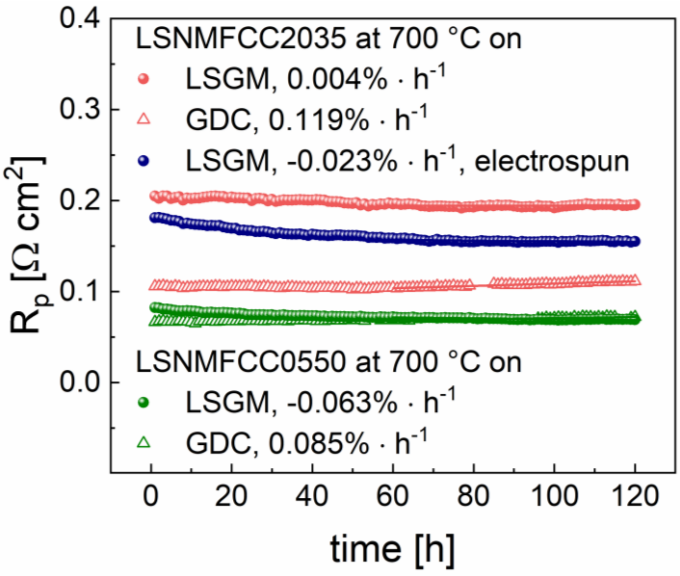

Fig. 11-23. Polarization resistance R_p changes for LSNMFCC2035 and LSNMFCC0550 electrodes manufactured on LSGM or GDC as a function of time. Measurements conducted in air during 120 h experiments. Note the calculated change rates in the last 60 h.

It is of importance to assess the stability of the cells in a long-term operation, and such studies were performed at 700 °C. As gathered in Fig. 11-23, cells with LSNMFCC2035

and LSNMFCC0550 electrodes, all demonstrate an excellent long-term stability of the performance up to 120 h. To be specific, the visible relative increase for the cells based on the GDC electrolyte is calculated as lower than 0.1% h^{-1} with either LSNMFCC2035 or LSNMFCC0550 electrode (last 60 h of operation). Interestingly, the R_p values were even found as almost not changing or even decreasing with time in the case of all tested cells on the LSGM electrolyte, including the electrode manufactured with the electrospun LSNMFCC2035 material (discussed in the next chapter). In order to get understanding of the very stable or even decreasing behavior of R_p, the DRT analysis is again adopted. As visible in Fig. 11-24a, when GDC is used as the electrolyte, despite a slightly smaller peak 4 after the 120 h tests, all other peaks undergo a rising change, which is particularly visible for peaks 3, 5, 6 and 7. This indicates that the processes of oxygen adsorption and dissociation become a little bit sluggish with time, with a slight change in the charge transfer at the interface of the electrode with electrolyte also visible. When it comes to the cell manufactured on LSGM (Fig. 11-24b), the biggest change is visible on peak 3, denoting an improved oxygen reduction process after 120 h. Some small enhancements can be also detected on peaks 5 and 6, implying a better oxygen adsorption process.

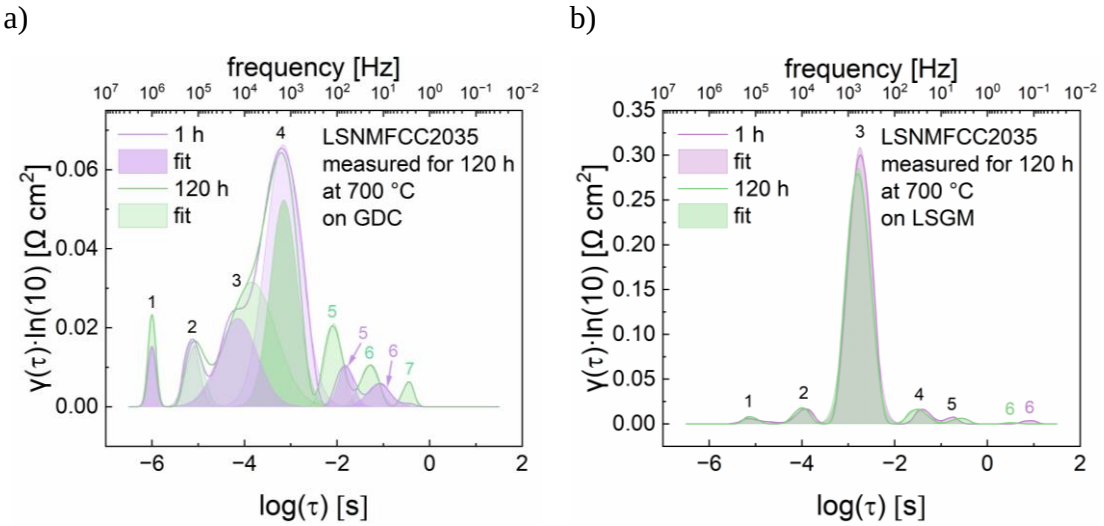

Fig. 11-24. Comparison based on results of the DRT analysis as a function of log(τ) for cells with LSNMFCC2035 oxygen electrode based on a) GDC, and b) LSGM, compared at the beginning and after 120 h long-term measurements at 700 °C.

Considering morphology of the electrodes after the tests, as visible in Figs. 11-25a and b, LSNMFCC2035 electrodes maintain a good adhesion with either GDC or LSGM after the 120 h measurements, as well as show a desired porosity in the electrode layer. Moreover, in the respective EDS maps, there is no segregation visible in the elemental distribution across or on the electrode/electrolyte interface, indicating a good chemical stability of LSNMFCC2035 material used as the oxygen electrode. Small bright spots in the Cu maps can be noticed, however, it seems that this level of precipitation can be neglected. Also, in Figs. 11-26a and b, a detailed elemental analysis is realized on the selected spots (colorful circles) to elaborate more on the LSGM electrolyte. The actual

measured elemental ratios are in good accordance with the expected ones, while no significant signal from other elements could be detected. These results confirm the good chemical stability of LSGM as well.

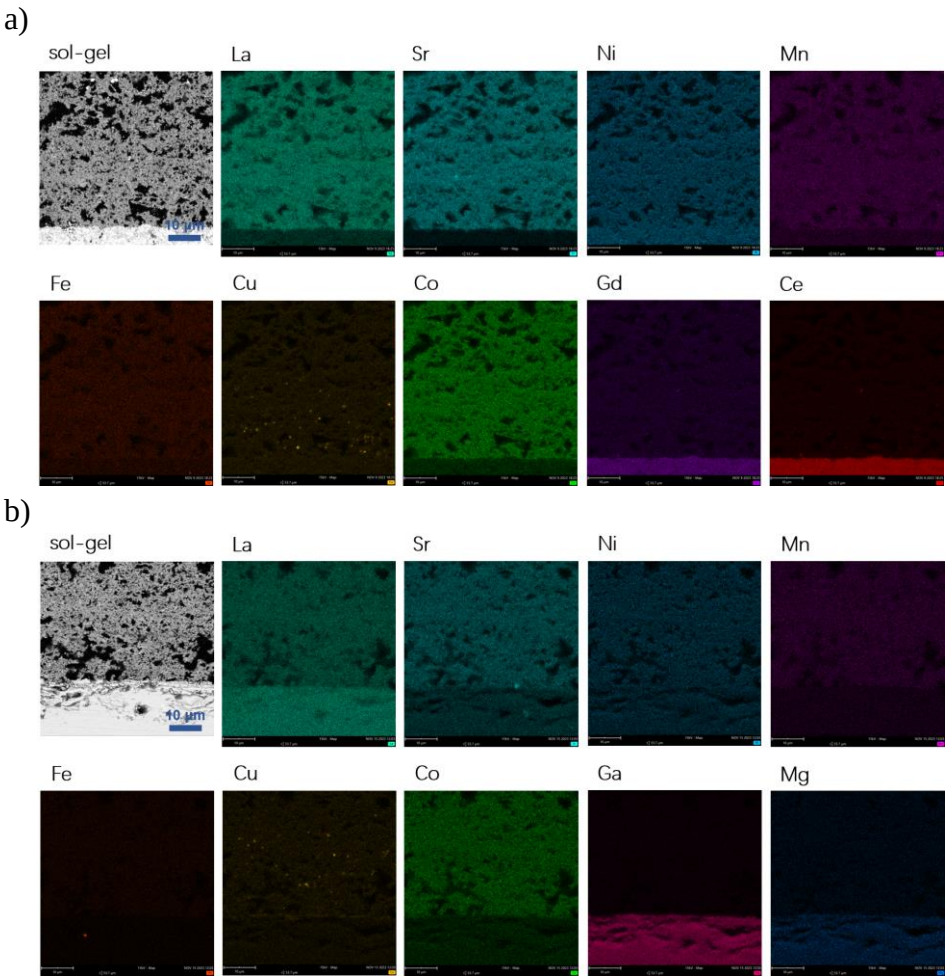

Fig. 11-25. Morphology (cross-section) of the measured cells with LSNMFCC2035 used as the oxygen electrode, together with the corresponding elemental maps obtained by EDS. a) Data for cells on GDC, and b) LSGM.

a)

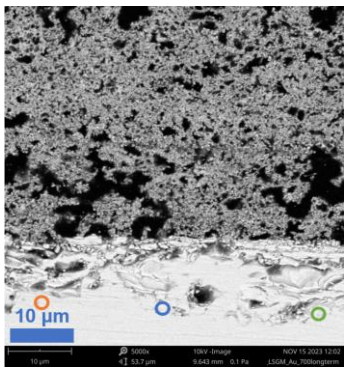

b)

spot from sol-gel	La	Sr	Ga	Mg	O
○	27.0	7.4	18.9	4.1	42.6
○	28.7	7.5	20.2	3.9	39.7
○	28.9	7.5	20.4	3.9	39.3
average atomic content [%]	28.2	7.5	19.8	4.0	40.5
measured ratio	3.8:1		5.0:1		
expected ratio	4:1		4:1		

Fig. 11-26. Elemental analysis of selected spots for LSNMFCC2035 on LSGM. a) The marked spots selected as the analysis points, and b) the summary of the analysis results.

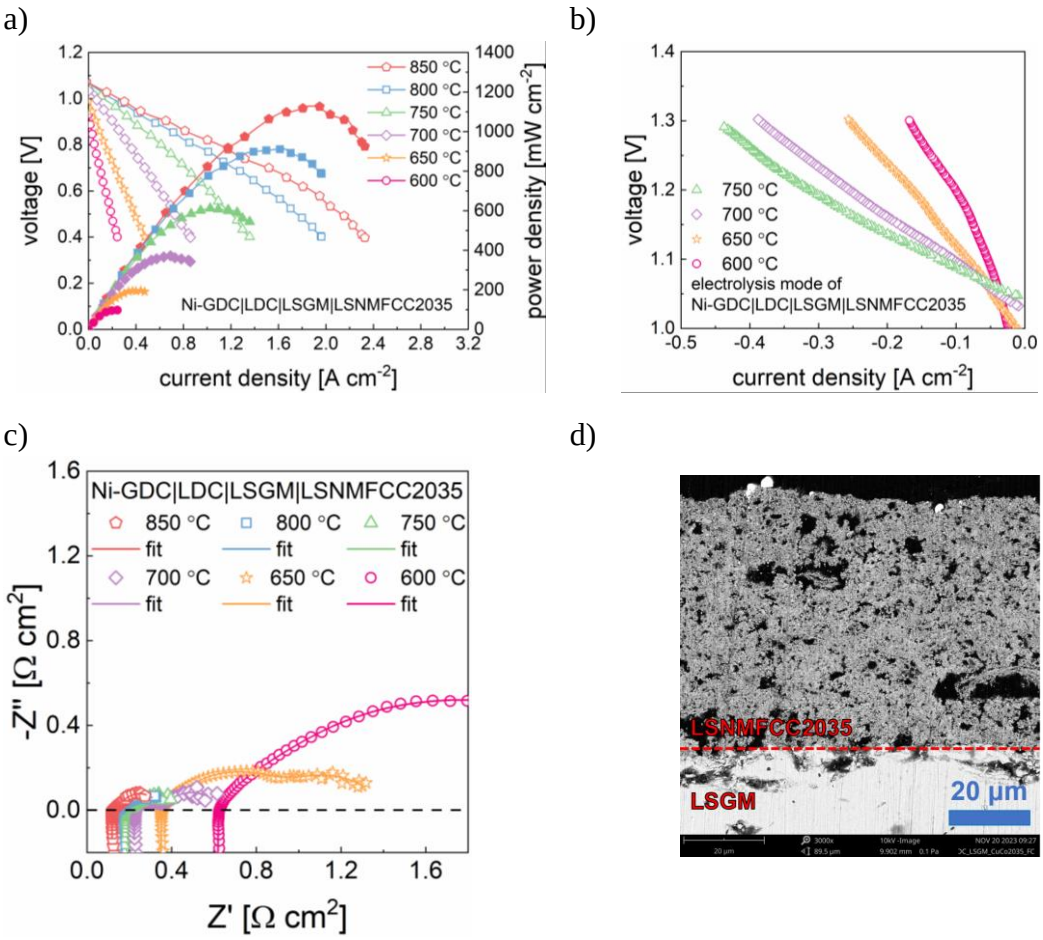

Fig. 11-27. a) Current density-voltage curves and power density output, and b) performance in the electrolysis mode for the Ni-GDC|LDC|LSGM|LSNMFCC2035 full cell. c) EIS data measured under open circuit conditions. d) SEM micrograph the of cross-section of the measured full cell.

Finally, the output power density, which is of importance to assess the actual properties of the LSNMFCC2035 oxygen electrode material could be also measured as a function of temperature in the LSGM-based cell. As it is shown in Fig. 11-27a, the I-V curves show an expected, increasing trend of the current density with the increasing temperature, yielding a peak power density of 1125 mW cm^{-2} and 910 mW cm^{-2} at 850 °C and 800 °C, respectively in the fuel cell mode. When it comes to the electrolysis mode (Fig. 11-27b), LSNMFCC2035 also performs satisfactorily, yielding a current density of 0.44 A cm^{-2} with the voltage of 1.3 V at 750 °C. The results confirm that the developed multicomponent oxygen electrode can work efficiently in both, fuel cell and electrolysis modes. The EIS curves presented in Fig. 11-27c show the low ohmic resistance values of the measured full cell, as well as the low polarization resistances. This is true at each temperature. There are three arcs identified up to 800 °C, with the high frequency arc at 850 °C merging with the one at middle frequency. Additionally, as visible in Fig. 11-27d, the LSNMFCC2035 electrode layer maintains the good adhesion with the LSGM electrolyte and shows desired porosity as well after tests. This is in good accordance with

results presented for the symmetrical cell (Fig. 11-25b). Overall the results are among the best published for the multicomponent or high-entropy perovskite electrodes [178,298,299].

While remarkable power density output could be measured for the constructed full cell with Ni-GDC|LDC|LSGM|LSNMFCC2035 configuration, indicating that the developed LSNMFCC2035 material is suitable for making functional oxygen electrodes, a question remains if the properties can be still improved, e.g. to the level of R_p values characteristic for the LSNMFCC0550 electrode (Fig. 11-21c). This issue is discussed in the next chapter.

12. Improvement of selected oxygen electrodes by electrospinning

As it was mentioned previously in the chapter 7, electrospinning is an interesting synthesis method that may help obtaining samples with a special fiber-like morphology, which can be expected to make a noticeable impact on the electrochemical properties [209,300]. Consequently, several trials have been conducted to modify morphology of the considered oxygen electrode materials by this method. For the relevant experiments, GBSCC0911, as well as LSNMFCC0550 and LSNMFCC2035 perovskites were selected.

12.1. Electrospun GBSCC0911 applied as the oxygen electrode material

As the most important characterization, XRD results are presented in Fig. 12-1 for the GBSCC0911 ES sintered at 1000 °C for 6 h. It is evident that the electrospun material maintains the same tetragonal *P*4/*mmm* symmetry as the GBSCC0911 synthesized via the SG method. Regardless of some minor peaks visible in the range of 35-40 deg, there are no obvious differences identified between both GBSCC0911 samples.

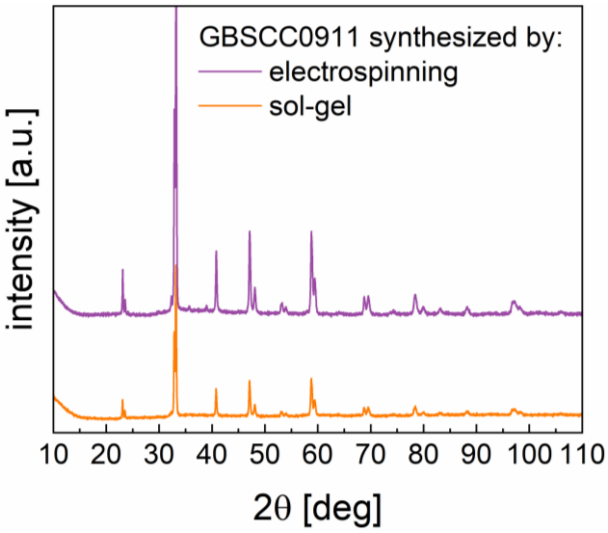

Fig. 12-1. Comparison of the XRD results for GBSCC0911 synthesized by SG and ES (after sintering) methods.

When the phase identification could be positively realized, it is obviously of a great interest to have observation on the micro-morphology upon the obtained GBSCC0911 ES. Expectedly, it should exhibit the characteristic features of this synthesis method. As presented in Fig. 12-2a, immediately after the electrospinning, the material exhibits the nanofiber-like morphology. The diameter of the fibers is in the 200-500 nm range. All nanofibers demonstrate relatively straight shape and smooth surface. As shown in Fig. 12-2b, the nanofibers became coarsened and curved after the sintering at the high temperature (optimized at 1000 °C for 6 h), but still, the fiber-like morphology is

maintained, with the diameter of individual units growing to ca. 400-600 nm range, but at the same time, very porous, interconnected structure formed. It is worth noting that the observed porosity seems as more suitable for application, being more uniform and open, with well-joined particles visible in the micrograph. It can be stated that such morphology is better in comparison to the one presented in Fig. 9-3c for the GBSCC0911 sample from the SG method.

a) b)

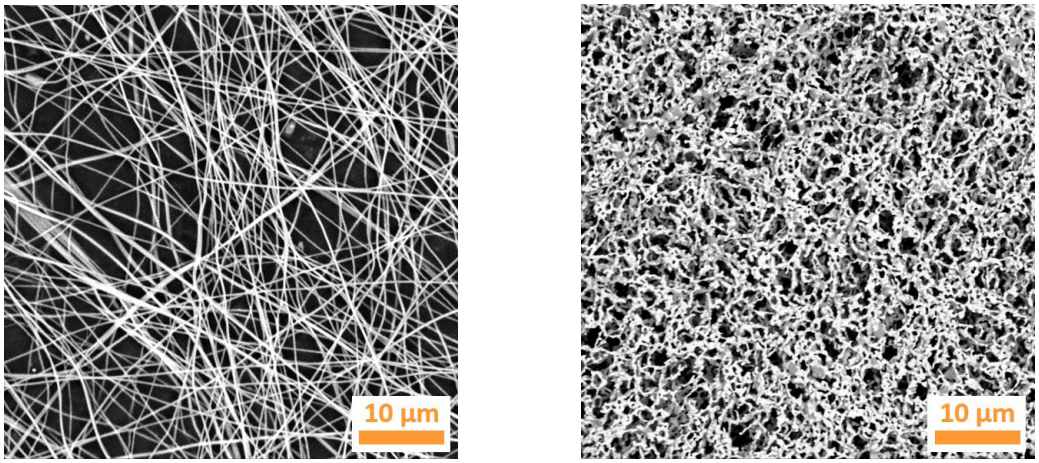

Fig. 12-2. a) SEM micrograph of the obtained GBSCC0911 ES sample before sintering, and b) the same sample after sintering at 1000 °C for 6 h in air.

Importantly, since the obtained structure is the same, but morphology prevents most of the other experimental methods to be conducted (i.e. studies of the electrical conductivity), the ES sample was directly used in manufacturing of the electrode layers. However, it should be stated that preparation of the electrode slurry involves grinding, which may influence morphology of the final electrode sinter. Also, since the good chemical compatibility of GBSCC0911 SG with the GDC electrolyte was confirmed, the obtained GBSCC0911 ES was applied as the oxygen electrode in symmetrical cell with GDC and the Pt current collector (the most stable configuration). As shown in Fig. 12-3a, the R_p values of the GBSCC0911 ES electrode are obviously smaller than those of the standard GBSCC0911 one at 850 °C, indicating the improved electrocatalytic activity, induced likely by the altered morphology. There are two arcs visible in both EIS data, with the small arc at the low frequency part ascribed to the oxygen adsorption and dissociation processes, and the bigger arc at high frequency, mainly regarded as the oxygen reduction process. Since very minor differences can be distinguished on the small arcs, in fact the main enhancement took place on the high frequency arc, suggesting the improved oxygen reduction on the GBSCC0911 ES electrode. However, data at lower temperatures are not so favorable, with only very minor or no improvement at all registered (Fig. 12-3b). This is in fact surprising, and has no simple explanation.

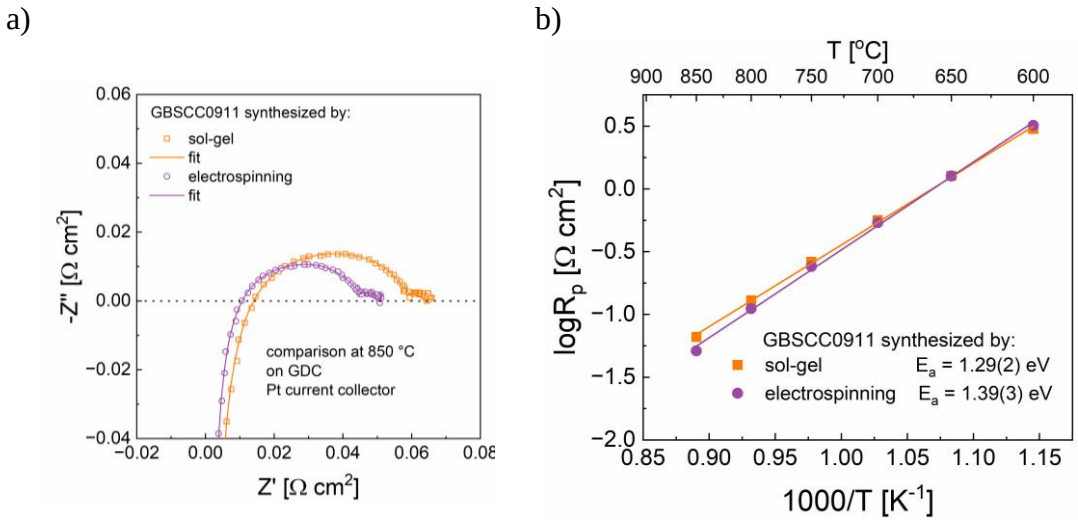

Fig. 12-3. Comparison of a) EIS curves of symmetrical cells with GBSCC0911 SG and GBSCC0911 ES electrodes, data compared at 850 °C, and b) the related electrode polarization resistance R_p presented in Arrhenius-type coordinates.

After the symmetrical cell measurements, the SEM observations of the cross-section of the cell proved that the ES electrode layer maintains a good adhesion with the GDC electrolyte (Fig. 12-4). Moreover, although there are elemental precipitations of Cu and Ce, they are rather minor, and may possibly stem from the process of sample's preparation for SEM observations. Apart from that, there are no other elemental segregations at the interface of electrode/electrolyte taking place, implying a rather stable behavior of the prepared GBSCC0911 ES material.

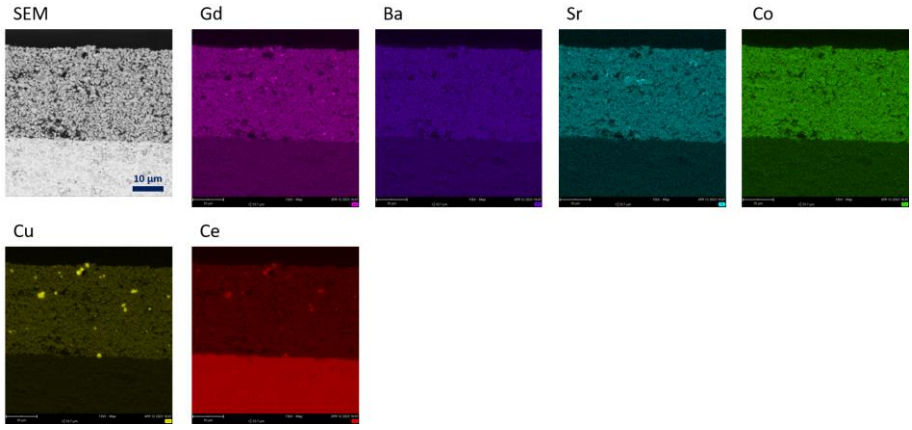

Fig. 12-4. Morphology (cross-section) of the measured GBSCC0911 ES oxygen electrode on the GDC electrolyte, together with the corresponding elemental maps obtained by EDS.

Similarly as in previous studies, it is necessary to characterize the output power, which can be delivered by the full cell with GBSCC0911 ES used as the oxygen electrode. With

the GDC applied as the electrolyte support, and Pt used as the current collector, the full cell with GBSCC0911 ES reaches a peak power density of 381 mW cm^{-2} and 143 mW cm^{-2} at 850 °C and 700 °C, respectively. Interestingly, the power density of GBSCC0911 ES is slight lower than that of the similar cell with GBSCC0911 SG electrode at 850 °C (426 mW cm^{-2}), but is higher at 700 °C (118 mW cm^{-2}). The relevant data are gathered in Figs. 12-5a and 12-6a. Such a difference can be illustrated in the polarization resistance changes. As depicted clearly in Figs. 12-7a and b, the polarization resistances of GBSCC0911 ES-based full cell are smaller at both temperatures than those of the standard cell, which is in accordance with the results of the symmetrical cell. Nonetheless, the two considered full cells exhibit similar ohmic resistances at 700 °C, which overall yield a better performance of the cell with the GBSCC0911 ES electrode. At the same time, the ohmic resistance is apparently higher for the cell with standard GBSCC0911 at 850 °C, resulting in a lower power output density.

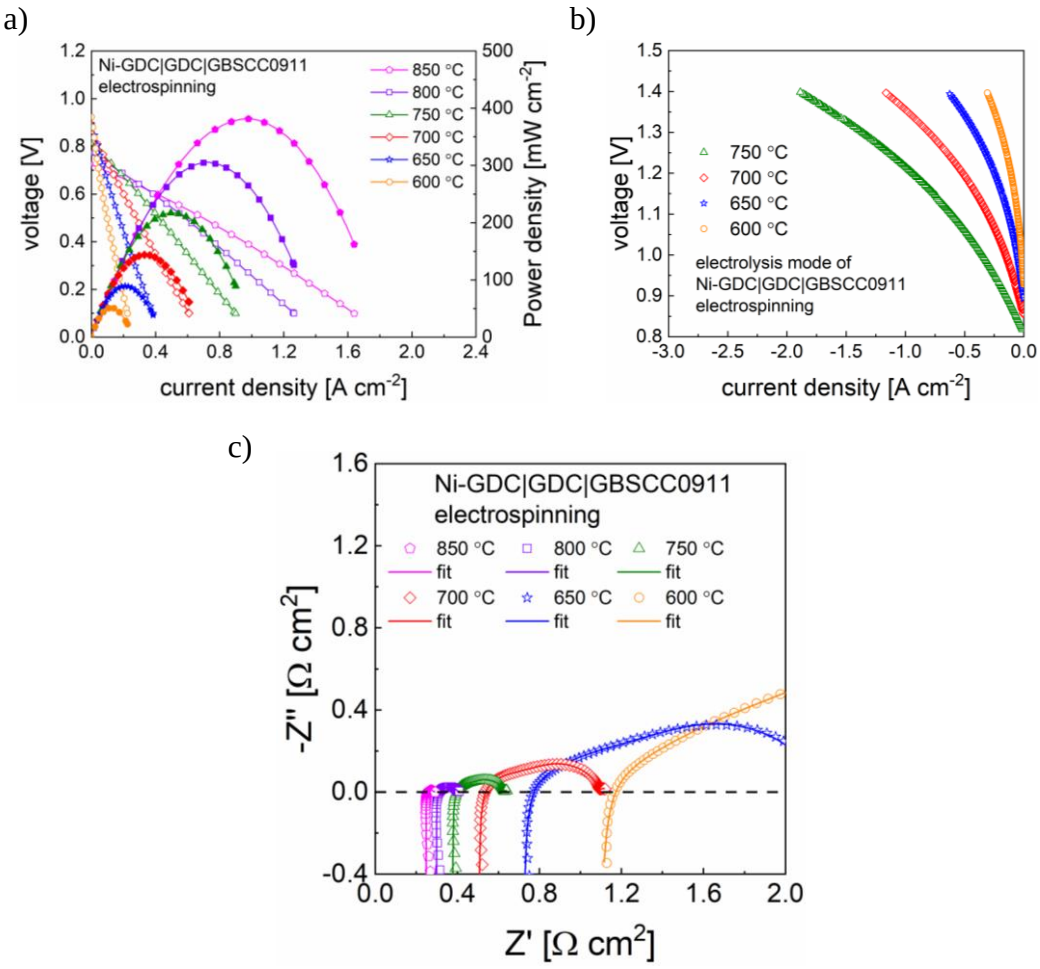

Fig. 12-5. a) Current density-voltage (I-V) curves and power density output, and b) performance in the electrolysis mode for the Ni-GDC|GDC|GBSCC0911 ES full cell. c) EIS data measured under open circuit voltage conditions.

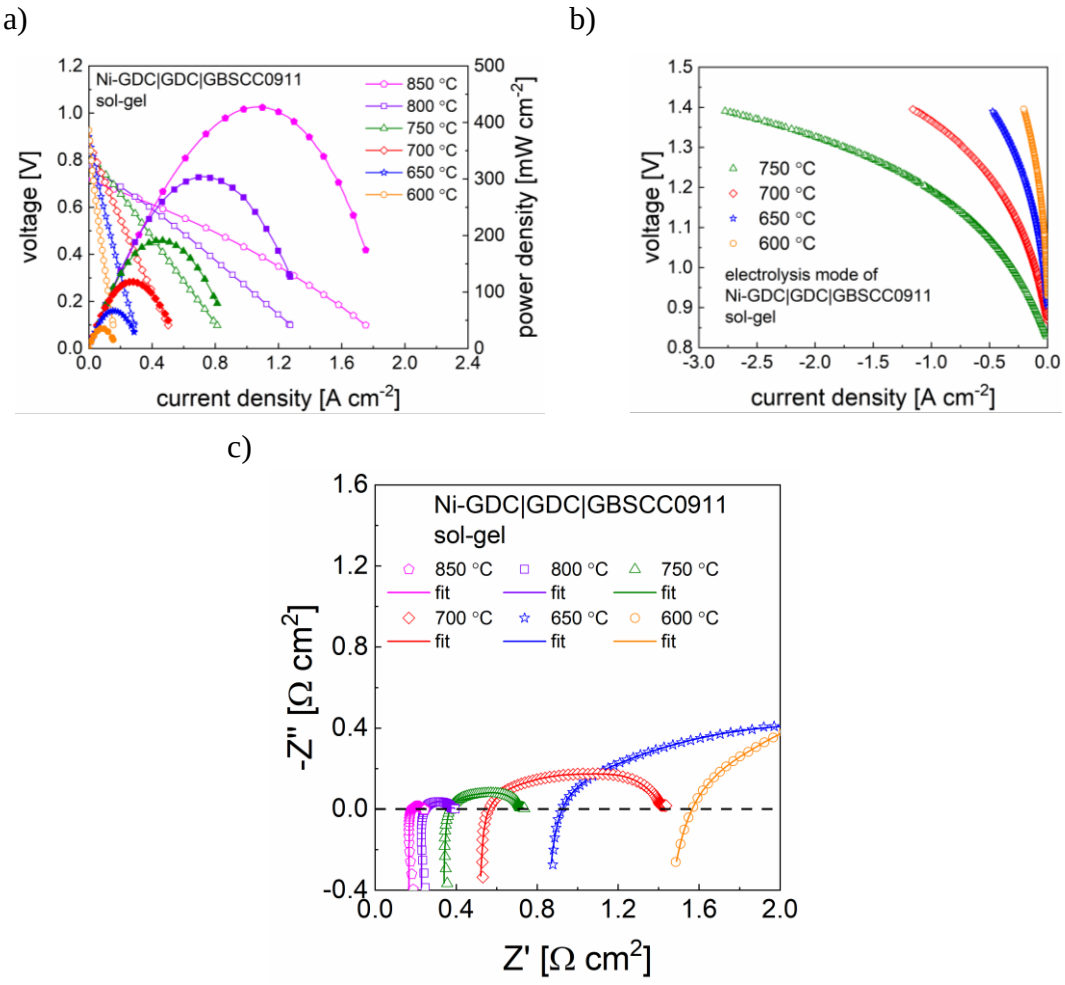

Fig. 12-6. a) Current density-voltage (I-V) curves and power density output, and b) performance in the electrolysis mode for the Ni-GDC|GDC|GBSCC0911 SG full cell. c) EIS data measured under open circuit voltage conditions.

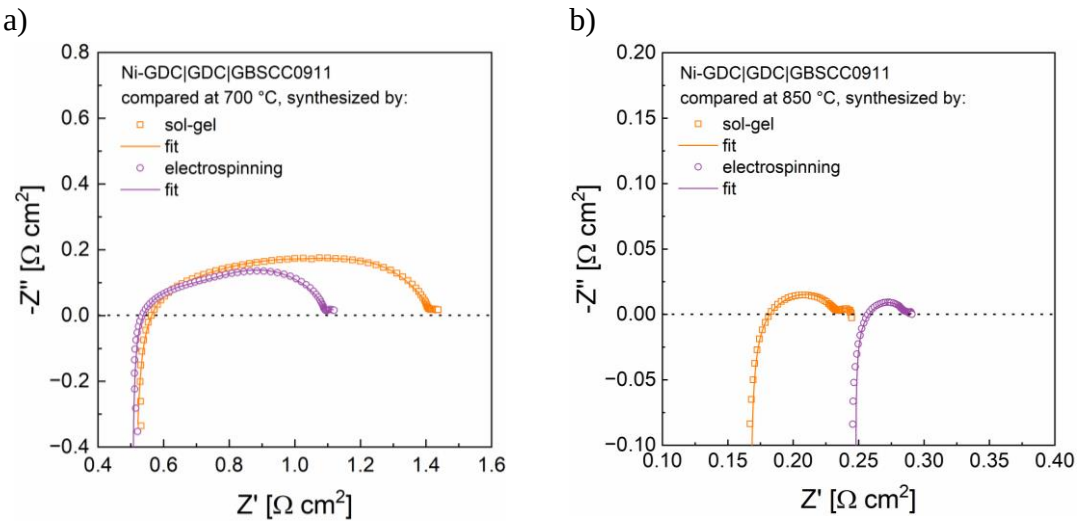

Fig. 12-7. Comparison of the EIS data from full cells with GBSCC0911 ES and SG oxygen electrodes at a) 700 °C, and b) 850 °C. Fits are also shown.

There are three arcs detected in the EIS data for the full cells (Fig. 12-5c and Fig. 12-6c). Moreover, both cells show quite a good performance in the electrolysis mode, reaching near 1.89 A cm^{-2} and 2.77 A cm^{-2} with the voltage of 1.4 V at 750 °C, respectively (Fig. 12-5b and Fig. 12-6b).

Summarizing this subchapter, it can be stated the ES method enables achieving better performance is some cases, but there are still unresolved issues, likely related to the worsened properties of the electrode/electrolyte interface, which hinder full utilization of this method to improve characteristics of the GBSCC electrodes.

12.2. Electrospun LSNMFCC0550 and LSNMFCC2035 applied as the oxygen electrode materials

In order to study the possible enhancement that the electrospinning method may have on the LSNMFCC electrode materials, the ES synthesis method was adopted in preparation of LSNMFCC0550 and LSNMFCC2035 oxides. it is worth noting that the intention of synthesis and SEM observations of LSNMFCC0550 is only for a better reference for LSNMFCC2035. As shown in Fig. 12-8a and b, both samples prepared by this route and sintered at 900 °C for 6 h in air could be successfully synthesized. Notably, the XRD patterns show that ES samples exhibit the same *R*-3*c* symmetry as SG samples, without and impurity or secondary phase detected. Also, the respective peaks overlap closely, so it can be stated that the unit cell parameters are very similar for samples obtained from both methods.

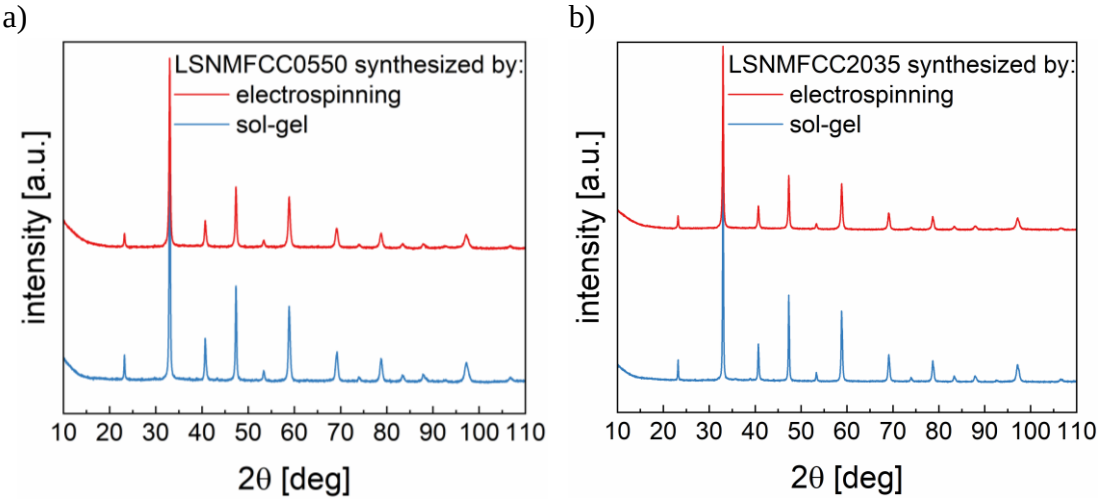

Fig. 12-8. Comparison of the XRD patterns of the samples synthesized via SG and ES methods for a) LNMFCC0550, and b) LSNMFCC2035 perovskite oxides.

When focusing on the micro-morphology of the ES samples, as can be seen in Figs. 12-9a and b, both, LSNMFCC0550 ES and LSNMFCC2035 ES exhibit desirable nano-fiber structure before sintering, with a diameter on the order of 200-500 nm for

LSNMFCC0550 ES, and slightly bigger fibers for LSNMFCC2035 ES. After high temperature sintering (Figs. 12-9c, d, e and f), those nanofibers are partially maintained, with the agglomeration being also observed. Summarizing, samples with the same crystal phase and interesting micro-morphology can be obtained via the ES method in the LSNMFCC series.

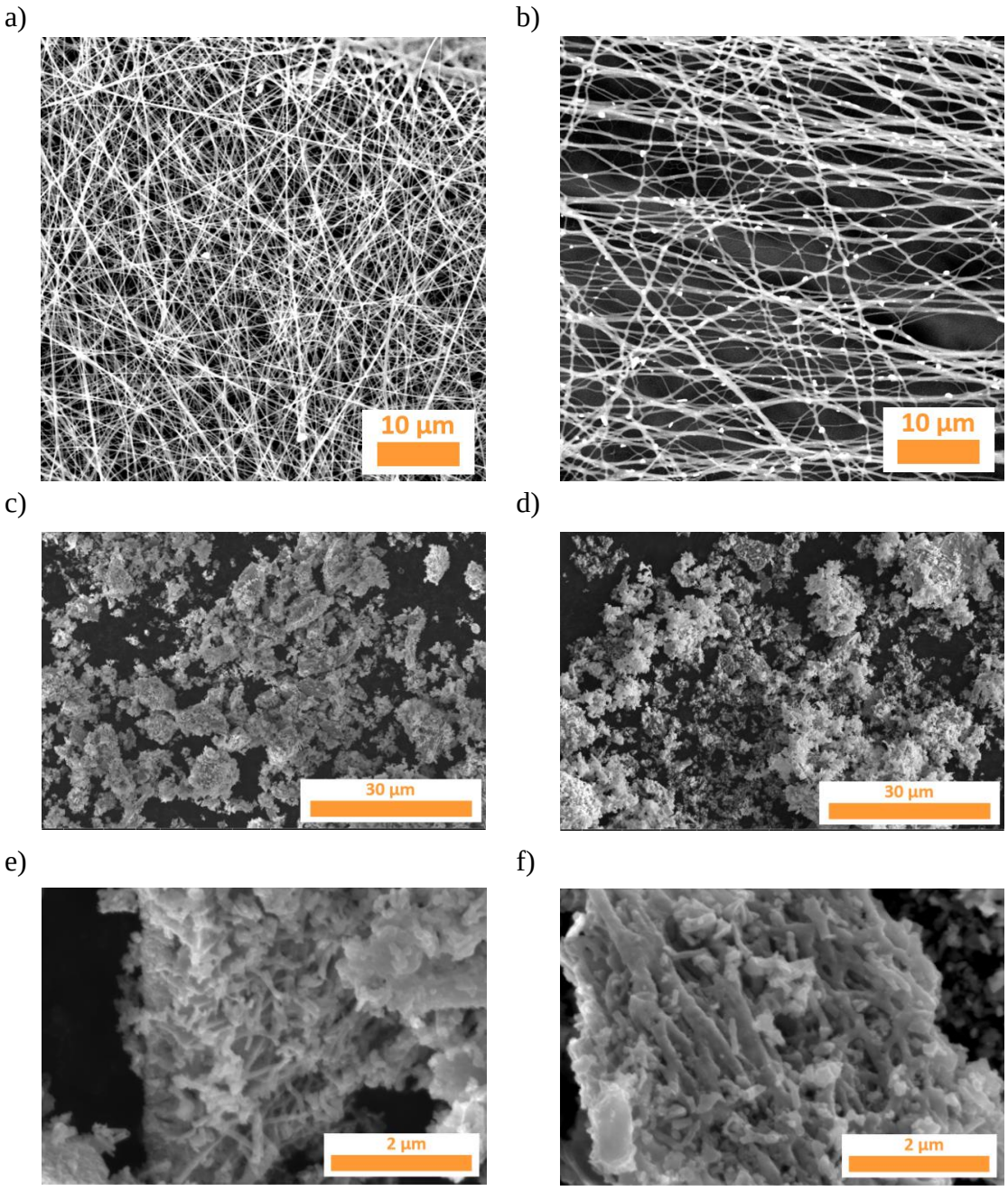

Fig. 12-9. SEM micrographs of the obtained LSNMFCC0550 ES and LSNMFCC2035 ES samples, a) and b) before sintering, c) and d) after sintering at 900 °C for 6 h in air as observed at low resolution, and e) and f) after sintering, with higher resolution, respectively.

When it comes to the characterization of the electrochemical properties, as discussed in the previous chapter, only LSNMFCC2035 composition was selected, due to its lowest Co-content and the highest configurational entropy among the LSNMFCC series. Another reason was to conduct trials in order to evaluate possible options to enhance its electrocatalytic activity. The considered LSNMFCC2035 ES electrodes were applied on the GDC and LSGM electrolytes. As presented in Figs. 12-10a and b, the LSNMFCC2035 ES exhibits the similar behavior as observed for the standard LSNMFCC2035, for which the R_p values on GDC are smaller than those obtained on the LSGM electrolyte. Also, analyzing Fig. 12-10c, it is clear that the LSNMFCC2035 ES electrode demonstrates excellent electrocatalytic activity, yielding R_p values of 0.014 Ω cm^2 and 0.024 Ω cm^2 at 850 °C on GDC and LSGM, respectively. This is even better than for the standard LSNMFCC0550 electrode on the GDC electrolyte at the same temperature (Fig. 11-21). The obtained results denote that electrospinning method can improve the performance of the low Co-content LSNMFCC2035 material to achieve values as good as those observed for the SG-synthesized LSNMFCC0550.

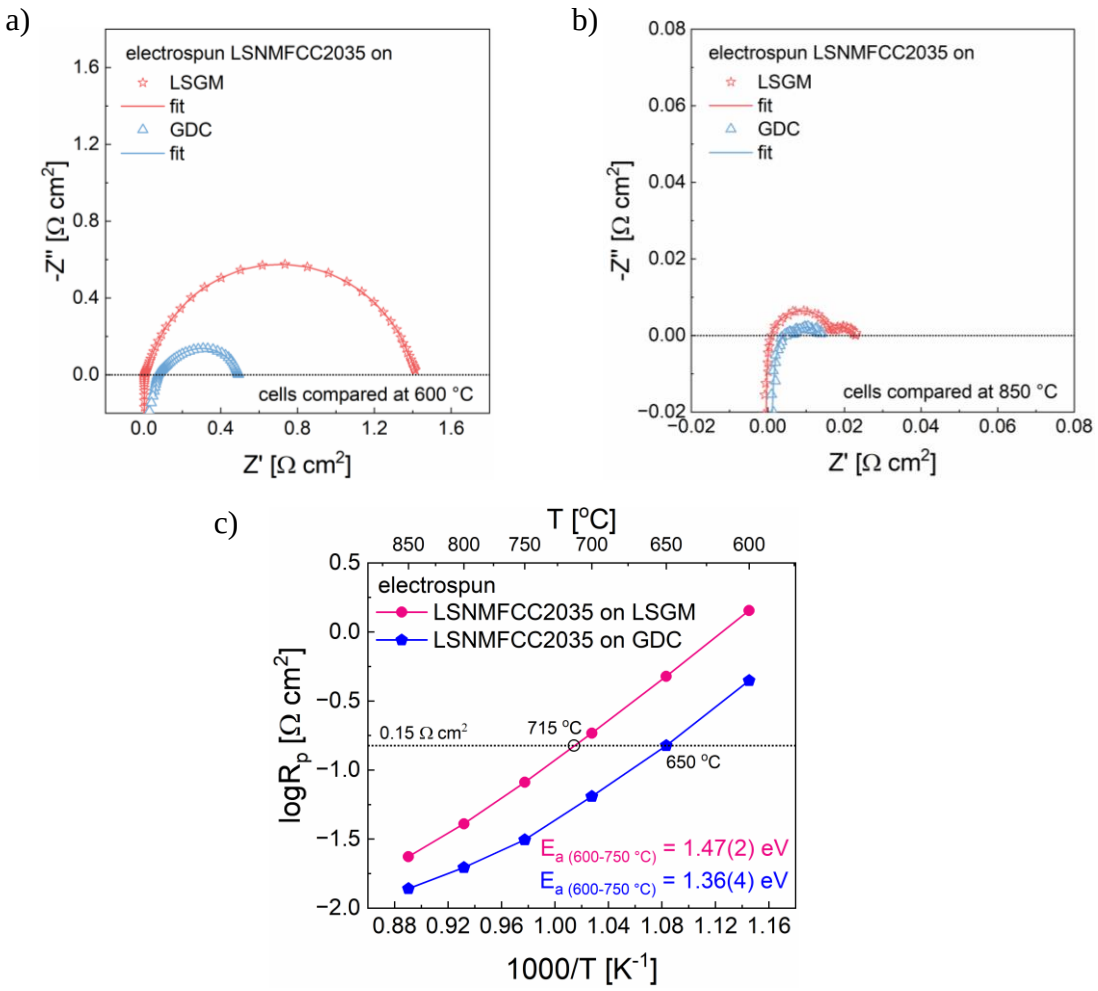

Fig. 12-10. EIS data comparison of the symmetrical cells with LSNMFCC2035 ES oxygen electrode on LSGM or GDC at a) 600 °C, and b) 850 °C. c) The related electrode polarization resistance R_p presented in Arrhenius-type coordinates.

The improvement made by the ES method can be shown more clearly via the DRT analysis of the EIS data. As shown in Fig. 12-11a, at the lower temperature, the biggest improvement is in peak 4, which is related to the reduction of oxygen in the ORR. This means that the ES method mainly enhances the rate-limiting step, with some minor improvements for the charge transfer through the electrode-electrolyte interface, and the oxygen adsorption and dissociation processes. When it is at the higher temperature (Fig. 12-11b), the major enhancement takes place at the high frequencies, including peaks 1, 2, 3, and 4, while some minor improvements can be also seen in peak 5. This indicates the boosted charge transfer at the interface, but also the improved incorporation of the reduced oxygen into the lattice, as well as the enhanced reduction of oxygen at 850 °C.

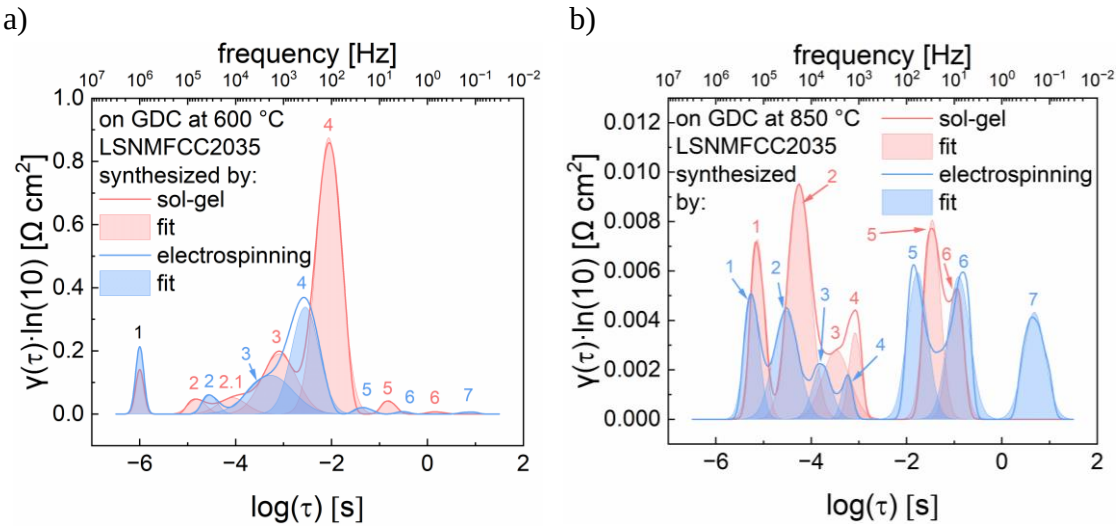

Fig. 12-11. Results of the DRT analysis as a function of log(τ) for symmetrical cells with LSNMFCC2035 electrodes synthesized via SG or ES methods, compared at a) 600 °C, and b) 850 °C.

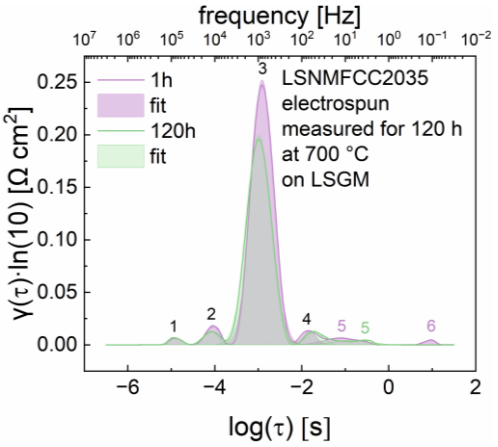

Fig. 12-12. Comparison based on results of DRT analysis as a function of log(τ) for cells with LSNMFCC2035 ES used as the oxygen electrode and based on the LSGM electrolyte. Data compared at the beginning and at the end of the 120 h long-term measurements at 700 °C.

a)

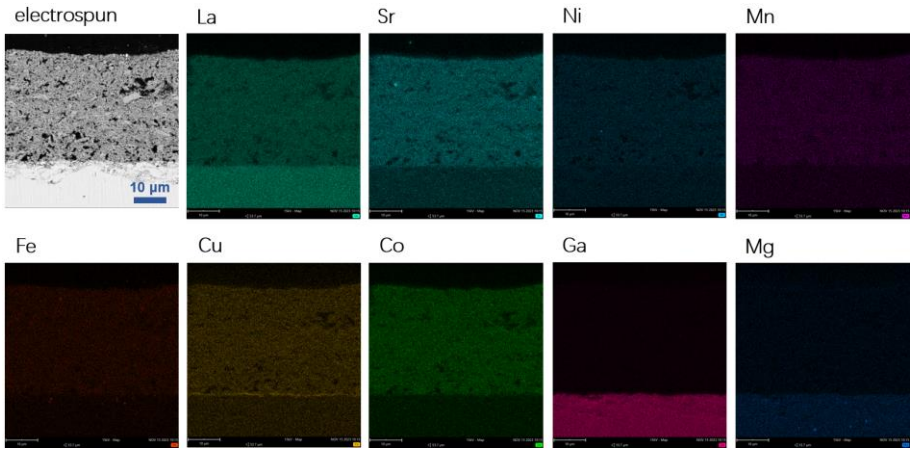

b)

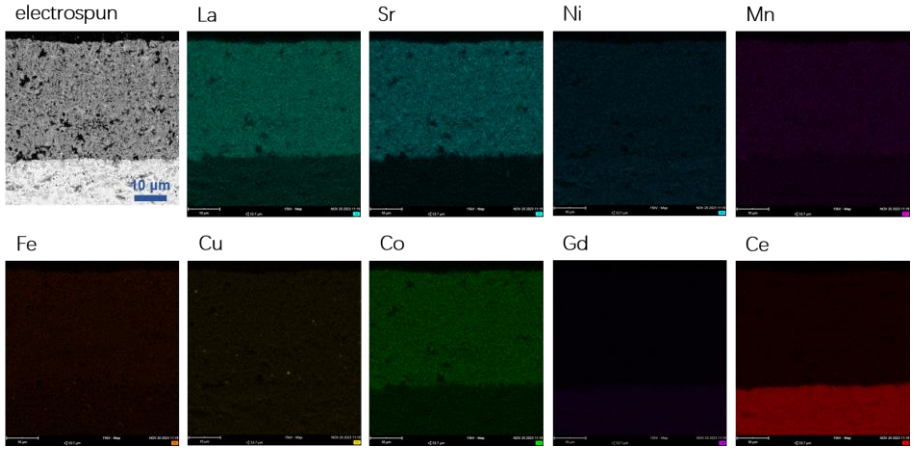

c)

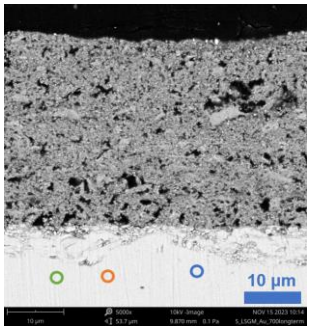

d)

spot from electrospun	La	Sr	Ga	Mg	O
○	30.5	7.1	21.4	3.4	37.6
○	30.7	7.1	21.1	3.4	37.7
○	30.1	7.5	21.5	3.7	37.2
average atomic content [%]	30.4	7.2	21.3	3.5	37.5
measured ratio	4.2:1		6.1:1		
expected ratio	4:1		4:1		

Fig. 12-13. Morphology (cross-section) of the measured cells with the LSNMFCC2035 ES used as the oxygen electrode, together with the corresponding elemental maps obtained by EDS for a) the cell manufactured on the LSGM electrolyte after 120 h measurements at 700 °C, and b) the GDC electrolyte after short-term measurements. c) The elemental analysis of selected spots for LSNMFCC2035 ES on LSGM after the long-term measurements, the marked spots selected as the analyzed points, and d) the summary of the analysis results.

Also, as presented in Fig. 11-23, LSNMFCC2035 ES demonstrates very good performance stability in the long-term measurements on LSGM, which yields a relative change of -0.023% h^{-1} in the last 60 hours of the measurements. Similarly to the cell with

standard LSNMFCC2035 electrode, the decreased R_p values can be ascribed to the boosted process of the oxygen reduction (Fig. 12-12). Moreover, as can be seen in Fig. 12-13a, the LSNMFCC2035 ES electrode maintains the good adhesion with the LSGM electrolyte, and the porosity of the layer is kept well after the long-term measurements. There is a slight segregation of Cu at the interface, but it can be neglected. Similar results can be also seen on GDC (Fig. 12-13b) after the short-term measurements. Additionally, in Figs. 12-13c and d, the elemental analysis of the selected spots is shown, indicating that the LSGM electrolyte still maintains the good chemical stability as well, without significant elemental segregation detected.

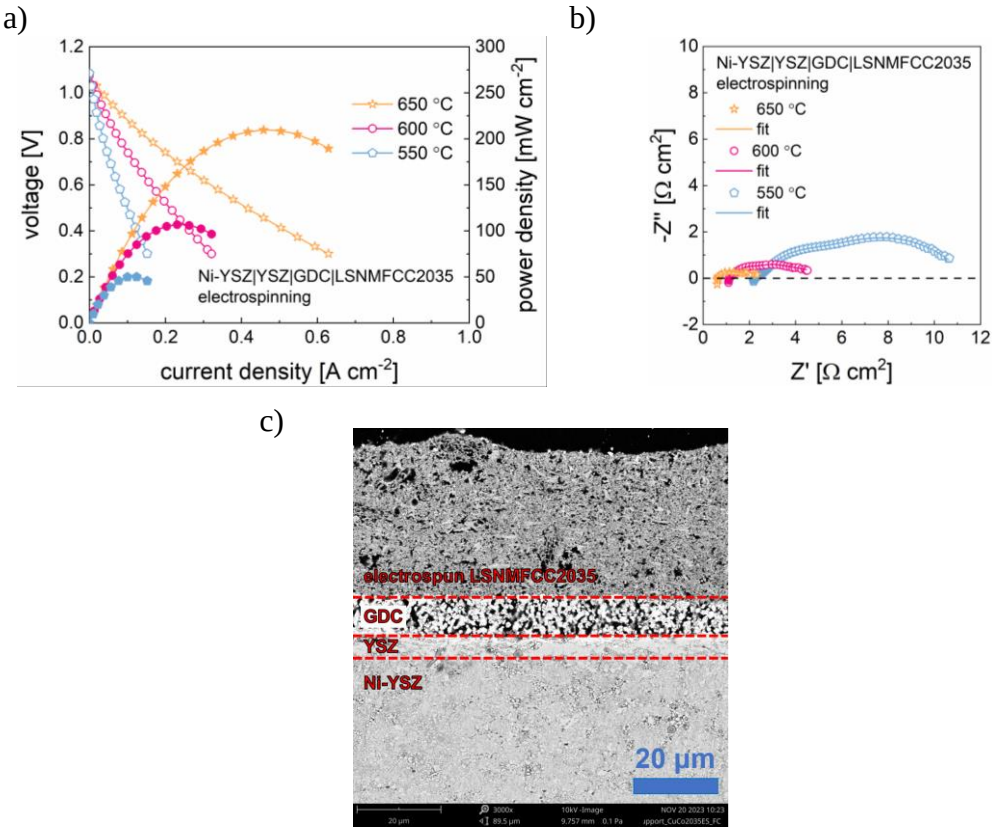

Fig. 12-14. a) Current density-voltage (I-V) curves and the power density output, as well as b) the related EIS data measured under open circuit conditions of the Ni-YSZ-supported full cell with the LSNMFCC2035 ES applied as the oxygen electrode. c) SEM micrograph of the cross-section of the full cell after the measurements.

In the full cell measurements, LSNMFCC2035 ES enables to achieve a good power density output in an anode-supported YSZ-based full cell. Specifically, the full cell could reach a peak power density of 209 mW cm^{-2} at 650 °C, demonstrating quite a good performance in the low temperature range (Fig. 12-14a). As seen in Fig. 12-14b, the measured full cell shows also the low ohmic resistance, as well as the small polarization resistance in the measured temperature range. Finally, the SEM micrographs show that the LSNMFCC2035 ES can keep a good adhesion with the GDC buffer layer in the anode-supported full cell (Fig. 12-14c).

Last but not least, a general summary can be presented, showing the best materials developed in this work. The related R_p data as a function of temperature are presented in Fig. 12-15. As it is explicitly shown, the optimized LBCu electrode, sintered at 800 °C, demonstrates the lowest R_p values on the LSGM electrolyte in the lower temperature range (600-750 °C). This is followed by the LSNMFCC2035 ES electrode on the GDC electrolyte, and the GBSCC0911 electrode on LSGM. The obtained results suggest that for manufacturing of IT-SOCs working in the low temperature range, LBCu is a more suitable choice, which meets the 0.15 Ω cm^2 threshold at around 625 °C. However, considering the practical application, more detailed long-term stability studies are needed. For the other two electrodes, the LSNMFCC2035 ES and GBSCC0911 reach the limit at 650 °C and ca. 684 °C, respectively. Considering lower overall Co content and better stability, for the higher temperature range, LSNMFCC2035 ES electrode seems as the better option.

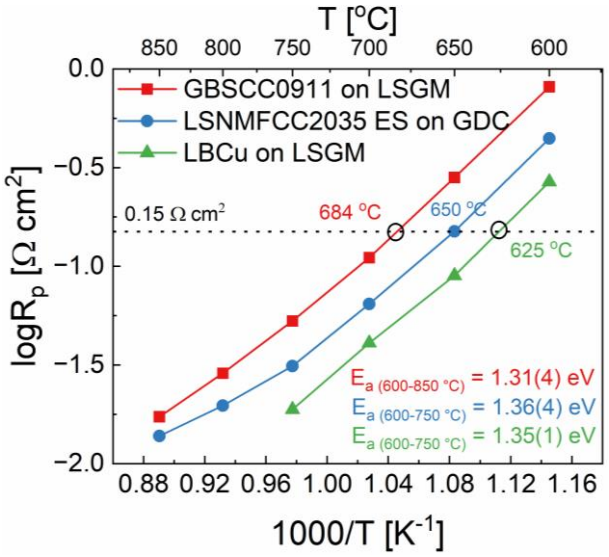

Fig. 12-15. Comparison of the obtained electrodes, with the lowest polarization resistance R_p in each system, as presented in Arrhenius-type coordinates.

13. Conclusions

The conducted in this thesis studies of the Cu-based and doped with copper perovskite-type oxides, in particular, $La_{1.5}Ba_{1.5}Cu_3O_{7\pm\delta}$, $GdBa_{0.5}Sr_{0.5}Co_{2-x}Cu_xO_{5+\delta}$ (x = 1-1.15), and $La_{0.6}Sr_{0.4}Ni_{0.15}Mn_{0.15}Fe_{0.15}Cu_xCo_{0.55-x}O_{3-\delta}$ (x = 0.05-0.2) successfully proved the feasibility of using the copper element as a replacement for Co for the development of functional oxygen electrodes for Solid Oxide Cells. Also, it is documented that the electrospinning technique is a useful method for obtaining oxygen electrodes with enhanced characteristics. Below, there are presented the main conclusions arising from those studies.

$La_{1.5}Ba_{1.5}Cu_3O_{7\pm\delta}$

- The phase-pure Cu-based perovskite-type, $La_{1.5}Ba_{1.5}Cu_3O_{7\pm\delta}$, can be successfully synthesized by either the sol-gel or solid-state method in air. Powder produced by the sol-gel route is fine and homogeneous. The as-synthesized LBCu material demonstrates *P*4/*mmm* tetragonal symmetry at room temperature, with an interesting triple perovskite structure. In the unit cell, there are present partially mixed La/Ba layers and La layers (along the *c*-axis), as well as the oxygen sublattice shows complex features with different occupancies at the respective structural sites. This creates varying crystal coordination for Cu cations.

- The obtained LBCu keeps the oxygen content equal to 7.23 at RT. The oxygen release process starts at ca. 300 °C in air, and proceeds continuously and smoothly. A final difference by 0.33 was observed at 800 °C, while in different atmospheres the respective changes are only somewhat different. Still, the average oxidation state of copper is maintained above +2 in air up to 800 °C, yielding favorable electronic transport properties. The measured total electrical conductivity is above 10 S cm^{-1} in the temperature range of interest, fulfilling the basic requirement for the oxygen electrode material. The good thermal stability of LBCu can be proven by HT-XRD studies, which can also provide the TEC values of $13.2 \cdot 10^{-6}$ K^{-1} (up to 400 °C) and $18.8 \cdot 10^{-6}$ K^{-1} (400-900 °C). Such moderate values are obviously lower than those reported for various Co-based materials.

- LBCu is chemically compatible with the LSGM electrolyte up to 900 °C, while reactivity was detected when it is mixed and annealed with LDC and GDC20 electrolyte materials. The somewhat limited stability influences possibility of manufacturing the electrode layers, but the annealing temperature can be optimized. If properly prepared, the LBCu layers (sintering at 800 °C) exhibit excellent electrocatalytic activity, yielding low R_p values of 0.019 Ω cm^2 and 0.041 Ω cm^2, respectively at 750 °C and 700 °C. This indicates that the requirement of 0.15 Ω cm^2 can be met as low as at ca. 625 °C. Results of the conducted DRT analysis show that the rate-limiting step for the LBCu can be associated with the reduction of oxygen,

previously adsorbed and dissociated. The manufactured, optimized electrode also exhibits the stable performance in a symmetrical cell, keeping the polarization resistance value below 0.1 Ω cm^2 at 650 °C for 120 h.

- As the oxygen electrode in a LSGM-based full cell, LBCu electrode enables reaching a power density output of over 160 mW cm^{-2} and 250 mW cm^{-2}, respectively at 600 °C and 650 °C. In the electrolysis mode, a current density of 0.37 A cm^{-2} could be obtained with the voltage of 1.5 V at 800 °C. The recorded parameters indicate very good performance as the fully Co-free oxygen electrode for IT-SOCs. Also, the results in the lowered temperature range indicate an improvement over previously published data.

$GdBa_{0.5}Sr_{0.5}Co_{2-x}Cu_xO_{5+\delta}$ ($1 \leq x \leq 1.15$)

- The A-site layered $GdBa_{0.5}Sr_{0.5}Co_{2-x}Cu_xO_{5+\delta}$ double perovskite oxides can be prepared by the sol-gel synthesis method, particularly for the Co/Cu ratio close to 1. Materials in the as-synthesized GBSCC series ($1 \leq x \leq 1.15$) are pure, and exhibit stable *P*4/*mmm* tetragonal symmetry up to 1000 °C in air. A desired micro-morphology with fine, homogenous powder can be obtained. However, for higher Cu content, the presence of secondary phases hinders the synthesis process. The unit cell parameters in the series were found to vary rather slightly.

- The oxygen content at RT for the considered materials remains in the 5.49-5.64 range, indicating formation of the oxygen vacancies in the Gd-related structural layers. It decreases for the samples with higher copper content. Similarly as for LBCu, oxygen is released from the oxides above 250-300 °C, and the process starts at lower temperatures for materials with higher Cu doping. The average oxidation state of copper and cobalt remains in the vicinity of +3, suggesting presence of mixed charge states, which facilitates electronic transport. The total electrical conductivity remains above 10 S cm^{-1} in the IT-SOCs operating temperature range of 600-800 °C. Regarding thermal expansion, moderate TEC values can be measured, showing about $14 \cdot 10^{-6}$ K^{-1} (RT to 300 °C) and $17 \cdot 10^{-6}$ K^{-1} (300-1000 °C), with a noticeable decrease for samples with higher x values. Consequently, the chemical expansion effect seems to be quite limited.

- GBSCC materials were found to exhibit good chemical stability with both, LSGM and GDC up to 950 °C and 900 °C, respectively. This allowed proceeding with the systematic studies of the nature of the electrochemical reaction occurring at the GBSCC oxygen electrodes manufactured on these two electrolytes, as well as demonstrating role of the used current collector. The studies were conducted on the best performing GBSCC0911 electrode, having the relatively high copper content equal to 1.1. The optimized oxygen electrode (LSGM electrolyte, Ag current collector) exhibits one of the best reported electrocatalytic activity, yielding R_p

values as low as 0.017 Ω cm^2 and 0.029 Ω cm^2 at 850 °C and 800 °C, respectively. The conducted DRT analyses allowed identifying all steps of the electrochemical processes, which enabled stating that the rate-limiting step of the ORR is the reduction of (previously adsorbed and dissociated) oxygen. The same reason also happened in electrodes manufactured on the GDC electrolyte and those, in which Pt current collector was utilized, but there is a performance decrease observed for such electrodes. A stable performance of the GBSCC0911 electrode can be obtained on either LSGM or GDC electrolytes, but with Pt current collector, as documented by the 120 h experiment conducted at 700 °C. Unfortunately, Ag current collector is not suitable for the long-term operation.

- The electrospinning method can be successfully applied to preparation of the GBSCC0911 precursor, based on which the optimized GBSCC0911 ES electrode can be obtained. Such oxygen electrode was found exhibit lower R_p at higher temperatures (700-850 °C) in comparison to the standard one (made with the sol-gel method-based material).

- While both, GBSCC1010 and GBSCC0911 electrodes demonstrate superior performance in the LSGM-based full cells, e.g. above 1500 mW cm^{-2} and 1200 mW cm^{-2} at 900 °C and 850 °C, respectively, the GBSCC0911 material is recommended, due to the decreased Co content. The GBSCC0911-based cell could work also in the electrolysis mode as well, reaching e.g. 0.44 A cm^{-2} current density with 1.3 V voltage at 750 °C. Also, the GBSCC0911 ES electrode enabled to obtain desirable power density output of 381 mW cm^{-2} at 850 °C in a GDC-supported full cell.

$La_{0.6}Sr_{0.4}Ni_{0.15}Mn_{0.15}Fe_{0.15}Cu_xCo_{0.55-x}O_{3-\delta}$ (x = 0.05-0.2)

- Multicomponent LSNMFCC perovskite-type oxides can be successfully synthesized by the sol-gel method, yielding fine, homogeneous powders. Nevertheless, Co cannot be completely replaced by Cu in the studied series. All the as-synthesized samples exhibit rhombohedral *R*-3*c* symmetry, which is maintained in air up to 900 °C. Regarding the unit cell parameters, higher Cu content influences the *c* parameter more obviously, and the unit cell volume increases with higher x value.

- Surprisingly, the oxygen contents in the studied LSNMFCC oxides shows almost no relation with the chemical composition, with the equilibrated values of 2.86-2.88 at room temperature. Again, the observed oxygen contents dependence on temperature is rather mild. TEC values of the LSNMFCC series are also relatively moderate, about $15 \cdot 10^{-6}$ K^{-1} (up to 400 °C) and $20.5 \cdot 10^{-6}$ K^{-1} (400-900 °C), while there is a sight increasing trend with the increasing Co content in the low temperature range. Of importance, LSNMFCC series demonstrates excellent total electrical conductivity, above 200 S cm^{-1} in the measured temperature range, while the (unusual) negative sign of Seebeck coefficient suggest the electrons are the main charge carriers.

- Both, GDC and LSGM materials can be applied as the electrolyte working with the LSNMFCC oxygen electrodes, since the good chemical compatibilities can be confirmed with GDC (up to 900 °C) and LSGM (850 °C). Although the LSNMFCC0550 electrode (with the highest Co content) shows the superior electrocatalytic activity, which reaches the R_p value of 0.015 Ω cm^2 at 850 °C, lower than that of LSNMFCC2035 electrode (0.018 Ω cm^2) on GDC electrolyte at the same temperature. Both considered electrodes have good performance stability in the long-term operation on either LSGM or GDC.

- The LSNMFCC0550 and LSNMFCC2035 samples can be also obtained via the electrospinning, forming the desired elongated nanofibers. Interestingly, the LSNMFCC2035 ES oxygen electrode shows large improvement of the properties, yielding the enhanced R_p performance of 0.014 Ω cm^2 at 850 °C on GDC. The DRT analysis unveiled that the enhancement caused by the electrospinning is mainly related the boosted reduction process, but other steps of the ORR are also improved.

- The LSGM-supported full cell with the LSNMFCC2035 electrode reaches a peak power density over 1100 mW cm^{-2} at 850 °C, also a current density of 0.44 A cm^{-2} at the voltage of 1.3 V at 750 °C can be obtained in the electrolysis mode, indicating the feasibility of preparation of the functional multicomponent oxygen electrodes for IT-SOCs.

Comparison of three systems

- Based on the obtained electrochemical properties, the direct comparison of the considered, outstanding oxygen electrode materials can be done, with a selection for application at different operation temperatures. It is evident that LBCu is the most suitable candidate at low temperature range (600-750 °C), while the GBSCC0911 and LSNMFCC2035 ES electrodes are applicable at higher temperatures (750-850 °C). Considering the decreased Co content, the latter one of those two seems as the better choice.

13.1. Perspectives

The feasibility of Cu-based perovskite materials applied as oxygen electrodes in IT-SOCs is comprehensively proved and confirmed. Therefore, in order to make bigger progress along this direction, other complex perovskite-type oxides with either double or triple crystal structure characteristics, multicomponent occupancy at different sites, as well as with disordered oxygen vacancies can be further proposed and studied. This can give rise to more interesting and possibly surprising properties in the physicochemical and/or electrochemical part.

References

[1] R. Fouquet, A Brief History of Energy, in: J. Evans, L. C. Hunt (Eds.), International Handbook on the Economics of Energy, Edward Elgar Publishing, 2009. https://doi.org/10.4337/9781849801997.00006.

[2] B.D. Solomon, K. Krishna, The coming sustainable energy transition: History, strategies, and outlook, Energy Policy 39 (2011) 7422–7431. https://doi.org/10.1016/j.enpol.2011.09.009.

[3] A.P. Loeb, Steam Versus Electric Versus Internal Combustion Choosing Vehicle Technology at the Start of the Automotive Age, Transportation Research Record: Journal of the Transportation Research 1885 (2004) 1–7.

[4] M. Palocz-Andresen, Decreasing Fuel Consumption and Exhaust Gas Emissions in Transportation: sensing, control and reduction of emissions, Springer Berlin Heidelberg, Berlin, Heidelberg, 2012. https://doi.org/10.1007/978-3-642-11976-7.

[5] A. Markeviius, V. Katinas, E. Perednis, M. Tamaauskien, Trends and sustainability criteria of the production and use of liquid biofuels, Renewable and Sustainable Energy Reviews 14 (2010). https://doi.org/10.1016/j.rser.2010.07.015.

[6] D. Banister, K. Anderton, D. Bonilla, M. Givoni, T. Schwanen, Transportation and the Environment, Annu Rev Environ Resour 36 (2011) 247–270. https://doi.org/10.1146/annurev-environ-032310-112100.

[7] N.H. Afgan, D. Al Gobaisi, M.G. Carvalho, M. Cumo, Sustainable energy development, Renewable and Sustainable Energy Reviews 2 (1998) 235–286. https://doi.org/doi.org/10.1016/S1364-0321(98)00002-1.

[8] J. Goudsblom, Energy and Civilization, International Review of Sociology 22 (2012) 405–411. https://doi.org/10.1080/03906701.2012.753780.

[9] H. Jiang, G. Feng, X. Liu, H. Cao, S. Wang, L. Ma, D.K. Ferguson, Drilling wood for fire: discoveries and studies of the fire-making tools in the Yanghai cemetery of ancient Turpan, China, Veg Hist Archaeobot 27 (2018) 197–206. https://doi.org/10.1007/s00334-017-0611-5.

[10] X. Wu, C. Zhang, P. Goldberg, D. Cohen, Y. Pan, T. Arpin, O. Bar-Yosef, Early Pottery at 20,000 Years Ago in Xianrendong Cave, China, Science (1979) 336 (2012) 1696–1700. https://doi.org/10.1126/science.1218643.

[11] A.D. Tillman, Wood as an Energy Resource, Elsevier, 2012. https://doi.org/10.1016/B978-0-12-691260-9.X5001-0.

[12] P.L. Viollet, From the water wheel to turbines and hydroelectricity. Technological evolution and revolutions, Comptes Rendus - Mecanique 345 (2017) 570–580. https://doi.org/10.1016/j.crme.2017.05.016.

[13] T.S. Reynolds, Stronger Than a Hundred Men: A History of the Vertical Water Wheel, JHU Press, 1983.

[14] A. Blakers, M. Stocks, B. Lu, C. Cheng, A review of pumped hydro energy storage, Progress in Energy 3 (2021). https://doi.org/10.1088/2516-1083/abeb5b.

[15] G.M. Joselin Herbert, S. Iniyan, E. Sreevalsan, S. Rajapandian, A review of wind energy technologies, Renewable and Sustainable Energy Reviews 11 (2007) 1117–1145. https://doi.org/10.1016/j.rser.2005.08.004.

[16] J. Kimball, Physics of Sailing, CRC Press, 2009. https://doi.org/doi.org/10.1201/9781420073775.

[17] J.H. Parry, The Discovery of the Sea, University of California Press, 1981.

[18] R.L. Hills, Power from Wind: A History of Windmill Technology, Cambridge University Press, 1996.

[19] M. Ragheb, History of Harnessing Wind Power, in: Wind Energy Engineering: A Handbook for Onshore and Offshore Wind Turbines, Elsevier Inc., 2017: pp. 127–143. https://doi.org/10.1016/B978-0-12-809451-8.00007-2.

[20] H. Díaz, C. Guedes Soares, Review of the current status, technology and future trends of offshore wind farms, Ocean Engineering 209 (2020). https://doi.org/10.1016/j.oceaneng.2020.107381.

[21] B.G. Miller, Coal Energy Systems, Elsevier Academic Press, 2005.

[22] T.T. Read, The Earliest Industrial Use of Coal, Transactions of the Newcomen Society 20 (1939) 119–133. https://doi.org/10.1179/tns.1939.010.

[23] G. Clark, D. Jacks, Coal and the Industrial Revolution, 1700-1869, Eur Rev Econ Hist 11 (2007) 39–72. https://doi.org/10.1017/S1361491606001870.

[24] Z. Bian, H.I. Inyang, J.L. Daniels, F. Otto, S. Struthers, Environmental issues from coal mining and their solutions, Mining Science and Technology 20 (2010) 215–223. https://doi.org/10.1016/S1674-5264(09)60187-3.

[25] L. Maugeri, The age of oil: the mythology, history, and future of the world's most controversial resource, Praeger, 2006.

[26] J.P. Womack, D.T. Jones, D. Roos, The machine that changed the world: The story of lean production--Toyota's secret weapon in the global car wars that is now revolutionizing world industry, Simon and Schuster, 2007.

[27] S. Paraschiv, L.S. Paraschiv, Trends of carbon dioxide (CO2) emissions from fossil fuels combustion (coal, gas and oil) in the EU member states from 1960 to 2018, Energy Reports 6 (2020) 237–242. https://doi.org/10.1016/j.egyr.2020.11.116.

[28] M.J. Economides, R.E. Oligney, Natural Gas: The Revolution Is Coming, 2001.

[29] M. Balat, Global trends on production and utilization of natural gas, Energy Sources, Part B: Economics, Planning and Policy 4 (2009) 333–346. https://doi.org/10.1080/15567240701621125.

[30] F.J. da Silva, A.G.B. de Lima, Y.J.R. da Costa, C.R.B. Filho, M.B. Grilo, Dual-Fuel (Natural Gas/Biodiesel) Engines: Fundamentals, Performance and Environmental Impact, in: 2013: pp. 47–68. https://doi.org/10.1007/978-3-642-40680-5_3.

[31] IEA, Electricity Information: Overview, International Energy Agency (2021). https://www.iea.org/reports/electricity-information-overview/electricity-consumption (accessed April 5, 2024).

[32] A.K. Erenoğlu, O. Erdinç, A. Taşcikaraoğlu, History of Electricity, in: Pathways to a Smarter Power System, Elsevier, 2019: pp. 1–27. https://doi.org/10.1016/B978-0-08-102592-5.00001-6.

[33] C.J. Brockman, The History of Electricity Before the Discovery of the Voltaic Pile, 1929. https://pubs.acs.org/sharingguidelines.

[34] A. Binnie, Using the History of Electricity and Magnetism to Enhance Teaching, 2001.

[35] P. Benjamin, The Intellectual Rise in Electricity: A History, Longmans, Green & Company, 1895.

[36] L. Fabbrizzi, The invention of Volta's Pile and its diffusion in Europe at war in the year 1800, in: Pure and Applied Chemistry, Walter de Gruyter GmbH, 2023. https://doi.org/10.1515/pac-2023-0504.

[37] The Metropolitan Museum of Art, Franklin's Experiment, June 1752 – Demonstrating the identity of Lightning and Electricity, from which he invented the Lightning Rod, Currier & Ives (1876).

[38] J.R. Nielsen, Hans Christian Oersted—Scientist, Humanist and Teacher, Am J Phys 7 (1939) 10–22. https://doi.org/10.1119/1.1991388.

[39] G.D. Friedlander, Retrospective: Ampère: Father of electrodynamics: The master mathematician, teacher, and practitioner of electrical science is celebrated on the 200th anniversary of his birth, IEEE Spectr 12 (1975) 75–78.

[40] M. Faraday, V. Experimental researches in electricity, Philos Trans R Soc Lond 122 (1832). https://royalsocietypublishing.org/.

[41] J.C. Maxwell, A dynamical theory of the electromagnetic field, Royal Society (1865).

[42] K.G. Beauchamp, History of Telegraphy, The institution of Engineering and Technology, 2001.

[43] S.F.B. Morse, First telegraphic message---24 May 1844, Library of Congress (1844). http://hdl.loc.gov/loc.mss/mmorse.071009 (accessed December 24, 2023).

[44] G. Adair, Thomas Alva Edison: Inventing the Electric Age, Oxford University Press, 1996.

[45] K.M. Swezey, Nikola Tesla: Electricity today is generated, transmitted, and converted to mechanical power by means of his inventions, 1958.

[46] Ember, Electricity production by source, World, Our World in Data (2024). ourworldindata.org/grapher/electricity-production-by-source (accessed December 31, 2023).

[47] P. Breeze, Coal-fired Power Plants, 2014.

[48] J.P. Longwell, E.S. Rubint, J. Wilson, Coal: Energy for the future, 1995. https://doi.org/doi.org/10.1016/0360-1285(95)00007-0.

[49] Georgia Power, A Coal-Fired Thermoelectric Power Plant, United States Geological Survey (2018).

[50] GE VERNOVA, AIR-COOLED GENERATOR (GEN-A), (2024). https://www.gevernova.com/gas-power/products/generators/air-cooled (accessed May 1, 2024).

[51] IEA, Greenhouse Gas Emissions from Energy Data Explorer, International Energy Agency (2023). www.iea.org/data-and-statistics/data-tools/greenhouse-gas-emissions-from-energy-data-explorer (accessed January 3, 2024).

[52] S. Faramawy, T. Zaki, A.A.-E. Sakr, Natural gas origin, composition, and processing: A review, J Nat Gas Sci Eng 34 (2016) 34–54. https://doi.org/10.1016/j.jngse.2016.06.030.

[53] BP, Statistical Review of World Energy 2022, 2022.

[54] IEA, Natural Gas, International Energy Agency (2024). https://www.iea.org/energy-system/fossil-fuels/natural-gas (accessed May 1, 2024).

[55] Office of Fossil Energy and Carbon Management, How Gas Turbine Power Plants Work, U.S. Department of Energy (n.d.). https://www.energy.gov/fecm/how-gas-turbine-power-plants-work (accessed January 5, 2024).

[56] M. Hafner, G. Luciani, The Palgrave Handbook of International Energy Economics, n.d.

[57] Å. Killingtveit, Hydropower, in: Managing Global Warming: An Interface of Technology and Human Issues, Elsevier, 2018: pp. 265–315. https://doi.org/10.1016/B978-0-12-814104-5.00008-9.

[58] IEA, Hydropower Special Market Report, n.d. www.iea.org/t&c/.

[59] Water Power Technologies Office, Types of Hydropower Plants, U.S. Department of Energy (n.d.). https://www.energy.gov/eere/water/types-hydropower-plants (accessed January 7, 2024).

[60] A. Galindo, What is Nuclear Energy? The Science of Nuclear Power, IAEA (2022). https://www.iaea.org/newscenter/news/what-is-nuclear-energy-the-science-of-nuclear-power (accessed May 1, 2024).

[61] I. Chatzis, M. Irena, What is Fusion, and Why Is It So Difficult to Achieve?, IAEA (2021). https://www.iaea.org/bulletin/what-is-fusion-and-why-is-it-so-difficult-to-achieve (accessed January 8, 2024).

[62] IEA, Nuclear Power and Secure Energy Transitions From today's challenges to tomorrow's clean energy systems, n.d. www.iea.org/t&c/.

[63] The U.S. Nuclear Regulatory Commission, The Boiling Water Reactor (BWR), The U.S. Nuclear Regulatory Commission (2017). https://www.nrc.gov/reading-rm/basic-ref/students/animated-bwr.html (accessed May 3, 2024).

[64] Wind Energy Technologies Office, How Do Wind Turbines Work?, U.S. Department of Energy (n.d.). https://www.energy.gov/eere/wind/how-do-wind-turbines-work (accessed January 8, 2024).

[65] U.S. Energy Information Administration, Solar explained Photovoltaics and Electricity, U.S. Energy Information Administration (n.d.). https://www.eia.gov/energyexplained/solar/photovoltaics-and-electricity.php (accessed January 9, 2024).

[66] EPA, What Is CHP?, United States Environmental Protection Agency (n.d.). https://www.epa.gov/chp/what-chp (accessed May 1, 2024).

[67] Industrial Efficiency & Decarbonization Office, Combined Heat and Power Basics, U.S. Department of Energy (n.d.). https://www.energy.gov/eere/iedo/combined-heat-and-power-basics (accessed January 12, 2024).

[68] IEA, Global Hydrogen Review 2023, 2023. www.iea.org.

[69] L. Truche, F.-V. Donzé, E. Goskolli, B. Muceku, C. Loisy, C. Monnin, H. Dutoit, A. Cerepi, A deep reservoir for hydrogen drives intense degassing in the Bulqizë ophiolite, Science (1979) 383 (2024) 618–621. https://doi.org/10.1126/science.adk9099.

[70] S. Griffiths, B.K. Sovacool, J. Kim, M. Bazilian, J.M. Uratani, Industrial decarbonization via hydrogen: A critical and systematic review of developments, socio-technical systems and policy options, Energy Res Soc Sci 80 (2021). https://doi.org/10.1016/j.erss.2021.102208.

[71] W.M. Haynes, ed., Abundance of Elements in the Earth's Crust and in the Sea, in: CRC Handbook of Chemistry and Physics, Internet Version, 2005: pp. 14–17.

[72] Office of Energy Efficiency & Renewable Energy, Hydrogen Fuel Cell Engines Module 1: Hydrogen Properties Contents, n.d. https://www.energy.gov/sites/default/files/2014/03/f12/fcm01r0.pdf (accessed January 23, 2024).

[73] N. Armaroli, V. Balzani, The hydrogen issue, ChemSusChem 4 (2011) 21–36. https://doi.org/10.1002/cssc.201000182.

[74] P.P. Edwards, V.L. Kuznetsov, W.I.F. David, Hydrogen energy, Philosophical Transactions of the Royal Society A: Mathematical, Physical and Engineering Sciences 365 (2007) 1043–1056. https://doi.org/10.1098/rsta.2006.1965.

[75] IEA, Carbon Capture, Utilisation and Storage, International Energy Agency (n.d.). https://www.iea.org/energy-system/carbon-capture-utilisation-and-storage (accessed January 24, 2024).

[76] A. Kovač, M. Paranos, D. Marciuš, Hydrogen in energy transition: A review, Int J Hydrogen Energy 46 (2021) 10016–10035. https://doi.org/10.1016/j.ijhydene.2020.11.256.

[77] T. Capurso, M. Stefanizzi, M. Torresi, S.M. Camporeale, Perspective of the role of hydrogen in the 21st century energy transition, Energy Convers Manag 251 (2022). https://doi.org/10.1016/j.enconman.2021.114898.

[78] J.J. Spivey, K.M. Dooley, Catalysis Volume 20, Royal Society of Chemistry, 2007.

[79] K.E. Cox, K.E. Williamson, Hydrogen: Its Technology and Implication, 1975.

[80] J.D. Holladay, J. Hu, D.L. King, Y. Wang, An overview of hydrogen production technologies, Catal Today 139 (2009) 244–260. https://doi.org/10.1016/j.cattod.2008.08.039.

[81] Bioenergy Technologies Office, Bioenergy Basics, U.S. Department of Energy (n.d.). https://www.energy.gov/eere/bioenergy/bioenergy-basics (accessed January 25, 2024).

[82] X.L. Yan, R. Hino, NUCLEAR HYDROGEN PRODUCTION HANDBOOK, 2011.

[83] International Renewable Energy Agency., Hydrogen from renewable power : technology outlook for the energy transition, 2018.

[84] S.A. Grigoriev, V.N. Fateev, D.G. Bessarabov, P. Millet, Current status, research trends, and challenges in water electrolysis science and technology, Int J Hydrogen Energy 45 (2020) 26036–26058. https://doi.org/10.1016/j.ijhydene.2020.03.109.

[85] Hydrogen and Fuel Cell Technologies Office, Hydrogen Production: Electrolysis, U.S. Department of Energy (n.d.). https://www.energy.gov/eere/fuelcells/hydrogen-production-electrolysis (accessed January 26, 2024).

[86] Y. Zheng, J. Wang, B. Yu, W. Zhang, J. Chen, J. Qiao, J. Zhang, A review of high temperature co-electrolysis of H2O and CO2 to produce sustainable fuels using solid oxide electrolysis cells (SOECs): Advanced materials and technology, Chem Soc Rev 46 (2017) 1427–1463. https://doi.org/10.1039/c6cs00403b.

[87] R. Hino, K. Haga, H. Aita, K. Sekita, 38. R&D on hydrogen production by high-temperature electrolysis of steam, in: Nuclear Engineering and Design, 2004: pp. 363–375. https://doi.org/10.1016/j.nucengdes.2004.08.029.

[88] C. Jiang, S.J.A. Moniz, A. Wang, T. Zhang, J. Tang, Photoelectrochemical devices for solar water splitting-materials and challenges, Chem Soc Rev 46 (2017) 4645–4660. https://doi.org/10.1039/c6cs00306k.

[89] L.J. Minggu, W.R. Wan Daud, M.B. Kassim, An overview of photocells and photoreactors for photoelectrochemical water splitting, Int J Hydrogen Energy 35 (2010) 5233–5244. https://doi.org/10.1016/j.ijhydene.2010.02.133.

[90] E. Eroglu, A. Melis, Photobiological hydrogen production: Recent advances and state of the art, Bioresour Technol 102 (2011) 8403–8413. https://doi.org/10.1016/j.biortech.2011.03.026.

[91] Andrea Willige, The colors of hydrogen: Expanding ways of decarbonization, MITSUBISHI HEAVY INDUSTRIES SPECTRA (2022). https://spectra.mhi.com/the-colors-of-hydrogen-expanding-ways-of-decarbonization (accessed June 11, 2024).

[92] A. Azzouz, Achievement in hydrogen storage on adsorbents with high surface-to-bulk ratio - Prospects for Si-containing matrices, Int J Hydrogen Energy 37 (2012) 5032–5049. https://doi.org/10.1016/j.ijhydene.2011.12.024.

[93] T.B. Gupta, ed., Hydrogen fuel: production, transport, and storage, CRC press, 2008.

[94] M. Momirlan, T.N. Veziroglu, The properties of hydrogen as fuel tomorrow in sustainable energy system for a cleaner planet, Int J Hydrogen Energy 30 (2005) 795–802. https://doi.org/10.1016/j.ijhydene.2004.10.011.

[95] A. Witkowski, A. Rusin, M. Majkut, K. Stolecka, Comprehensive analysis of hydrogen compression and pipeline transportation from thermodynamics and safety aspects, Energy 141 (2017) 2508–2518. https://doi.org/10.1016/j.energy.2017.05.141.

[96] D. Stolte, B. Emonts, eds., Hydrogen Science and Engineering, 2 Volume Set: Materials, Processes, Systems, and Technology, John Wiley & Sons, 2016.

[97] A. Gupta, G. V. Baron, P. Perreault, S. Lenaerts, R.G. Ciocarlan, P. Cool, P.G.M. Mileo, S. Rogge, V. Van Speybroeck, G. Watson, P. Van Der Voort, M. Houlleberghs, E. Breynaert, J. Martens, J.F.M. Denayer, Hydrogen Clathrates: Next Generation Hydrogen Storage Materials, Energy Storage Mater 41 (2021) 69–107. https://doi.org/10.1016/j.ensm.2021.05.044.

[98] R. Chahine, T.K. Bose, Low-pressure adsorption storage of hydrogen, 19 (1994) 161–164.

[99] Z. Yang, Y. Xia, R. Mokaya, Enhanced hydrogen storage capacity of high surface area zeolite-like carbon materials, J Am Chem Soc 129 (2007) 1673–1679. https://doi.org/10.1021/ja067149g.

[100] Y.J. Han, S.J. Park, Influence of nickel nanoparticles on hydrogen storage behaviors of MWCNTs, Appl Surf Sci 415 (2017) 85–89. https://doi.org/10.1016/j.apsusc.2016.12.108.

[101] B. Sakintuna, F. Lamari-Darkrim, M. Hirscher, Metal hydride materials for solid hydrogen storage: A review, Int J Hydrogen Energy 32 (2007) 1121–1140. https://doi.org/10.1016/j.ijhydene.2006.11.022.

[102] Y. Liu, X. Zhang, K. Wang, Y. Yang, M. Gao, H. Pan, Achieving ambient temperature hydrogen storage in ultrafine nanocrystalline TiO2@C-doped NaAlH4, J Mater Chem A Mater 4 (2016) 1087–1095. https://doi.org/10.1039/c5ta09400c.

[103] A. Klerke, C.H. Christensen, J.K. Nørskov, T. Vegge, Ammonia for hydrogen storage: Challenges and opportunities, J Mater Chem 18 (2008) 2304–2310. https://doi.org/10.1039/b720020j.

[104] D. Teichmann, W. Arlt, P. Wasserscheid, R. Freymann, A future energy supply based on Liquid Organic Hydrogen Carriers (LOHC), Energy Environ Sci 4 (2011) 2767–2773. https://doi.org/10.1039/c1ee01454d.

[105] K. Hassmann, SOFC Power Plants, the Siemens-Westinghouse Approach, Fuel Cells 1 (2001) 78–84. https://doi.org/10.1002/1615-6854(200105)1:1<78::aid-fuce78>3.0.co;2-q.

[106] S.C. Singhal, K. Kendall, High-temperature Solid Oxide Fuel Cells: Fundamentals, Design and Applications, Elsevier, 2003.

[107] A. Schnettler, At the Dawn of the Hydrogen Economy, Siemens Energy (2024). https://www.powermag.com/siemens-dawn-hydrogen-economy/ (accessed June 11, 2024).

[108] M.B. Mogensen, M. Chen, H.L. Frandsen, C. Graves, J.B. Hansen, K. V. Hansen, A. Hauch, T. Jacobsen, S.H. Jensen, T.L. Skafte, X. Sun, Reversible solid-oxide

cells for clean and sustainable energy, Clean Energy 3 (2019) 175–201. https://doi.org/10.1093/ce/zkz023.

[109] R. O'Hayre, S. Cha, W. Colella, F.B. Prinz, Fuel Cell Fundamentals, Wiley, 2016. https://doi.org/10.1002/9781119191766.

[110] B. Zhu, Y. Mi, C. Xia, B. Wang, J.-S. Kim, P. Lund, T. Li, A nanoscale perspective on solid oxide and semiconductor membrane fuel cells: materials and technology, Energy Materials 1 (2022) 100002. https://doi.org/10.20517/energymater.2021.03.

[111] A.J. Appleby, From Sir William Grove to Today: Fuel Cells and The Future, 1990.

[112] M.L. Perry, T.F. Fuller, A Historical Perspective of Fuel Cell Technology in the 20th Century, J Electrochem Soc 149 (2002) S59. https://doi.org/10.1149/1.1488651.

[113] L. van Biert, K. Visser, Fuel cells systems for sustainable ships, in: Sustainable Energy Systems on Ships: Novel Technologies for Low Carbon Shipping, Elsevier, 2022: pp. 81–121. https://doi.org/10.1016/B978-0-12-824471-5.00010-4.

[114] A.K.M. Mohiuddin, A. Rahman, M.F. Chemani, M.B. Zakaria, INVESTIGATION OF PEM FUEL CELL FOR AUTOMOTIVE USE, IIUM Engineering Journal 16 (2015) 69–78. https://doi.org/10.31436/iiumej.v16i2.605.

[115] S. Mekhilef, R. Saidur, A. Safari, Comparative study of different fuel cell technologies, Renewable and Sustainable Energy Reviews 16 (2012) 981–989. https://doi.org/10.1016/j.rser.2011.09.020.

[116] Hydrogen and Fuel Cell Technologies Office, Comparison of Fuel Cell Technologies, U.S. Department of Energy (n.d.). https://www.energy.gov/eere/fuelcells/comparison-fuel-cell-technologies (accessed February 27, 2024).

[117] Hydrogen and Fuel Cell Technologies Office, Types of Fuel Cells, U.S. Department of Energy (n.d.). https://www.energy.gov/eere/fuelcells/types-fuel-cells (accessed February 27, 2024).

[118] S.M. Haile, Fuel cell materials and components, Acta Mater 51 (2003) 5981–6000. https://doi.org/10.1016/j.actamat.2003.08.004.

[119] S. Santhanam, M.P. Heddrich, M. Riedel, K.A. Friedrich, Theoretical and experimental study of Reversible Solid Oxide Cell (r-SOC) systems for energy storage, Energy 141 (2017) 202–214. https://doi.org/10.1016/j.energy.2017.09.081.

[120] S.P. Jiang, Challenges in the development of reversible solid oxide cell technologies: A mini review, Asia-Pacific Journal of Chemical Engineering 11 (2016) 386–391. https://doi.org/10.1002/apj.1987.

[121] H. Il Ji, J.H. Lee, J.W. Son, K.J. Yoon, S. Yang, B.K. Kim, Protonic ceramic electrolysis cells for fuel production: a brief review, Journal of the Korean Ceramic Society 57 (2020) 480–494. https://doi.org/10.1007/s43207-020-00059-4.

[122] A. Mahmood, S. Bano, J.H. Yu, K.H. Lee, Performance evaluation of SOEC for CO2/H2O co-electrolysis: Considering the effect of cathode thickness, Journal of CO2 Utilization 33 (2019) 114–120. https://doi.org/10.1016/j.jcou.2019.05.014.

[123] A.D.N. Kamkeng, M. Wang, Long-term performance prediction of solid oxide electrolysis cell (SOEC) for CO2/H2O co-electrolysis considering structural degradation through modelling and simulation, Chemical Engineering Journal 429 (2022). https://doi.org/10.1016/j.cej.2021.132158.

[124] D.J.L. Brett, A. Atkinson, N.P. Brandon, S.J. Skinner, Intermediate temperature solid oxide fuel cells, Chem Soc Rev 37 (2008) 1568–1578. https://doi.org/10.1039/b612060c.

[125] J.B. Goodenough, Y.H. Huang, Alternative anode materials for solid oxide fuel cells, J Power Sources 173 (2007) 1–10. https://doi.org/10.1016/j.jpowsour.2007.08.011.

[126] S.P.S. Shaikh, A. Muchtar, M.R. Somalu, A review on the selection of anode materials for solid-oxide fuel cells, Renewable and Sustainable Energy Reviews 51 (2015) 1–8. https://doi.org/10.1016/j.rser.2015.05.069.

[127] N.Q. Minh, Ceramic Fuel Cells, Journal of the American Ceramic Society (1995) 563–88. https://doi.org/10.1111/j.1151-2916.1993.tb03645.x.

[128] R.M. Ormerod, Solid oxide fuel cells, Chem Soc Rev 32 (2003) 17–28. https://doi.org/10.1039/b105764m.

[129] O.A. Marina, N.L. Canfield, J.W. Stevenson, Thermal, electrical, and electrocatalytical properties of lanthanum-doped strontium titanate, Solid State Ion (2002) 21–28. www.elsevier.com/locate/ssi.

[130] X. Li, H. Zhao, N. Xu, X. Zhou, C. Zhang, N. Chen, Electrical conduction behavior of La, Co co-doped SrTiO3 perovskite as anode material for solid oxide fuel cells, Int J Hydrogen Energy 34 (2009) 6407–6414. https://doi.org/10.1016/j.ijhydene.2009.05.079.

[131] X. Li, H. Zhao, W. Shen, F. Gao, X. Huang, Y. Li, Z. Zhu, Synthesis and properties of Y-doped SrTiO3 as an anode material for SOFCs, J Power Sources 166 (2007) 47–52. https://doi.org/10.1016/j.jpowsour.2007.01.008.

[132] S. Tao, J.T.S. Irvine, Synthesis and Characterization of (La0.75Sr0.25)Cr0.5Mn0.5O3−δ, a Redox-Stable, Efficient Perovskite Anode for SOFCs, J Electrochem Soc 151 (2004) A252. https://doi.org/10.1149/1.1639161.

[133] J. Sfeir, P.A. Buffat, P. Mockli, N. Xanthopoulos, R. Vasquez, H.J. Mathieu, J. Van herle, K.R. Thampi, Lanthanum chromite based catalysts for oxidation of methane directly on SOFC anodes, J Catal 202 (2001) 229–244. https://doi.org/10.1006/jcat.2001.3286.

[134] Y.-H. Huang, R.I. Dass, J.C. Denyszyn, J.B. Goodenough, Synthesis and Characterization of Sr2MgMoO6−δ : An Anode Material for the Solid Oxide Fuel Cell, J Electrochem Soc 153 (2006) A1266. https://doi.org/10.1149/1.2195882.

[135] Z. Xie, H. Zhao, Z. Du, T. Chen, N. Chen, X. Liu, S.J. Skinner, Effects of Co doping on the electrochemical performance of double perovskite oxide Sr2MgMoO6-δ as an anode material for solid oxide fuel cells, Journal of Physical Chemistry C 116 (2012) 9734–9743. https://doi.org/10.1021/jp212505c.

[136] A.K. Dorai, Y. Masuda, J.H. Joo, S.K. Woo, S.D. Kim, Influence of Fe doping on the electrical properties of Sr2MgMoO6-δ, Mater Chem Phys 139 (2013) 360–363. https://doi.org/10.1016/j.matchemphys.2013.02.039.

[137] Z. Xie, H. Zhao, T. Chen, X. Zhou, Z. Du, Synthesis and electrical properties of Al-doped Sr2MgMoO6-δ as an anode material for solid oxide fuel cells, Int J Hydrogen Energy 36 (2011) 7257–7264. https://doi.org/10.1016/j.ijhydene.2011.03.075.

[138] Z. Du, H. Zhao, S. Yi, Q. Xia, Y. Gong, Y. Zhang, X. Cheng, Y. Li, L. Gu, K. Świerczek, High-Performance Anode Material Sr2FeMo0.65Ni0.35O6-δ with in Situ Exsolved Nanoparticle Catalyst, ACS Nano 10 (2016) 8660–8669. https://doi.org/10.1021/acsnano.6b03979.

[139] J.B. Goodenough, Oxide-ion electrolytes, Annu Rev Mater Res 33 (2003) 91–128. https://doi.org/10.1146/annurev.matsci.33.022802.091651.

[140] K.C. Wincewicz, J.S. Cooper, Taxonomies of SOFC material and manufacturing alternatives, J Power Sources 140 (2005) 280–296. https://doi.org/10.1016/j.jpowsour.2004.08.032.

[141] J.M. Ralph, J.A. Kilner, B.C.H. Steele, Improving Gd-Doped Ceria Electrolytes for Low Temperature Solid Oxide Fuel Cells, MRS Online Proceedings Library (1999) 309.

[142] E. Ivers-Tiffée, Solid: Oxygen Ions, Encyclopedia of Electrochemical Power Sources (2009) 181–187.

[143] K. Huang, R.S. Tichy, J.B. Goodenough, Superior Perovskite Oxide-Ion Conductor; Strontium- and Magnesium-Doped LaGaO3: II, ac Impedance Spectroscopy, Journal of the American Ceramic Society 81 (1998) 2576–2580.

[144] K. Huang, J.-H. Wan, J.B. Goodenough, Increasing Power Density of LSGM-Based Solid Oxide Fuel Cells Using New Anode Materials, J Electrochem Soc 148 (2001) A788. https://doi.org/10.1149/1.1378289.

[145] K.D. Kreuer, Proton-Conducting Oxides, Annu Rev Mater Res 33 (2003) 333–359. https://doi.org/10.1146/annurev.matsci.33.022802.091825.

[146] C. Sun, R. Hui, J. Roller, Cathode materials for solid oxide fuel cells: A review, Journal of Solid State Electrochemistry 14 (2010) 1125–1144. https://doi.org/10.1007/s10008-009-0932-0.

[147] L. Li, Z. Dong, T. Xia, X. Li, Q. Li, L. Sun, H. Zhao, L. Huo, A series of bifunctional ReBaCo2O5+δ perovskite catalysts towards intermediate-temperature oxygen reduction reaction and oxygen evolution reaction, Chemical Engineering Journal 468 (2023). https://doi.org/10.1016/j.cej.2023.143762.

[148] S.B. Adler, J.A. Lane, B.C. H Steele -, C. Wang, W.L. Worrell, S. Park, al -, M. Liu, H. Hu -, Electrode Kinetics of Porous Mixed-Conducting Oxygen Electrodes Fabrication and Performance of Thin-Film YSZ Solid Oxide Fuel Cells Effect of Interfacial Resistance on Determination of Transport Properties of MixedConducting Electrolytes, 1996.

[149] J. Richter, P. Holtappels, T. Graule, T. Nakamura, L.J. Gauckler, Materials design for perovskite SOFC cathodes, Monatsh Chem 140 (2009) 985–999. https://doi.org/10.1007/s00706-009-0153-3.

[150] S.P. Jiang, Development of lanthanum strontium manganite perovskite cathode materials of solid oxide fuel cells: A review, J Mater Sci 43 (2008) 6799–6833. https://doi.org/10.1007/s10853-008-2966-6.

[151] R.H. Mitchell, Perovskites Modern and Ancient, Almaz Press Inc., 2002.

[152] J.M. Ralph, A.C. Schoeler, M. Krumpelt, Materials for lower temperature solid oxide fuel cells, J Mater Sci 36 (2001) 1161–1172.

[153] J.B. Goodenough, ed., Structure and Bonding Series, Localized to Itinerant Electronic Transition in Perovskite Oxides, Springer, 2001.

[154] C.N.R. Rao, B. Raveau, Transition metal oxides: structure, properties and synthesis of ceramics oxides, Wiley-VCH, 1998.

[155] J.-W. Kim, A. V Virkar, K.-Z. Fung, K. Mehta, S.C. Singhal, Polarization effects in intermediate temperature, anode-supported Solid Oxide Fuel Cells, 1999.

[156] Y. Takeda, R. Kanno, M. Noda, O. Yamamoto, Perovskite Electrodes for High Temperature Solid Electrolyte Fuel Cells, Bull. Inst. Chem. Res., Kyoto Univ 64 (1986).

[157] A.N. Petrov, O.F. Kononchuk, A. V Andreev, V.A. Cherepanov, P. Kofstad, Crystal structure, electrical and magnetic properties of La1-xSrxCoO3-y, Solid State Ion 80 (1995) 189–199.

[158] J.A. Kilner, R.J. Brook, A STUDY OF OXYGEN ION CONDUCTIVITY IN DOPED NON-STOICHIOMETRIC OXIDES, 1982.

[159] K.T. Lee, A. Manthiram, Comparison of Ln0.6Sr0.4Co3−δ (Ln=La, Pr, Nd, Sm, and Gd) as Cathode Materials for Intermediate Temperature Solid Oxide Fuel Cells, J Electrochem Soc 153 (2006) A794. https://doi.org/10.1149/1.2172572.

[160] E. V. Tsipis, V. V. Kharton, Electrode materials and reaction mechanisms in solid oxide fuel cells: A brief review : II. Electrochemical behavior vs. materials science aspects, Journal of Solid State Electrochemistry 12 (2008) 1367–1391. https://doi.org/10.1007/s10008-008-0611-6.

[161] J.H. Lee, K.N. Kim, J.W.S.J. Kim, B.K. Kim, H.W. Lee, J. Moon, An investigation of the interfacial stability between the anode and electrolyte layer of LSGM-based SOFCs, in: J Mater Sci, 2007: pp. 1866–1871. https://doi.org/10.1007/s10853-006-1315-x.

[162] O. Gwon, S. Yoo, J. Shin, G. Kim, Optimization of La1-xSrxCoO3-δ perovskite cathodes for intermediate temperature solid oxide fuel cells through the analysis of crystal structure and electrical properties, Int J Hydrogen Energy 39 (2014) 20806–20811. https://doi.org/10.1016/j.ijhydene.2014.07.137.

[163] X. Lou, S. Wang, Z. Liu, L. Yang, M. Liu, Improving La0.6Sr0.4Co0.2Fe0.8O3-δ cathode performance by infiltration of a Sm0.5Sr0.5CoO3-δ coating, Solid State Ion 180 (2009) 1285–1289. https://doi.org/10.1016/j.ssi.2009.06.014.

[164] Z. Shao, S.M. Halle, A high-performance cathode for the next generation of solid-oxide fuel cells, Nature 431 (2004) 170–173. https://doi.org/10.1038/nature02863.

[165] S.J. Skinner, J.A. Kilner, Oxygen diffusion and surface exchange in La2-xSrxNiO4+δ, 2000. www.elsevier.com/locate/ssi.

[166] G. King, P.M. Woodward, Cation ordering in perovskites, J Mater Chem 20 (2010) 5785–5796. https://doi.org/10.1039/b926757c.

[167] S. Choi, S. Yoo, J. Kim, S. Park, A. Jun, S. Sengodan, J. Kim, J. Shin, H.Y. Jeong, Y. Choi, G. Kim, M. Liu, Highly efficient and robust cathode materials for low-temperature solid oxide fuel cells: PrBa0.5Sr0.5Co2-xFexO5+δ, Sci Rep 3 (2013). https://doi.org/10.1038/srep02426.

[168] J.-H. Kim, A. Manthiram, LnBaCo2O5+δ Oxides as Cathodes for Intermediate-Temperature Solid Oxide Fuel Cells, J Electrochem Soc 155 (2008) B385. https://doi.org/10.1149/1.2839028.

[169] J.-H. Kim, F. Prado, A. Manthiram, Characterization of GdBa1−xSrxCo2O5+δ (0≤x≤1.0) Double Perovskites as Cathodes for Solid Oxide Fuel Cells, J Electrochem Soc 155 (2008) B1023. https://doi.org/10.1149/1.2965792.

[170] D.S. Tsvetkov, N.S. Saricheva, V. V. Sereda, A.Y. Zuev, Oxygen nonstoichiometry and electrochemical properties of GdBaCo2-xFexO6-δ double perovskite cathodes, J Fuel Cell Sci Technol 8 (2011). https://doi.org/10.1115/1.4003631.

[171] Q. Zhou, F. Wang, Y. Shen, T. He, Performances of LnBaCo2O5+x-Ce0.8Sm0.2O1.9 composite cathodes for intermediate-temperature solid oxide fuel cells, J Power Sources 195 (2010) 2174–2181. https://doi.org/10.1016/j.jpowsour.2009.10.062.

[172] H. Wang, C. Tablet, A. Feldhoff, J. Caro, A cobalt-free oxygen-permeable membrane based on the perovskite-type oxide Ba0.5Sr0.5Zn0.2Fe0.8O3-δ, Advanced Materials 17 (2005) 1785–1788. https://doi.org/10.1002/adma.200401608.

[173] B. Wei, Z. Lü, X. Huang, M. Liu, N. Li, W. Su, Synthesis, electrical and electrochemical properties of Ba0.5Sr0.5Zn0.2Fe0.8O3-δ perovskite oxide for IT-SOFC cathode, J Power Sources 176 (2008) 1–8. https://doi.org/10.1016/j.jpowsour.2007.09.120.

[174] J. Lu, Y.M. Yin, Z.F. Ma, Preparation and characterization of new cobalt-free cathode Pr0.5Sr0.5Fe0.8Cu0.2O3-δ for IT-SOFC, Int J Hydrogen Energy 38 (2013) 10527–10533. https://doi.org/10.1016/j.ijhydene.2013.05.164.

[175] Y. Zhang, H. Zhao, Z. Du, K. Świerczek, Y. Li, High-Performance SmBaMn2O5+δ Electrode for Symmetrical Solid Oxide Fuel Cell, Chemistry of Materials 31 (2019) 3784–3793. https://doi.org/10.1021/acs.chemmater.9b01012.

[176] A. Olszewska, Y. Zhang, Z. Du, M. Marzec, K. Świerczek, H. Zhao, B. Dabrowski, Mn-rich SmBaCo0.5Mn1.5O5+δ double perovskite cathode material for SOFCs,

Int J Hydrogen Energy 44 (2019) 27587–27599. https://doi.org/10.1016/j.ijhydene.2019.08.254.

[177] X. Che, Y. Shen, H. Li, T. He, Assessment of LnBaCo1.6 Ni0.4O5+δ (Ln = Pr, Nd, and Sm) double-perovskites as cathodes for intermediate- temperature solid-oxide fuel cells, J Power Sources 222 (2013) 288–293. https://doi.org/10.1016/j.jpowsour.2012.08.044.

[178] J. Dąbrowa, A. Olszewska, A. Falkenstein, C. Schwab, M. Szymczak, M. Zajusz, M. Moździerz, A. Mikuła, K. Zielińska, K. Berent, T. Czeppe, M. Martin, K. Świerczek, An innovative approach to design SOFC air electrode materials: high entropy La1-xSrx(Co,Cr,Fe,Mn,Ni)O3-δ(x = 0, 0.1, 0.2, 0.3) perovskites synthesized by the sol-gel method, J Mater Chem A Mater 8 (2020) 24455–24468. https://doi.org/10.1039/d0ta06356h.

[179] J. Dąbrowa, A. Stępień, M. Szymczak, M. Zajusz, P. Czaja, K. Świerczek, High-entropy approach to double perovskite cathode materials for solid oxide fuel cells: Is multicomponent occupancy in (La,Pr,Nd,Sm,Gd)BaCo2O5+δ affecting physicochemical and electrocatalytic properties?, Front Energy Res 10 (2022). https://doi.org/10.3389/fenrg.2022.899308.

[180] L. Shen, Z. Du, Y. Zhang, X. Dong, H. Zhao, Medium-Entropy perovskites Sr(FeαTiβCoγMnζ)O3-δ as promising cathodes for intermediate temperature solid oxide fuel cell, Appl Catal B 295 (2021). https://doi.org/10.1016/j.apcatb.2021.120264.

[181] A. Sarkar, L. Velasco, D. Wang, Q. Wang, G. Talasila, L. de Biasi, C. Kübel, T. Brezesinski, S.S. Bhattacharya, H. Hahn, B. Breitung, High entropy oxides for reversible energy storage, Nat Commun 9 (2018). https://doi.org/10.1038/s41467-018-05774-5.

[182] Y.S. Yoo, M. Choi, J.H. Hwang, H.N. Im, B. Singh, S.J. Song, La2NiO4+δ as oxygen electrode in reversible solid oxide cells, Ceram Int 41 (2015) 6448–6454. https://doi.org/10.1016/j.ceramint.2015.01.083.

[183] K. Hosoi, H. Hagiwara, S. Ida, T. Ishihara, La0.8Sr0.2FeO3-δ as Fuel Electrode for Solid Oxide Reversible Cells Using LaGaO3-Based Oxide Electrolyte, Journal

of Physical Chemistry C 120 (2016) 16110–16117. https://doi.org/10.1021/acs.jpcc.5b12755.

[184] Energy Education, Copper, Energy Education (2024). https://energyeducation.ca/encyclopedia/Copper (accessed May 7, 2024).

[185] Royal Society of Chemistry, Copper, Royal Society of Chemistry (2024). https://www.rsc.org/periodic-table/element/29/copper (accessed May 7, 2024).

[186] J.G. Bednorz, K.A. Miiller, Condensed Possible High Tc Superconductivity in the Ba-La-Cu-0 System, 1986.

[187] Z. Hiroi, M. Takano, Absence of superconductivity in the doped antiferromagnetic spin-ladder compound (La,Sr)CuO2.5, Nature 377 (1995) 41–43.

[188] J.B. Torrance, Y. Tokura, A.I. Nazzal, A. Bezinge, T.C. Huang, S.S.P. Parkin, Anomalous Disappearance of High-T, Superconductivity at High Hole Concentration in Metallic La2-xSrxCuO4, Phys Rev Lett 61 (1988).

[189] J.F. Bringley, B.A. Scott, S.J. La Placa, T.R. Mcguire, F. Mehran, M.W. Mcelfresh, D.E. Cox, Structure and properties of the LaCuO3-δ perovskites, Phys Rev B 47 (1993) 15269. https://doi.org/doi.org/10.1103/PhysRevB.47.15269.

[190] T. Taniguchi, S. Kitagawa, K. Ishida, S. Asano, K. Kudo, M. Takahama, P. Xie, T. Noji, M. Fujita, 139La-NMR Study of Spin Dynamics Coupled with Hole Mobility in T*-type La0.86Eu0.86Sr0.28CuO4−δ, J Physical Soc Japan 91 (2022) 074710. https://doi.org/10.7566/JPSJ.91.074710.

[191] D.H. Kim, G.F. Dionne, C.A. Ross, Structure and magnetism of epitaxial SrTi0.78Cu 0.22O3-δ films with mixed-valence Cu ions, J Appl Phys 114 (2013). https://doi.org/10.1063/1.4821022.

[192] J.M. Kweun, C. Li, Y. Zheng, M. Cho, Y.Y. Kim, K. Cho, Bulk-surface relationship of an electronic structure for high-throughput screening of metal oxide catalysts, Appl Surf Sci 370 (2016) 279–290. https://doi.org/10.1016/j.apsusc.2016.02.093.

[193] J. Hwang, R.R. Rao, L. Giordano, Y. Katayama, Y. Yu, Y. Shao-Horn, Perovskites in catalysis and electrocatalysis, Science (1979) 358 (2017) 751–756. http://science.sciencemag.org/.

[194] J.S. Zhou, L.G. Marshall, J.B. Goodenough, Mass enhancement versus Stoner enhancement in strongly correlated metallic perovskites: LaNiO3 and LaCuO3, Phys Rev B Condens Matter Mater Phys 89 (2014). https://doi.org/10.1103/PhysRevB.89.245138.

[195] M. Karppinen, H. Yamauchi, T. Ito, H. Suematsu, O. Fukunaga, High-pressure synthesis and thermal decomposition of LaCuO3, Materials Science and Engineering: B 41 (1996) 59–62.

[196] M. Karppinen, H. Yamauchi, H. Suematsu, O. Fukunaga, Synthesis of various LaCuO3-y phases by a high-pressure technique and subsequent post-annealing treatments, 1996.

[197] J.F. Bringley, B.A. Scott, S.J. La Placa, R.F. Boehme, T.M. Shaw, M.W. McElfresh, S.S. Trail, D.E. Cox, Synthesis of the defect perovskite series LaCu03–δ with copper valence varying from 2+ to 3+, Nature 347 (1990) 263–265.

[198] A. Dwivedi, M.A. Rodriguez, A.N. Cormack, Defect-Chemical Aspects in the Synthesis of Metallic Conductors La1-xBaxCuO3 (x = 0.0 to 0.5), Journal of the American Ceramic Society 75 (1992) 1993–1996.

[199] A. Niemczyk, Z. Du, A. Olszewska, M. Marzec, M. Gajewska, K. Świerczek, H. Zhao, B. Poudel, B. Dabrowski, Effective oxygen reduction on A-site substituted LaCuO3-δ: toward air electrodes for SOFCs based on perovskite-type copper oxides, J Mater Chem A Mater 7 (2019) 27403–27416. https://doi.org/10.1039/c9ta09244g.

[200] H.C. Yu, F. Zhao, A. V. Virkar, K.Z. Fung, Electrochemical characterization and performance evaluation of intermediate temperature solid oxide fuel cell with La0.75Sr0.25CuO2.5-δ cathode, J Power Sources 152 (2005) 22–26. https://doi.org/10.1016/j.jpowsour.2005.03.173.

[201] N.A. Shah, D.G. Kuberkar, B.T. Savalia, M.R. Gonal, R. Prasad, R.G. Kulkarni, Effect of calcium substitution on superconductivity and hole concentration in La1.5Ba1.5Cu3Oz, Bull. Mater. Sci 21 (1998) 463–468.

[202] C.C. Torardi, E.M. Mccarron, M.A. Subramanian, A.W. Sleight, D.E. Cox, Structure of La1.5Ba1.5Cu3O7.3, Mater Res Bull 22 (1987) 1563–1571.

[203] A. Niemczyk, K. Zheng, K. Cichy, K. Berent, K. Küster, U. Starke, B. Poudel, B. Dabrowski, K. Świerczek, High Cu content LaNi1-xCuxO3-δ perovskites as candidate air electrode materials for Reversible Solid Oxide Cells, Int J Hydrogen Energy 45 (2020) 29449–29464. https://doi.org/10.1016/j.ijhydene.2020.07.267.

[204] S.F. Wang, C.T. Yeh, Y.R. Wang, Y.F. Hsu, Effects of (LaSr)(CoFeCu)O3-δ cathodes on the characteristics of intermediate temperature solid oxide fuel cells, J Power Sources 201 (2012) 18–25. https://doi.org/10.1016/j.jpowsour.2011.10.074.

[205] S.H. Jo, P. Muralidharan, D.K. Kim, Enhancement of electrochemical performance and thermal compatibility of GdBaCo2/3Fe2/3Cu2/3O5+δ cathode on Ce1.9Gd0.1O1.95 electrolyte for IT-SOFCs, Electrochem Commun 11 (2009) 2085–2088. https://doi.org/10.1016/j.elecom.2009.08.054.

[206] L.L. Hench, J.K. West, The Sol-Gel Process, 1990. https://pubs.acs.org/sharingguidelines.

[207] D. Navas, S. Fuentes, A. Castro-Alvarez, E. Chavez-Angel, Review on Sol-Gel Synthesis of Perovskite and Oxide Nanomaterials, Gels 7 (2021). https://doi.org/10.3390/gels7040275.

[208] Y. Zhang, L. Shen, Y. Wang, Z. Du, B. Zhang, F. Ciucci, H. Zhao, Enhanced oxygen reduction kinetics of IT-SOFC cathode with PrBaCo2O5+δ/Gd0.1Ce1.9O2-δ coherent interface, J Mater Chem A Mater 10 (2022) 3495–3505. https://doi.org/10.1039/d1ta09615j.

[209] S.T. Aruna, L.S. Balaji, S.S. Kumar, B.S. Prakash, Electrospinning in solid oxide fuel cells – A review, Renewable and Sustainable Energy Reviews 67 (2017) 673–682. https://doi.org/10.1016/j.rser.2016.09.003.

[210] Y.Z. Long, X. Yan, X.X. Wang, J. Zhang, M. Yu, Electrospinning: The Setup and Procedure, in: Electrospinning: Nanofabrication and Applications, Elsevier, 2018: pp. 21–52. https://doi.org/10.1016/B978-0-323-51270-1.00002-9.

[211] O.F. Dippo, K.S. Vecchio, A universal configurational entropy metric for high-entropy materials, Scr Mater 201 (2021). https://doi.org/10.1016/j.scriptamat.2021.113974.

[212] S.J. McCormack, A. Navrotsky, Thermodynamics of high entropy oxides, Acta Mater 202 (2021) 1–21. https://doi.org/10.1016/j.actamat.2020.10.043.

[213] B.H. Toby, R factors in Rietveld analysis: How good is good enough? , Powder Diffr 21 (2006) 67–70. https://doi.org/10.1154/1.2179804.

[214] B.H. Toby, R.B. Von Dreele, GSAS-II: The genesis of a modern open-source all purpose crystallography software package, J Appl Crystallogr 46 (2013) 544–549. https://doi.org/10.1107/S0021889813003531.

[215] D.C. Harris, T.A. Hewston, Determination of Cu3+/Cu2+ Ratio in the Superconductor YBa2Cu3O8-x, 1987.

[216] H.A. Blackstead, J.D. Dow, D.B. Pulling, Iodometric titration of copper-oxide superconductors and Tokura's Rule, 1996.

[217] S.P. Mulvaney, C.D. Keating, Raman spectroscopy, Anal Chem 72 (2000). https://doi.org/10.1021/a10000155.

[218] A. Mineshige, S. Okada, K. Sakai, M. Kobune, S. Fujii, H. Matsumoto, T. Shimura, H. Iwahara, Z. Ogumi, Oxygen nonstoichiometry in SrCeO3-based high-temperature protonic conductors evaluated by Raman spectroscopy, in: Solid State Ion, 2003: pp. 41–45. https://doi.org/10.1016/S0167-2738(03)00232-7.

[219] A.A. Emery, C. Wolverton, High-Throughput DFT calculations of formation energy, stability and oxygen vacancy formation energy of ABO3 perovskites, Sci Data 4 (2017). https://doi.org/10.1038/sdata.2017.153.

[220] J. Yu, R. Devanathan, W.J. Weber, First-principles study of defects and phase transition in UO2, Journal of Physics Condensed Matter 21 (2009). https://doi.org/10.1088/0953-8984/21/43/435401.

[221] J. Kupecki, R. Kluczowski, D. Papurello, A. Lanzini, M. Kawalec, M. Krauz, M. Santarelli, Characterization of a circular 80 mm anode supported solid oxide fuel cell (AS-SOFC) with anode support produced using high-pressure injection molding (HPIM), Int J Hydrogen Energy (2019) 19405–19411. https://doi.org/10.1016/j.ijhydene.2018.02.143.

[222] J. Peña-Martínez, D. Marrero-López, J.C. Ruiz-Morales, P. Núñez, C. Sánchez-Bautista, A.J. Dos Santos-García, J. Canales-Vázquez, On Ba0.5Sr0.5Co1-

yFeyO3-δ (y = 0.1-0.9) oxides as cathode materials for La0.9Sr0.1Ga0.8Mg0.2O2.85 based IT-SOFCs, Int J Hydrogen Energy 34 (2009) 9486–9495. https://doi.org/10.1016/j.ijhydene.2009.09.041.

[223] D. Chen, R. Ran, K. Zhang, J. Wang, Z. Shao, Intermediate-temperature electrochemical performance of a polycrystalline PrBaCo2O5+δ cathode on samarium-doped ceria electrolyte, J Power Sources 188 (2009) 96–105. https://doi.org/10.1016/j.jpowsour.2008.11.045.

[224] S. Dierickx, A. Weber, E. Ivers-Tiffée, How the distribution of relaxation times enhances complex equivalent circuit models for fuel cells, Electrochim Acta 355 (2020). https://doi.org/10.1016/j.electacta.2020.136764.

[225] T.H. Wan, M. Saccoccio, C. Chen, F. Ciucci, Influence of the Discretization Methods on the Distribution of Relaxation Times Deconvolution: Implementing Radial Basis Functions with DRTtools, Electrochim Acta 184 (2015) 483–499. https://doi.org/10.1016/j.electacta.2015.09.097.

[226] N.A. Shah, D.G. Kuberkar, B.T. Savalia, M.R. Gonal, R. Prasad, R.G. Kulkarni, Effect of calcium substitution on superconductivity and hole concentration in Lal.sBaisCu3Oz, 1998.

[227] K. Li, A. Niemczyk, K. Świerczek, A. Stępień, Y. Naumovich, J. Dąbrowa, M. Zajusz, K. Zheng, B. Dabrowski, Co-free triple perovskite La1.5Ba1.5Cu3O7±δ as a promising air electrode material for solid oxide fuel cells, J Power Sources 532 (2022). https://doi.org/10.1016/j.jpowsour.2022.231371.

[228] T. Kawasa, T. Horita, Cathodes, in: High-Temperature Solid Oxide Fuel Cells for the 21st Century: Fundamentals, Design and Applications, Joe Hayton, 2015: pp. 161–189.

[229] C. Graves, S.D. Ebbesen, S.H. Jensen, S.B. Simonsen, M.B. Mogensen, Eliminating degradation in solid oxide electrochemical cells by reversible operation, Nat Mater 14 (2015) 239–244. https://doi.org/10.1038/nmat4165.

[230] S.R. Bishop, D. Marrocchelli, C. Chatzichristodoulou, N.H. Perry, M.B. Mogensen, H.L. Tuller, E.D. Wachsman, Chemical expansion: Implications for electrochemical energy storage and conversion devices, Annu Rev Mater Res 44 (2014) 205–239. https://doi.org/10.1146/annurev-matsci-070813-113329.

[231] ¨ H Ullmann, N. Trofimenko, F. Tietz, D. Stover, A. Ahmad-Khanlou, Correlation between thermal expansion and oxide ion transport in mixed conducting perovskite-type oxides for SOFC cathodes, 2000. www.elsevier.com/locate/ssi.

[232] J. Mizusaki, Y. Mima, S. Shigeru, Y. And, K. Fuekir, Nonstoichiometry of the perovskite-type oxides La1-xSrxCoO3-δ, J Solid State Chem 80 (1989) 102–111. https://doi.org/10.1016/0022-4596(89)90036-4.

[233] D. Fu, F. Jin, T. He, A-site calcium-doped Pr1-xCaxBaCo2O5+δ double perovskites as cathodes for intermediate-temperature solid oxide fuel cells, J Power Sources 313 (2016) 134–141. https://doi.org/10.1016/j.jpowsour.2016.02.071.

[234] V. V. Kharton, A. V. Kovalevsky, M. V. Patrakeev, E. V. Tsipis, A.P. Viskup, V.A. Kolotygin, A.A. Yaremchenko, A.L. Shaula, E.A. Kiselev, J.C. Waerenborgh, Oxygen nonstoichiometry, mixed conductivity, and mössbauer spectra of Ln0.5A0.5FeO3-δ (Ln = La-Sm, A = Sr, Ba): Effects of cation size, Chemistry of Materials 20 (2008) 6457–6467. https://doi.org/10.1021/cm801569j.

[235] E.I. Leonidova, A.A. Markov, M. V. Patrakeev, I.A. Leonidov, V.L. Kozhevnikov, Oxygen nonstoichiometry and the thermodynamic properties of manganites Ca1-x-ySrxLayMnO3-δ, Russian Journal of Physical Chemistry A 85 (2011) 343–347. https://doi.org/10.1134/S003602441102021X.

[236] S.R. Bishop, K.L. Duncan, E.D. Wachsman, Surface and Bulk Defect Equilibria in Strontium-Doped Lanthanum Cobalt Iron Oxide, J Electrochem Soc 156 (2009) B1242. https://doi.org/10.1149/1.3194783.

[237] M. Kuhn, Y. Fukuda, S. Hashimoto, K. Sato, K. Yashiro, J. Mizusaki, Oxygen Nonstoichiometry and Thermo-Chemical Stability of Perovskite-Type La0.6Sr0.4Co1- yFeyO3-δ (y=0, 0.2, 0.4, 0.5, 0.6, 0.8, 1) Materials, J Electrochem Soc 160 (2013) F34–F42. https://doi.org/10.1149/2.050301jes.

[238] M. Søgaard, P.V. Hendriksen, M. Mogensen, F.W. Poulsen, E. Skou, Oxygen nonstoichiometry and transport properties of strontium substituted lanthanum cobaltite, Solid State Ion 177 (2006) 3285–3296. https://doi.org/10.1016/j.ssi.2006.09.005.

[239] M. Kuhn, S. Hashimoto, K. Sato, K. Yashiro, J. Mizusaki, Oxygen nonstoichiometry and thermo-chemical stability of La0.6Sr0.4CoO3-δ, J Solid State Chem 197 (2013) 38–45. https://doi.org/10.1016/j.jssc.2012.08.001.

[240] K. Venkataraman, R. Baurceanu, V.A. Maroni, Characterization of MBa2Cu3O7-x Thin Films by Raman Microspectroscopy, Appl Spectrosc 59 (2005).

[241] N. Tsuda, K. Nasu, A. Fujimori, K. Siratori, Electronic Conduction in Oxides, Springer Science & Business Media, 2000.

[242] E. Vøllestad, M. Schrade, J. Segalini, R. Strandbakke, T. Norby, Relating defect chemistry and electronic transport in the double perovskite Ba1-xGd0.8La0.2+xCo2O6-δ (BGLC), J Mater Chem A Mater 5 (2017) 15743–15751. https://doi.org/10.1039/c7ta02659e.

[243] T. Ishihara, Perovskite Oxide for Solid Oxide Fuel Cells, Springer Science & Business Media, 2009.

[244] N. Jaiswal, K. Tanwar, R. Suman, D. Kumar, S. Uppadhya, O. Parkash, A brief review on ceria based solid electrolytes for solid oxide fuel cells, J Alloys Compd 781 (2019) 984–1005. https://doi.org/10.1016/j.jallcom.2018.12.015.

[245] M. Morales, J.J. Roa, J. Tartaj, M. Segarra, A review of doped lanthanum gallates as electrolytes for intermediate temperature solid oxides fuel cells: From materials processing to electrical and thermo-mechanical properties, J Eur Ceram Soc 36 (2016) 1–16. https://doi.org/10.1016/j.jeurceramsoc.2015.09.025.

[246] Z. Bi, B. Yi, Z. Wang, Y. Dong, H. Wu, Y. She, M. Cheng, A high-performance anode-supported SOFC with LDC-LSGM bilayer electrolytes, Electrochemical and Solid-State Letters 7 (2004). https://doi.org/10.1149/1.1667016.

[247] K. Li, K. Świerczek, P. Winiarz, A. Brzoza-Kos, A. Stępień, Y. Zhang, K. Zheng, K. Cichy, A. Niemczyk, Y. Naumovich, Optimizing the Copper Content in GdBa0.5Sr0.5Co2-xCuxO5+δ Double Perovskites as the High Performance Oxygen Electrodes for Reversible Solid Oxide Cells, ECS Trans 111 (2023) 1223–1230. https://doi.org/10.1149/11106.1223ecst.

[248] K. Li, K. Świerczek, P. Winiarz, A. Brzoza-Kos, A. Stępień, Z. Du, Y. Zhang, K. Zheng, K. Cichy, A. Niemczyk, Y. Naumovich, Unveiling the Electrocatalytic

Activity of the GdBa0.5Sr0.5Co2-xCuxO5+δ (x ≥ 1) Oxygen Electrodes for Solid Oxide Cells, ACS Appl Mater Interfaces 15 (2023) 39578–39593. https://doi.org/10.1021/acsami.3c08667.

[249] L. Zhao, J. Shen, B. He, F. Chen, C. Xia, Synthesis, characterization and evaluation of PrBaCo2-xFexO5+δ as cathodes for intermediate-temperature solid oxide fuel cells, Int J Hydrogen Energy 36 (2011) 3658–3665. https://doi.org/10.1016/j.ijhydene.2010.12.064.

[250] Y.N. Kim, J.H. Kim, A. Manthiram, Effect of Fe substitution on the structure and properties of LnBaCo2-xFexO5+δ (Ln = Nd and Gd) cathodes, J Power Sources 195 (2010) 6411–6419. https://doi.org/10.1016/j.jpowsour.2010.03.100.

[251] X. Huang, J. Feng, H.R.S. Abdellatif, J. Zou, G. Zhang, C. Ni, Electrochemical evaluation of double perovskite PrBaCo2-xMnxO5+δ (x = 0, 0.5, 1) as promising cathodes for IT-SOFCs, Int J Hydrogen Energy 43 (2018) 8962–8971. https://doi.org/10.1016/j.ijhydene.2018.03.163.

[252] J.H. Kim, A. Manthiram, Layered NdBaCo2-xNixO5+δ perovskite oxides as cathodes for intermediate temperature solid oxide fuel cells, Electrochim Acta 54 (2009) 7551–7557. https://doi.org/10.1016/j.electacta.2009.08.021.

[253] R.D. Shannon, Revised Effective Ionic Radii and Systematic Studies of Interatomie Distances in Halides and Chaleogenides, 1976.

[254] Yu.G. Pashkevich, V.P. Gnezdilov, P. Lemmens, K.-Y. Choi, K.V. Lamonova, A.A. Gusev, G. Güntherodt, S.N. Barilo, S.V. Shiryaev, G.L. Bychkov, RAMAN STUDIES OF SINGLE AND POLYCRYSTALLINE COBALTATITES GdBaCo2O5+δ WITH δ CLOSE TO 0.5, in: Spectroscopy of Emerging Materials, 2005: pp. 195–204. http://www.wtv-books.de/nato-pco.htm.

[255] D. Marrocchelli, N.H. Perry, S.R. Bishop, Understanding chemical expansion in perovskite-structured oxides, Physical Chemistry Chemical Physics 17 (2015) 10028–10039. https://doi.org/10.1039/c4cp05885b.

[256] V.A. Cherepanov, T. V. Aksenova, L.Y. Gavrilova, K.N. Mikhaleva, Structure, nonstoichiometry and thermal expansion of the NdBa(Co,Fe)2O5+δ layered perovskite, Solid State Ion 188 (2011) 53–57. https://doi.org/10.1016/j.ssi.2010.10.021.

[257] Y.N. Kim, A. Manthiram, Layered LnBaCo2−xCuxO5+δ (0≤x≤1.0) Perovskite Cathodes for Intermediate-Temperature Solid Oxide Fuel Cells, J Electrochem Soc 158 (2011) B276. https://doi.org/10.1149/1.3527006.

[258] S.L. Cooper, T. Egami, J.B. Goodenough, J.-S. Zhou, Localized to Itinerant Electronic Transition in Perovskite Oxides, Springer, 2003.

[259] J. Hermet, G. Geneste, G. Dezanneau, Molecular dynamics simulations of oxygen diffusion in GdBaCo2O5.5, Appl Phys Lett 97 (2010). https://doi.org/10.1063/1.3504250.

[260] H. Shiiba, M. Nakayama, T. Kasuga, R.W. Grimes, J.A. Kilner, Calculation of arrangement of oxygen ions and vacancies in double perovskite GdBaCo2O5+δ by first-principles DFT with Monte Carlo simulations, Physical Chemistry Chemical Physics 15 (2013) 10494–10499. https://doi.org/10.1039/c3cp50316j.

[261] C. Shivakumara, M.S. Hegde, G.N. Subbanna, Synthesis, structure and IR absorption studies of LnBaCuCoO5 (Ln = rare earth) oxides, Bulletin of Materials Science 19 (1996) 607–613.

[262] M. West, A. Manthiram, Layered LnBa1-xSrxCoCuO5+δ (Ln = Nd and Gd) perovskite cathodes for intermediate temperature solid oxide fuel cells, Int J Hydrogen Energy 38 (2013) 3364–3372. https://doi.org/10.1016/j.ijhydene.2012.12.133.

[263] Z. Du, Z. Zhang, A. Niemczyk, A. Olszewska, N. Chen, K. Świerczek, H. Zhao, Unveiling the effects of A-site substitutions on the oxygen ion migration in A2-xA′xNiO4+δ by first principles calculations, Physical Chemistry Chemical Physics 20 (2018) 21685–21692. https://doi.org/10.1039/c8cp04392b.

[264] A. Olszewska, K. Świerczek, W. Skubida, Z. Du, H. Zhao, B. Dabrowski, Versatile Application of Redox Processes for REBaCoMnO5+δ (RE: La, Pr, Nd, Sm, Gd, and Y) Oxides, Journal of Physical Chemistry C 123 (2019) 48–61. https://doi.org/10.1021/acs.jpcc.8b08585.

[265] G.C. Kostogloudis, P. Fertis, C. Ftikos, Electronic conductivity in the Pr1-xSrxCo1-yMnyO3-δ system, Solid State Ion 118 (1999) 241–249.

[266] D. Stroud, Generahxed effective-medium approach to the conductivity of an inhomogeneous materials, n.d.

[267] A. Kabir, B. Lemieszek, M. Varenik, V. Buratto Tinti, S. Molin, I. Lubomirsky, V. Esposito, F. Kern, Enhanced Mechanical and Electromechanical Properties of Compositionally Complex Zirconia Zr1-x(Gd1/5Pr1/5Nd1/5Sm1/5Y1/5)xO2−δ Ceramics, ACS Appl Mater Interfaces 16 (2024) 12765–12772. https://doi.org/10.1021/acsami.3c17501.

[268] G.M. Tomboc, X. Zhang, S. Choi, D. Kim, L.Y.S. Lee, K. Lee, Stabilization, Characterization, and Electrochemical Applications of High-Entropy Oxides: Critical Assessment of Crystal Phase–Properties Relationship, Adv Funct Mater 32 (2022). https://doi.org/10.1002/adfm.202205142.

[269] A. Sarkar, B. Breitung, H. Hahn, High entropy oxides: The role of entropy, enthalpy and synergy, Scr Mater 187 (2020) 43–48. https://doi.org/10.1016/j.scriptamat.2020.05.019.

[270] Y. Chen, X. Nie, B. Wang, C. Xia, W. Dong, X. Wang, H. Wang, B. Zhu, Tuning La0.6Sr0.4Co0.2Fe0.8O3-δ perovskite cathode as functional electrolytes for advanced low-temperature SOFCs, Catal Today 355 (2020) 295–303. https://doi.org/10.1016/j.cattod.2019.05.064.

[271] M. Liu, M. Liu, D. Ding, K. Blinn, X. Li, L. Nie, Enhanced performance of LSCF cathode through surface modification, Int J Hydrogen Energy 37 (2012) 8613–8620. https://doi.org/10.1016/j.ijhydene.2012.02.139.

[272] H. Kozuka, K. Ohbayashi, K. Koumoto, Electronic conduction in La-based perovskite-type oxides, Sci Technol Adv Mater 16 (2015). https://doi.org/10.1088/1468-6996/16/2/026001.

[273] J. Mizusaki, SOLID STATE IOIIICS Nonstoichiometry, diffusion, and electrical properties of perovskite-type oxide electrode materials, Solid State Ion 52 (1992) 79–91.

[274] H.C. Yu, K.Z. Fung, Electrode properties of La1-xSrxCuO2.5-δ as new cathode materials for intermediate-temperature SOFCs, J Power Sources 133 (2004) 162–168. https://doi.org/10.1016/j.jpowsour.2004.02.002.

[275] M. Zheng, X. Liu, W. Su, Preparation and performance of La1-xSrxCuO3-δ as cathode material in IT-SOFCs, J Alloys Compd 395 (2005) 300–303. https://doi.org/10.1016/j.jallcom.2004.11.034.

[276] N.P. Brandon, S. Skinner, B.C.H. Steele, Recent Advances in Materials for Fuel Cells, Annu Rev Mater Res 33 (2003) 183–213. https://doi.org/10.1146/annurev.matsci.33.022802.094122.

[277] Q. Sun, L. Sun, Y. Dou, Q. Li, N. Li, L. Huo, H. Zhao, Insights into the oxygen reduction reaction on Cu-doped SrFeO3-δ cathode for solid oxide fuel cells, J Power Sources 497 (2021). https://doi.org/10.1016/j.jpowsour.2021.229877.

[278] X. Kong, G. Liu, Z. Yi, X. Ding, NdBaCu2O5+δ and NdBa0.5Sr0.5Cu2O5+δ layered perovskite oxides as cathode materials for IT-SOFCs, Int J Hydrogen Energy 40 (2015) 16477–16483. https://doi.org/10.1016/j.ijhydene.2015.09.006.

[279] Q. Li, X. Zeng, L. Sun, H. Zhao, L. Huo, J.C. Grenier, Electrochemical performance of La2Cu1-xCoxO4 cathode materials for intermediate-temperature SOFCs, Int J Hydrogen Energy 37 (2012) 2552–2558. https://doi.org/10.1016/j.ijhydene.2011.11.014.

[280] X. Ding, X. Gao, J. Shen, J. Wang, W. Zhu, X. Wang, J. Jiang, Cobalt-free Sr0.7Y0.3CuO2+δ as a cathode for intermediate-temperature solid oxide fuel cell, Int J Hydrogen Energy 39 (2014) 1030–1038. https://doi.org/10.1016/j.ijhydene.2013.10.161.

[281] T. Noh, J. Ryu, J. Kim, Y.N. Kim, H. Lee, Structural and impedance analysis of copper doped LSM cathode for IT-SOFCs, J Alloys Compd 557 (2013) 196–201. https://doi.org/10.1016/j.jallcom.2013.01.002.

[282] C. Yao, J. Yang, S. Chen, J. Meng, K. Cai, Q. Zhang, Copper doped SrFe0.9-xCuxW0.1O3-δ (x = 0–0.3) perovskites as cathode materials for IT-SOFCs, J Alloys Compd 868 (2021). https://doi.org/10.1016/j.jallcom.2021.159127.

[283] Y. Zhang, H. Zhao, M. Zhang, Z. Du, W. Guan, S.C. Singhal, K. Świerczek, Boosting the Electrode Reaction Kinetics of SSOFCs by the Synergistic Effect of Nanoparticle Codecoration on Both the Cathode and Anode, Chemistry of Materials (2022). https://doi.org/10.1021/acs.chemmater.2c02861.

[284] M.J. Escudero, A. Aguadero, J.A. Alonso, L. Daza, A kinetic study of oxygen reduction reaction on La2NiO4 cathodes by means of impedance spectroscopy, Journal of Electroanalytical Chemistry 611 (2007) 107–116. https://doi.org/10.1016/j.jelechem.2007.08.006.

[285] Y. Chen, S. Yoo, Y. Choi, J.H. Kim, Y. Ding, K. Pei, R. Murphy, Y. Zhang, B. Zhao, W. Zhang, H. Chen, Y. Chen, W. Yuan, C. Yang, M. Liu, A highly active, CO2-tolerant electrode for the oxygen reduction reaction, Energy Environ Sci 11 (2018) 2458–2466. https://doi.org/10.1039/c8ee01140k.

[286] M. Li, Z. Sun, W. Yang, T. Hong, Z. Zhu, Y. Zhang, X. Wu, C. Xia, Mechanism for the enhanced oxygen reduction reaction of La0.6Sr0.4Co0.2Fe0.8O3-δ by strontium carbonate, Physical Chemistry Chemical Physics 19 (2017) 503–509. https://doi.org/10.1039/c6cp06204k.

[287] X. Meng, S. Lü, W.W. Yu, Y. Ji, Y. Sui, M. Wei, Layered perovskite LnBa0.5Sr0.5Cu2O5+δ (Ln = Pr and Nd) as cobalt-free cathode materials for solid oxide fuel cells, Int J Hydrogen Energy 43 (2018) 4458–4470. https://doi.org/10.1016/j.ijhydene.2018.01.033.

[288] Y.X. Liu, S.F. Wang, Y.F. Hsu, H.W. Kai, P. Jasinski, Characteristics of LaCo0.4Ni0.6-xCuxO3-δ ceramics as a cathode material for intermediate-temperature solid oxide fuel cells, J Eur Ceram Soc 38 (2018) 1654–1662. https://doi.org/10.1016/j.jeurceramsoc.2017.11.019.

[289] J.H. Kim, A. Manthiram, Layered LnBaCo2O5+δ perovskite cathodes for solid oxide fuel cells: An overview and perspective, J Mater Chem A Mater 3 (2015) 24195–24210. https://doi.org/10.1039/c5ta06212h.

[290] J. Peña-Martînez, A. Tarancón, D. Marrero-López, J.C. Ruiz-Morales, P. Núñez, Evaluation of GdBaCo2O5+δ as cathode material for doped lanthanum gallate electrolyte IT-SOFCs, Fuel Cells 8 (2008) 351–359. https://doi.org/10.1002/fuce.200800026.

[291] R. Su, Z. Lu, S. Jiang, Y. Shen, W. Su, K. Chen, Ag decorated (Ba,Sr)(Co,Fe)O3 cathodes for solid oxide fuel cells prepared by electroless silver deposition, Int J Hydrogen Energy 38 (2013) 2413–2420. https://doi.org/10.1016/j.ijhydene.2012.11.126.

[292] J. Xia, C. Wang, X. Wang, L. Bi, Y. Zhang, A perspective on DRT applications for the analysis of solid oxide cell electrodes, Electrochim Acta 349 (2020). https://doi.org/10.1016/j.electacta.2020.136328.

[293] D.A. Osinkin, An approach to the analysis of the impedance spectra of solid oxide fuel cell using the DRT technique, Electrochim Acta 372 (2021). https://doi.org/10.1016/j.electacta.2021.137858.

[294] Z. Du, K. Li, H. Zhao, X. Dong, Y. Zhang, K. Świerczek, A SmBaCo2O5+δ double perovskite with epitaxially grown Sm0.2Ce0.8O2-δ nanoparticles as a promising cathode for solid oxide fuel cells, J Mater Chem A Mater 8 (2020) 14162–14170. https://doi.org/10.1039/d0ta05602b.

[295] A. Olszewska, Z. Du, K. Świerczek, H. Zhao, B. Dabrowski, Novel ReBaCo1.5Mn0.5O5+δ (Re: La, Pr, Nd, Sm, Gd and Y) perovskite oxide: Influence of manganese doping on the crystal structure, oxygen nonstoichiometry, thermal expansion, transport properties, and application as a cathode material in solid oxide fuel cells, J Mater Chem A Mater 6 (2018) 13271–13285. https://doi.org/10.1039/c8ta03479f.

[296] C. Kuroda, K. Zheng, K. Świerczek, Characterization of novel GdBa0.5Sr0.5Co 2-xFexO5+δ perovskites for application in IT-SOFC cells, Int J Hydrogen Energy 38 (2013) 1027–1038. https://doi.org/10.1016/j.ijhydene.2012.10.085.

[297] W. Xia, X. Liu, F. Jin, X. Jia, Y. Shen, J. Li, Evaluation of calcium codoping in double perovskite PrBaCo2O5+δ as cathode material for IT-SOFCs, Electrochim Acta 364 (2020). https://doi.org/10.1016/j.electacta.2020.137274.

[298] G. Deng, K. Kang, Y. Liu, C. Wang, C.C. Wang, New Oxygen Regulation Strategy to Enhance the Oxygen Reduction Reaction of the Pr0.6Sr0.4Co0.2Fe0.8O3−δ Cathode through A-Site High-Entropy Engineering, ACS Sustain Chem Eng (2024). https://doi.org/10.1021/acssuschemeng.4c00707.

[299] Q. Yang, G. Wang, H. Wu, B.A. Beshiwork, D. Tian, S. Zhu, Y. Yang, X. Lu, Y. Ding, Y. Ling, Y. Chen, B. Lin, A high-entropy perovskite cathode for solid oxide fuel cells, J Alloys Compd 872 (2021). https://doi.org/10.1016/j.jallcom.2021.159633.

[300] J. Gong, P. Wu, Z. Bai, J. Ma, T. Li, Y. Yao, C. Jiang, Insight into the Electrospinning Process for SOFC Cathode Nanofibers, Journal of Physical Chemistry C 125 (2021) 7044–7053. https://doi.org/10.1021/acs.jpcc.1c00317.